Multijet Background Estimation For SUSY Searches And Particle Flow Offline Reconstruction Using The ATLAS Detector At The LHC

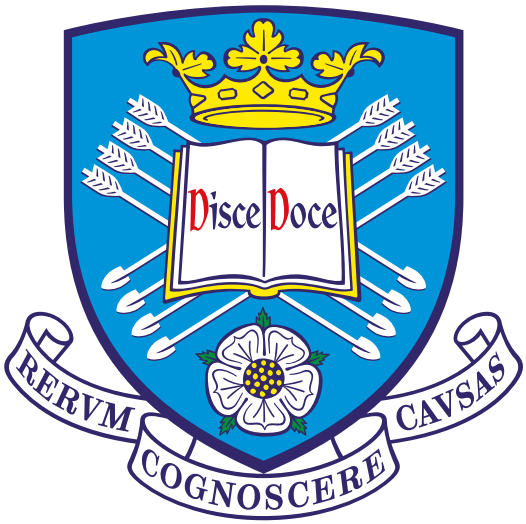

Gareth Thomas Fletcher

A Thesis Submitted for the Degree of Doctor of Philosophy in Physics

Department of Physics and Astronomy

The University of Sheffield

March 2015

Abstract

This thesis describes the jet smearing method, a data-driven technique for estimating the multijet background to Supersymmetry (SUSY) searches using the ATLAS detector at the Large Hadron Collider (LHC).

The final 2011 and 2012 "ATLAS jets, missing transverse energy and zero leptons analysis" searches for SUSY are also documented. These analyses used the full ATLAS 2011 4.7 fb^{-1} $\sqrt{s} = 7$ TeV and 2012 20.3 fb^{-1} $\sqrt{s} = 8$ TeV data sets. No statistically significant excess was found in either of these analyses; therefore, 95% C.L. mass exclusion limits were set on the mSUGRA/CMSSM $m_0 - m_{1/2}$ and $m_{\tilde{q}} - m_{\tilde{g}}$ mass planes, and the simplified squark-gluino-neutralino pMSSM model. The jet smearing method was used in these analyses to estimate the multijet distributions of the Signal, Validation and Control Regions and also to calculate the multijet background Transfer Factors.

This thesis also describes the missing transverse energy ($E_{\mathrm{T}}^{\mathrm{miss}}$) performance studies of the ATLAS particle flow (PFlow) offline reconstruction algorithm in $Z \to \mu\mu$, $t\bar{t}$ and Wt events using Monte Carlo simulated data and the ATLAS 2012 $\sqrt{s} = 8$ TeV data set. The particle flow $E_{\mathrm{T}}^{\mathrm{miss}}$ algorithms out-performed `MET_RefFinal` in most aspects, including resolution, scale and pile-up independence. The particle flow algorithm also described the expected M_T distribution in $t\bar{t}$ and Wt events better than `MET_RefFinal`.

Acknowledgements

First, I would like to thank my supervisor, Dan Tovey. There is no that doubt without his guidance, wisdom and direction over the course of my degree, this thesis would not have been written.

I would also like to give a special thank you to Mark Hodgkinson and Chris Young for all the help which you have both given me during my degree. It has been a pleasure to work with you both over the years, and I doubt some of the results would have been possible without either of you. I would like to thank James Foley for helping to proof read many chapters of my thesis.

Next, I would like to thank the Sheffield ATLAS group. I am sure that every person within the group has given me some help and guidance during my degree. I don't think the experience during my degree would have been as enjoyable without my numerous friends and colleagues within the Particle Physics and Particle Astrophysics group: to name a few Tim, Martin, Kerry, Steve, Ed and Brias. I also wish the group luck in future Bubble Chamber cups! I am sure my excellent defending will be missed.

I would like to thank the UK LTA 2012-14 crowd. My time at CERN would have never been as enjoyable without all of you. I would like to mention a few people in particular: Sam, Richard, Shaun, Carl and Nikki. It was a pleasure to organise the 2013 UK LTA CERN ski trip to Tignes, but I couldn't have done it without the other members of the committee (Sam, Rebecca and Tom).

Finally, I would like to give a special thank you to my family, my parents, Sue and Paul, and my brother and sister, James and Rachel. A special thank you to my sister for proof reading some of the first drafts; I know how challenging that must have been. Without the love and support of my family, I don't think I would have managed to complete my PhD, so this thesis is dedicated to you.

Contents

Author's Contribution **1**

1 Introduction **3**

2 Theoretical Background **5**
2.1 Introduction . . . 5
2.2 Standard Model . . . 5
2.2.1 Particle Content . . . 6
2.2.2 SM Gauge Group Theory . . . 7
2.2.3 The Electromagnetic Force . . . 8
2.2.4 The Strong Interaction . . . 8
2.2.5 The Weak Force and Electroweak Unification . . . 10
2.2.6 Mass and Higgs Mechanism . . . 11
2.2.7 Failings of the SM . . . 14
2.3 Supersymmetry . . . 16
2.3.1 Overview . . . 16
2.3.2 Minimal Supersymmetric Standard Model . . . 17
2.3.3 Unification of the Fundamental Forces . . . 19
2.3.4 Supersymmetry Breaking . . . 20
2.3.5 Implications of the Higgs Mass Measurement . . . 21
2.4 SUSY at the LHC . . . 21
2.4.1 Production Mechanisms . . . 21
2.4.2 Jet Algorithms . . . 22
2.4.3 Missing Transverse Energy . . . 25
2.4.4 SUSY Decays . . . 25
2.5 General Searches for SUSY at the LHC . . . 25
2.6 Summary . . . 31

3 The LHC and the ATLAS Detector **33**
3.1 Introduction . . . 33
3.2 The LHC . . . 33
3.3 The ATLAS Detector . . . 34
3.3.1 Overview of Physics Goals . . . 34
3.3.2 Coordinate System and Transverse Quantities . . . 35

3.3.3 Detector Overview . . . 37
3.3.4 Inner Detector . . . 38
3.3.5 Calorimetry . . . 40
3.3.6 Muon System . . . 44
3.3.7 Magnet Systems . . . 46
3.3.8 Trigger . . . 46
3.4 The Structure of an Event and MC Production . . . 48
3.4.1 Monte Carlo Production . . . 49
3.4.2 Monte Carlo Reweighting . . . 50
3.4.3 ATLAS 2011 $\sqrt{s} = 7$ TeV Monte Carlo Samples . . . 51
3.4.4 ATLAS 2012 $\sqrt{s} = 8$ TeV Monte Carlo Samples . . . 52
3.5 Data Samples . . . 53
3.6 The Reconstruction Stage . . . 54
3.6.1 Jets . . . 55
3.6.2 b-jets . . . 55
3.6.3 Electrons . . . 58
3.6.4 Photons . . . 58
3.6.5 Muons . . . 59
3.6.6 Missing Transverse Energy . . . 59
3.6.7 Resolving Overlapping Objects . . . 60
3.7 Systematic Uncertainties . . . 61
3.7.1 Jet Energy Scale and Jet Energy Resolution . . . 61
3.7.2 b-tagging Efficiencies . . . 63
3.7.3 Lepton Efficiencies . . . 63
3.7.4 Missing Transverse Energy . . . 64
3.7.5 Luminosity . . . 64
3.7.6 Monte Carlo Simulation . . . 64
3.8 Summary . . . 64

4 Particle Flow **65**
4.1 Introduction . . . 65
4.2 Background and Motivation . . . 65
4.3 ATLAS Particle Flow Algorithm . . . 67
4.3.1 Track-Cluster Matching . . . 67
4.3.2 Charged Shower Subtraction . . . 68
4.3.3 Calibration . . . 70
4.3.4 Particle Flow Object List . . . 70
4.4 $E_{\mathrm{T}}^{\mathrm{miss}}$ Performance in $Z \to \mu\mu$ Events . . . 70
4.4.1 $E_{\mathrm{T}}^{\mathrm{miss}}$ Algorithms . . . 73

4.4.2 Event Selection . . . 74
4.4.3 $Z \to \mu\mu$ MC Results . . . 74
4.4.4 $Z \to \mu\mu$ Data to MC Comparison Results . . . 80
4.4.5 Magnitude of the $E_{\mathrm{T}}^{\mathrm{miss}}$ and Muon Event Cleaning . . . 84
4.5 $E_{\mathrm{T}}^{\mathrm{miss}}$ Performance in $t\bar{t}$ and Wt Events . . . 88
4.5.1 $E_{\mathrm{T}}^{\mathrm{miss}}$ Algorithms . . . 89
4.5.2 Event Selection . . . 89
4.5.3 W Boson Reconstruction . . . 90
4.5.4 Results . . . 91
4.6 Summary . . . 97

5 Introduction to the Jet Smearing Method **99**
5.1 Introduction . . . 99
5.2 Jet Response . . . 99
5.3 Overview . . . 100
5.3.1 Motivation . . . 101
5.3.2 Jet Smearing . . . 102
5.3.3 Key Assumptions of the Method . . . 103
5.4 Seed Selection . . . 103
5.4.1 Seed Selection in the 2011 Analysis . . . 105
5.4.2 Seed Selection in the 2012 Analysis . . . 106
5.5 Summary . . . 107

6 Measuring the Jet Response **109**
6.1 Introduction . . . 109
6.2 MC Jet Response . . . 109
6.2.1 Generation of the MC Jet Response . . . 110
6.2.2 2011 MC Response Maps . . . 111
6.2.3 2012 MC Response Maps . . . 111
6.2.4 Modifying the MC Jet Response . . . 112
6.3 Dijet p_{T} Balance Analysis . . . 114
6.3.1 Event Selection . . . 115
6.3.2 The 2011 $\sqrt{s} = 7$ TeV Data Set Analysis . . . 115
6.3.3 The 2012 $\sqrt{s} = 8$ TeV Data Set Analysis . . . 117
6.4 Dijet $\Delta\phi$ Analysis . . . 121
6.4.1 Introduction and Motivation . . . 121
6.4.2 Analysis Method . . . 121
6.4.3 Results . . . 122
6.5 Mercedes Analysis . . . 125
6.5.1 Introduction . . . 125

6.5.2 Event Selection . . . 126
6.5.3 Non-Modified Jet Response R_2 Distributions . . . 129
6.5.4 Low-Side Tail Modification . . . 133
6.5.5 R_2 Distributions with the Modified Low-Side Tail . . . 140
6.6 Uncertainties of the Jet Smearing Method . . . 142
6.6.1 Statistical Uncertainties . . . 142
6.6.2 Uncertainties on the Shape of the Jet Response Function . . . 145
6.6.3 Seed Selection Cut . . . 146
6.7 Validation Studies . . . 147
6.7.1 The $|\eta|$ Dependence of the Jet Response . . . 147
6.7.2 Transition Point Study . . . 151
6.7.3 Forward Jet Smearing Study . . . 154
6.8 Summary . . . 155

7 Jets, Missing Transverse Energy and Zero Leptons Analysis Search for SUSY 157
7.1 Introduction . . . 157
7.2 Analysis Strategy . . . 157
7.2.1 Analysis Variables . . . 158
7.2.2 Event Selection . . . 160
7.2.3 SM Background Estimation . . . 160
7.2.4 Statistical Interpretation . . . 162
7.3 SUSY Search using the 2011 Data Set . . . 163
7.3.1 Triggers and Simulated Samples . . . 164
7.3.2 Event Selection . . . 164
7.3.3 Background Estimation . . . 166
7.3.4 Results . . . 170
7.4 SUSY Search using the 2012 Data Set . . . 173
7.4.1 Triggers and Simulated Samples . . . 173
7.4.2 Event Selection . . . 173
7.4.3 Background Estimation . . . 176
7.4.4 Results . . . 181
7.5 Summary . . . 185

8 Summary 187

APPENDICES 187

A Particle Flow Auxiliary Information 189
A.1 Gaussian Fitting to $E_{\mathrm{T}}^{\mathrm{miss}}$ Distributions . . . 189

Bibliography 191

List of Tables

2.1 The fermionic particle content of the Standard Model . . . 7
2.2 The bosonic particle content of the Standard Model . . . 7
2.3 Chiral supermultiplets within in the MSSM . . . 18
2.4 Gauge supermultiplets within in the MSSM . . . 18
2.5 Mixing within in the MSSM . . . 19

3.1 Technical design parameters of the LHC . . . 36
3.2 Summary of the different objects in the ATLAS trigger menu . . . 48
3.3 Calorimeter energy resolution goals of the ATLAS detector . . . 62

4.1 $Z \to \mu\mu$ event selection cuts . . . 75
4.2 `MET_RefFinal` $E_{\mathrm{T}}^{\mathrm{miss}}$ results . . . 87
4.3 Particle flow `RefFinal` $E_{\mathrm{T}}^{\mathrm{miss}}$ results . . . 87
4.4 Particle flow `Hybrid` $E_{\mathrm{T}}^{\mathrm{miss}}$ results . . . 88
4.5 $t\bar{t}$ and Wt pre-event selection cuts . . . 90

5.1 Single-jet triggers in the 2011 analysis . . . 105
5.2 Single jet triggers in the 2012 analysis . . . 106

6.1 Dijet balance pre-event selection cuts . . . 116
6.2 σ_A fit parameters for the 2011 analysis . . . 118
6.3 σ_A fit parameters for the 2012 analysis . . . 119
6.4 Dijet $\Delta\phi$ analysis final event selection cuts . . . 122
6.5 $\sigma_{\Delta\phi(j_1,j_2)}$ fit parameters for the 2012 analysis . . . 123
6.6 Event pre-selection cuts for the Mercedes analysis . . . 126
6.7 Mercedes event angular selection cuts . . . 128
6.8 Values of $\Delta\sigma_{\mathrm{tail}}$ for the 2011 inclusive jet response . . . 139
6.9 Values of $\Delta\sigma_{\mathrm{tail}}$ for the 2012 b-veto jet response . . . 139
6.10 Values of $\Delta\sigma_{\mathrm{tail}}$ for the 2012 b-tag jet response . . . 139

7.1 Triggers used for the 2011 analysis . . . 164
7.2 MC simulated samples used in the 2011 analysis . . . 164
7.3 Summary of the 2011 analysis Signal Region selection criteria . . . 165
7.4 SM background CRs used in the 2011 analysis . . . 166
7.5 multijet background Transfer Factors calculated in the 2011 analysis . . . 167

7.6 SR results table for the 2011 data set analysis 171
7.7 Trigger used in the 2012 analysis 173
7.8 Simulated MC samples used in the 2012 analysis 174
7.9 Summary of the 2012 analysis Signal Region selection criteria 175
7.10 SM Background CRs used in the 2012 analysis 176

List of Figures

2.1 Particle content within the SM . . . 6
2.2 A spontaneous symmetry breaking scalar field potential . . . 12
2.3 Example radiative corrections to the Higgs mass squared . . . 17
2.4 The evolution of the gauge groups couplings in the SM and the MSSM . . . 19
2.5 MSSM Higgs boson mass as a function of $\tilde{t}_1$ mass . . . 21
2.6 $\sqrt{s} =$ 8 TeV NLO cross-sections for sparticle production at the LHC . . . 22
2.7 A schematic showing an example $t\bar{t}h$ event structure . . . 23
2.8 Two dimensional schematics of lack of infra-red and collinear safety in jet algorithms. 24
2.9 Dijet event recorded with the ATLAS detector . . . 24
2.10 Direct $\tilde{q}$ and $\tilde{g}$ decays . . . 26
2.11 ATLAS searches SUSY summary plots . . . 27
2.12 CMS searches SUSY summary plots . . . 28
2.13 LHC searches summary plots for mSUGRA/CMSSM and the $\tilde{t}_1$ quark . . . 29
2.14 LHC searches summary plots for mSUGRA/CMSSM and the $\tilde{t}_1$ quark . . . 30

3.1 The LHC accelerator complex . . . 35
3.2 The ATLAS coordinate system . . . 36
3.3 The ATLAS detector . . . 38
3.4 The ATLAS inner detector . . . 39
3.5 The ATLAS calorimeters . . . 41
3.6 An ATLAS electromagnetic calorimeter module . . . 42
3.7 An ATLAS hadronic calorimeter module . . . 43
3.8 Measuring the p_{T} of muons in the ATLAS muon system. . . . 44
3.9 Schematics of the ATLAS muon system. . . . 45
3.10 Schmetic of the ATLAS muon trigger system . . . 45
3.11 Schematic of the ATLAS manget systems . . . 46
3.12 Photograph of the ATLAS toroid mangets . . . 47
3.13 Schematic of the event reconstruction process of the ATLAS detector . . . 50
3.14 MSTW2008 parton distribution functions for the LHC . . . 51
3.15 The $\langle\mu\rangle$ distributions of the 2012 data set and two MC samples . . . 52
3.16 Summary of the recorded luminosity of the ATLAS detector for the 2011 and 2012 data sets . . . 54
3.17 Schematic showing the ATLAS jet reconstruction and calibration processes . . . 56
3.18 Schematic showing a B-meson decay within a jet . . . 57

3.19 The b-tagging efficiency of the MV1 algorithm . . . 57
3.20 The ATLAS jet p_{T} resolution measured in 2012 $\sqrt{s} = 8$ TeV data for central jets . 63

4.1 The p_{T} resolution of a charged particle with $|\eta| = 1$ in the ATLAS detector . . . 66
4.2 Schematic of the different measurements available for hadronic particles in the CDF detector in a hypothetical narrow jet event . . . 67
4.3 Schematic showing the splitting of a hadronic shower between different layers of the calorimeter . . . 69
4.4 Schematic showing the optimal outcome of the charged shower subtraction algorithm 69
4.5 A Z boson with accompanying jet candidate event recorded with the ATLAS detector. 71
4.6 $E_{\mathrm{T}}^{\mathrm{miss}}$ transverse energy projections with respect to the Z boson . . . 71
4.7 Schematic showing the jet-vertex Fraction of two jets . . . 73
4.8 Parallel and perpendicular $E_{\mathrm{T}}^{\mathrm{miss}}$ distributions for the 0 – 10 GeV Z boson p_{T} bin . . 76
4.9 Parallel and perpendicular $E_{\mathrm{T}}^{\mathrm{miss}}$ distributions as a function of the Z boson p_{T} . . . 77
4.10 Hybrid parallel $E_{\mathrm{T}}^{\mathrm{miss}}$ distributions in different bins of Z boson p_{T} . . . 78
4.11 Parallel and perpendicular $E_{\mathrm{T}}^{\mathrm{miss}}$ distributions as a function of $\langle\mu\rangle$ . . . 79
4.12 Parallel and perpendicular $E_{\mathrm{T}}^{\mathrm{miss}}$ resolution as a function of NPV . . . 80
4.13 MET_RefFinal and particle flow parallel $E_{\mathrm{T}}^{\mathrm{miss}}$ distributions as a function of Z boson p_{T} . . . 82
4.14 MET_RefFinal and particle flow parallel $E_{\mathrm{T}}^{\mathrm{miss}}$ distributions as a function of NPV . 83
4.15 The magnitude of the $E_{\mathrm{T}}^{\mathrm{miss}}$ distributions in $Z \to \mu\mu$ events without any muon event cleaning cuts . . . 84
4.16 The magnitude of the $E_{\mathrm{T}}^{\mathrm{miss}}$ distributions in $Z \to \mu\mu$ events with the additional muon cleaning cuts . . . 85
4.17 The $\left|E_{\mathrm{T}}^{\mathrm{miss}}\right|$ distributions for MET_RefFinal and particle flow in $Z \to \mu\mu$ events . . 86
4.18 Double ratio of $t\bar{t}/Z \to \mu\mu$ for particle flow divided by MET_RefFinal . . . 88
4.19 Single muon decays of $t\bar{t}$ and Wt events . . . 89
4.20 The M_T distribution for the ATLAS 2012 data set in $t\bar{t}$ and Wt events . . . 92
4.21 The M_{jj} distribution for the ATLAS 2012 data set in $t\bar{t}$ and Wt events . . . 93
4.22 W mass peak within the M_T distribution for the ATLAS 2012 data set in $t\bar{t}$ and Wt events after the application of the cut on M_{jj} . . . 95
4.23 W mass peak within the M_{jj} distribution for the ATLAS 2012 data set in $t\bar{t}$ and Wt events after the application of the cut on M_T . . . 96

5.1 Jet smearing schematic . . . 103
5.2 $E_{\mathrm{T}}^{\mathrm{miss}}$-significance distributions . . . 104
5.3 Leading jet p_{T} distributions for the pseudo-data in the 2011 data set analysis . . . 106
5.4 Leading jet p_{T} distributions for pseudo-data in the 2012 data set analysis . . . 108

6.1 The 2011 inclusive MC jet response map . . . 111

6.2 Truth jet p_{T} projections of the 2011 inclusive MC jet response map . . . 112
6.3 The 2012 MC jet response maps . . . 112
6.4 Truth jet p_{T} projections of the 2012 MC jet response maps . . . 113
6.5 p_{T} asymmetry against average dijet p_{T} in the 2011 $\sqrt{s} = 7$ TeV data set analysis . 116
6.6 Summary of the 2011 dijet p_{T} balance analysis results . . . 117
6.7 p_{T} asymmetry against average dijet p_{T} in the 2012 $\sqrt{s} = 8$ TeV data set analysis . 119
6.8 Summary of the 2012 b-veto dijet p_{T} balance analysis results . . . 120
6.9 $|\pi - \Delta\phi_{(j_1,j_2)}|$ against average dijet p_{T} in the 2012 $\sqrt{s} = 8$ TeV data set analysis . . 123
6.10 Summary of the results from the 2012 b-veto dijet $\Delta\phi$ analysis. . . . 124
6.11 Mercedes event topolgies . . . 125
6.12 Mercedes event topolgies after jet relabeling . . . 128
6.13 $\Delta\phi$ distributions for candidate Mercedes events . . . 129
6.14 ATLAS candidate Mercedes event displays . . . 130
6.15 2011 Mercedes analysis inclusive MC R_2 distributions . . . 131
6.16 2012 Mercedes analysis b-tag MC R_2 distributions . . . 131
6.17 2012 Mercedes analysis b-veto MC R_2 distributions . . . 132
6.18 Crystal Ball fit to the MC jet response function . . . 134
6.19 Example Low-side tail shapes produced with the double Gaussian fitting method . 135
6.20 Gaussian R_2 pseudo-data distributions . . . 136
6.21 The 2011 normailised tail region R_2 distributions . . . 138
6.22 The 2012 normailised tail region R_2 distributions . . . 138
6.23 2011 Mercedes analysis optimal inclusive R_2 distributions . . . 140
6.24 2012 Mercedes analysis optimal b-tag R_2distributions . . . 140
6.25 2012 Mercedes analysis optimal b-veto R_2 distributions . . . 141
6.26 Seed event smearing schematic . . . 144
6.27 2011 Mercedes analysis R_2 $|\eta|$ distributions . . . 148
6.28 2012 b-veto Mercedes analysis R_2 $|\eta|$ distributions . . . 149
6.29 2012 b-tag Mercedes analysis R_2 $|\eta|$ distributions . . . 150
6.30 The transition point jet response functions . . . 151
6.31 2012 b-veto Mercedes analysis transition point R_2 distributions . . . 152
6.32 2012 b-tagged Mercedes analysis transition point R_2 distributions . . . 153
6.33 2012 b-veto Mercedes analysis R_2 distributions with the smearing of forward jets . 155
6.34 2012 b-tag Mercedes analysis R_2 distributions with the smearing of forward jets . . 156

7.1 One-step $\tilde{q}$ and $\tilde{g}$ decays . . . 158
7.2 Candidate for a SUSY event with zero leptons . . . 159
7.3 A schematic showing an example simplistic analysis region layout . . . 162
7.4 CR2 m_{eff} (incl.) distributions for SRs A, C and D . . . 168
7.5 Minimum $\Delta\phi$(jet,$E_{\mathrm{T}}^{\mathrm{miss}}$) distribution for SRs A, C and D . . . 169

7.6 Mass exclusion limits on the sq-gl-neutralino simplified pMSSM model and the $m_0 - m_{1/2}$ mSUGRA/CMSSM mass plane in the 2011 analysis 172
7.7 The multijets background Transfer Factors in the 2012 analysis 177
7.8 CRQ m_{eff} (incl.) distributions for CRQs 2j, 3j and 5j 178
7.9 Minimum $\Delta\phi$(jet,$E_{\text{T}}^{\text{miss}}$) distributions for SRs 2j, 3j and 5j 179
7.10 The observed $E_{\text{T}}^{\text{miss}}/m_{\text{eff}}$ distributions for CRQs 2j, 3j and 5j 180
7.11 Summary of the Signal Region results 181
7.12 Mass exclusion limits on the mSUGRA/CMSSM model in the $m_0 - m_{1/2}$ and $m_{\tilde{q}} - m_{\tilde{g}}$ mass planes in the 2012 analysis 182
7.13 Mass exclusion limits on the sq-gl-neutrino simplified pMSSM model in the $m_{\tilde{q}} - m_{\tilde{g}}$ mass plane in the 2012 analysis 183
7.14 Mass exclusion limits for the strong production of squarks and gluinos in direct decays to the LSP in the 2012 analysis 184
7.15 ATLAS searches for SUSY in the mSUGRA/CMSSM model 185

A.1 Gaussian fits to $E_{\text{T}}^{\text{miss}}$ distributions 190

Author's Contribution

It should be noted that the content of this thesis builds upon the work performed by a large number of people within the ATLAS collaboration. The work carried out by the author over his degree is summarised in this section.

Multijet Background Estimation

The main research content of this thesis is the development of a data-driven method of multijet background estimation called the 'jet smearing method' (see Chapters 5 and 6). This method was used for estimating the multijet background to supersymmetry (SUSY) searches. The author provided the multijet background estimations for the ATLAS "jets, $E_{\mathrm{T}}^{\mathrm{miss}}$ and zero leptons" analysis using the jet smearing method. These predictions were directly used in two published papers ([1] and [2]) and several conference notes ([3], [4] and [5]). The method was also used in several other ATLAS SUSY analyses, where the author provided his assistance to implement the method. This included searches for direct stop quark production ([6]) and Z+jets ([7]).

The author was also responsible for the research and development of the jet smearing method, which included work that led to the inclusion of ϕ-angular smearing into the jet smearing method; this is documented in Chapter 6 of this thesis.

Finally, the author was responsible for the coordination and the multijet sections of the internal documentation summarising the implementation of the method during run-I of the Large Hadron Collider (LHC) [8].

Particle Flow

The author contributed to the missing transverse energy ($E_{\mathrm{T}}^{\mathrm{miss}}$) performance studies of the particle flow offline reconstruction algorithm. The $E_{\mathrm{T}}^{\mathrm{miss}}$ performance studies were performed on Monte Carlo simulation and 2012 $\sqrt{s}$= 8 TeV data in $Z \rightarrow \mu\mu$, $t\bar{t}$ and Wt events. The author studied how the particle flow reconstruction algorithm compared to the standard ATLAS offline reconstruction algorithm. These studies are documented in detail in Chapter 4.

Service Work

The author was responsible for creating the SCT offline data quality twiki shifting tool. This tool was used by offline data quality shifters to check the validity of recorded data towards the end of the 2012 data taking period. The author also undertook numerous online data quality shifts in the ATLAS control room at point 1 during the 2012 data taking period. The shifter would monitor the luminosity and quality of the data being recorded during stable beams, and report any potential issues with the recorded data. For example, if the data was not suitable for physics analysis.

Additional Contributions

The author presented the results from the ATLAS 2012 "jets, $E_{\mathrm{T}}^{\mathrm{miss}}$ and zero leptons" analysis at the national 2014 IOP HEPP & APP conference in Egham. The author has also presented several posters about the jet smearing multijet background estimation technique.

The author was an ATLAS cavern guide and a CERN public guide during LS1. The author has also participated in numerous outreach activities bringing the high energy research performed at CERN to the wider public.

Chapter 1

Introduction

The scope of high energy particle physics research has been extended by the construction of the Large Hadron Collider (LHC) and its physics experiments. With over two years of data now recorded at an unprecedented energy scale (for collider physics), the analysis of this data has increased our fundamental understanding of the interactions of particles. This thesis focuses primarily on the estimation of the multijet background in zero lepton supersymmetry (SUSY) searches using the ATLAS detector at the LHC. Also, missing transverse energy ($E_{\mathrm{T}}^{\mathrm{miss}}$) performance studies of the Particle Flow offline reconstruction algorithm are documented.

Chapter 2 gives a brief overview of the Standard Model (SM) of particle physics and an introduction to its supersymmetric extension. The SM is the current theoretical framework used in particle physics to describe the interactions of particles. The motivations behind supersymmetry and possible SUSY scenarios that could be found at the LHC are also discussed in this chapter.

Chapter 3 provides an overview of the CERN accelerator complex, LHC machine and a detailed description of the ATLAS detector. Topics which are important to physics analyses are also covered, such as the data and Monte Carlo samples used, object reconstruction of physics objects with the ATLAS detector and the overlap removal procedure.

The $E_{\mathrm{T}}^{\mathrm{miss}}$ performance studies of the Particle Flow offline reconstruction algorithm are documented in Chapter 4. Event reconstruction is an essential part of data preparation for physics analysis, and therefore, must be researched extensively. This chapter compares the $E_{\mathrm{T}}^{\mathrm{miss}}$ performance of the Particle Flow reconstruction algorithm to the standard ATLAS offline reconstruction algorithm. It focuses on $E_{\mathrm{T}}^{\mathrm{miss}}$ performance of $Z \to \mu\mu$, $t\bar{t}$ and Wt events in MC simulation and the 2012 $\sqrt{s} = 8\,\mathrm{TeV}$ data set recorded with the ATLAS detector.

Chapter 5 provides an introduction to the jet smearing method. It provides an overview of the method, and explains the motivations and main assumptions behind the method. Following the introduction of the jet smearing method, Chapter 6 describes the measurement of the jet response

of the ATLAS detector and the techniques used to constrain the jet response to the ATLAS 2011 $\sqrt{s} = 7\,\text{TeV}$ and 2012 $\sqrt{s} = 8\,\text{TeV}$ data sets. It also documents the investigative studies which were used to validate the jet smearing method.

Chapter 7 describes the "ATLAS jets, $E_{\text{T}}^{\text{miss}}$ and zero leptons" analysis search for supersymmetry using the ATLAS 2011 $\sqrt{s} = 7\,\text{TeV}$ and 2012 $\sqrt{s} = 8\,\text{TeV}$ data sets. The chapter includes several mass exclusion contours for different theoretical SUSY models. It also explains how the jet smearing method was used to estimate the multijet background Transfer Factors and multijet background distributions in the Signal and Control Regions of the analysis.

Finally, Chapter 8 provides a brief summary of Chapters 2–7 and a few final concluding remarks about the research that is documented in this thesis.

Chapter 2

Theoretical Background

2.1 Introduction

This chapter will provide a brief overview of the Standard Model (SM) and an introduction to one of its supersymmetric (SUSY) extensions, the Minimal Supersymmetric Standard Model (MSSM). The SM is the theoretical framework used in particle physics to describe and predict the interactions of particles. Some of the predictions made by the SM have been confirmed to very high levels of accuracy, such as the anomalous magnetic moment of the electron, which is in agreement with experiment for over ten orders of magnitude [9]. Section 2.2 will outline the particle content and interactions described by the SM and provide a brief overview of the Higgs mechanism responsible for the electroweak symmetry breaking of the SM. Itshould be noted that this section closely follows the prescriptions detailed in several books on the SM, and non-experts are encouraged to consult references [10, 11, 12, 13]. Next, section 2.3 will give a brief introduction to supersymmetry, which will include why supersymmetry is one of the most favoured extensions to the SM and the implications of the measured Higgs boson mass for supersymmetry. Then, section 2.4 will provide a description of the strong production mechanisms of SUSY particles at the LHC and introduce jet algorithms and missing transverse energy ($E_{\mathrm{T}}^{\mathrm{miss}}$). Finally, section 2.5 briefly outlines some of the general searches for supersymmetric particles at the Large Hadron Collider (LHC).

2.2 Standard Model

The Standard Model of particle physics (see for example [10, 11, 12, 13]) was constructed in the late 1960s and 1970s to explain the vast amounts of experimental data being analysed in particle physics at the time. The SM is a quantum field theory, and postulates that all the matter in the Universe is made up of fundamental elementary fermions that interact via particle fields mediated by gauge bosons [10, 12]. It provides a single description of the matter content and interactions within the Universe. However, the SM is known to be incomplete, as it does not have a true candidate particle for dark matter (see section 2.2.7) and does not encompass gravity within its theoretical framework.

2.2.1 Particle Content

In the Standard Model, fundamental particles are proposed as excitations of quantum fields. The fundamental particles are then divided into two groups based on a quantum number which describes their intrinsic angular momentum, known as *spin* (s). The matter particles are fermions with half-integer spin $s = 1/2$ (in units of $\hbar$) [10, 11]. The interactions between the matter particles are mediated by a group of bosons with integer spin [1]. The bosons are responsible for the three interactions described within the SM: the strong interaction, the weak interaction and electromagnetism[2]. The fermions are divided further based on their sensitivity to the strong interaction. Fermions that are sensitive to the strong interaction are called quarks; otherwise, they fall into the category known as leptons [10, 11].

Figure 2.1 shows the particle content of the SM, where the quarks and leptons are shown in three generations and the force carriers are shown in the bosons section. The SM also postulates a fundamental scalar boson responsible for the electroweak symmetry breaking within the SM (see section 2.2.6), known as the Higgs boson.

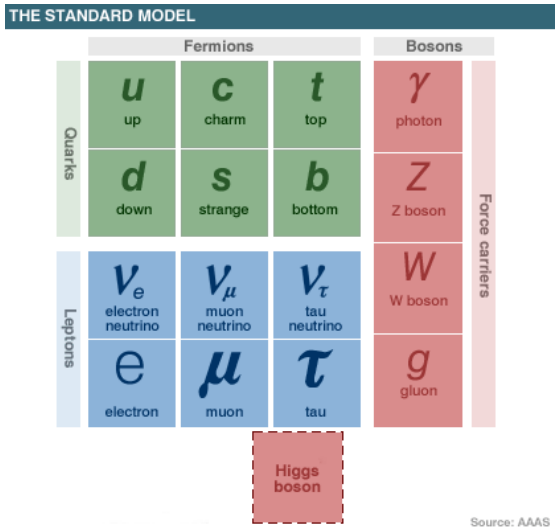

Figure 2.1: The particle content within the Standard Model. The quarks and leptons are shown in the fermions section and the force carriers are shown in the bosons section. The Higgs boson is also shown which is involved the electroweak symmetry breaking within the SM. This figure was taken from [14].

Table 2.1 lists the fundamental fermions within the SM, along with some of their elementary properties. Table 2.2 lists the force carriers within the SM, along with their elementary properties.

[1] Bosons can also interact with each other, or even themselves, not just the matter particles.
[2] Gravity is negligible at this scale, therefore, The Standard Model does not model it.

Leptons			Quarks		
Particle	Mass (MeV/c^2)	Charge (e)	Particle	Mass (MeV/c^2)	Charge (e)
electron (e)	0.511	-1	up (u)	$2.3^{+0.7}_{-0.5}$	$\frac{2}{3}$
electron neutrino (ν_e)	$< 2 \times 10^{-6}$	0	down (d)	$4.8^{+0.7}_{-0.3}$	$-\frac{1}{3}$
muon (μ)	105.65	-1	charm (c)	1275 ± 25	$\frac{2}{3}$
muon neutrino(ν_μ)	$< 2 \times 10^{-6}$	0	strange (s)	95 ± 5	$-\frac{1}{3}$
tau (τ)	1776.82	-1	top (t)	173200 ± 800	$\frac{2}{3}$
tau neutrino (ν_τ)	$< 2 \times 10^{-6}$	0	bottom (b)	4650 ± 30	$-\frac{1}{3}$

Table 2.1: The fermionic particle content within the SM, showing the three families of quarks and leptons. Some of their important elementary properties are also shown, with their values taken from Reference [15].

Force	Gauge boson	Mass (MeV/c^2)	Charge (e)
Strong	gluon (g)	0	0
Weak	$W^\pm$	80385 ± 15	± 1
	Z	91188 ± 2	0
Electromagnetism	photon (γ)	0	0

Table 2.2: The bosonic particle content within the SM. Showing the three interactions described by the SM and their corresponding gauge boson(s) that mediate the force. Some of the elementary properties of the gauge bosons are also shown, with their values taken from Reference [15].

2.2.2 SM Gauge Group Theory

The Standard Model is made from the combination of three different local symmetry groups. The local symmetries that are applied to the Lagrangian ($\mathcal{L}$) correspond to a local gauge invariance that is imposed on the relativistic quantum fields within the gauge group. The local gauge invariances also add new interaction terms to the Lagrangian that describes the kinematics of the quantum fields. These terms appear in the form of new vector fields (gauge fields). The new gauge fields have to be massless to preserve the gauge invariance of the Lagrangian; however, the new vector fields can acquire mass from spontaneous symmetry breaking and the Higgs mechanism (see section 2.2.6). The local symmetry groups of the SM are

$$\mathrm{SU(3)_C} \times \mathrm{SU(2)_L} \times \mathrm{U(1)_Y}. \tag{2.1}$$

The $\mathrm{SU(3)_C}$ symmetry group is generated by the colour charge associated with the strong interac-

tion (see section 2.2.4). The $SU(2)_L \times U(1)_Y$ symmetry groups, which represent the left-handed isospin and hypercharge symmetries within the SM (see section 2.2.5), are generated by the unified electroweak interaction, .

2.2.3 The Electromagnetic Force

Quantum electrodynamics (QED) is the simplest QFT within the SM. QED is based on the $U(1)_Q$ Abelian (commuting) gauge group and describes the electromagnetic interactions between the charged fermions and a massless gauge boson, the photon (γ) [13]. The QED Lagrangian, $\mathcal{L}_{QED}$, for a charged fermion (ψ) of mass, m, and charge, Q, is given by:

$$\mathcal{L}_{QED} = \bar{\psi}\left(i\not{D}_{QED} - m\right)\psi - \frac{1}{4}F_{\mu\nu}F^{\mu\nu}. \tag{2.2}$$

F is the electric field tensor can be expressed in terms of the photon vector field, $F^{\mu\nu} = \partial^\mu A^\nu - \partial^\nu A^\mu$ [13]. In order to maintain the $U(1)_Q$ local gauge invariance, the *covariant derivative* ($\not{D}$) replaces the usual partial derivative (∂). The covariant derivative also depends the photon vector field, A [13]:

$$\not{D}_{QED,\mu} = \partial_\mu + iQA_\mu. \tag{2.3}$$

Due to the Abelian nature of the $U(1)_Q$ gauge group, this does not allow for any self-interaction terms for the photon field [13].

2.2.4 The Strong Interaction

The strong interaction or quantum chromodynamics (QCD) describes the interaction between 'coloured' particles, called partons (quarks and gluons). QCD introduces a new type of particle charge called 'colour'. This charge can be compared to the electric charge in electrodynamics, where only particles with an electric charge feel the effects of an electric field, whereas only particles with colour charge feel the effects of the strong interaction. The strong force is described by the $SU(3)_C$ non-Abelian gauge group. The non-Abelian nature of the gauge group allows for self-interaction terms for the gluon, the gauge boson that mediates the force. The non-Abelian nature of the force means that it is more complex than the electromagnetic force, and the SU(3) nature of the gauge group gives eight different coloured gluons [13, 16].

The QCD Lagrangian ($\mathcal{L}_{\text{QCD}}$) has a similar composition to the electromagnetic force:

$$\mathcal{L}_{\text{QCD}} = \sum_n \bar{\psi}_n^b \left(i\gamma^\mu \not{D}_{\text{QCD},\mu} - m_n \right) \psi_n^b - \frac{1}{4} G^\alpha_{\mu\nu} G^{\alpha\,\mu\nu}. \tag{2.4}$$

Here, the index n runs over all of the quark flavours (u, d, ...) and the gluon index α runs from 1 to 8. The three colour charges (red, blue, green) are denoted by the index b. The gluon field tensor $G^\alpha_{\mu\nu}$ is comparable to the electric field tensor, but with the additional self-interaction term of the gluon vector fields (see Eq.(2.5)). The covariant derivative ($\not{D}_{\text{QCD},\mu}$) is expressed in terms of the gluon gauge field, A^α_μ, the strong coupling constant (g_s) and the generators of the SU(3)_C group, T_α [16]:

$$\not{D}_{\text{QCD},\mu} = \partial_\mu + i g_s T^\alpha A^\alpha_\mu; \tag{2.5}$$

$$G^\alpha_{\mu\nu} = \partial_\mu A^\alpha_\nu - \partial_\nu A^\alpha_\mu - g_s f^{ijk} A^j_\mu A^k_\nu. \tag{2.6}$$

The f^{ijk} are the structure constants of the non-Abelian gauge group, which can be defined by the commutation relationships of the group generators [16]:

$$\left[T^i, T^j \right] = i f^{ijk} T^k. \tag{2.7}$$

The strong interaction is the strongest of the three interactions described in the SM. One of its most important characteristics is that the strength of the field increases with the distance between the coloured particles due to the gluon self-interaction [10, 11]. This leads to the concept of confinement: since the strength of the colour field increases with distance, at some point it becomes energetically favourable to create a quark-antiquark pair ($q\bar{q}$) from the vacuum. The quark-antiquark pair can then bind to the original two partons, and hence reduce the strength of the field. This process is known as hadronisation. This means partons can only exist in bound colour neutral states called hadrons, such as the proton [10, 11].

There are two groups of hadrons: baryons, which are made up of a collection of three valence quarks, and mesons, which are made from a valence quark-antiquark. The effects of the hadronisation of coloured particles are seen in particle detectors, as clusters of hadrons travelling approximately collinearly, referred to as a '*jet*'. Jets are an important physics object for this thesis and are

described in more detail in sections 2.4.2 and 3.6.1.

2.2.5 The Weak Force and Electroweak Unification

The weak force is responsible for the β decay of unstable nuclei in nuclear physics. The Lagrangian was constructed from left-handed doublets in the $SU(2)_L$ gauge group and is invariant in the weak isospin (I) space [13]. Right-handed particles in the SM appear as singlets and as such are not affected by the weak force. Right-handed neutrinos are therefore omitted from the SM, since no direct evidence for them has been found in nature; however, they could still be added to the theory as right-handed singlet matter fields (ν_R) [13].

In the Standard Model, the electromagnetic and weak interactions unify at an energy $\sim$ 100 GeV (electroweak scale). The unified interaction is described by the $SU(2)_L \times U(1)_Y$ gauge group [13]. The weak hypercharge (Y) gauge group is related to the electromagnetic charge (Q) by the relationship Y = Q - I_3. Here, I_3 is the third component of the weak isospin.

The electroweak Lagrangian is

$$\mathcal{L}_{\mathrm{EW},f} = \sum_f \bar{\psi}_f i \not{D}_{\mathrm{EW},\mu} \psi_f, \tag{2.8}$$

where ψ_f are the chiral matter fields of the quarks and leptons, which are organised into the $SU(2)_L$ doublets and singlets (see Eq. (2.9) and (2.10)):

$$\psi_{\mathrm{Leptons}} = \begin{pmatrix} \nu_L^e \\ e_L \end{pmatrix}, e_R, \begin{pmatrix} \nu_L^\mu \\ \mu_L \end{pmatrix}, \mu_R, \begin{pmatrix} \nu_L^\tau \\ \tau_L \end{pmatrix}, \tau_R; \tag{2.9}$$

$$\psi_{\mathrm{Quarks}} = \begin{pmatrix} u_L \\ d_L \end{pmatrix}, u_R, d_R, \begin{pmatrix} c_L \\ s_L \end{pmatrix}, c_R, s_R, \begin{pmatrix} t_L \\ b_L \end{pmatrix}, t_R, b_R. \tag{2.10}$$

As with the previous gauge field theories, additional fields are added to define a covariant derivative: this maintains the $SU(2)_L \times U(1)_Y$ gauge symmetry of the electroweak force. The covariant derivative requires the addition of two extra vector fields, B_μ and W_μ^i:

$$\not{D}_{\mathrm{EW},\mu} = \partial_\mu + ig\frac{Y}{2}B_\mu + ig'\frac{\tau_L^i}{2}W_\mu^i, \tag{2.11}$$

where g and g' are the gauge coupling constants for the $U(1)_Y$ and $SU(2)_L$ symmetry groups and τ_L^i are the generators of the $SU(2)_L$ group. The physical electroweak gauge fields are produced by mixing linear combinations of the B_μ and W_μ^i fields:

$$Z_\mu = \cos\theta_W W_\mu^3 - \sin\theta_W B_\mu, \tag{2.12a}$$

$$A_\mu = \sin\theta_W W_\mu^3 + \cos\theta_W B_\mu, \tag{2.12b}$$

$$W_\mu^\pm = \frac{1}{\sqrt{2}}\left(W_\mu^1 \mp i W_\mu^2\right), \tag{2.12c}$$

In these equations, θ_W is the Weinberg (weak mixing) angle, which is often expressed in terms of the gauge couplings: $\tan\theta_W = g/g'$ [13].

2.2.6 Mass and Higgs Mechanism

At this point in the theory, the fermions and physical gauge bosons are still massless since there are no mass terms in the Lagrangians. However, from Table 2.2, it can be seen that the $W^\pm$ and Z bosons are massive. Trivially, adding mass terms to the Lagrangians would break the gauge symmetry of the model, so a different process is required for particles to become massive. The process which describes how these bosons acquire their mass, without breaking the gauge invariance of the Standard Model, is called the Higgs mechanism [17, 18, 19]. The Higgs mechanism introduces '*spontaneous symmetry breaking*' [17] of the $SU(2)_L \times U(1)_Y$ gauge group by introducing a new complex scalar doublet field, called the Higgs field [17].

To understand how the addition of a scalar field can add mass to a Lagragian, the simple example of a real scalar field (ϕ) can be used. ϕ is given the potential $\mathcal{U}(\phi)$:

$$\mathcal{U}(\phi) = -\frac{1}{2}\mu^2\phi^2 + \frac{1}{4}\lambda\phi^4, \tag{2.13}$$

where μ and λ are constants. The minimum of $\mathcal{U}(\phi)$ can easily found to be at $\phi = \pm\sqrt{\mu^2/\lambda}$. An example of a potential of this type is shown in Figure 2.2.

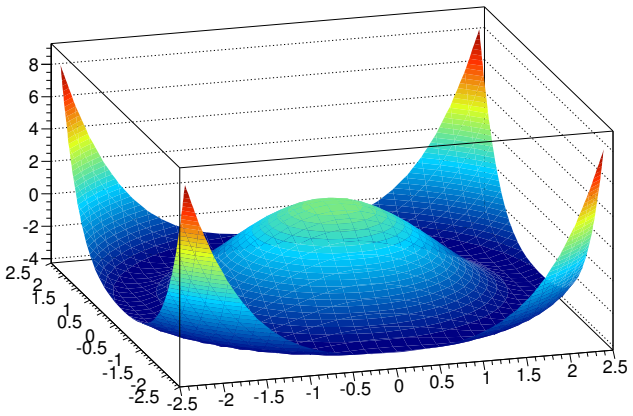

Figure 2.2: The potential of $\mathcal{U}(\phi) = -1/2\mu^2\phi^2 + 1/4\lambda\phi^4$ with $\mu^2 > 0$ and $\lambda > 0$. A potential of this type can be used in the spontaneous symmetry breaking of a scalar field [13].

The Lagrangian ($\mathcal{L}$) of ϕ is simply given by $\mathcal{L} = \mathcal{T} - \mathcal{U}$ [13]:

$$\mathcal{L} = \frac{1}{2}(\partial_\mu\phi)(\partial^\mu\phi) + \frac{1}{2}\mu^2\phi^2 - \frac{1}{4}\lambda\phi^4. \tag{2.14}$$

This almost provides the Lagrangian with a real mass term (ϕ^2 term), but it has the wrong sign. However, the correct sign can be achieved by redefining the ground state of the potential using a new field parameter, η defined as

$$\eta \equiv \phi \pm v \quad \text{with} \quad v = \sqrt{\mu^2/\lambda}\,. \tag{2.15}$$

Replacing ϕ with η, the Lagrangian (in terms of η) is given by [13]

$$\mathcal{L} = \frac{1}{2}(\partial_\mu\eta)(\partial^\mu\eta) - \lambda v^2\eta^2 \pm \lambda v\eta^3 - \frac{1}{4}\lambda\eta^4 + \text{const.} \tag{2.16}$$

Now it can be seen that the mass term has the correct sign, which corresponds to a field with mass [13]:

$$m = \sqrt{2\lambda v^2} = \sqrt{2}\mu. \tag{2.17}$$

In Eq. (2.16), it can also be seen that there are third and fourth order terms in the Lagrangian. These terms correspond to the triple and quartic scalar couplings of the field [13]. It should also be noted that the original Lagrangian in Eq.(2.14) was symmetric under the exchange of $\phi \to -\phi$ but the new Lagrangian is not symmetric in terms of η. It is said that the symmetry has been

'*broken*'. This occurred because one of the degenerate ground states had to be arbitrarily chosen, thus *spontaneously* breaking the symmetry of the Lagrangian.

The $SU(2)_L \times U(1)_Y$ group follows a similar approach, but a weak isospin doublet of two complex fields (Φ) is used instead [13]:

$$\Phi = \begin{pmatrix} \phi^+ \\ \phi^0 \end{pmatrix}. \tag{2.18}$$

Φ is given a potential ($\mathcal{U}(\Phi)$) similar to that in Eq.(2.13) [13].

$$\mathcal{U}(\Phi) = \mu^2(\Phi^\dagger\Phi) + \lambda(\Phi^\dagger\Phi)^2. \tag{2.19}$$

Only $\lambda > 0$ is considered, so that the energy of the potential is bounded below, as an unbounded minimum energy would not be physical. Conversely only $\mu^2 < 0$ is considered, as this leads to a non-unique ground state energy [13]. This type of potential provides the Higgs field with the important property that its minimum potential is not at the zero value of the field; therefore, it has a non-vanishing vacuum expectation value (VEV).

By requiring U(1) gauge invariance and Φ transforming as $\Phi \rightarrow \Phi e^{i\theta}$, where θ is real, the Lagrangian for Higgs field is found to have the following form [13]:

$$\mathcal{L} = (D_\mu\Phi)^\dagger(D^\mu\Phi) - \mu^2\Phi^\dagger\Phi - \lambda(\Phi^\dagger\Phi)^2 - \frac{1}{4}F^{\mu\nu}F_{\mu\nu}, \tag{2.20}$$

where D_μ has the same form as the covariant derivative in Eq.(2.3).

The same method is used to redefine the ground state of the potential; however, since the field is a complex scalar field, two new field variables are required (η and ξ). The field variable around the direction of the circle of minimal radius (ξ) corresponds to a massless Goldstone boson [13]. The Goldstone boson introduces unwanted interaction terms to the Lagrangian; however, it can be removed by taking a gauge since the symmetry is only local. The additional terms in the Lagrangian following the substitution include mass terms for three weak gauge bosons, $W^\pm$ and Z^0. The remaining degree of freedom results in a new massive scalar boson being predicted, the Higgs boson (h) [17]. Recent experimental evidence for a Higgs scalar boson was presented at CERN in July 2012 by the ATLAS and CMS collaborations, which found evidence for a Higgs-boson-like

resonance at a mass of ≈125 GeV [20, 21, 22].

The masses of the bosons predicted by the theory are related in the following way [13]:

$$m_H = \sqrt{2}\mu, \tag{2.21a}$$

$$m_{W^\pm} = \frac{1}{2}vg, \tag{2.21b}$$

$$m_Z = \frac{1}{2}v\sqrt{g^2 + g'^2}, \tag{2.21c}$$

$$\cos\theta_W = \frac{m_W}{m_Z}. \tag{2.21d}$$

In these equations, v is related to the VEV of the Higgs field and is equal to $\sqrt{\frac{\mu^2}{\lambda}}$ [13].

Fermions can also acquire mass through the Higgs mechanism by interactions between the fermionic and Higgs scalar fields, called Yukawa couplings.

2.2.7 Failings of the SM

As previously mentioned, the SM is one of the most successful theoretical models for explaining the interactions of the fundamental particles of the Universe; however, it is not without fault. The SM has several free parameters that have to be determined experimentally. It is not clear why there are three generations of quarks and leptons, and why their masses differ by orders of magnitude. Experimental evidence shows that neutrinos oscillate between their different flavours [23, 24], which implies they must have mass. However, in the Standard Model, the weak interaction only couples to left-handed particles; therefore, neutrinos are treated as massless, since they have no right-handed counterpart. There is also no realistic dark matter particle candidate in the Standard Model, contradictory to the indirect evidence for dark matter [25, 26, 27]. The unification of all of the fundamental forces is a desirable concept, where a 'theory of everything' could be used to describe the Universe. The electromagnetic and weak forces unify at the EW scale, so there is no theoretical reason why the EW and strong forces should not unify at some energy scale. However, all three forces do not unify in the SM.

Dark Matter Relic Density

The indirect evidence for dark matter particles has been building since the 1930s [25, 26]. There is now overwhelming evidence in support of nonluminous (dark) matter in the Universe [25, 26]. The evidence also suggests that DM is not baryonic matter, and from current data it is five times more

abundant than the baryonic matter particles described in the SM. The energy densities (Ω) of the baryonic (B) and non-baryonic dark matter (DM) are [26]:

$$\Omega_B \simeq 0.0456 \pm 0.0016. \tag{2.22a}$$

$$\Omega_{DM} \simeq 0.227 \pm 0.014. \tag{2.22b}$$

All of the indirect evidence of dark matter is based on its gravitational interactions. Therefore, it is only known that DM is massive and at most weakly interacting (WIMP) [25, 26]. One possibility is that DM particles were produced alongside the baryonic particles in the early Universe, but at some point the amount of dark matter production was 'frozen out', and the density of the remaining dark matter is the relic density of the dark matter in the Universe [25, 26].

Hierarchy Problem

The electroweak scale of the Higgs boson mass [28] conflicts with the fact that the radiative corrections to the tree level mass of the Higgs boson diverge quadratically up to the cut-off scale of new physics, at a momentum Λ, where the SM is no longer valid (see Eq.(2.23)). The radiative corrections appear in virtual loop diagrams (Figure 2.3 shows an example) of particles that couple to the Higgs field. This means that a considerable amount of 'fine-tuning' is required to keep the Higgs mass at the electroweak scale ($\sim$100 GeV) if the SM is to remain valid up to high energies. The unnatural amount of fine-tuning to the Higgs mass is known as the 'gauge hierarchy problem' [29] is used to fix this problem in the SM. The radiative corrections to the Higgs mass squared can be expressed as

$$\Delta m_H^2 = -\frac{\lambda_f^2}{8\pi^2}\left[\Lambda_{UV}^2 + \dots\right], \tag{2.23}$$

where λ_f is the Yukawa coupling of any fermion (f) and Λ_{UV} is the ultraviolet momentum cut-off, which is the momentum where new physics enters and supersedes the SM. Gravity is not included in the SM, so the SM can only be valid up to the Planck scale, where gravitational interactions become comparable to those of the other forces. This means that the Λ_{UV} momentum cut-off in the SM is naturally of the order of the Planck mass (M_P) $\sim 10^{19}$ GeV, and Δm_H^2 could be of the order of 10^{34} GeV^2 if there is no new physics between the EW and Planck scales.

2.3 Supersymmetry

Supersymmetry (SUSY) [30, 31, 32, 33, 34, 35, 36, 37, 38] (see for example [39] or [40]) is one of the most favoured extensions to the Standard Model; it is well motivated, as it provides natural solutions to some of the problems of the Standard Model, such as the gauge hierarchy problem mentioned in section 2.2.6 and the lack of a potential dark matter particle.

At the time of writing, no evidence for SUSY has been found; therefore, searching for SUSY still remains one of the primary physics goals of the LHC. This section will give an overview of supersymmetry with emphasis on possible SUSY scenarios that could be discovered at the LHC.

2.3.1 Overview

Supersymmetry is a framework that proposes a new symmetry between the fermions and bosons in the Standard Model. For every particle in the Standard Model, SUSY proposes a supersymmetric partner ('*sparticle*'). The supersymmetric partner is introduced with a quantum spin difference of $1/2$ compared to its Standard Model counterpart. The supersymmetric transformations can be thought of in terms of an operator Q that generates the transformations [39]:

$$Q|\text{Boson}\rangle = |\text{Fermion}\rangle \quad , \quad Q|\text{Fermion}\rangle = |\text{Boson}\rangle. \tag{2.24}$$

Here, the particles have the same quantum numbers, but differ in spin by $\pm 1/2$.

However, since no boson has been found with the same mass and properties as the electron (the 'selectron'), supersymmetry must be a broken symmetry, where the masses of the sparticles are much heavier than their Standard Model counterparts [39]. Various methods are used to generate the symmetry breaking (see [39] and section 2.3.4) which pose no serious problems for the theory [39].

Supersymmetry can, however, introduce terms which make it possible to violate lepton and baryon number, leading to (amongst other things), proton decay. Therefore, in a large number of SUSY models, a new multiplicative conservation law is applied, called R-parity conservation [41, 42, 43, 44]:

$$R\text{-parity} = (-1)^{3(B-L)+2s}, \tag{2.25}$$

where B is the baryon number of the particle, L is the lepton number of the particle and s is the spin of the particle.

From Eq.(2.25), it can be seen that Standard Model particles will have R-parity$= +1$, whereas SUSY particles will have R-parity$= -1$. This means that the lightest supersymmetric particle (LSP)

is stable, since it is unable to decay without violating R-parity conservation. Since a charged particle has yet to be discovered with these properties, it must be neutral and weakly interacting. This weakly interacting, stable and massive particle provides a possible dark matter candidate for cold dark matter (CDM) models (see [26]).

The primary motivation behind supersymmetry was a natural solution to the gauge hierarchy problem. The gauge hierarchy problem relates to the radiative corrections to the Higgs boson mass (described in section 2.2.6). Since supersymmetric particles also couple to the Higgs field, the Higgs boson will also receive radiative corrections from the sparticles; however, these corrections will have the opposite sign due to the spin $1/2$ difference. Therefore, the radiative corrections to the Higgs boson mass from the Standard Model particles will cancel with the corrections from their supersymmetric partners. This provides a natural solution to the problem, without the level of fine-tuning required in the SM. Examples of radiative corrections to the Higgs mass squared are shown in Figure 2.3.

Figure 2.3: Example radiative corrections to the Higgs mass squared: (a) from a fermion, in this case, the top quark (t); and (b) a scalar boson, for example, the stop quark (the supersymmetric partner to the top quark).

If an 'unnatural' amount of fine-tuning is to be avoided, this implies that the masses of the sparticles must be on the ~1 TeV mass scale [39], and therefore, these particles should be within the reach of SUSY analyses performed at the LHC (see Chapter 7).

2.3.2 Minimal Supersymmetric Standard Model

The Minimal Supersymmetric Standard Model (MSSM) (see [39] and [40]) is the supersymmetric extension to the Standard Model that proposes the smallest possible overall extra particle content.

'*Supermultiplets*' are formed between the fermions in the Standard Model and the scalar fermions (sfermions), and also between the gauge bosons in the Standard Model with a '*gaugino*' sparticle [39]. To make the MSSM a consistent quantum theory, another Higgs doublet is required, whilst retaining the original Higgs doublet from the Standard Model [39]. The resulting chiral and gauge

supermultiplets are shown in Tables 2.3 and 2.4 [39].

Name		Spin 0	Spin 1/2
quarks, squarks (×3 families)	Q	$(\tilde{u}_L, \tilde{d}_L)$	(u_L, d_L)
	$\bar{u}$	$\tilde{u}^*_R$	$u^\dagger_R$
	$\bar{d}$	$\tilde{d}^*_R$	$d^\dagger_R$
leptons, sleptons (×3 families)	L	$(\tilde{\nu}, \tilde{e}_L)$	(ν, e_L)
	$\bar{e}$	$\tilde{e}^*_R$	$e^\dagger_R$
Higgs, Higgsinos	H_u	(H^+_u, H^0_u)	$(\tilde{H}^+_u, \tilde{H}^0_u)$
	H_d	(H^0_d, H^-_d)	$(\tilde{H}^0_d, \tilde{H}^-_d)$

Table 2.3: The chiral supermultiplets within the MSSM [39]. Only the first generations of the squarks, quarks, sleptons and leptons are shown; the other two generations follow the same format as the first generations shown in this table.

Name	Spin $\frac{1}{2}$	Spin 1
gluino, gluon	$\tilde{g}$	g
winos, W	$\tilde{W}^\pm, \tilde{W}^0$	$W^\pm, W^0$
bino, B	$\tilde{B}^0$	B^0

Table 2.4: Gauge supermultiplets within the MSSM [39].

Mixing

After the supersymmetry breaking process (see section 2.3.4), massive particles with the same quantum numbers mix to form the physically observable mass states. The neutral fermionic sparticles, consisting of the wino ($\tilde{W}^0$), bino ($\tilde{B}^0$) and two higgsinos ($\tilde{H}^0_u, \tilde{H}^0_d$), mix together to form four neutral gauginos collectively called 'neutralinos' $\tilde{\chi}^0_i (i=1,2,3,4)$. The charged fermionic sparticles, consisting of the charged winos ($\tilde{W}^\pm$) and higgsinos ($\tilde{H}^+_u, \tilde{H}^-_d$), also mix and form four charged gauginos collectively called 'charginos' $\tilde{\chi}^\pm_j (j=1,2)$.

There is also mixing in the squark and slepton sectors. However, it is proportional to the mass of the particle's Standard Model counterpart, so there is a non-negligible amount of mixing only in the third generation. The $\tilde{t}_L$ and $\tilde{t}_R$ mix to form the mass states $\tilde{t}_1$ and $\tilde{t}_2$. The same is also true for the $\tilde{b}$ and $\tilde{\tau}$.

Table 2.5 summarises the mixing in the MSSM, and shows the original interaction states and the observable mass states after mixing.

Interaction states	Mixed Mass states	Name
$\tilde{W}^0$, $\tilde{B}^0$, $\tilde{H}_u^0$, $\tilde{H}_d^0$	$\tilde{\chi}_1^0$, $\tilde{\chi}_2^0$, $\tilde{\chi}_3^0$, $\tilde{\chi}_4^0$	Neutralinos
$\tilde{W}^{\pm}$, $\tilde{H}_u^+$, $\tilde{H}_d^-$	$\tilde{\chi}_1^{\pm}$, $\tilde{\chi}_2^{\pm}$	Charginos
$(\tilde{t}_L$, $\tilde{t}_R)$, $(\tilde{b}_L$, $\tilde{b}_R)$	$(\tilde{t}_1$, $\tilde{t}_2)$, $(\tilde{b}_1$, $\tilde{b}_2)$	stop and sbottom
$(\tilde{\tau}_L$, $\tilde{\tau}_R)$	$(\tilde{\tau}_1$, $\tilde{\tau}_2)$	stau

Table 2.5: Mixing within the MSSM. The neutral gauginos mix to form the neutralinos ($\tilde{\chi}^0$). The charged gauginos mix to form the charginos ($\tilde{\chi}^{\pm}$). In the squark and slepton sectors, only the third generation of particles mix.

2.3.3 Unification of the Fundamental Forces

The unification of the electromagnetic and weak force, where both forces are components of the same unified electroweak force, was briefly discussed in section 2.2.5. So is there any reason why the strong force could not unify with the electroweak force at some energy scale? *Grand unification theory* (GUT) describes the unification of all of the fundamental forces which makes it a highly desirable beyond the SM theory. The variation of the coupling strengths of the fundamental forces over energy scale is shown in Figure 2.4. The dashed lines show the inverse of the coupling strengths ($\alpha^{-1}(Q)$) (where Q relates to the resolution scale) of the SM gauge groups; it can be seen that it is not possible for all of the forces in the SM to unify at one energy. The solid lines show the couplings of the gauge groups in the MSSM. The additional particle content of the MSSM allows the gauge groups to unify at energy scale of $\sim 10^{16}$ GeV [39].

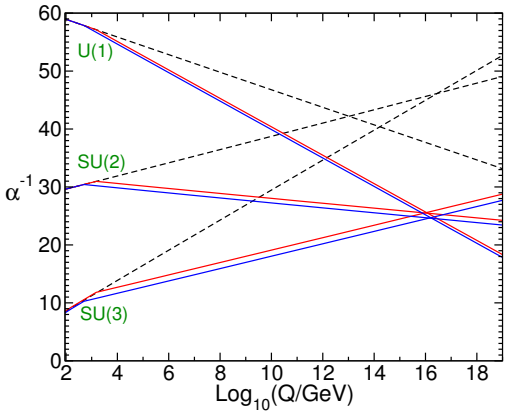

Figure 2.4: The evolution of the gauge group couplings in the SM and the MSSM. The dashed lines show the inverse of the coupling strengths ($\alpha^{-1}(Q)$) of the SM gauge groups. The solid lines show the inverse of the coupling strengths of the gauge groups within the MSSM. This Figure was taken from [39].

2.3.4 Supersymmetry Breaking

Supersymmetry must be a broken symmetry, or else the masses of the sparticles would be identical to their Standard Model counterparts. Similarly to how the gauge bosons acquire mass in the SM, supersymmetry is broken spontaneously where the underlying Lagrangian density is invariant under the supersymmetric transformations, but the vacuum ground state is not [39]. Furthermore, the mechanisms used to break the symmetry must ensure that they do not change the relationships between the dimensionless couplings that cancel the quadratic divergences of the radiative corrections to the Higgs mass squared, or else supersymmetry would not provide the solution to the hierarchy problem [45]. This type of supersymmetry breaking is referred to as 'soft' [39].

Simplified Models and Supergravity

Due to the large number of free parameters in the MSSM (usually around $\approx$100), such as sparticle masses and branching ratios, it is not possible to generate enough simulated SUSY events to cover all of the phase space within the MSSM. Therefore, when analyses perform searches for supersymmetry they tend to probe simplified models (see Chapter 7). Most of the simplified models are based on the MSSM, but assumptions are made to reduce the overall number of free parameters.

Supergravity [39] refers to a subset of SUSY models which break supersymmetry by gravitational interactions at the GUT scale, where all of the fundamental interactions are unified. The simplest supergravity model is called the minimal supergravity (mSUGRA) or constrained minimal supersymmetric standard model (CMSSM) [46, 47, 48, 49, 50, 51], which uses the gravitino to mediate the SUSY breaking.

The mSUGRA/CMSSM branch of simplified models reduces the number of parameters of the MSSM down to just five: m_0 (the mass of spin-0 particles at the GUT scale), $m_{1/2}$ (the mass of spin-$^1/_2$ particles at the GUT scale), A_0 (The common scalar trilinear coupling), tan β (the ratio of the vacuum expectation values of Higgs doublets) and $sign(\mu)$ (the sign of the Higgs mixing parameter).

Searches for SUSY in mSUGRA/CMSSM models are often interpreted in the m_0-$m_{1/2}$ mass plane for fixed values of tanβ, A_0 and μ. Examples of such interpretations can be found in section 2.5 and Chapter 7.

2.3.5 Implications of the Higgs Mass Measurement

In the most simplistic and natural SUSY models, for example the mSUGRA/CMSSM, the predicted mass of the Higgs boson is at the low EW scale (~W/Z mass) [39]. This conflicts with the heavier mass of the Higgs boson measured by ATLAS and CMS (~125 GeV), and has also called into question some of the more constrained models (mSUGRA/CMSSM). Figure 2.5 shows the MSSM lightest scalar Higgs boson mass (h^0) as a function of the lightest stop quark mass ($\tilde{t}_1$). A light stop quark at the EW scale is still achievable with large amounts of mixing between the two stop states [52]. This means SUSY may not be as natural as first thought (see [53],[54]): some fine-tuning (at the order of 10% [52]) could be required. A summary of the searches for the lightest stop quark is detailed in section 2.5. SUSY may also be more complex and less constrained, such as in pMSSM models [55].

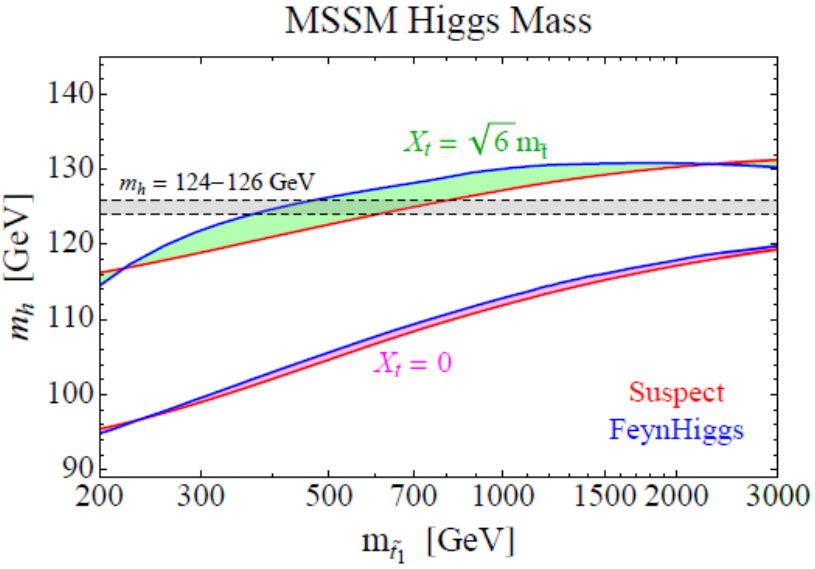

Figure 2.5: The predicted mass of the MSSM lightest scalar Higgs boson as a function of $\tilde{t}_1$ mass for different scenarios of $\tilde{t}_L$ and $\tilde{t}_R$ mixing. The upper blue and red lines show the predicted MSSM Higgs mass in the case of maximal stop mixing computed with FeynHiggs and Suspect respectively. The lower blue and red lines show the predicted MSSM Higgs mass from FeynHiggs [56] and SuSpect [57] in the case of no mixing between the stop quarks. This figure was taken from [52].

2.4 SUSY at the LHC

2.4.1 Production Mechanisms

In a hadron collider, the strong interaction is the dominant channel for SUSY production. Figure 2.6 shows the cross-section for sparticle production against sparticle mass at the LHC, with a centre of

mass (CoM) energy $\sqrt{s} = 8\,\text{TeV}$. From Figure 2.6, it can be seen that the $\tilde{g}\tilde{g}$, $\tilde{q}\tilde{g}$ and $\tilde{q}\tilde{q}$ channels are the dominant production mechanisms at the LHC.

R-parity conservation has the following implications for SUSY sparticle production at the LHC:

- sparticles must always be produced in pairs to conserve *R*-parity;
- the produced sparticles will eventually decay to the LSP, which is stable. Since the LSP is neutral and weakly interacting, it will not be detected, leading to an imbalance of transverse momentum of the observed particles.

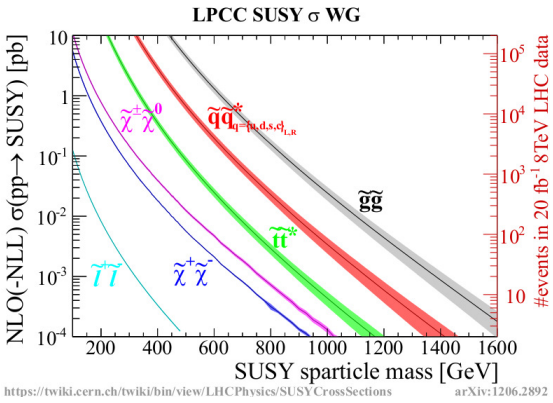

Figure 2.6: The $\sqrt{s} = 8\,\text{TeV}$ NLO cross-sections for sparticle production against sparticle mass at the LHC. The different coloured lines show the cross-sections for various different sparticles and the coloured bands show the uncertainty on the calculation of the theoritical cross-section. This figure was made by the LHC SUSY cross-sections working group using [58].

To conserve *R*-parity, squarks and gluinos will always decay to a lighter SUSY particle plus additional SM particles. SUSY particles will continue to decay until the LSP is reached (in most models the $\tilde{\chi}_1^0$). This can create long decay chains with many quarks/gluons produced early on in the chain, leading to a large number of jets in the decay. The LSP will not be detected, which leads to an imbalance of transverse momentum (p_T) of the observed final state particles in the event. Normally, the direction of the imbalance is not important, so transverse energy is used and it is referred to as missing transverse energy (E_T^miss), see section 2.4.3.

2.4.2 Jet Algorithms

As mentioned previously in the brief overview of the strong interaction (QCD) (section 2.2.4), high energy partons form jets within the detector. This section will provide more detail on how jets are reconstructed using jet finding algorithms, which is important for many chapters in this thesis.

Figure 2.7 shows an example structure of a $t\bar{t}h$ event. It can be seen in this figure that there are a substantial number of final state hadrons, many of which will become parts of jets. However, it is impossible to uniquely associate partons with a jet; for example, it would be impossible to tell at the detector level if a jet had originated from one hard parton or two softer partons travelling collinearly [59]. A jet may not have originated from the hard scatter; for example, it could have originated from a W boson decaying into two quarks. Here, if the W boson was highly boosted, the jets could merge and be unresolvable from each other. So experiments have to decide which jet criteria to use, and it must also be understood that the jets in the final state *do not* directly map back to the parton level interactions (Figure 2.7) [59].

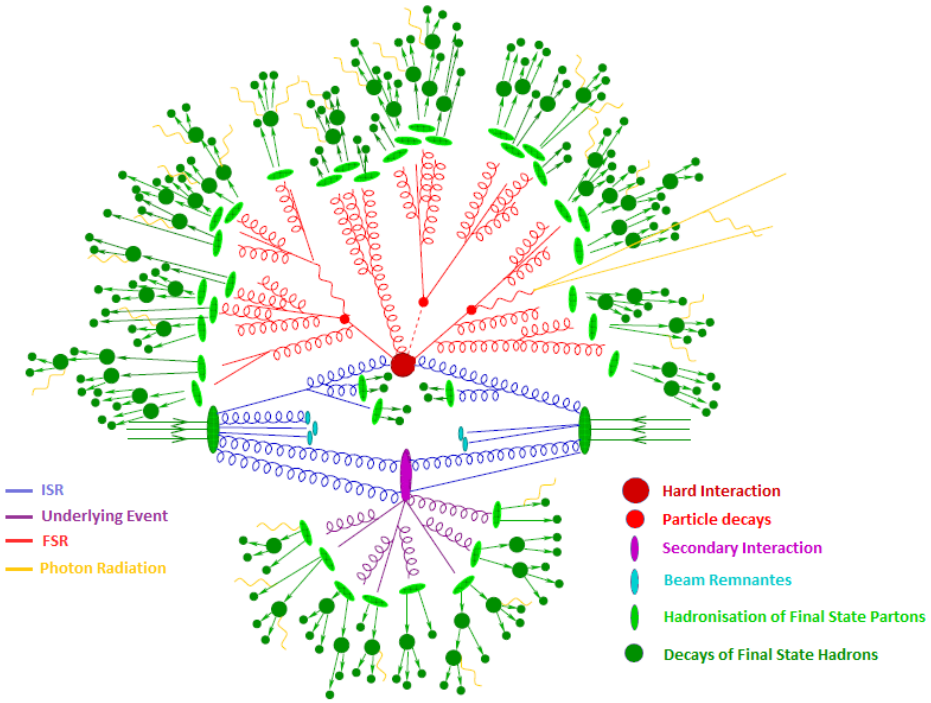

Figure 2.7: A schematic showing an example $t\bar{t}h$ event structure produced with the SHERPA Monte Carlo generator (see section 3.4.1). The unmodified version of this Figure was taken from [60].

The inputs into jet algorithms are either simulated hadrons/partons, such as Monte Carlo reconstructed jets (made from truth particles) or detector quantities, for example, calorimeter energy deposits and charged particle tracking information. There are a number of desired characteristics which jet algorithms should have: the most important ones are listed below.

- Infra-red safety. The reconstructed jet should not be affected by the emission of a small amount of soft radiation (FSR). If the jet algorithm is not infra-red safe, then this can lead to divergences in theoretical calculations [59].

- Collinear safety. The collinear splitting of a hard parton during the fragmentation process

should not affect the reconstructed jet. As with infra-red safety, if the algorithm is not collinear safe it will result in divergences in the theoretical predictions [59].

- Well-defined area (solid angle). Jets require calibration, and also need to be isolated from other physics objects; therefore, a well-defined area (solid angle) is required for jet calibration (see section 3.6.1) and the overlap removal process (see section 3.6.7).

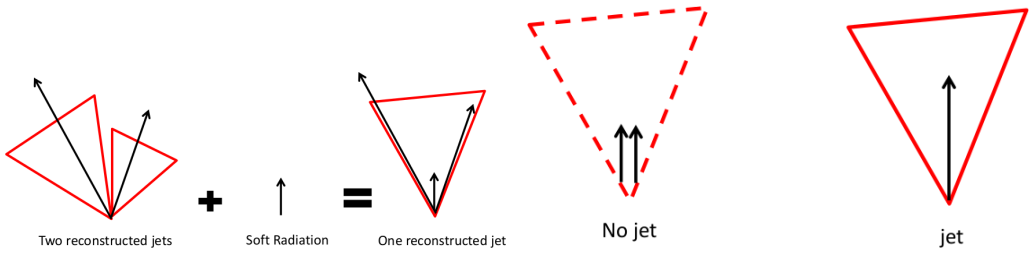

(a) Two dimensional schematic of lack of infra-red safety

(b) Two dimensional schematic of lack of collinear safety

Figure 2.8: Two dimensional schematics showing lack of infra-red safety (a) and collinear safety (b) in a jet reconstruction algorithm.

Figure 2.8 shows the problems that are encountered if a jet algorithm is not infra-red or collinear safe. It is clear that the reconstructed jets differ for different partons configurations, which will lead to divergences in the theoretical calculations of non-perturbative effects if they are not treated carefully [59].

Figure 2.9 shows an example dijet event candidate recorded with the ATLAS detector, where two energetic back-to-back jets leave large deposits of energy in the ATLAS calorimeters.

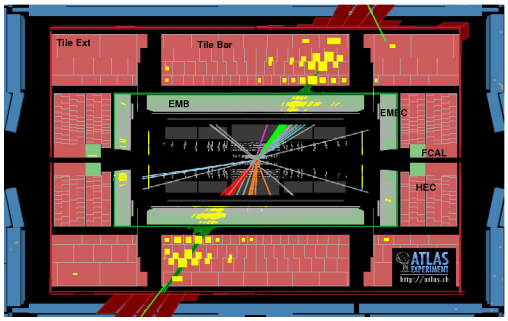

Figure 2.9: An example dijet event recorded with the ATLAS detector. This figure was taken from [61].

2.4.3 Missing Transverse Energy

Most particles that are produced in the proton collisions will interact with the particle detector at some level; however, there are some particles which will not, for example, neutrinos (ν). Neutrinos will leave the detector without interacting, so their presence has to be inferred from an imbalance in transverse momentum. Since the initial partons in the centre of mass (CoM) frame have a negligible amount of momentum in the transverse plane (they are travelling in the z-direction), conservation of momentum requires that the vectorial sum of their momentum in the transverse plane should be zero if all the particles have been detected. Hence, if there is a large imbalance of transverse momentum (*missing transverse momentum*) ($\vec{E}_{\mathrm{T}}^{\mathrm{miss}}$), then the event may contain invisible particles. $\vec{E}_{\mathrm{T}}^{\mathrm{miss}}$ is defined as:

$$\vec{E}_{\mathrm{T}}^{\mathrm{miss}} = -\sum_{\text{visible}} \vec{p_{\mathrm{T}}} = \sum_{\text{invisible}} \vec{p_{\mathrm{T}}}. \tag{2.26}$$

This principle can be used to detect any particles that do not interact with the detector, not just neutrinos. $\vec{E}_{\mathrm{T}}^{\mathrm{miss}}$ is important for SUSY analyses searching for R-parity conserving models, since the LSP is a neutral weakly interacting massive particle that will not interact with the detector. This means $\vec{E}_{\mathrm{T}}^{\mathrm{miss}}$ is a critical component for searches for these types of SUSY models.

2.4.4 SUSY Decays

Figure 2.10 shows an example of a direct $\tilde{q}$ and $\tilde{g}$ decay to the LSP; however, it is possible to go through a intermediate gaugino before the reaching the LSP (see Figure 7.1), which means that sleptons and leptons can appear in the decay chain. In the SUSY analysis chapter of this thesis, only non-leptonic decays of sparticles were considered, such as the decays shown in Figure 2.10. Throughout this thesis, a future referral to 'the zero lepton analysis' will refer to the ATLAS "jets and missing transverse energy and zero leptons" analysis described in Chapter 7.

2.5 General Searches for SUSY at the LHC

Over run-I of the LHC, large amounts of data were recorded, which made it possible for many different analyses to search for the existence of SUSY. This section will summarise the results of the direct searches for supersymmetry by ATLAS and CMS (see [62]). A full list of public SUSY results from ATLAS and CMS can be found at [63] and [64] respectively. Since no significant

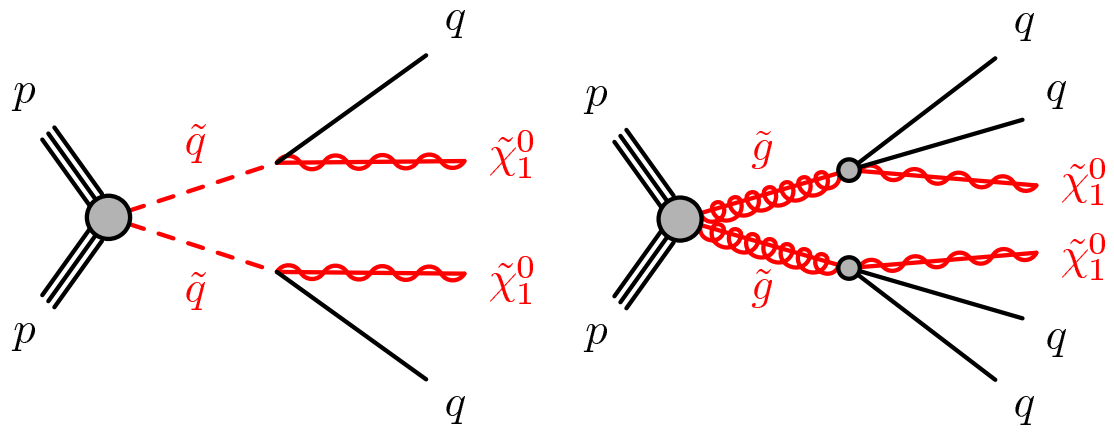

(a) Direct $\tilde{q}$ decay

(b) Direct $\tilde{g}$ decay

Figure 2.10: Direct $\tilde{q}$ and $\tilde{g}$ decays to the LSP ($\tilde{\chi}_1^0$) in the zero lepton channel with a characteristic final event object signature of jets and missing transverse energy (carried by the undetected $\tilde{\chi}_1^0$s).

excess has been observed during run-I with the $\sqrt{s} = 7\,\text{TeV}$ and $\sqrt{s} = 8\,\text{TeV}$ data sets by ATLAS or CMS, the LHC searches set exclusion contours on many different theoretical SUSY models [62].

Analyses, such as the ATLAS zero lepton analysis documented in Chapter 7, target a specific final state. They may also use a specific kinematic variable like α_T [65] or `Razor` [66] to enrich the Signal Regions (phase space regions where analyses conduct their searches for new physics) with supersymmetric events.

Figure 2.11 shows an overall summary of SUSY results for ATLAS using the $\sqrt{s} = 7\,\text{TeV}$ and $\sqrt{s} = 8\,\text{TeV}$ data sets and figure 2.12 shows the CMS SUSY results summary using the same data sets. It can be seen that there was a considerable number of different analyses searching for SUSY at the LHC with the run I data sets, and that the mass exclusion limits of many of these analyses were at the 1 TeV scale in the simplified models.

Figures 2.13 (a) and (b) show the mass exclusion contours in searches for the lightest stop quark ($\tilde{t}_1$). Figures 2.13 (a) and (b) show that light stop quarks masses up to $\approx 700\,\text{GeV}$ have been excluded to a 95% level with a massless $\tilde{\chi}_1^0$ by ATLAS and CMS. Figures 2.14 (a) and 2.14 (b) shows the mass exclusion contours of the ATLAS and CMS SUSY analyses in the mSUGRA/CMSSM m_0-$m_{1/2}$ mass plane. It can be seen in these Figures that a large portion of the mSUGRA/CMSSM m_0-$m_{1/2}$ mass plane was excluded to a 95% level by CMS[3].

[3]Figure 7.15 in Chapter 7 shows the corresponding figure for the ATLAS SUSY analyses

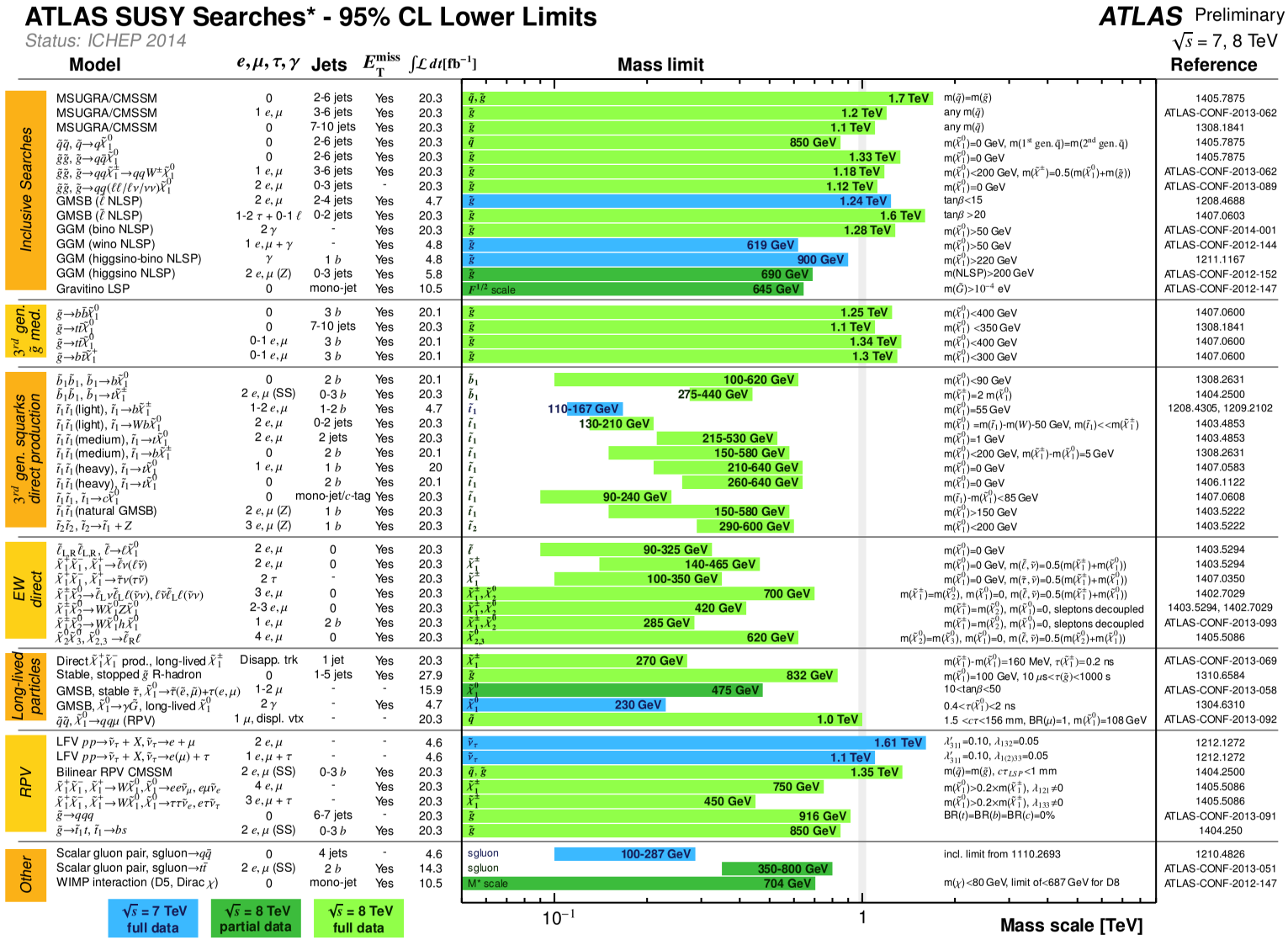

*Only a selection of the available mass limits on new states or phenomena is shown. All limits quoted are observed minus 1σ theoretical signal cross section uncertainty.

Figure 2.11: Summary of the ATLAS searches for SUSY with the run I data sets, taken from [63].

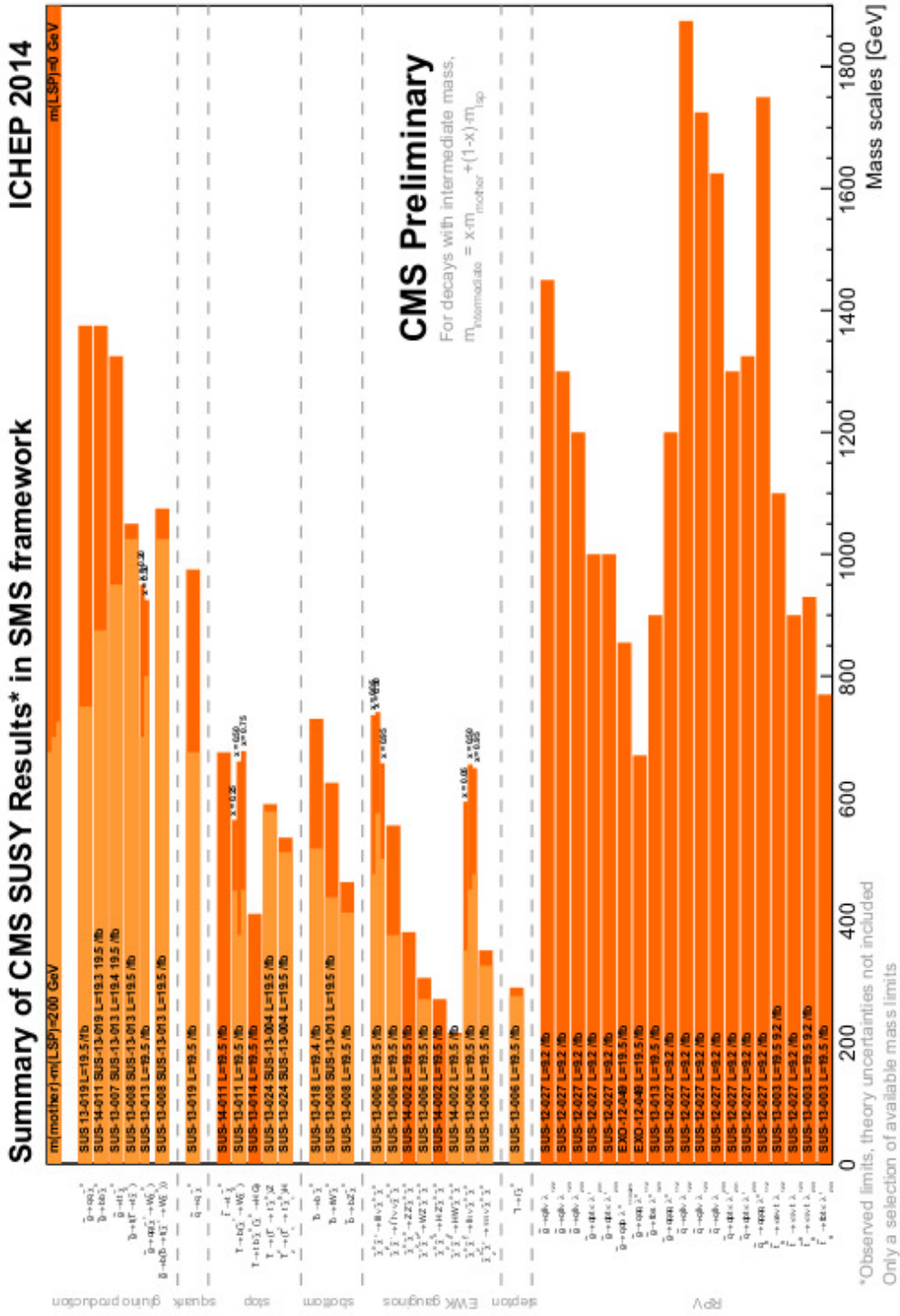

Figure 2.12: Summary of the CMS searches for SUSY with the run I data sets, taken from [64].

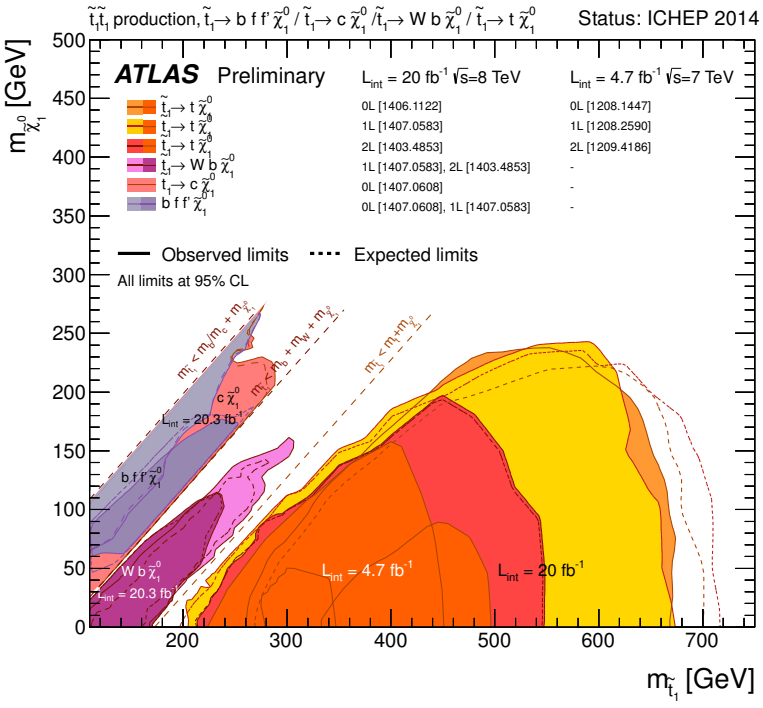

(a) ATLAS light Stop quark Summary

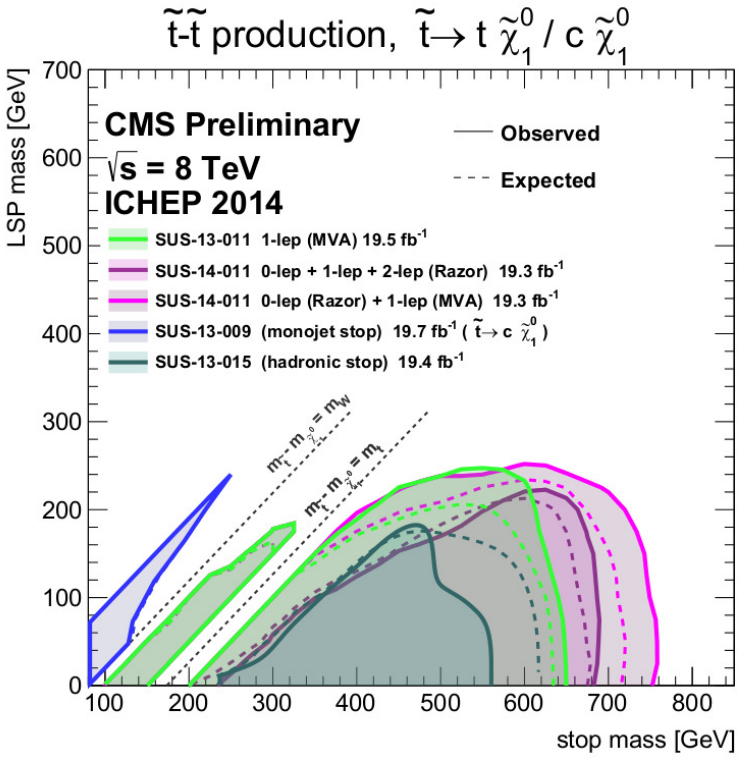

(b) CMS light Stop quark Summary

Figure 2.13: The summary of the LHC searches for SUSY from ATLAS and CMS with the run-I $\sqrt{s} = 7\,\text{TeV}$ and $\sqrt{s} = 8\,\text{TeV}$ data sets. The mass exclusion limits on the lightest stop quark ($\tilde{t}_1$) are shown in Figures (a) and (b). These figures were taken from [63] (a) and [62] (b).

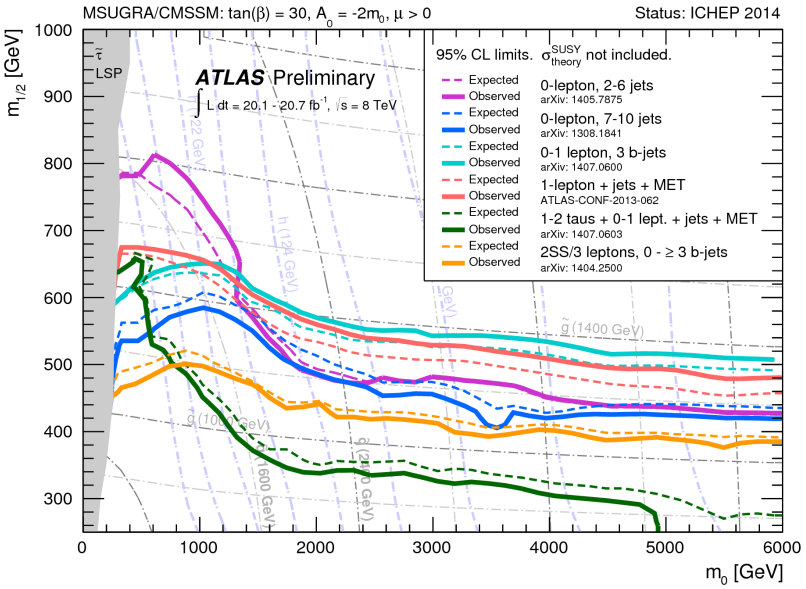

(a) ATLAS mSUGRA/CSSM Summary

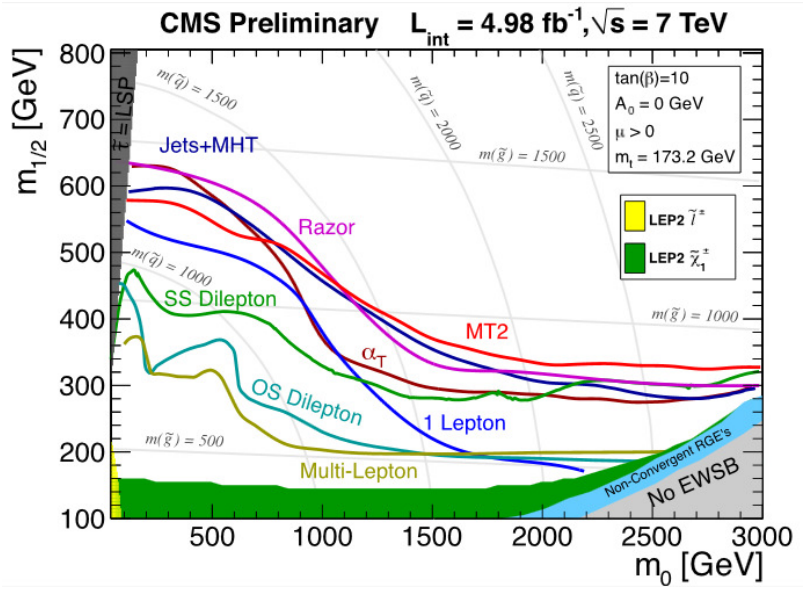

(b) CMS mSUGRA/CSSM Summary

Figure 2.14: The summary of the LHC searches for SUSY from ATLAS and CMS with the run-I $\sqrt{s} = 7\,\text{TeV}$ and $\sqrt{s} = 8\,\text{TeV}$ data sets. The ATLAS and CMS mass exclusion contours for the mSUGRA/CMSSM $m_0 - m_{1/2}$ mass plane are shown in Figures (a) and (b). These figures were taken from [63] (a) and [64] (a) .

2.6 Summary

This chapter gave an overview of the theoretical background that was relevant to this thesis. In section 2.2, the Standard Model was introduced. It focused on the particle content of the Standard Model, the strong force and the electroweak symmetry breaking within the SM. Section 2.3 gave a brief introduction to supersymmetry, one of the possible extensions to the Standard Model. Described in this section were the motivations behind supersymmetry, such as a natural solution to the gauge hierarchy problem and an introduction to the MSSM and some of its simplified versions. Next, section 2.4 described the types of supersymmetric particles that could be discovered at the LHC. This section included the strong production mechanisms for sparticles at the LHC and their decays. It also focused on jet algorithms and event kinematic variables used in searches for SUSY at the LHC. Finally, section 2.5 summarised some of the general searches for supersymmetry that were performed by the ATLAS and CMS collaborations with the run-I $\sqrt{s} = 7$ TeV and $\sqrt{s} = 8$ TeV data sets.

Chapter 3

The LHC and the ATLAS Detector

3.1 Introduction

The LHC and ATLAS detector are the machinery behind the production of data samples used in this thesis. These machines are some of the largest and most complex ever constructed, which are used for investigating the secrets of particles at the smallest of scales. This chapter will give a brief overview of the accelerator complex at CERN, and a detailed description of the ATLAS detector. Section 3.2 briefly describes the LHC and the accelerator complex at CERN; it will also describe how protons go from injection to collisions in the LHC. Next, Section 3.3 will cover the ATLAS detector: it will describe each subdetector system of the detector and how data events were recorded. Then, Section 3.4 describes the structure of an event and the production of MC simulated samples. A description of the ATLAS data sets used in the physics analyses chapters of this thesis is given in section 3.5. The standard ATLAS physics object reconstruction is described in section 3.6; however, this does not include particle flow reconstruction, which is documented in detail in Chapter 4. Finally, a brief discussion of the systematic uncertainties that are common to all of the physics analyses in this thesis is presented in section 3.7.

3.2 The LHC

The Large Hadron Collider [67] is a proton-proton collider[1] situated on the French-Swiss border at the European Centre for Nuclear Research (CERN). The collider sits in a 26.7 km circular tunnel approximately 100 m underground and is designed to collide protons at a centre-of-mass (CoM) energy $\sqrt{s} = 14$ TeV, which makes it the highest energy particle collider ever built. The high centre-of-mass energy is essential for the potential production of new exotic particles. The collider is designed to have a high luminosity of particle collisions, $1 \times 10^{34}\,\mathrm{cm}^{-2}\,\mathrm{s}^{-1}$. The high luminosity means that rare events (low cross-section) will occur at relatively high rates (with approximately

[1] The LHC is also designed to collide lead ions, and does so for approximately one month a year during data taking.

0.04 Higgs boson produced every second [68]). The overall collision rate is expected to be 40 MHz (40 million p-p interactions every second).

The proton beams are focused at four main points along the LHC ring, where large particle detectors have been constructed. The two largest particle detectors, A Toroidal LHC ApparatuS (ATLAS) [69] and Compact Muon Solenoid (CMS) [70], are general purpose particle detectors, which have a wide ranging physics programme. Large Hadron Collider beauty (LHCb) [71] focuses on b-physics, and has a very forward design that is optimised for b-physics at the LHC. Its physics programme focuses on rare decays of b-mesons and precise measurements of CP-violation in the SM [71]. The last particle physics experiment, A Large Ion Collider Experiment (ALICE) [72] is a heavy ion experiment that is specifically designed to look at lead-lead ion and proton-lead ion collisions. Its physics programme focuses on quark-gluon plasma, a primordial state of matter, which is thought to have existed in the early Universe not long after the Big Bang [72].

Figure 3.1 shows a schematic of the layout of the CERN accelerator complex. Protons destined for the LHC are injected with the linear accelerator (LINAC) 2 and accelerated to an energy of 1.4 GeV in the Booster. The Booster also groups the protons in bunches of around 10^{11} protons before injecting them into the Proton Synchrotron (PS). The PS accelerates the proton bunches up to an energy of 25 GeV before injecting them into the Super Proton Synchroton (SPS). The SPS is the last accelerator before the proton bunches are injected into the LHC; it accelerates the protons up to an energy of 450 GeV. After the proton bunches are injected into the LHC, they are accelerated to a maximum energy of 7 TeV per beam[2]. The LHC uses approximately 1300 8.3 T dipole magnets to circulate the proton bunches around the ring about ≈11 000 times a second, and over 300 quadrupole magnets to keep the beams focused. The proton bunches become uncollimated over time; therefore, another 5000 correcting magnets are used to keep the protons in bunches, and also to make orbital corrections as the protons circulate the LHC. Table 3.1 shows a summary of the technical parameters of the LHC machine [67].

3.3 The ATLAS Detector

3.3.1 Overview of Physics Goals

The ATLAS detector [69] is a general purpose particle detector, designed to be sensitive to physics within the full energy range of the LHC. ATLAS has a vast physics programme which is described in great detail within the physics sections of the expected performance report of the ATLAS detector

[2]The design centre of mass energy of the LHC machine is 14 TeV; however, due to problems with the dipole magnets, the LHC ran at ≈ $\frac{1}{2}$ its design centre-of-mass energy during run I.

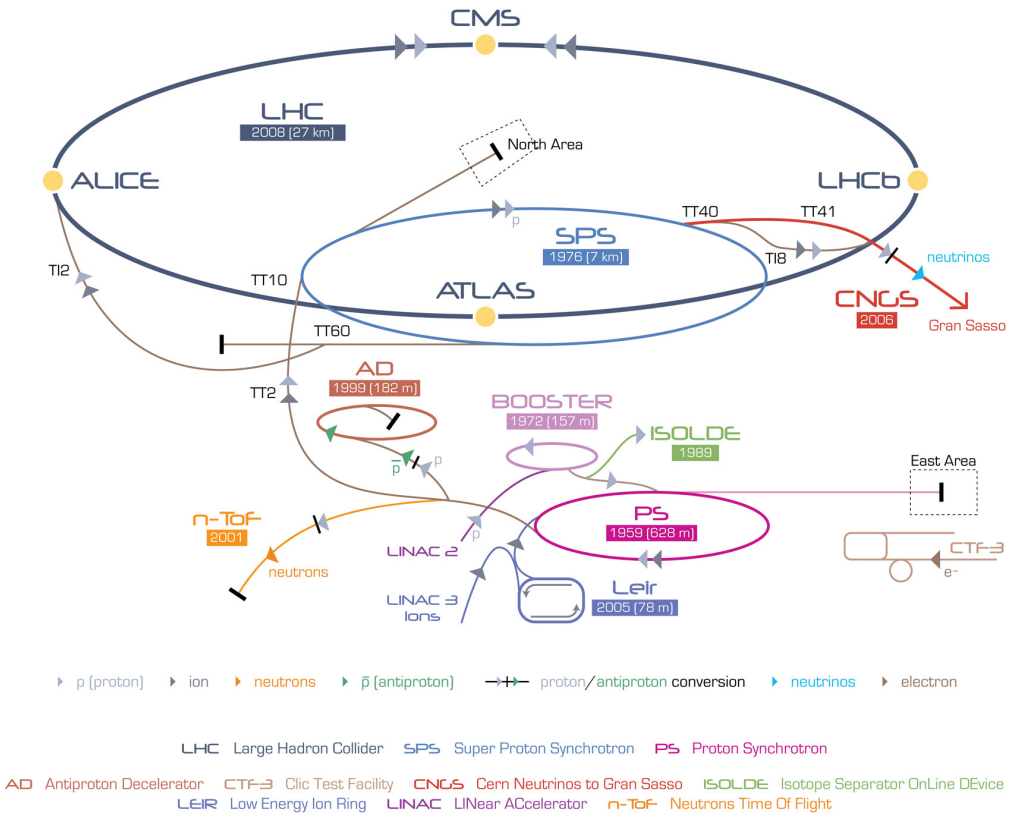

Figure 3.1: A schematic showing the layout of the accelerator complex at CERN. The LHC and previous particle accelerators constructed at CERN are shown. The yellow dots around the LHC ring show the main collision points of the proton bunches and the particle physics experiment that was constructed there. This figure was taken from the CERN public webpages [73].

(see Reference [74]). The ATLAS physics programme includes research on Higgs physics, supersymmetry, Standard Model physics, b and top physics and exotic searches for physics beyond the Standard Model (BSM) [74]. Furthermore, research is also performed on Combined Performance (CP) and non-collision backgrounds to improve the performance of the detector. Additionally, this research helps to increase the effectiveness of the physics analyses, as it is essential to use the detector to its full potential since some of the physics processes being studied are rare.

3.3.2 Coordinate System and Transverse Quantities

The ATLAS detector uses a right-handed Cartesian coordinate system with the x-axis pointing into the centre of the LHC collider ring, the y-axis pointing in the vertical direction towards the surface and the z-axis running parallel to the LHC beam pipe [74]. The ATLAS detector follows a concentric cylindrical symmetry; therefore, the spherical polar angles of θ and ϕ are used. The azimuthal angle (ϕ) is measured around the beam axis in the z-axis direction, and the polar θ angle is measured as the angle from the beam axis in the z-axis direction [74]. A schematic of the ATLAS coordinate

Parameter	Value
Machine circumference	26 658 m
Energy per beam (design)	7 TeV
Dipole field strength (at 7 TeV)	8.33 T
Number of dipole magnets	≈ 1200
Dipole magnet temperature	1.9 K
Number of quadrupole magnets	≈ 400
Number of correcting magnets	≈ 5000
Luminosity (design)	$10^{34}\,\mathrm{cm}^{-2}\,\mathrm{s}^{-1}$
Number of protons per bunch	1.15×10^{11}
Number of bunches per beam	2808
Time between bunches (at peak luminosity)	25 ns

Table 3.1: Technical design parameters of the LHC, taken from [67].

system is shown in Figure 3.2.

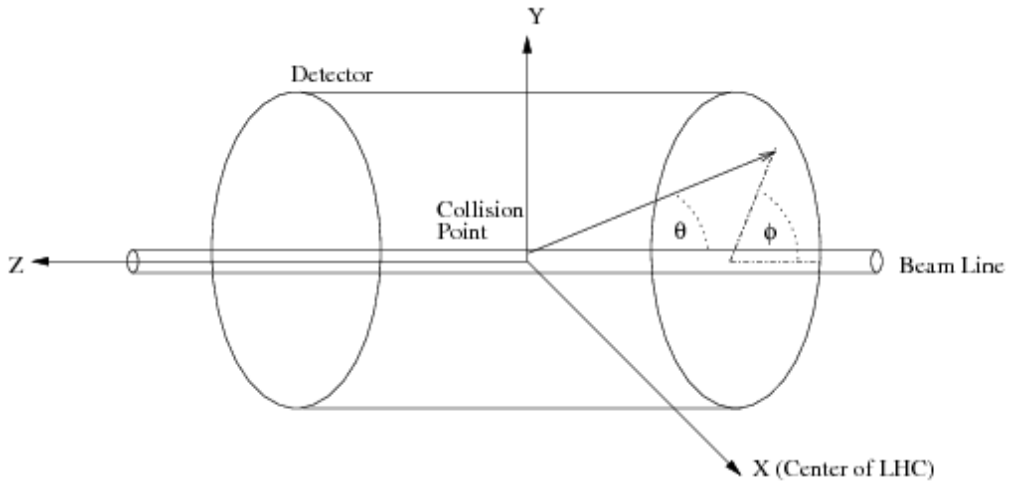

Figure 3.2: A schematic showing the coordinate system of the ATLAS Detector, taken from [75].

Since the LHC is a hadron collider, the hard scatter/collision actually occurs between partons within the protons and the exact momentum of the partons is impossible to determine. The CoM frame of the collision is normally Lorentz boosted in the z-direction, which means that most physics analyses use quantities that are invariant under a Lorentz boost.

Pseudorapidity (η) (an approximation of rapidity) is widely used instead of θ, since differences in η are invariant under a Lorentz boost. Rapidity, $y = 1/2 \ln\left[\frac{E+p_z}{E-p_z}\right]$, cannot be used since the

momentum of the parton in the z-direction is unknown. Pseudorapidity is defined as

$$\eta = -\ln\left[\tan\left(\frac{\theta}{2}\right)\right]. \tag{3.1}$$

It is also important to define a quantity that measures the distance between physics objects for jet formation (see 2.4.2) and resolving overlapping physics objects in the detector (see 3.6.7). The Lorentz invariant geometric variable ΔR in the $\eta - \phi$ plane is used for this. ΔR is defined as

$$\Delta R = \sqrt{(\Delta\phi)^2 + (\Delta\eta)^2}. \tag{3.2}$$

Since the partons in the hard scatter carry an unknown proportion of the momentum of the proton, conservation of momentum can only be applied in the transverse direction to the beam axis; therefore, transverse quantities, such as p_{T} and E_{T} the projections of momentum and energy in the $x-y$ plane, are used in the majority of ATLAS physics analyses.

3.3.3 Detector Overview

The ATLAS detector is made from several subdetectors positioned in a concentric cylindrical layer structure. The detector covers a near 4π solid angle that is ideal for measuring jets and missing transverse energy ($E_{\mathrm{T}}^{\mathrm{miss}}$) (see 2.4.3).

Figure 3.3 shows a schematic of the ATLAS detector. This section closely follows references [69] and [74], which provide an in-depth description of the ATLAS detector.

The inner detector (ID) (shown in light green in Figure 3.3) is the subdetector that is closest to the beam pipe. It focuses on vertex reconstruction and tracking charged particles [69]. The ID is also immersed in a magnetic field provided by the ATLAS solenoid magnet that surrounds the entire inner detector.

The next major subdetector system is the calorimeters (shown in orange in Figure 3.3). The calorimeters measure the energy deposited by particles. The ATLAS calorimeters consist of the Liquid Argon (LAr) electromagnetic calorimeter (ECAL), the hadronic calorimeter (HCAL) and the Forward calorimeter (FCAL) [69]. The ECAL is optimised to measure the energy deposited by electromagnetic particles, namely electrons and photons. The HCAL is a hadronic calorimeter which measures the energy deposited by hadrons. The FCAL measures the energy deposited by

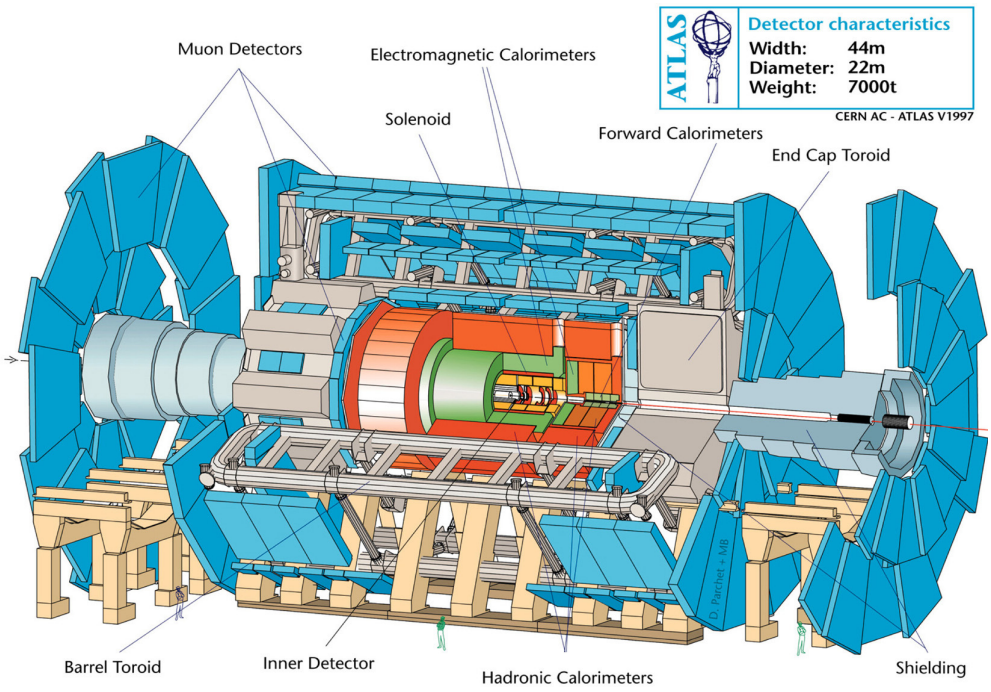

Figure 3.3: A schematic showing the different components of the ATLAS Detector, taken from [69].

forward particles ($|\eta| > 3.1$) [69]. All of the calorimeters are used in conjunction to measure the energy of jets, which can contain many different hadronic and electromagnetic particles.

The outermost subdetector consists of the muon chambers (shown in light blue in Figure 3.3). The muon chambers measure the direction and momentum of muons created in the hard scatter (or cosmic muons), and are also used for triggering events containing muons [74].

3.3.4 Inner Detector

The inner detector is a cylindrical tracking detector that is closest to the LHC beam pipe (≈50 mm away). The ID consists of the pixel detector, the semiconductor tracker (SCT) and the transition radiation tracker (TRT). The pixel detector and the SCT are precision silicon tracking detectors, and cover a pseudorapidity range of $|\eta| < 2.5$. The TRT is a straw tube detector that covers a pseudorapidity range of $|\eta| < 2$. The whole inner detector is immersed in a 2 T magnetic field, generated by the ATLAS solenoid magnet (see 3.3.7). The magnetic field curves the trajectory of charged particles as they pass through the inner detector, providing particle momentum measurements from the radius of curvature of the resultant track. Figure 3.4 shows a schematic of the ATLAS inner detector.

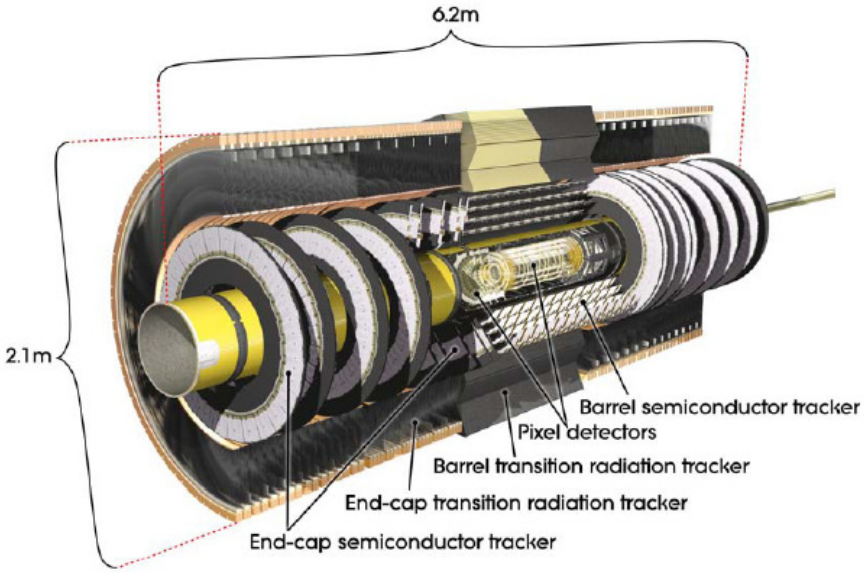

Figure 3.4: A schematic showing the composition of the ATLAS Inner Detector, taken from [69].

Pixel detector

The pixel detector is located at the centre of the ID, and has the highest granularity of all the detectors in the ID. The detector is constructed from 60 million silicon pixels, which have a minimum pixel size of 50×400 μm. The high granularity of the pixel detector is used to reconstruct vertices from particle collisions with high resolution. This also includes measuring the position of any secondary vertices which occur away from the primary vertices, since long lived B-mesons can travel a measurable distance away from the primary vertex before they decay. The pixel detector is one of the crucial components used to identify jets that have originated from b-quarks (b-jets).

SCT

The SCT is another silicon detector. It lies outside the pixel detector ≈300 mm away from the beam pipe. The SCT is also designed to track charged particles, and consists of 6 million silicon wafer strips each 80 μm wide. It has a track resolution of ≈200 μm [69], which is not as good as the pixel detector. The SCT is expected to have a hit efficiency (efficiency of detecting the ionisation from a charged particle passing through the detector) of over 99% [74] even at the design luminosity of the LHC. The SCT has 4 different layers of modules that sit around the barrel of the inner detector, and two endcap sections which have 9 disks of modules. With the endcap sections, the SCT can provide charged particle tracking up to a pseudorapidity of $|\eta| = 2.5$ [69]. The SCT contributes to the measurement of 8 different track parameters, including momentum, impact parameter and

vertex position [69].

TRT

The TRT is a straw tube detector that provides further tracking information about charged particles. The TRT can provide up to 32 hits per track, thus making a considerable contribution to the momentum measurement of the track. The TRT also has some particle identification capabilities through the amount of transition radiation (TR) a particle deposits in the detector. Transition radiation is the radiation emitted by a relativistic charged particle when it transverses an inhomogeneous medium [76]. For particle detectors, the inhomogeneous medium is the boundary region between two materials with different electrical properties [76]. The higher the velocity of the particle, the more transition radiation the particle deposits [76]. Therefore, the TRT is useful for distinguishing between electrons and charged pions ($\pi^{\pm}$) [69].

3.3.5 Calorimetry

The ATLAS detector uses two different calorimeter systems (electromagnetic and hadronic). These calorimeters accurately measure the deposition of energy from particles. They are sampling calorimeters constructed from alternating layers of an active material, where the energy measurements are taken, and an absorbing region, which is used to contain the particles within the calorimeter and limit the amount of 'punch-through' of high momentum particles into the muon chambers. Detailed descriptions of calorimetry techniques can be found in Reference [77].

The ATLAS calorimeters provide full angular coverage for particles up to $|\eta| < 4.9$, but precise energy measurements only for particles with pseudorapidity of $|\eta| < 2.5$ [69]. The large coverage is essential for measuring missing transverse energy ($E_{\mathrm{T}}^{\mathrm{miss}}$), since this requires the detector to measure the energy of all particles that have a significant transverse momentum. Therefore, the large coverage of the calorimeters improves the resolution of the $E_{\mathrm{T}}^{\mathrm{miss}}$. Figure 3.5 shows a schematic of the ATLAS calorimetry systems.

Electromagnetic Calorimeter

The electromagnetic calorimeter (ECAL) uses Liquid Argon (LAr) as its active medium, and lead as its absorbing medium. It is divided into three separate regions: the barrel region (covering $|\eta| < 1.475$) and two end-cap regions (covering $1.375 < |\eta| < 3.2$). Since the structure of the inner detector only extends to $|\eta| < 2.5$, this limits the precision of measurements in the electromagnetic

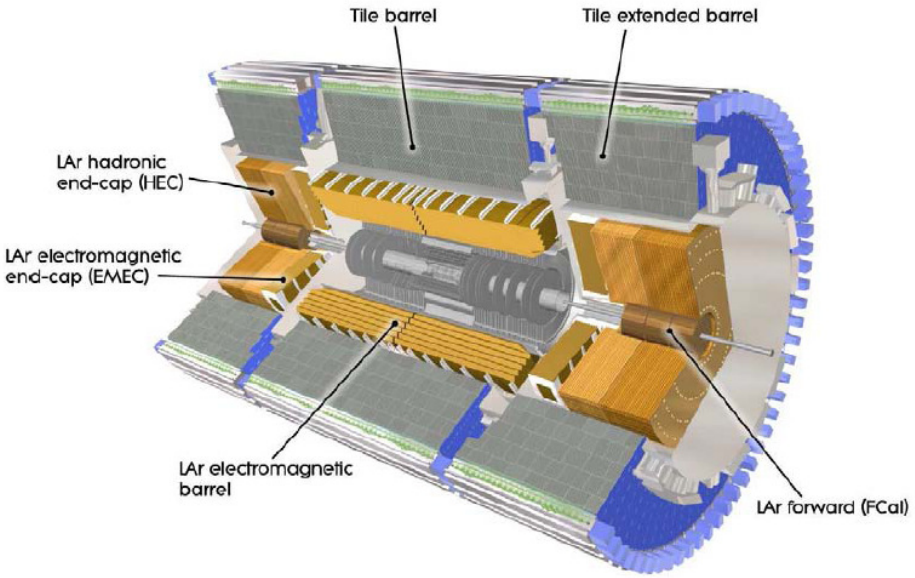

Figure 3.5: A schematic showing the layout of the ATLAS calorimeters, taken from [69]. Each calorimeter system is constructed from a large number of individual cells. Particles will deposit their energy in a number of cells as they traverse the calorimeter. The individual calorimeter cells are used as the primary input for jet formation in data (see section 2.4.2).

calorimeter outside this η region. This led to the design of the barrel region (low $|\eta|$) of the electromagnetic calorimeter having the highest level of granularity. Figure 3.6 shows a schematic of a module from the barrel region of the electromagnetic calorimeter.

Energy from particles is deposited into four different layers of the electromagnetic calorimeter:

- Pre-sampler – this layer sits in front of the electromagnetic calorimeter ($|\eta| < 1.8$), and is used to correct for energy loss caused by the ID and detector support systems.

- First sampling layer – this layer has the highest level of granularity, and is used to provide the very high η-ϕ resolution required for photon and π^0 differentiation. Only the lowest energy electrons and photons will be fully contained within this layer of the calorimeter.

- Second sampling layer – this layer is the main energy deposition layer in the electromagnetic calorimeter. It has $\approx$16 radiation lengths (X_0) of material, which can fully contain the electromagnetic shower from an electron or photon with an energy less than 50 GeV [74]. The η-ϕ resolution of the second layer is around a tenth of the first sampling layer, as the very high η-ϕ resolution is no longer required.

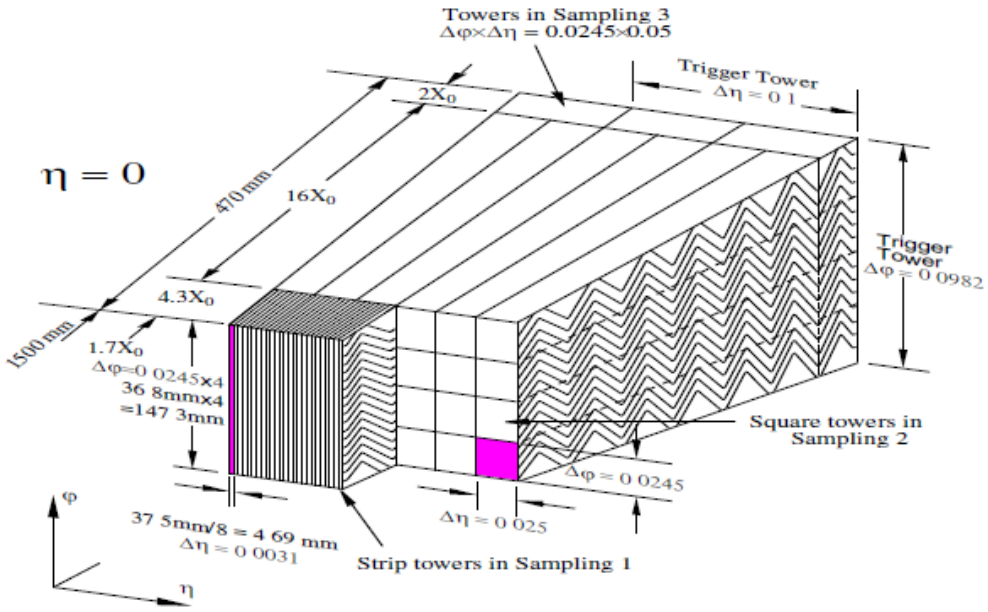

Figure 3.6: A schematic showing a module from the barrel region of the ATLAS electromagnetic calorimeter, taken from [69]. The schematic shows the $\eta - \phi$ granularity and the number of radiation lengths (X_0) for each layer of the electromagnetic calorimeter.

- Third sampling layer – only very high energy electrons and photons will make it to this layer of the electromagnetic calorimeter; therefore, the cells are coarser than the other layers of the calorimeter, without fear of loss in resolution or overlapping showers.

One important thing to note about the structure of the EM calorimeter is that there is a crack region where the endcap and barrel regions meet, at $|\eta| \approx 1.5$. Since there is less detector material in this region, the energy resolution of electrons and photons in the crack region is lower than the barrel and endcap regions [69].

Hadronic Calorimeter

The ATLAS Hadronic calorimeter is composed of five different sections: the barrel tile section ($|\eta| < 1.0$), two tile endcap sections, called the extended barrel ($1.0 < |\eta| < 1.7$) and two hadronic endcaps ($1.5 < |\eta| < 3.2$). In the tile regions, plastic scintillating panels 3 mm thick are used as the active material, and iron plates (5 mm master plate and a 4 mm spacer plate [69]) are used as the absorbing material. The tiles are laid in a staggered fashion to avoid any gaps appearing within sections of the calorimeter. The scintillation light caused by the tiles is collected by wavelength shifting fibres (WLS), which transport the photons to the photomultiplier tubes (PMTs). WLS fibres

are required as the plastic scintillating tiles emit light in the ultraviolet region of the electromagnetic spectrum. Light at this frequency is largely reabsorbed by the medium [78]. The photomultiplier tubes then convert the photons into an electrical signal that represents the energy sampled by the tile. Figure 3.7 shows an example schematic of a tile module which makes up part of the barrel region of the hadronic calorimeter.

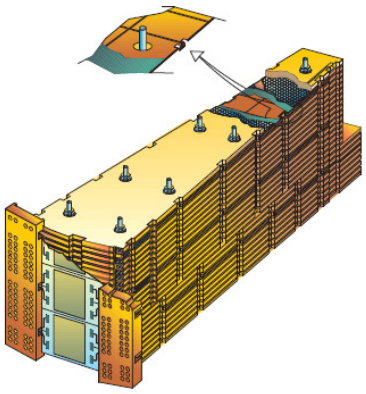

Figure 3.7: A schematic showing a tile module from the barrel region of the ATLAS hadronic calorimeter, taken from [69].

The hadronic endcap calorimeter (HEC) is made from LAr active material situated between copper absorption layers. The HEC is composed of two disks on either side of the detector: each has 32 modules divided into four different sampling layers.

Forward Calorimeter

The forward calorimeter (FCAL) is situated in the forward η regions of the ATLAS detector ($3.1 < |\eta| < 4.9$). The FCAL is designed to handle a large flux of low transverse momentum (p_{T}) particles. The FCAL is another calorimeter system that uses LAr as its active material. It consists of three compartments with different absorption materials. The first compartment, which helps to dissipate the heat produced from the high flux of particles, uses copper [69]. Copper is used to measure forward electromagnetic particles. The two other compartments are made from Tungsten, which has a very high radiation length; these compartments are designed for measuring forward hadronic particles.

3.3.6 Muon System

The ATLAS muon spectrometer (MS) is designed to trigger[3], track and measure the p_T of muons originating from the interaction point. For the muon chambers to be effective over a wide range of p_T and η, an intense magnetic field is required. The magnetic field is produced by the ATLAS toroidal magnetic system which covers the entire muon system (see section 3.3.7). Figure 3.8 shows how precise muon p_T measurements are achieved in the ATLAS muon systems.

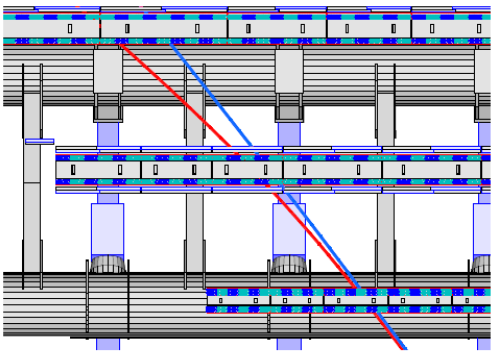

Figure 3.8: A schematic showing how the p_T of muons is measured in the ATLAS Muon System, taken from [69]. The trajectories of two muons (4 GeV red and 20 GeV blue) are shown as they pass though the muon spectrometer. It can be seen that the trajectory of the 20 GeV muon is curved less by the ATLAS toroidal magnetic field.

The muon system consists of two different types of muon chambers: muon drift tubes (MDT) and the cathode-strip chambers (CSC). Figure 3.9 shows a schematic of each type of muon chamber used in the ATLAS detector.

The muon drift tubes are located in the barrel region of the ATLAS detector, and provide precise measurements of the location of ionisation tracks from muons passing through the chamber. The most important track position is in the primary bending direction of the toroidal magnetic field, as this direction is used to calculate the curvature of the muon track, and hence the p_T of the muon. ID tracking information can also be used in conjunction with track information from the muon chambers for muons with E_T up to ~100 GeV [69]. Unfortunately, tracks from very high energy muons do not curve enough in the ID for this information to be useful; therefore, only the muon chamber track information can be used for high energy muons.

The cathode-strip chambers are located in the forward region of the ATLAS detector, and are designed to handle a high occupancy of low p_T forward muons, since the maximum counting rate of muons in the MDTs is only 150 Hz cm^{-2} [69]. The CSCs are multiwire proportional chambers, where the wires are oriented in the radial direction pointing to the centre of the muon CSC

[3]Input from the muon chambers is used at level 1 in the ATLAS trigger system.

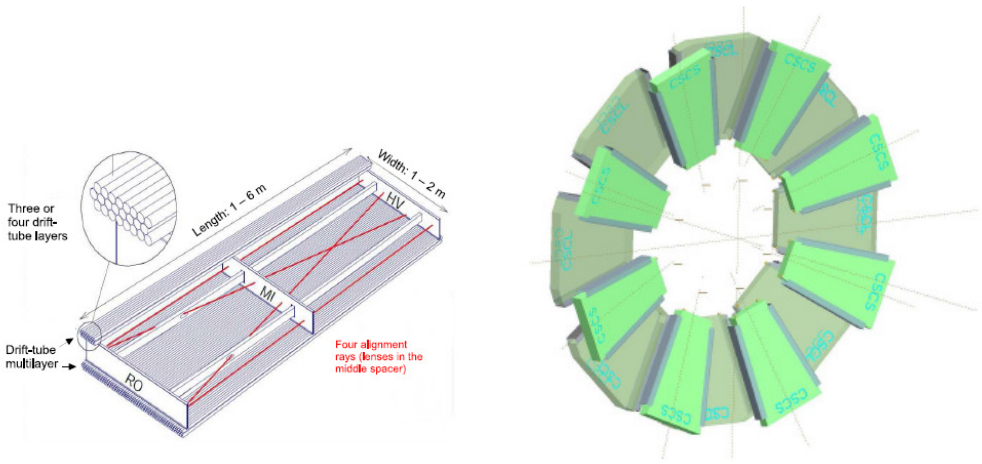

(a) Schematic of an ATLAS MDT chamber (b) Schematic of the ATLAS CSC wheel

Figure 3.9: Schematics showing the different types of muon chambers used in the ATLAS muon system, taken from [69]. Figure (a) shows a schematic of an ATLAS MDT chamber. Figure (b) shows a schematic of one of the ATLAS CSC muon chamber wheels.

wheel. The multiwire proportional chambers provide a higher maximum safe counting rate of 1000 Hz cm^{-2} with a similar track resolution to the MDT chambers [69].

Resistive plate chambers (RPCs) are used to trigger on muons in the barrel section, and thin gap chambers (TGCs) are used in the endcap sections. Figure 3.10 shows a schematic of the muon trigger system, and how different energy muons originating from the interaction point are detected using the muon systems.

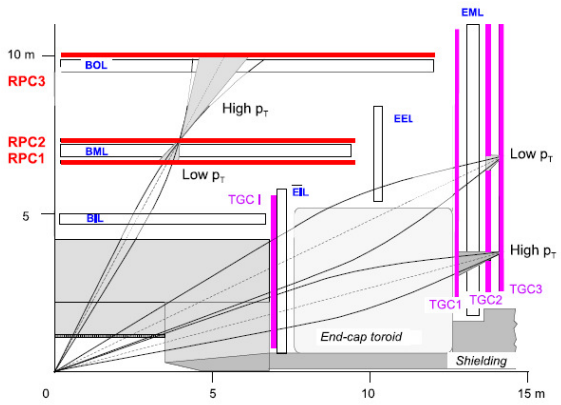

Figure 3.10: A schematic of how muons of different η are detected with the ATLAS muon trigger system, taken from [69]. The red sections show the locations of the RPC and TGC triggering detectors.

3.3.7 Magnet Systems

In order to measure the momentum of charged particles accurately, two different magnet systems are used within ATLAS. The first is a 2 T solenoid magnet which surrounds the inner detector. The second is a toroidal magnet system that has a magnetic field strength of 0.5 T in the barrel region and increases to 1 T in the endcap regions of the muon system. A schematic of the ATLAS magnet systems is shown in Figure 3.11. The eight toroid magnets are the iconic image of the ATLAS detector, and Figure 3.12 shows a photograph of their installation.

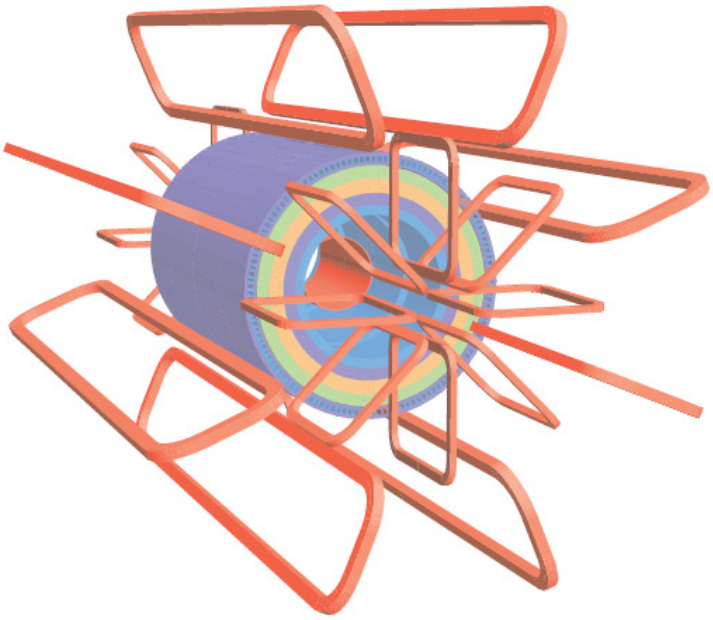

Figure 3.11: A schematic of the ATLAS magnet systems, taken from [69]. The red central cylinder shows the solenoid magnet and the eight toroid magnet sections with their endcaps are shown also in red outside the cylinder structure.

3.3.8 Trigger

Due to the high luminosity of the LHC ($\sim 10^{34}$ cm^{-2} s^{-1}), an interaction rate of approximately 40 MHz is expected; however, the current computing resources can only permanently record and store an event rate of 200 Hz. This means that the ATLAS detector requires a very sophisticated trigger system to record only the most interesting events. The trigger can only select a couple of events per million for permanent storage.

The ATLAS trigger system select events using a three tier system.

- The level 1 (L1) trigger is hardware based and is constructed from specialised electronics.

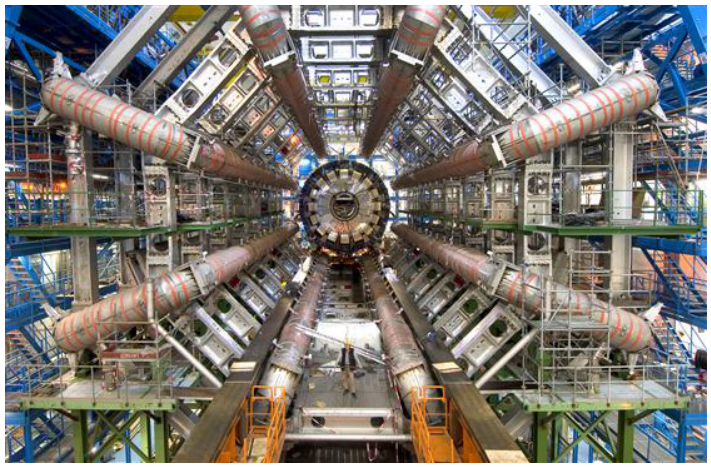

Figure 3.12: A photograph of the ATLAS toroid magnets taken in 2005 during the construction of the ATLAS detector, taken from [79].

It uses the raw information from the muon systems and calorimeters to search for high E_{T} physics objects, such as jets, electrons, photons, muons and decayed taus. The trigger then uses this information to create regions of interest (RoI); the RoIs are passed to the central trigger processor, which decides whether the event should be passed to the level 2 trigger.

- The level 2 (L2) trigger is software based. The trigger analyses the RoIs in the events passed to it by the L1 trigger. It performs a partial reconstruction in the regions of interest to measure important quantities, such as trajectory and energy. If the central trigger processor decides the RoIs in the event were significant, then the event is then passed to the high level trigger (tier 3).

- The high level (HL) trigger is the Event Filter (EF). Since there are finite computing resources that can only fully process and permanently store 200 events a second, the HL chooses 200 of the most interesting events that have passed the L2 trigger. The selection of these events is decided by the trigger menu, created from requests by the offline physics analysis and CP groups. The EF trigger also has access to the full event information not just the RoIs.

Trigger Chains and Menus

The three tier trigger system requires that event triggers must be configured in '*chains*'. Each trigger chain has a trigger '*item*' at each level of the ATLAS trigger. One of the simplest trigger configurations is the single jet trigger chain, where the existence of a jet-like object above a certain E_{T} threshold is tested for in each level of the trigger chain. An example single jet trigger chain is shown in Eq.(3.3). Here, the L1 trigger algorithm is searching for a jet-like object with E_{T} of at least

30 GeV before producing a RoI for the L2 trigger. The L2 trigger algorithm uses a tighter selection requirement (E_{T} >50 GeV) than the L1 trigger, and if this criterion is met, then the L2 trigger passes the event to the EF. Finally, if the event passes the requirements of the EF trigger (in this case a jet with E_{T} >55 GeV) it is recorded to permanent storage.

$$\text{L1\_J30} \rightarrow \text{L2\_j50} \rightarrow \text{EF\_j55} \tag{3.3}$$

Table 3.2 shows a summary of the different objects in the ATLAS trigger menu and their corresponding symbols.

Object	L1 symbol	HLT (L2,EF) symbol
Jet	J	j
Photon	EM	g
Electron	EM	e
Muon	MU	mu
Tau	TAU	tau
$E_{\mathrm{T}}^{\mathrm{miss}}$	XE	xe

Table 3.2: A summary table showing the different types of physics objects in the ATLAS trigger menu, and their corresponding symbols [74].

3.4 The Structure of an Event and MC Production

An event in the ATLAS detector is made up of several parts. Figure 2.7 shows an example of a simulated $t\bar{t}h$ event made with the SHERPA [60] Monte Carlo generator.

The main part of an event (hard collision) is caused by partons from the initial protons colliding. Events where more than one parton collide are referred to as *multi-parton interactions* (MPI); this type of event is rarer than single parton interactions, where only one parton from each proton collides. The partons which are not involved in the hard scatter can also produce additional activity in the event: any particles produced in these interactions are categorised as being part of the *underlying event*.

Highly accelerated charged particles emit radiation. This radiation is categorised by when in the event it is emitted. If the particle emitted the radiation before the hard collision, the radiation is categorised as *initial state radiation (ISR)*; on the other hand, if the radiation was emitted after the

hard collision, then it is part of the final state of the event, and therefore is categorised as *final state radiation* (FSR).

Since the LHC collides bunches of protons and not single protons, it is possible to get more than one particle collision in a bunch crossing; these additional soft collisions in the background of the event are referred to as *in-time pile-up*. In-time pile-up became increasingly important at the end of run I when the instantaneous luminosity of the LHC was comparatively high ($\sim 10^{33}$ cm^{-2} s^{-1}). This led to an average in-time pile-up of ≈ 20 collisions per bunch crossing ($\langle\mu\rangle$) (see section 3.5). The p-p beams consisted of approximately a thousand bunches during run I (see Table 3.1); therefore, it was possible for other collisions to take place in a bunch crossing other than the one of interest before the ATLAS detector event cycle was completed. This phenomenon is known as *out-of-time pile-up*, but it had less significant impact on the recorded data than in-time pile-up during run I. Any future references to the term pile-up in this thesis will refer to the in-time pile-up caused by multiple interactions within a bunch crossing.

3.4.1 Monte Carlo Production

The production of Monte Carlo samples within the ATLAS collaboration is a well-defined process, see reference [80]. The process is undertaken in four different steps: event generation, detector simulation, digitisation and event reconstruction. Figure 3.13 shows a diagram of the production process of data and Monte Carlo samples: data events go straight to the event reconstruction software after being recorded by the ATLAS detector, whereas the Monte Carlo simulated events require extra steps before the event reconstruction software can be run on the events.

Event generation consists of generating the particle four-vectors of a physics process at the particle level. This is performed by MC event generators, such as `PYTHIA` [81, 82] or `ALPGEN` [83]. The MC event generators calculate the QCD processes in events to a certain degree of accuracy, normally to leading order (LO) or next-to-leading order (NLO). All MC event generators require a parton distribution function (PDF) that describes the probability of a parton involved in the hard collision having a particular momentum fraction of the parent proton. Figure 3.14 shows an example set of PDFs for two different values of squared momentum transfer (Q^2) using the `MSTW2008NLO` [84] PDF set. MC generators can simulate not only the hard scatter, but the parton showers, hadronisation and underlying event as well. They may simulate the extra interactions internally, as with `PYTHIA` and `SHERPA` [81, 60], or they may be interfaced with specialised software like `JIMMY` [85], which simulates the underlying event (see section 3.4).

The detector simulation stage passes the simulated events through a full `GEANT4` [86] model of the ATLAS detector. The full simulation of the ATLAS detector is very time and cpu consuming;

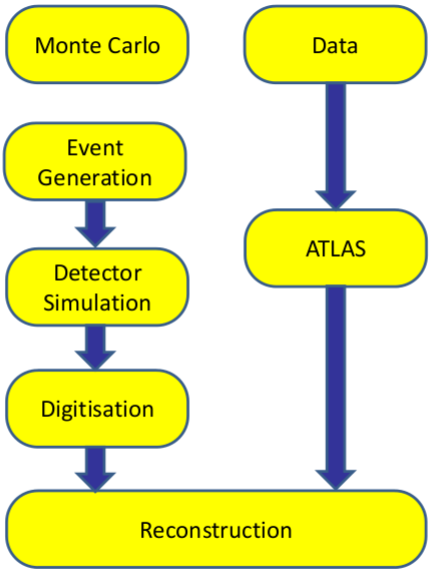

Figure 3.13: Schematic of the event reconstruction process. Monte Carlo samples undertake several steps (event generation, detector simulation and digitisation) during the simulation process before the reconstruction step, whereas data samples are just recorded by the detector before the samples are reconstructed.

therefore, several fast simulation software packages have been developed, such as ATLAS Fast (`ATLFAST`) [87]. `ATLFAST` uses an average shower shape profile to simulate particle showers in the calorimeters, which reduces the calorimeter simulation time compared to the full `GEANT4` detector simulation.

In the digitisation stage, the interactions (hits) of the detector simulation are converted into simulated times and voltages that mimic the actual response of the ATLAS detector, so that the MC simulated events enter the reconstruction software in the same format as the data events. The reconstruction of physics objects is described in section 3.6.

3.4.2 Monte Carlo Reweighting

In-time pile-up is defined in section 3.4. During run I, the LHC was running at a comparatively high instantaneous luminosity where on average $\approx$ 20 additional soft collisions occurred at the same time as the hard scatter. However, the exact run conditions were not known at the start of the MC production process, and the run conditions in the MC simulation were not the same as the

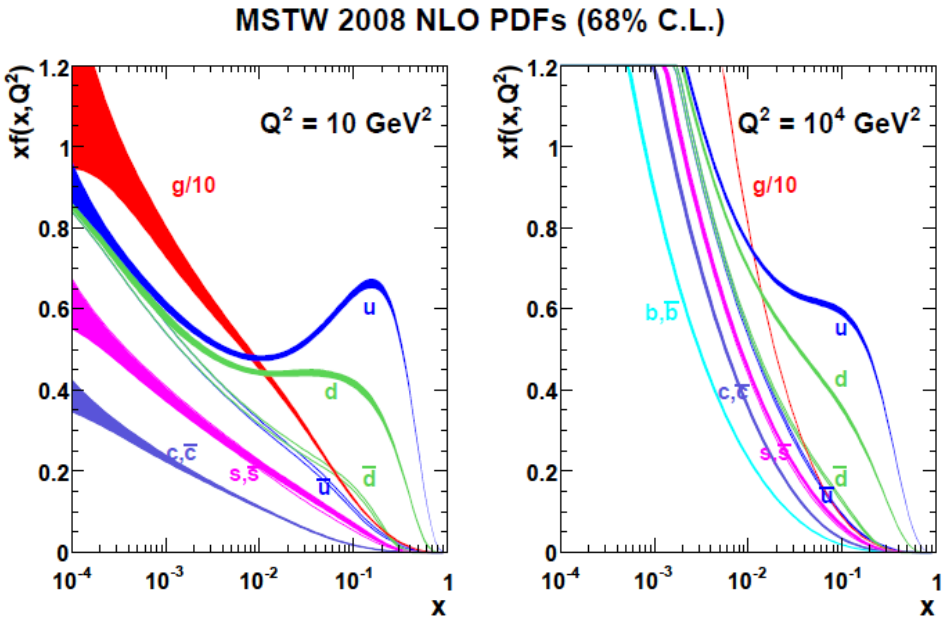

Figure 3.14: The `MSTW2008` NLO parton distribution functions for the LHC, shown within a 68% confidence limit for two different values of Q^2: 10 GeV^2 (left-hand) and 10^4 GeV^2 (right-hand). This figure was taken from [84].

recorded data. For example, $\langle\mu\rangle$ was different in MC simulation compared to the true data taking run conditions. This can be seen in Figure 3.15, which shows a comparison of $\langle\mu\rangle$ in data and two different MC samples from the `MC12a` campaign [88]. Therefore, the MC events were reweighted to match the $\langle\mu\rangle$ in data. The pile-up reweighting was performed with the ATLAS pile-up reweighting tool [89] by comparing the $\langle\mu\rangle$ distributions of data and MC samples.

The p_{T} of the electrons and muons in MC simulation were also rescaled and smeared to match distributions in data [90, 91].

3.4.3 ATLAS 2011 $\sqrt{s} = 7$ TeV Monte Carlo Samples

The 2011 MC samples were produced using the default ATLAS `MC11b` [92] (`PYTHIA` 6 pile-up) or `MC11c` [93] (`PYTHIA` 8 pile-up) parameters with the full `GEANT4` [86] detector simulation. The fragmentation and hadronisation of `ALPGEN` and `MC@NLO` samples was performed with `HERWIG` [94, 95], using `JIMMY`[85] to simulate the underlying event (see section 3.4).

QCD multijet events were generated with `PYTHIA` 6 [81], using the `MRST2007LO*` modified leading-order PDFs [96]. W and Z/γ^* were also produced with `ALPGEN`, where they were simulated with up to 5 additional partons.

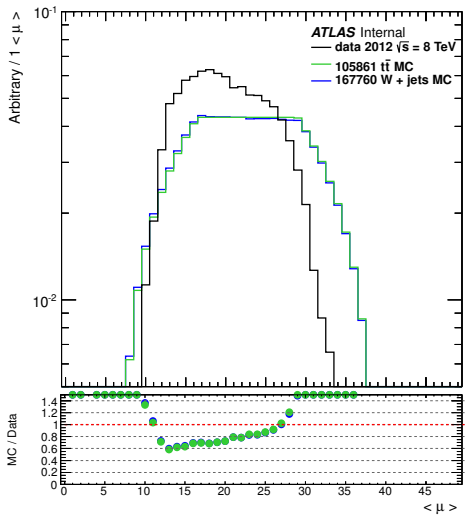

Figure 3.15: The $\langle\mu\rangle$ distributions of the 2012 data set (black) and two MC samples from the `MC12a` production campaign (green and blue).

The production of top quark pairs ($t\bar{t}$) was simulated using `ALPGEN` [83], with a top quark mass of 172.5 GeV and PDF set `CTEQ6L1` [97]; cross-checks were made with `MC@NLO` [98, 99] using the NLO PDF set `CTEQ6.6` [100]. Single top production was simulated with `AcerMC` [101], which was interfaced with `PYTHIA` and used the `MRST2007LO*` [96] PDF set.

3.4.4 ATLAS 2012 $\sqrt{s} =$ 8 TeV Monte Carlo Samples

ATLAS 2012 Monte Carlo samples were generated during the `MC12a` and `MC12b` official production campaigns [88, 102]. All samples used the full `GEANT4` detector simulation. The parton shower and fragmentation processes for `ALPGEN` and `MC@NLO` samples were simulated using `HERWIG` [94, 95], with `JIMMY` [85] for simulating the underlying event.

QCD multijet events were generated with `PYTHIA` 8 [82] using the `CT10` [103] next-to-leading-order PDF set with the `AU2` ATLAS tune [104]. W boson events were simulated with `ALPGEN` 2.14 [83] using the `CT10` [103] next-to-leading-order PDF set. The events were simulated with up to 5-6 extra partons in the final state.

Z/γ^* events were generated with `SHERPA` 1.4 [60]. Events were generated with up to 4 additional partons in the final state to improve the description of events which had several hard jets. `SHERPA` events were also generated with massive c and b quarks, which improved the simulation of flavour-tagging variables.

The production of top quark pairs ($t\bar{t}$) was simulated with `PowHeg` [105] interfaced with `PYTHIA`

6 [81] for the fragmentation and the hadronisation processes. The top-quark mass was fixed at 172.5 GeV, and the NLO PDF set `CT10` was used. `PYTHIA` 6 parameters used the `Perugia2011C` tune [104]. Single top events were simulated with `MC@NLO` for the s-channel and `AcerMC` [101] interfaced to `PYTHIA` 6 using PDF set `CTEQ6L1` for *Wt* processes.

3.5 Data Samples

The raw 2011 and 2012 data samples used in this thesis were recorded with the ATLAS detector. The ATLAS 2011 $\sqrt{s} = 7$ TeV data sample was recorded from the 22$^{\text{nd}}$ March 2011 to 30$^{\text{th}}$ October 2011, corresponding to runs 178044 to 191933 (data-taking periods B2 M10). The ATLAS 2012 $\sqrt{s} = 8$ TeV data sample was recorded from the 4$^{\text{th}}$ April 2012 to 6$^{\text{th}}$ December 2012, corresponding to runs 200804 to 215643 (data-taking periods A1 – L3).

Over the 2011 data taking period, the peak instantaneous luminosity increased from 1.3×10^{30} cm^{-2} s^{-1} to 3.6×10^{33} cm^{-2} s^{-1}, and the peak mean number of interactions per bunch crossing ($\langle\mu\rangle$) increased from 2.6 to 17.5. The raw recorded data corresponded to an integrated luminosity of 5.25 fb^{-1}, falling to 4.7 fb^{-1} after the application of basic data quality requirements using the 2011 SUSY working group *Good Run List* (GRL)[4] [107, 106]. The Good Run List selects data where all of the detector systems were in *good quality*. Good quality means that all of the detectors were performing sufficiently well for the data to be used in physics analyses. The application of the GRL caused a 10% loss of the raw integrated luminosity.

Over the 2012 data taking period, the peak instantaneous luminosity increased from 2.74×10^{30} cm^{-2} s^{-1} to 7.61×10^{33} cm^{-2} s^{-1}, and the peak mean number of interactions per bunch crossing increased from 5.9 to 36.53. The raw recorded data corresponded to an integrated luminosity of 21.7 fb^{-1}. The recorded luminosity fell to 20.3 fb^{-1} after the application of basic data quality requirements using the 2012 SUSY working group GRL[5] [107, 106]. The 7% loss of integrated luminosity to the 2012 data set following the application of the GRL was also a consequence of requiring all detector systems to be in '*good quality for physics*'.

Figures 3.16(a) and 3.16(b) show the integrated luminosity of the 2011 $\sqrt{s} = 7$ TeV and 2012 $\sqrt{s} = 8$ TeV data sets as a function of time over the 2011 and 2012 data taking periods. The blue histogram represents the integrated luminosity that was fit for physics analysis, referred to as 'good

[4] The official SUSY GRL for the 2011 data (`data11_7TeV.periodAllYear_DetStatus-v36-pro10_CoolRunQuery-00-04-08_Susy.xml`) was used [106].

[5] The official SUSY GRL for the 2012 data (`data12_8TeV.periodAllYear_DetStatus-v61-pro14-02_DQDefects-00-01-00_PHYS_StandardGRL_All_Good.xml`) was used [106].

quality'. The cyan distribution in Figure 3.16(c) shows the recorded luminosity as a function of $\langle\mu\rangle$ for the 2011 $\sqrt{s} = 7\,\text{TeV}$ data set, whereas The light green distribution shows the recorded luminosity as a function of $\langle\mu\rangle$ for the 2012 $\sqrt{s} = 8\,\text{TeV}$ data set.

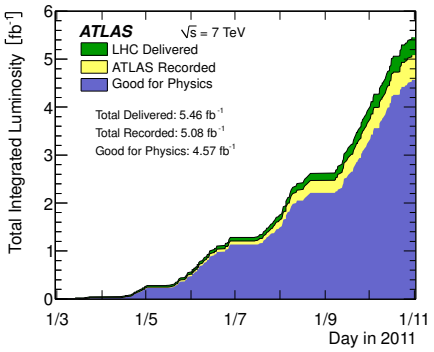

(a) Integrated luminosity of the 2011 data set

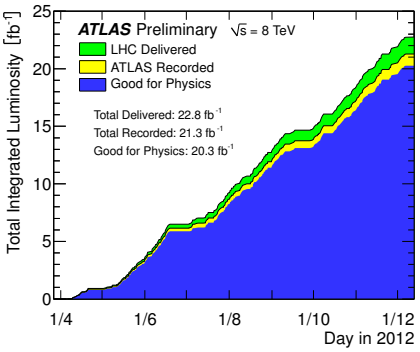

(b) Integrated luminosity of the 2012 data set

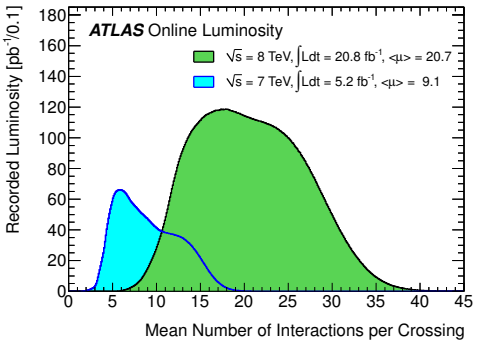

(c) $\langle\mu\rangle$ of the 2011 and 2012 data sets

Figure 3.16: A summary of the recorded luminosity of the ATLAS detector for the 2011 and 2012 data sets. The integrated luminosity distributions as a function of time for the 2011 $\sqrt{s} = 7\,\text{TeV}$ data set is shown in figure(a), and figure (b) for the 2012 $\sqrt{s} = 8\,\text{TeV}$ data set. The green distributions in figures (a) and (b) show the amount of luminosity that was delivered by the LHC during the 2011/2012 data taking period. The yellow distributions show the cumulative luminosity recorded by the ATLAS detector over the data taking period. Finally, the dark blue distributions show the cumulative luminosity that was of 'good quality' and fit for physics analysis. Figure (c) shows the recorded luminosity as a function of the mean number of interactions per bunch crossing ($\langle\mu\rangle$). The $\langle\mu\rangle$ distribution for the 2011 data taking period is shown in cyan, whereas the light green distribution shows $\langle\mu\rangle$ distribution for the 2012 data taking period. These figures were taken from the public ATLAS luminosity results [108].

3.6 The Reconstruction Stage

The reconstruction software attempts to reconstruct physics objects from the information recorded by the ATLAS detector. This section will summarise how the most important physics objects were reconstructed. This section closely follows the information contained in Reference [69].

3.6.1 Jets

Jets were reconstructed from *topological cell clusters* (topo-clusters) [109, 61] using the anti-k$_t$ sequential recombination jet algorithm [110] which is infrared and collinear safe. The size of the jet distance parameter depended on the analysis; however, most analyses use the ATLAS standard jet distance parameter $\Delta R = 0.4$, where ΔR is the geometric variable defined in section 3.3.2.

The jet reconstruction algorithm attempts to reconstruct the three-dimensional shower topology of each particle entering the calorimeter from the corresponding topo-clusters. Only topo-clusters with a positive energy were considered by the jet finding algorithm[6].

After jets are reconstructed, they require calibration. Two different jet calibrations were used: jets in the 2011 $\sqrt{s} = 7$ TeV data set were calibrated using the electromagnetic (EM) scheme, whereas jets in the 2012 $\sqrt{s} = 8$ TeV data were calibrated using the *local cluster weighting* (LCW) scheme. The corrections applied to topo-clusters were derived from Monte Carlo data [61]. The main difference between the LCW and EM calibration schemes was that the LCW calibration classifies clusters as either being electromagnetic or hadronic in origin, whereas the EM calibration does not. Then, based on this classification, the LCW applies an energy correction that is dependent on the type of particle which created the calorimeter deposit [69, 74, 61].

A final jet energy calibration, referred to as *jet energy scale* (JES), was then applied. The JES is an energy correction that relates the response of the calorimeter to the 'true' jet energy scale of reconstructed jets in MC samples [74, 61]. Figure 3.17 shows a schematic summarising the jet reconstruction and calibration processes.

3.6.2 *b*-jets

The identification of *b*-flavour jets originating from the hadronisation of *b*-quarks was performed using several *b*-tagging algorithms. These algorithms attempt to reconstruct the displaced secondary vertex from *B*-meson/baryon decay using the tracking information provided by the ID [111].

Figure 3.18 shows a schematic of a *B*-meson decay within a jet. It can be seen that the secondary vertex is displaced from the primary vertex by a distance equal to the decay length of the *b*-quark. The impact parameter of the track is the distance of closest approach between the track and the primary vertex [112]. This can be measured in the longitudinal (z) or transverse (d) direction from the primary vertex. Tracks which did not originate from the primary vertex, and hence came from a

[6] Negative energy clusters can arise from noise in the electronics within the calorimeters.

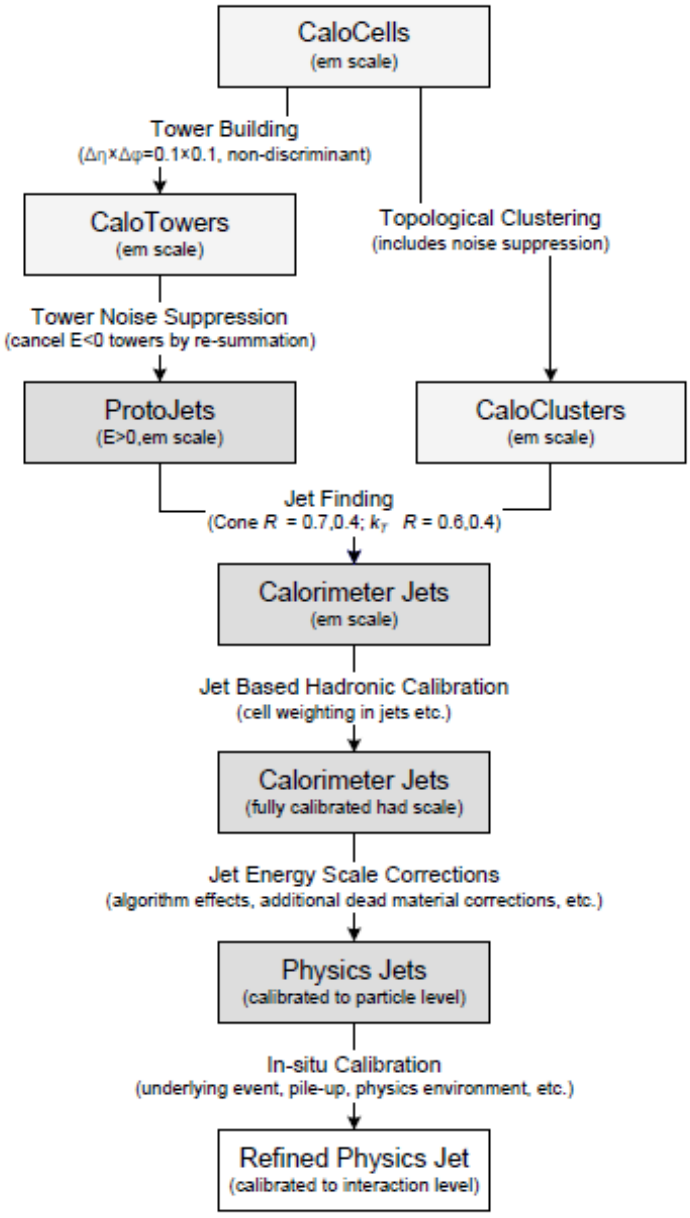

Figure 3.17: A schematic showing the jet reconstruction and calibration processes in the ATLAS reconstruction software, taken from [69].

secondary vertex, will usually have a large impact parameter (z_0,d_0) compared to tracks which did originate from the primary vertex [111, 112].

To improve the effectiveness of the *b*-tagging, the outcomes from several different algorithms were combined in a neural network [113]. The Multi-Variate 1 (`MV1`) algorithm [113] combined the outputs from the secondary vertex (`SV0`,`SV1`) [111, 113] and impact parameter (`IP3D`) algorithms [111, 113] with jet parameters (for example p_{T} and η) into a single weight (w). The combined weight

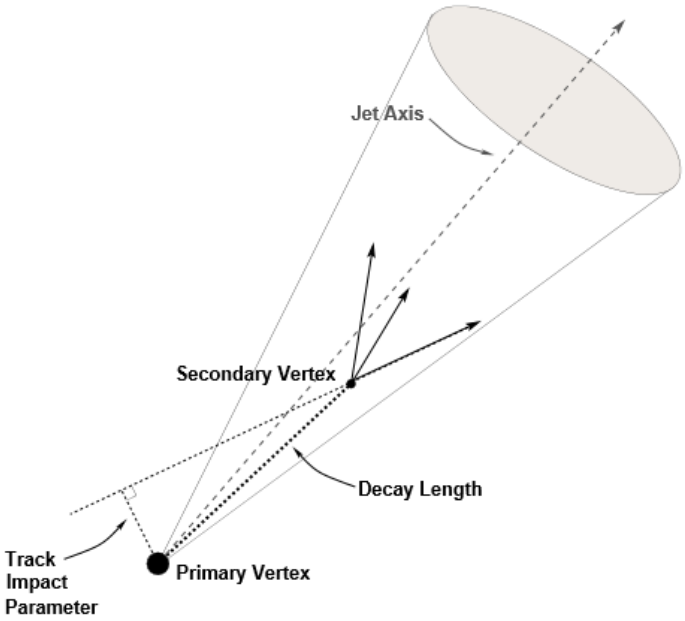

Figure 3.18: A schematic showing the decay of a b-quark within a jet, taken from [112].

was then used to tag b-jets in the reconstruction software at a particular *operating point* (OP). An operating point corresponds to a particular b-tagging efficiency and gluon/light-quark jet rejection power. Figure 3.19 shows the light-quark/gluon jet rejection as a function of b-tagging efficiency for the `MV1` algorithm [113]. Unless stated otherwise, the `MV1` b-tagging algorithm was used at 70% efficiency operating point to tag b-jets. This OP gave a b-jet mis-identification rate of approximately one in 150 light quark or gluon jets (see Figure 3.19).

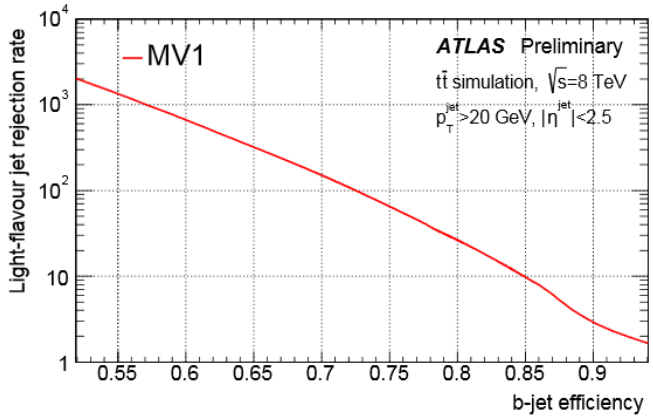

Figure 3.19: The gluon/light-quark jet rejection power as a function of b-tagging efficiency for the `MV1` b-flavour tagging algorithm. This study used jets with $p_{\mathrm{T}} > 20$ GeV and $|\eta| < 2.5$ in simulated $t\bar{t}$ events. This figure was taken from [113].

3.6.3 Electrons

The electron reconstruction software attempted to match EM topo-clusters to a reconstructed track in the ID [69]. The 'seed' deposits for the electron clusters were found using a sliding window algorithm [109] in $\eta - \phi$ space. Once the algorithm had seeded a cluster the electron cluster was matched to a track in the ID.

The reconstruction software also applied quality selection cuts to the electron candidates. The quality selection cuts had three main categories: *loose*, *medium*, and *tight*. The *loose* category was the least strict selection [7] [69, 74]. The requirements to pass the *medium* and *tight* selection were stricter: these selections gave a better quality electron candidate and fewer fakes, but they reduced the efficiency of the electron reconstruction [114, 115]. The quality section cuts included the calorimeter shower shape, the number of pixel and SCT hits, and the amount of leakage into the hadronic calorimeter.

Electrons used in signal events also had to be *isolated*: this reduced the number of electrons from heavy hadron decays mimicking the signature of an electron produced at the primary vertex. The isolation cut defined a cone of $\Delta R = 0.2$ around the electron, and the total transverse momentum of all the tracks within the cone had to be less than 10% of the transverse energy of the electron for the electron to be considered as isolated [74].

'Baseline' candidate electron had to pass the acceptance cuts[8] of $p_{\mathrm{T}} > 10$ GeV and $|\eta| < 2.47$.

3.6.4 Photons

Two different types of photons were reconstructed using the ATLAS reconstruction software. Unconverted photons were reconstructed using energy deposits in the electromagnetic calorimeter [116]. The same sliding window algorithm used in electron reconstruction was also used to find the seeds for photon clusters [69]. Converted photons which have undergone e^+e^- conversion in the ID were recovered in the photon reconstruction by matching a single or a pair of tracks to EM topo-clusters. For single track conversions, the track must not have originated from the first pixel layer. For paired track conversions, the tracks had to converge at a conversion vertex in the ID [116].

The fine segmentation of the first sampling layer of the EM calorimeter helped to discriminate against photons that had originated from π^0 decays within the EM calorimeter [69]. Quality selec-

[7] It should be noted that the different selection criteria did change over time as the object quality selection cuts were optimised to data.

[8] Applied after the p_{T} smearing procedure for electrons in MC

tion cuts, which were optimised for π^0 photon rejection, were also applied to photons, and focused on the shower shape of the EM cluster. Furthermore, by a single track isolation cut, most π^0 photons could be rejected whilst retaining the majority of converted photons [69].

3.6.5 Muons

The muon reconstruction algorithm combined an ionisation track within the muon spectrometer (MS) with a corresponding track in the ID [69, 74]. Two different types of muons were used in the analysis chapters of this thesis: '`combined`' muons, which were constructed from tracks that were independently reconstructed in both the MS and inner detector using the `STACO` algorithm [91], and '`segment-tagged`' muons, which used the MS to tag ID tracks as muons, but did not require a fully reconstructed track in the MS [69].

All muon candidates had to pass quality selection cuts (see [117]). Muons were required to have at least 2 hits in the pixel, 5 hits in the SCT and an extension of the ionisation track into the TRT with a minimum of 9 hits [91]. Signal muons had to be *isolated* as well, such that the total p_{T} of the tracks in a cone of $\Delta R < 0.2$ (p_{T}cone20) around the candidate muon must be less than 1.8 GeV (excluding the muon track). The isolation cut reduced the number of fake muons caused, for example, when jets punch-through into the muon chambers; however, as with electrons, it reduced the overall efficiency of the muon reconstruction process [91].

'Baseline' candidate muons had to pass the acceptance cuts[9] of $p_{\mathrm{T}} > 10$ GeV and $|\eta| < 2.4$.

3.6.6 Missing Transverse Energy

Many different $E_{\mathrm{T}}^{\mathrm{miss}}$ calculations are used throughout ATLAS, but only `MET_RefFinal` and `MET_Simplified20` [118] are relevant to the SUSY analyses described in this thesis. Other $E_{\mathrm{T}}^{\mathrm{miss}}$ algorithms not commissioned for use in physics analyses are described in Chapter 4, but these algorithms are only relevant to the $E_{\mathrm{T}}^{\mathrm{miss}}$ performance studies documented in that chapter.

The `MET_RefFinal` $E_{\mathrm{T}}^{\mathrm{miss}}$ algorithm (see Eq.(3.4)) used topo-clusters and egamma-clusters (electron and photon clusters). First, an attempt was made to match each cluster to a reconstructed physics object, in the following order: electrons, photons, jets and muons. If a match was found, the corresponding four-vector of the physics object was used instead of the raw calorimeter cluster measurement; this provided a more refined calibration [118]. Any remaining clusters that did not belong to a reconstructed physics object were included in the `SoftTerm` (`CellOut`) of the $E_{\mathrm{T}}^{\mathrm{miss}}$. In

[9] Applied after the p_{T} smearing procedure for muons in MC

Chapter 4, various different `SoftTerm` algorithms are used in the particle flow $E_{\mathrm{T}}^{\mathrm{miss}}$ performance studies (see section 4.4.1).

$$\begin{aligned}(E_{\mathrm{T}}^{\mathrm{miss}})_{\mathrm{x(y)}}^{\mathrm{RefFinal}} =& (E_{\mathrm{T}}^{\mathrm{miss}})_{\mathrm{x(y)}}^{\mathrm{RefEle}} + (E_{\mathrm{T}}^{\mathrm{miss}})_{\mathrm{x(y)}}^{\mathrm{RefGamma}} + (E_{\mathrm{T}}^{\mathrm{miss}})_{\mathrm{x(y)}}^{\mathrm{RefJet}} + (E_{\mathrm{T}}^{\mathrm{miss}})_{\mathrm{x(y)}}^{\mathrm{RefMuon}} \\ &+ (E_{\mathrm{T}}^{\mathrm{miss}})_{\mathrm{x(y)}}^{\mathrm{SoftTerm}}. \end{aligned} \tag{3.4}$$

Each term in Eq.(3.4) was computed from the negative vectorial sum of the calibrated cluster momentuma of the corresponding objects. Contributions from electrons were included in $(E_{\mathrm{T}}^{\mathrm{miss}})_{\mathrm{x(y)}}^{\mathrm{RefEle}}$, using electrons that passed the `medium` purity criteria with $p_{\mathrm{T}} > 10$ GeV. Contributions from photons were included in $(E_{\mathrm{T}}^{\mathrm{miss}})_{\mathrm{x(y)}}^{\mathrm{RefGamma}}$, using photons that passed the `tight` purity criteria with $p_{\mathrm{T}} > 10$ GeV. Contributions from jets were included at the jet energy scale in $(E_{\mathrm{T}}^{\mathrm{miss}})_{\mathrm{x(y)}}^{\mathrm{RefJet}}$, using jets with $p_{\mathrm{T}} > 20$ GeV. Contributions from muons were included in $(E_{\mathrm{T}}^{\mathrm{miss}})_{\mathrm{x(y)}}^{\mathrm{RefMuon}}$, using muons which passed the `tight` purity criteria with $p_{\mathrm{T}} > 10$ GeV. The default $(E_{\mathrm{T}}^{\mathrm{miss}})_{\mathrm{x(y)}}^{\mathrm{SoftTerm}}$ term was computed from locally calibrated topo-clusters and tracks which were not included as part of a reconstructed object. Taus were not independently calibrated and were treated the same as jets.

Before the 2012 data taking period, `MET_RefFinal` was not fully commissioned and validated for use in physics analyses, so a simplified $E_{\mathrm{T}}^{\mathrm{miss}}$ definition, called `MET_Simplified20` was used. `MET_Simplified20` ignored the $(E_{\mathrm{T}}^{\mathrm{miss}})_{\mathrm{x(y)}}^{\mathrm{RefGamma}}$ and $(E_{\mathrm{T}}^{\mathrm{miss}})_{\mathrm{x(y)}}^{\mathrm{RefTau}}$ terms by calibrating tau leptons and photons as jets. The $(E_{\mathrm{T}}^{\mathrm{miss}})_{\mathrm{x(y)}}^{\mathrm{RefMuon}}$ term was simplified to the vectorial sum of the momenta of the baseline muons (see section 3.6.5). Eq. (3.5) shows the formula for `MET_simplified20`.

$$\begin{aligned}(E_{\mathrm{T}}^{\mathrm{miss}})_{\mathrm{x(y)}}^{\mathrm{Simplified20}} =& (E_{\mathrm{T}}^{\mathrm{miss}})_{\mathrm{x(y)}}^{\mathrm{RefEle}} + (E_{\mathrm{T}}^{\mathrm{miss}})_{\mathrm{x(y)}}^{\mathrm{RefJet}} + (E_{\mathrm{T}}^{\mathrm{miss}})_{\mathrm{x(y)}}^{\mathrm{SoftTerm}} \\ &- \sum_{\substack{\textit{baseline} \\ \textit{muons}}} p_{x(y)}. \end{aligned} \tag{3.5}$$

3.6.7 Resolving Overlapping Objects

When reconstructed objects overlapped in the detector, for example, a muon originating from a B-meson decay within a jet, a classification was required to remove all but one of the overlapping physics objects. The overlap removal procedure used the simple geometric variable ΔR, and was based on previous studies in MC simulation [74]. Overlap removal was applied in the following order:

(1) If an electron and a jet were found within $\Delta R < 0.2$, the object was interpreted as an *electron* and the overlapping jet was ignored.

(2) If an electron and a jet were found within $0.2 \leq \Delta R < 0.4$, the object was interpreted as a *jet* and the nearby electron was ignored.

(3) If a muon and a jet were found within $\Delta R < 0.4$, the object was interpreted as a *jet* and the muon was ignored.

The overlap removal procedure occurred after the $E_{\mathrm{T}}^{\mathrm{miss}}$ was calculated, so any physics objects removed during overlap removal process would still have been present during the $E_{\mathrm{T}}^{\mathrm{miss}}$ calculation. This prevented any fake $E_{\mathrm{T}}^{\mathrm{miss}}$ caused by removing overlapping objects being included in the $E_{\mathrm{T}}^{\mathrm{miss}}$ calculation.

3.7 Systematic Uncertainties

A brief description of the systematics that were common to all of the physics analyses in this thesis is provided in this section.

3.7.1 Jet Energy Scale and Jet Energy Resolution

Jet Energy Resolution (JER)

Energy resolution is a very important parameter for many ATLAS analyses. For example, a good energy resolution improves the ability to reconstruct the top quark mass in hadronic decays, which can be used to reject top background events or find top final state objects. A good jet energy resolution also improves the resolution of $E_{\mathrm{T}}^{\mathrm{miss}}$. Many SUSY analyses use $E_{\mathrm{T}}^{\mathrm{miss}}$ to select events, so it is important that the $E_{\mathrm{T}}^{\mathrm{miss}}$ has a good energy resolution. The $E_{\mathrm{T}}^{\mathrm{miss}}$ resolution is discussed further in Chapter 4.

The energy resolution of the ATLAS calorimeters can be expressed as [69, 77]

$$\frac{\sigma}{E} = \frac{A}{\sqrt{E}} \oplus \frac{B}{E} \oplus C. \tag{3.6}$$

Here, A is the stochastic term and depends on the fluctuations of the shower development, since calorimeter topo-clusters are combined from many small deposits when the shower develops. A

depends on the design of the calorimeter. B is the noise term and is caused by extra low energy particles from noise in the electronics; the noise term changes over time as the calorimeter degrades over its lifetime. C is the constant term and relates to the inefficiencies of the calorimeter which are not understood, such as an imperfect calibration, dead regions of the calorimeter or truncated particle showers [77].

Eq.(3.6) shows that the resolution of the calorimeter depends on the energy of the initial particle, hence the resolution terms (A, B, C) are quoted as a percentage of the energy of the particle (E) in GeV. Table 3.3 shows the energy resolution performance goals for the calorimeter systems in the ATLAS detector [69]. These performance goals were achieved by the detector hardware and CP corrections applied to physics objects during event reconstruction [61, 114, 115, 119], for example, see Figure 3.20 for the energy resolution of jets in the barrel calorimeter.

Calorimeter Component	Required Design Energy Resolution
Electromagnetic Calorimeter	$\sigma/E = 10\%/\sqrt{E} \oplus 0.7\%$
Hadronic Calorimeter	
Barrel and Endcap Regions ($\lvert\eta\rvert < 3.2$)	$\sigma/E = 50\%/\sqrt{E} \oplus 3\%$
Forward Region ($3.2 < \lvert\eta\rvert < 4.9$)	$\sigma/E = 100\%/\sqrt{E} \oplus 10\%$

Table 3.3: The calorimeter energy resolution performance goals of the ATLAS detector [69].

The JER uncertainty covered the reconstruction efficiency of jets and any possible underestimation of the JER in MC simulation. It was applied to the energy of the jet using an additional p_{T} and η dependent smearing [120]. Figure 3.20 shows the ATLAS jet p_{T} resolution as a function of jet p_{T} for central jets in the 2012 data set [119]. It can be seen in this figure that the two different methods (bisector and dijet) used for determining the jet p_{T} resolution were consistent with the expect result from MC simulation. Overall, the jet p_{T} resolution is good in data with the worst resolution at low p_{T}, which was approximately 15%.

Jet Energy Scale

An uncertainty on the jet energy scale (JES) accounted for mis-modelling jets in MC events, the description of the calorimeter, such as noise, and the material budget of the detector. The uncertainty was derived in an in-situ jet analysis and single pion test-beam measurements [120]. The impact of this uncertainty was assessed by modifying the jet parameters (p_{T},η,..) and jet calibration by $\pm 1\sigma$, and then seeing how this affected the kinematic distributions and selection efficiency [120].

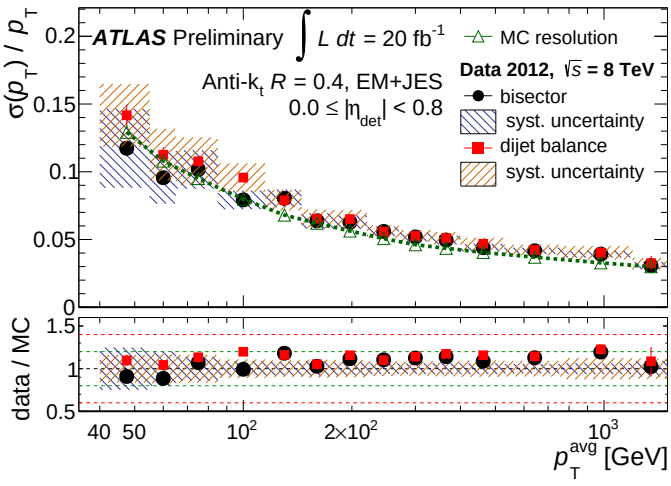

Figure 3.20: The ATLAS jet p_{T} resolution measured in 2012 $\sqrt{s} =$ 8 TeV data events for central jets ($|\eta| < 0.8$). Data from the bisector analysis [119] are shown in black with systematic uncertainties shown by the blue hashed region. Data from the dijet analysis [119] are shown in red with systematic uncertainties shown by the brown hashed region. The expected resolution from MC simulation is shown by the green triangles. This figure was taken from [119].

3.7.2 *b*-tagging Efficiencies

Scale factors for the *b*-tagging efficiency and mis-tagging probability of *b*-jets were measured in data [121]. The scale factors were applied to simulated events to improve the MC and data comparisons of *b*-jet distributions. The *b*-tag scale factors were derived as a function of jet p_{T}. The uncertainty on the scale factors was independently found by varying the mis-tag rate, b-tagging efficiency and c-/τ-tagging efficiency, the combination of which provided the final uncertainty. For the `MV1` *b*-jet tagging algorithm this corresponded to an uncertainty ranging from 5-19% dependent on the p_{T} of the jet [121].

3.7.3 Lepton Efficiencies

Leptons were used throughout the physics analyses in this thesis. However, the electron and muon triggers, and the lepton reconstruction were mis-modelled in the MC, so leptons in MC events were rescaled to match data distributions. The scale factors were derived from $Z \to \mu\mu$ and $Z \to ee$ events as a function of various lepton kinematics, such as E_{T} and η, using a *tag and probe* analysis (see reference [114, 122]). The analysis tags one of the leptons from the Z resonance with a strict criterion then probes the other lepton involved in the Z decay. This creates an unbiased probe sample which can be used to measure the reconstruction efficiency in data [114, 122].

3.7.4 Missing Transverse Energy

The systematic uncertainty on the $E_{\mathrm{T}}^{\mathrm{miss}}$ was propagated from the individual uncertainties on the $E_{\mathrm{T}}^{\mathrm{miss}}$ terms (see section 3.6.6). An additional uncertainty was also provided for the `SoftTerm` and mis-modelling the pile-up of reconstructed objects not associated with the primary vertex [118].

3.7.5 Luminosity

An uncertainty on the total amount of recorded luminosity in a data set was determined from the counting rates of the ATLAS luminosity detectors [123], and by using van der Meer (vdM) scans [124]. The total uncertainty in the integrated luminosity of the 2011 data set was ± 3.9%, and for the 2012 data set ± 2.8%.

3.7.6 Monte Carlo Simulation

There were many uncertainties involved in Monte Carlo simulation, from theoretical uncertainties on the event generation to mis-modelling the description of ATLAS detector. Generator comparisons [1, 2] and physics validation studies were used to constrain the uncertainties on MC simulation (see [125]). Also, if MC samples had low statistics, then statistical uncertainties become significant.

3.8 Summary

In this chapter, the LHC and the ATLAS detector were described. Section 3.2 gave a brief overview of the LHC machine and the operation of the CERN accelerator complex. Section 3.3 described the subsystems of the ATLAS detector and covered the main subdetectors and systems critical for recording data. Section 3.4 described the structure of events in p-p collisions at the LHC and the production of MC samples. The data samples that were used in the analysis chapters of this thesis were documented in section 3.5. Section 3.6 described the standard ATLAS physics object reconstruction. Finally, a brief overview of systematic uncertainties that were common to all of the data analyses in this thesis was given in section 3.7.

Chapter 4

Particle Flow

4.1 Introduction

Particle Flow (PFlow) or Energy Flow (EFlow) event reconstruction aims to take full advantage of all the particle detectors subsystems to improve the energy resolution of reconstructed physics objects (see section 3.6). It is of particular interest to SUSY analyses, since it has the potential to improve the jet energy resolution, and therefore, the $E_{\mathrm{T}}^{\mathrm{miss}}$ resolution as well. This chapter will describe $E_{\mathrm{T}}^{\mathrm{miss}}$ performance studies of the particle flow reconstruction algorithm using the ATLAS detector. The $E_{\mathrm{T}}^{\mathrm{miss}}$ performance studies used $Z \rightarrow \mu\mu$, $t\bar{t}$ and Wt events to measure the $E_{\mathrm{T}}^{\mathrm{miss}}$ performance of the PFlow reconstruction algorithm compared to the standard ATLAS offline reconstruction.

It should be noted that the analysis sections (4.4–4.5) of this chapters are proof of principle studies designed to prove the gains that could be obtained by using particle flow.

4.2 Background and Motivation

The main motivation for using particle flow is that at low energy the tracking detectors provide a better p_{T} resolution for charged particles than the calorimeters. The p_{T} resolution (σ) of a charged particle in the ATLAS tracking detectors can be expressed as a function of p_{T} [69]:

$$\frac{\sigma}{p_{\mathrm{T}}} = 0.05\% p_{\mathrm{T}} \oplus 1\%, \tag{4.1}$$

where p_{T} is in units of GeV.

The p_{T} resolution of particles in the calorimeters is detailed in section 3.7.1, with Table 3.3 showing the performance goals for the ATLAS calorimeters. Figure 4.1 shows the *ideal* p_{T} resolution as a function of p_{T} for charged particles in the EM and hadronic calorimeters compared to the tracking p_{T} resolution. It can be seen in this figure that the p_{T} resolution of low p_{T} particles is better in

the tracking detectors than the calorimeters; therefore, if the p_T measurement from the tracking detectors is used instead of the calorimeter deposits for low-p_T charged particles, there should be an improved p_T resolution for those charged particles.

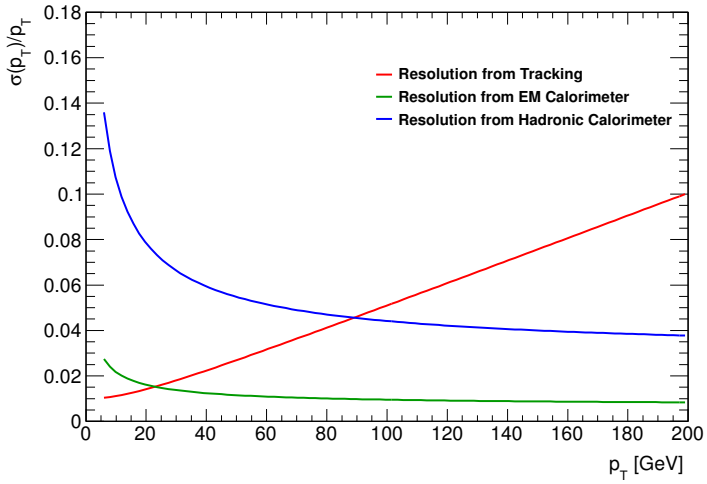

Figure 4.1: The p_T resolution as a function of p_T of a charged particle with $|\eta| = 1$. The red line shows the p_T resolution of the charged particle from the tracking detectors. The blue and green lines show the p_T resolution from the hadronic and EM calorimeters respectively. This figure was made with information from [69].

Previous experiments have used particle flow algorithms, for example, experiments at LEP [126, 127] and the Tevatron [128]. At the LHC, particle flow has also been used by the CMS experiment [129]. The algorithm varies from experiment to experiment but it has the same general stages, as listed below.

(1) Track-cluster matching – tracks from charged particles in the tracking detector are extrapolated to the calorimeters.

(2) Charged fraction subtraction – the removal of energy from calorimeter cell (see section3.3.5) deposits from the clusters with associated tracks from the tracking detectors. This removes any double counting of energy already deposited by the charged particles in the calorimeters.

(3) Cluster annihilation – removal of calorimeter clusters with associated tracks. If the remaining energy after subtraction is consistent with zero (within uncertainty), the cluster is removed.

(4) Neutral particle calibration – since energy deposits from neutral particles will not be removed from the cluster, they must be calibrated to the correct energy scale.

Figure 4.2 shows a schematic of the different measurements available for example hadronic particles

in the CDF detector (taken from [128]). This figure shows that the track momentum measurement is only available for the charged hadrons (in this figure,π^+).

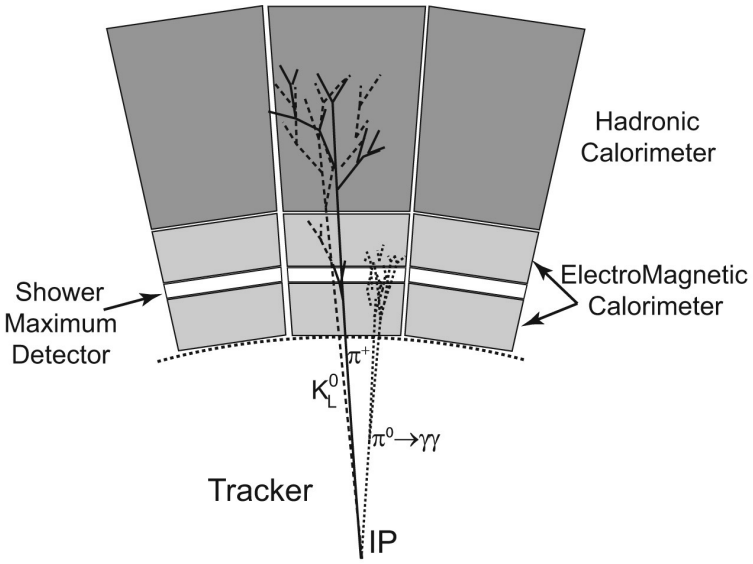

Figure 4.2: A schematic of the different measurements available for hadronic particles in the CDF detector in an example hypothetical narrow jet event. This figure was taken from [128].

4.3 ATLAS Particle Flow Algorithm

This section will describe the different stages of the ATLAS particle flow algorithm in more detail [130].

4.3.1 Track-Cluster Matching

Reconstructed tracks constructed from hits in the ATLAS ID were extrapolated through the magnetic field of the ID to the calorimeters; this provided the extrapolated impact coordinates of the tracks to different layers of the calorimeters. The extrapolated impact coordinates were then used to find the topo-cluster that was closest to the extrapolated track with the geometric variable D [130]:

$$D = \sqrt{\frac{\left(\eta_{\text{Track}} - \eta_{\text{Cluster}}\right)^2}{\sigma_\eta^2} + \frac{\left(\phi_{\text{Track}} - \phi_{\text{Cluster}}\right)^2}{\sigma_\phi^2}}, \tag{4.2}$$

where η_{Track} and ϕ_{Track} are the extrapolated η and ϕ track coordinates at the second layer of the EM calorimeter, η_{Cluster} and ϕ_{Cluster} are the η and ϕ coordinates of the topo-cluster in the calorimeter,

σ_η is the standard deviation of the η coordinates of all the cells within the topological cluster, and σ_ϕ is the standard deviation of the ϕ coordinates of the cells within the topological cluster. Using the variance of the topo-cluster coordinates (σ^2) means D takes into account the geometric size of the topological cluster within the calorimeter; therefore, the track matching algorithm is not biased towards large calorimeter clusters.

If no track was matched to the topo-cluster, it remained unmodified and the measurements from the calorimeters were used. The particle flow algorithm treats the cluster as a neutral cluster made from a neutral particle. However, if tracks were matched to the cluster, then the cluster continued to the charged shower subtraction process.

4.3.2 Charged Shower Subtraction

Charged shower subtraction removes the energy deposited by the charged particle from the topo-cluster with the associated tracks. The amount of energy removed was determined by measuring the calorimeter response, E/P, where E is the energy of the cluster in the calorimeter and P is the momentum of the associated track. E/P was expected to vary depending on the region of the calorimeter (e.g. the 'crack' region ($|\eta| \approx 1.5$) of the EM calorimeter) and the energy of the incident particle. Single pion MC samples of different energies were used to measure E/P in different bins of η and E to take into account changes of the calorimeter response. Another important parameter was the layer of first interaction: this was the layer of the calorimeter that the pion started to shower, and it also had the highest energy density. The layer of first interaction was found using the longitudinal energy density profile of the pion shower in the calorimeter. Energy was subtracted from calorimeter cells in the topo-cluster until the total amount of energy subtracted from the cluster was consistent with the fraction from the E/P distribution. This was performed in rings of calorimeter cells starting at the impact coordinates of the layer of first interaction [130].

It was possible for deposits from hadronic showers to split into different clusters between layers of the calorimeter (see Figure 4.3); in this case, a split-shower recovery algorithm attempted to recover the other clusters associated with the charged pion. If the split-shower recovery did not recover all the cells from the hadronic particle, then there would be double counting of some of the energy from the pion. In Figure 4.3, some of the energy from the neutral pion would also be removed in the main cluster, as the momentum of the charged pion track would be much greater than the energy of the charged fraction of the main cluster, and therefore the algorithm would continue to subtract energy from the main cluster until the total energy subtracted was consistent with the momentum of the track: this is the origin of the 'confusion' term, where neutral cell deposits are also removed by the algorithm.

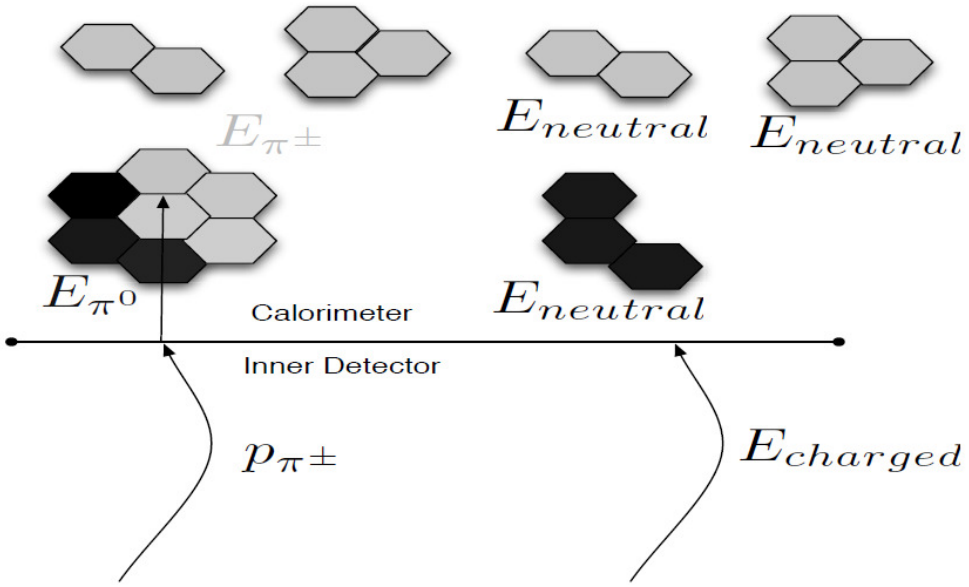

Figure 4.3: An example schematic showing the splitting of a hadronic shower in the calorimeter caused by a charged pion. The grey cells show the deposits from the $\pi^{\pm}$, whereas the black cells show the deposits from a π^0. The right-hand part of the figure shows how the algorithm would treat the cluster if the split-shower recovery method was not active, treating the other clusters from the $\pi^{\pm}$ as if they were made from a different neutral particle. This figure was taken from [130].

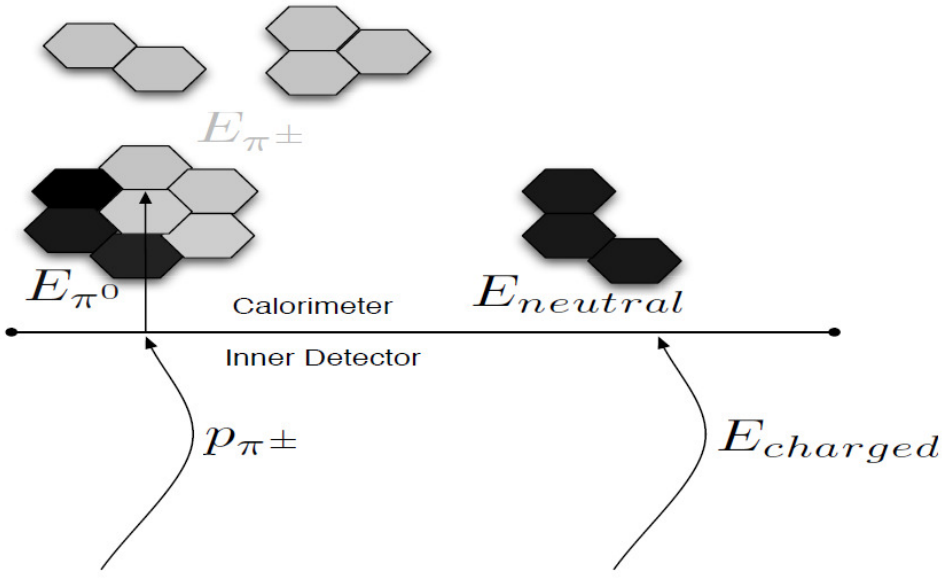

Figure 4.4: An example schematic showing the optimal outcome of the charged shower subtraction algorithm. The grey cells show the deposits from the $\pi^{\pm}$, whereas the black cells show the deposits from a π^0. The right-hand part of the figure shows how the cluster would look after the charged shower subtraction (in the optimal case). This figure was taken from [130].

After the charged shower subtraction process, only energy from neutral particles should be in the calorimeter cluster and the track momentum of charged particle associated with the cluster can be used as the the charged fraction energy of the hadronic shower. This is shown in Figure 4.4 with all the cells from the $\pi^{\pm}$ removed and only the cells from the π^{0} remaining.

4.3.3 Calibration

The particle flow algorithm was performed before any of the topo-clusters were calibrated; this meant the calorimeter deposits were at the EM scale (see section 3.6.1). After the charged shower subtraction process, only neutral deposits remained in the calorimeter; therefore, these clusters must now be fully calibrated to the appropriate energy scale. If they were not, then jets formed with the remaining topo-clusters would not be properly calibrated (see section 3.6.1).

4.3.4 Particle Flow Object List

Once the particle flow reconstruction algorithm was complete, a particle flow object list was created from all of the final reconstructed objects. This included all of the charged PFlow objects (tracks) and neutral PFlow objects (topo-clusters). However, not all of the tracks in the event would have originated from the primary vertex, due to pile-up in the event (see section 3.4). Therefore, a pile-up track suppression cut is required. The pile-up track suppression cut compares the track impact parameter (z_0) to the z_0 of the selected primary vertex. If the difference between the track impact parameter and the primary vertex is greater than 2 mm, it is considered as a pile-up track, and was not included in the jet formation algorithm or the soft term of the $E_{\mathrm{T}}^{\mathrm{miss}}$. This provides an inherent pile-up suppression built directly into the particle flow reconstruction algorithm, which should make reconstructed particle flow objects more robust to pile-up.

4.4 $E_{\mathrm{T}}^{\mathrm{miss}}$ Performance in $Z \rightarrow \mu\mu$ Events

Missing transverse energy ($E_{\mathrm{T}}^{\mathrm{miss}}$) is described in section 3.6.6. $E_{\mathrm{T}}^{\mathrm{miss}}$ is an important kinematic variable for searches for supersymmetry because in R-parity conserving scenarios $E_{\mathrm{T}}^{\mathrm{miss}}$ is a key signature of supersymmetric events (see section 2.4). This section will cover the $E_{\mathrm{T}}^{\mathrm{miss}}$ performance of the ATLAS particle flow reconstruction algorithm compared to the standard ATLAS offline reconstruction in $Z \rightarrow \mu\mu$ events.

Three different $E_{\mathrm{T}}^{\mathrm{miss}}$ performance variables were studied: the resolution, scale and pile-up dependence of the $E_{\mathrm{T}}^{\mathrm{miss}}$.

The first part of this section will focus on the $E_{\mathrm{T}}^{\mathrm{miss}}$ performance in $Z \to \mu\mu$ events. Figure 4.5 shows an example $Z(\to \mu\mu)$ boson with accompanying jets event. It can be seen in this figure that the accompanying jets were produced in the opposite direction to the Z boson, as they recoiled against each other balancing the total p_{T} of the event. Since the direction of the Z boson changes on an event-to-event basis, the parallel and perpendicular projections of the $E_{\mathrm{T}}^{\mathrm{miss}}$ in relation to the Z boson in the transverse plane were used. These projections are illustrated in Figure 4.6.

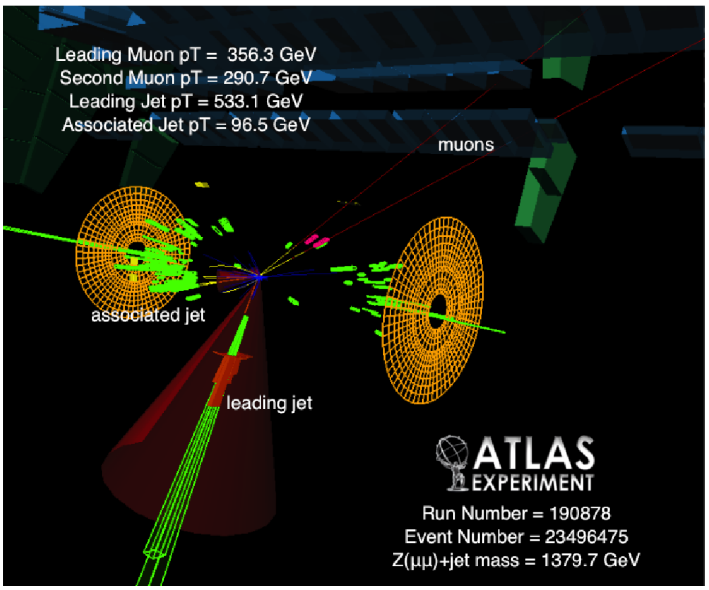

Figure 4.5: A Z boson with accompanying jet candidate event recorded with the ATLAS detector. This figure was taken from [131].

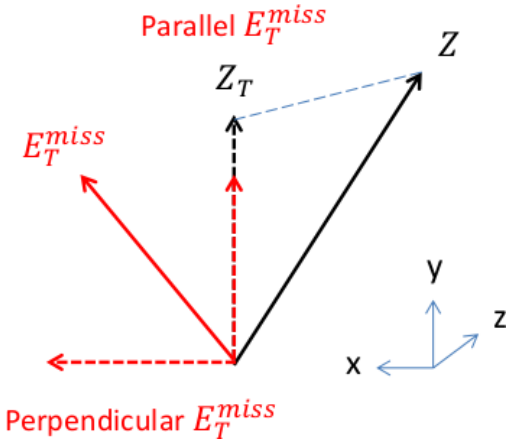

Figure 4.6: The missing transverse energy projections in the parallel and perpendicular directions in relation to the Z boson (projected into the transverse plane Z_T).

The parallel missing transverse energy can be given by

$$\text{Parallel-}E_{\mathrm{T}}^{\mathrm{miss}} = \frac{(E_{\mathrm{T}}^{\mathrm{miss}})_x \times Z_{px} + (E_{\mathrm{T}}^{\mathrm{miss}})_y \times Z_{py}}{\sqrt{Z_{px}^2 + Z_{py}^2}}, \tag{4.3}$$

where $(E_{\mathrm{T}}^{\mathrm{miss}})_{x(y)}$ is the component of the $E_{\mathrm{T}}^{\mathrm{miss}}$ in the $x(y)$ direction and $Z_{px(y)}$ is the momentum component of the Z boson in the $x(y)$ direction.

If the magnitude ($\left|E_{\mathrm{T}}^{\mathrm{miss}}\right| = \sqrt{(E_{\mathrm{T}}^{\mathrm{miss}})_x^2 + (E_{\mathrm{T}}^{\mathrm{miss}})_y^2}$) of the $E_{\mathrm{T}}^{\mathrm{miss}}$ is known, then the perpendicular $E_{\mathrm{T}}^{\mathrm{miss}}$ is just given by

$$\text{Perp-}E_{\mathrm{T}}^{\mathrm{miss}} = \sqrt{\left|E_{\mathrm{T}}^{\mathrm{miss}}\right|^2 - \left(\text{Parallel-}E_{\mathrm{T}}^{\mathrm{miss}}\right)^2} \tag{4.4}$$

In theory, there is no missing transverse energy from the final state objects ('*real* $E_{\mathrm{T}}^{\mathrm{miss}}$') in $Z \to \mu\mu$ events[1]. This makes $Z \to \mu\mu$ events ideal for measuring the resolution and scale of the $E_{\mathrm{T}}^{\mathrm{miss}}$. The resolution of the $E_{\mathrm{T}}^{\mathrm{miss}}$ provides some insight into how well the reconstruction software is working. The narrower the width of the $E_{\mathrm{T}}^{\mathrm{miss}}$ distribution, the better the reconstruction algorithm is performing, as, on average, the $E_{\mathrm{T}}^{\mathrm{miss}}$ is giving a result closer to the true value of the $E_{\mathrm{T}}^{\mathrm{miss}}$. The scale relates to the p_{T} balance of the event. Since no *real* $E_{\mathrm{T}}^{\mathrm{miss}}$ is expected in $Z \to \mu\mu$ events, the jets and other hadronic particles should balance the Z boson (CoM); therefore, the mean of the $E_{\mathrm{T}}^{\mathrm{miss}}$ distribution should be approximately zero (in an ideal detector).

The pile-up dependence of the $E_{\mathrm{T}}^{\mathrm{miss}}$ is also an important parameter. Pile-up collisions are expected to introduce many *soft* (low-p_{T}) hadronic particles into the background of the event. How the performance of the $E_{\mathrm{T}}^{\mathrm{miss}}$ changes as a function of $\langle\mu\rangle$ and the number of primary vertices (NPV) is important, as the LHC is expected to run at an even higher luminosity during run II. Therefore, $E_{\mathrm{T}}^{\mathrm{miss}}$ algorithms are required to be robust against increases in pile-up, or physics analyses could lose sensitivity.

To remove jets that contain a large fraction of topo-clusters that originated from pile-up vertices, a jet-vertex fraction (JVF) [132] cut is often used; for this cut, a large fraction of tracks within a jet must originate from the primary vertex associated with the hard collision. The primary jet-vertex fraction for a jet is defined as [132]:

$$JVF = \frac{\sum_{\text{PV Tracks}} |p_{\mathrm{T}}|}{\sum_{\text{Tracks}} |p_{\mathrm{T}}|}, \tag{4.5}$$

where 'PV Tracks' refers to tracks within the jet which originated from the primary vertex. These are tracks within the jet which have an impact parameter z_0 <1 mm from the primary vertex. 'Tracks' refers to all tracks within the topo-cluster regardless of origin.

Figure 4.7 (taken from [133]) shows a schematic of the jet-vertex fraction for two jets originating

[1] pile-up collisions can introduce missing energy into the event that is not associated with the primary hard scatter.

from different primary vertices. A jet with a high JVF ($JVF > 0.8$) corresponds to a jet that has the majority of its tracks from the same primary vertex. A *loose* JVF cut ($\approx$0.15) can reject jets that have a high proportion of their tracks from pile-up vertices[133].

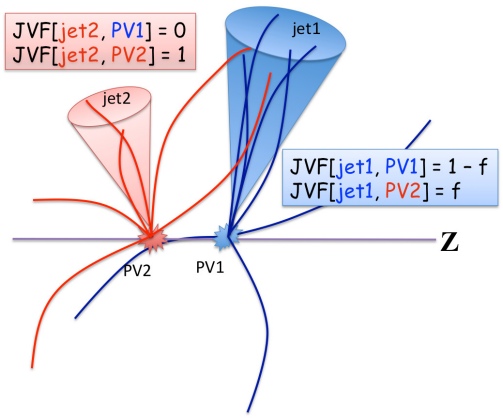

Figure 4.7: A schematic showing the jet-vertex fraction (JVF) of two jets from two different primary vertices. This figure was taken from [133].

4.4.1 $E_{\mathrm{T}}^{\mathrm{miss}}$ Algorithms

The $E_{\mathrm{T}}^{\mathrm{miss}}$ algorithms used in the performance studies remained close to the `MET_RefFinal` algorithm in section 3.6.6; however, various different jet p_{T} thresholds and $|\eta|$ regions were used for accepting jets into the `RefJet` $E_{\mathrm{T}}^{\mathrm{miss}}$ term. The full jet calibration was only applied to topo-clusters inside jets within the `RefJet` term. The jet-vertex fraction cut was also used in some $E_{\mathrm{T}}^{\mathrm{miss}}$ algorithms; as a result, only jets that passed the jet-vertex fraction cut (see Eq.(4.5)) were included in the `RefJet` term. This removed jets from the `RefJet` term that were mainly made from topo-clusters originating from pile-up vertices.

Two different `SoftTerm` algorithms were used in the $Z \rightarrow \mu\mu$ $E_{\mathrm{T}}^{\mathrm{miss}}$ performance analysis:

- `RefFinal` - the `RefFinal SoftTerm` is the ATLAS standard. It uses uncalibrated topo-clusters below the `RefJet` p_{T} threshold, and does not use tracks which originate from a pile-up vertex. For particle flow this means any charged reconstructed objects (tracks) in the EFlow objects list must pass the pile-up track rejection cut.

- `Hybrid` - the `Hybrid SoftTerm` term only uses charged objects (tracks). Any neutral topo-clusters are ignored in the `CellOut` term. However, neutral clusters included in jets that are above the jet p_{T} threshold are still included in the `RefJet` term.

4.4.2 Event Selection

$Z \rightarrow \mu\mu$ MC events were generated with `PowHeg+PYTHIA 8` [82, 105] using the `CT10` PDF set [103]; $t\bar{t}$ MC was generated with `MC@NLO` [98, 99] interfaced with `Jimmy` [85] using the `CT10` PDF set [103]. Data events were selected from the `Draw_Zmumu` event stream recorded in the 2012 data taking period. The stream uses a combination of single-muon and multi-muon triggers to select potential $Z \rightarrow \mu\mu$ events. Eq.(4.6) shows an example muon trigger chain used in the `Draw_Zmumu` stream:

$$\text{L1\_MU15} \rightarrow \text{L2\_mu36\_tight} \rightarrow \text{EF\_mu36\_tight}. \tag{4.6}$$

Here, "tight" is the cleaning cuts applied to the potential muon object and mu36 denotes a muon-like object with $p_{\mathrm{T}} > 36\,\mathrm{GeV}$.

Table 4.1 shows the event selection cuts for the $Z \rightarrow \mu\mu$ $E_{\mathrm{T}}^{\mathrm{miss}}$ performance analysis. The cut on the location of the primary vertex (cut 3(c) in Table 4.1) removed events where the reconstructed primary vertex in the MC event did not match the truth location. Since the correct primary vertex was not reconstructed properly, these events were not suitable for use in the analysis.

4.4.3 $Z \rightarrow \mu\mu$ MC Results

After events had passed the pre-selection cuts, the parallel $E_{\mathrm{T}}^{\mathrm{miss}}$ and perpendicular $E_{\mathrm{T}}^{\mathrm{miss}}$ for each different $E_{\mathrm{T}}^{\mathrm{miss}}$ algorithm (see section 4.4.1) were measured against Z boson p_{T} (Zp_{T}), NPV and $\langle\mu\rangle$. This was only performed in simulated $Z \rightarrow \mu\mu$ events; therefore, no cut on the p_{T} of the Z boson was required, since no comparison to data was made. Figure 4.8 shows an example parallel (a) and perpendicular (b) $E_{\mathrm{T}}^{\mathrm{miss}}$ distribution for the Z boson p_{T} bin of 0 - 10 GeV. A Gaussian function was fitted to each $E_{\mathrm{T}}^{\mathrm{miss}}$ distribution (see Figure 4.8) to obtain the resolution and scale of the $E_{\mathrm{T}}^{\mathrm{miss}}$. The mean of the Gaussian fit to the perpendicular $E_{\mathrm{T}}^{\mathrm{miss}}$ (b) was fixed to zero to improve the fitting; this means that the scale of the perpendicular $E_{\mathrm{T}}^{\mathrm{miss}}$ could not be obtained from the fit. The simple Gaussian fit does not provide a perfect fit to the $E_{\mathrm{T}}^{\mathrm{miss}}$ distributions, but a Gaussian fit was justifiable for this proof of principle study.

Figure 4.9 shows the resolution and scale of the parallel $E_{\mathrm{T}}^{\mathrm{miss}}$ distribution as function of Z boson p_{T}. PFlow standard refers to the particle flow algorithm with the standard `RefFinal CellOut` term. This figure shows that the particle flow `RefFinal` algorithm had an improved $E_{\mathrm{T}}^{\mathrm{miss}}$ resolution compared to `MET_RefFinal`, but a slightly worse scale at high Z boson p_{T}. Different pile-up suppression techniques were tested for the `Hybrid` PFlow $E_{\mathrm{T}}^{\mathrm{miss}}$ algorithm; the best resolution was provided using the `Hybrid CellOut` term with the standard jet p_{T} cut (20 GeV for all η).

Cut	Description	Value
1	Data Quality (Data)	run and luminosity block appears in GRL
2	Trigger (Data)	`Draw_Zmumu` Trigger stream with two muons with p_T >25 GeV or dimuon invariant mass pair >55 GeV
3(a)	Event Cleaning (Data)	No bad quality jets: `bad_Loose--`
3(b)	Event Cleaning (Data)	No hard p_T forward muons with $\|\eta\| > 2.4$ and $p_T > 20$ GeV
3(c)	Event Cleaning (MC)	Reconstructed PV near Truth PV: $\|PV\ z_{reco} - PV\ z_{truth}\|$ <5 mm
4(a)	Muon type cut	Is a `Combined STACO` muon
4(b)	Muon η cut	Non-Forward: $\|\eta\| < 2.4$
4(c)	Muon isolation cut	Isolated: $p_T$cone20 < 1800 MeV
5(a)	Z window	Best muon pair invariant mass: 80 GeV< M_Z <100 GeV
5(b)	Z p_T cut (MC)	Z boson p_T> 32 GeV

Table 4.1: The $Z \rightarrow \mu\mu$ event selection cut table. Cut 5(b), the Z boson p_T cut, was applied to MC to match a selection cut for data events taken from the `Draw_Zmumu` stream. For more information on the Muon type and p_T isolation cut, see section 3.6.5. The variable $p_T$cone20 was defined in section 3.6.5.

The Gaussian fits to the PFlow `Hybrid` E_T^{miss} algorithm failed in the 20-30 GeV Z boson p_T bin (see Figure 4.9), since the scale (mean) of the E_T^{miss} distribution was split in two, depending on whether the Z boson was recoiling against accompanying jets.

Figure 4.10 shows this phenomenon in more detail within three different Z boson p_T bins for the PFlow Hybrid E_T^{miss} algorithm: 0-10 GeV (a), 20-30 GeV ((b) and (d)) and 40-60 GeV (c). At low Z boson p_T (a), it can be seen that the E_T^{miss} distribution was dominated by events with no jets ('zero jet events'). As the p_T of the Z boson increases, it was accompanied more often by jets (see figures (b) and (c)); this resulted in the events without any accompanying jets becoming unbalanced (with a large negative mean, see (b)) and Z boson events with accompanying jets becoming the dominant contribution to the distribution. This effect was most predominant in the 20-30 GeV Z boson p_T bin ((b) and (d)), where the Z boson was almost always produced with accompanying jets; however, since the jets were low p_T, they were not likely to be included in the `RefJet` term of the E_T^{miss}. If

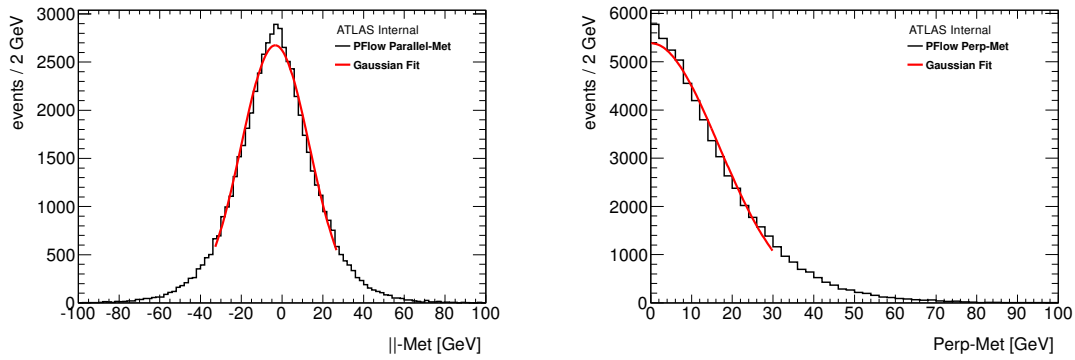

(a) PFlow Parallel

(b) PFlow Perp

Figure 4.8: The parallel and perpendicular $E_{\mathrm{T}}^{\mathrm{miss}}$ distributions for the $0-10\,\mathrm{GeV}$ Z boson p_{T} bin. For both figures, the $E_{\mathrm{T}}^{\mathrm{miss}}$ distribution from the PFlow reconstruction algorithm is shown in black, and the Gaussian fit to this distribution is shown in red. The fitting was performed in the Gaussian region of the $E_{\mathrm{T}}^{\mathrm{miss}}$ distribution to avoid any bias from the non-Gaussian tails of the $E_{\mathrm{T}}^{\mathrm{miss}}$ distribution.

the jet was not included in the `RefJet` term, then all neutral clusters were removed from the jet; this led to a large imbalance of the p_{T} in the event and a cumulative distribution that could not be fitted effectively. If the jet p_{T} cut of the `RefJet` was reduced to 15 GeV, then the jets that were produced with the Z boson had a higher probability of being included in the `RefJet` term; therefore, this improved the p_{T} balance of the event and resulted in fewer Z boson events with no accompanying jets. This effect is shown in Figure 4.10(d).

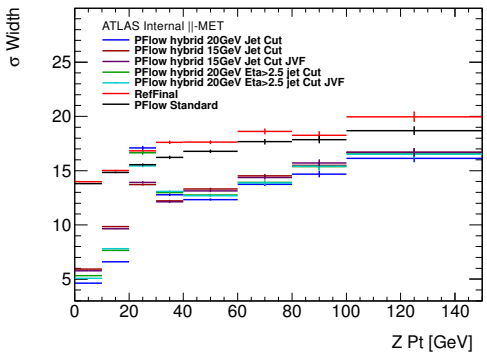

(a) Parallel-$E_{\mathrm{T}}^{\mathrm{miss}}$ Resolution

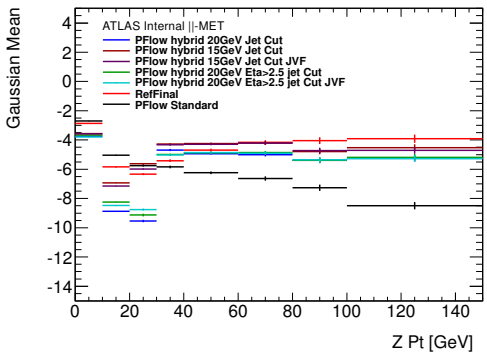

(b) Parallel-$E_{\mathrm{T}}^{\mathrm{miss}}$ Scale

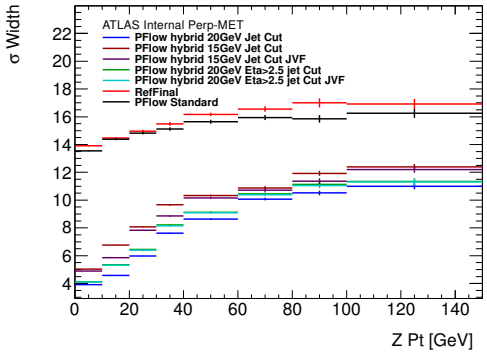

(c) Perp-$E_{\mathrm{T}}^{\mathrm{miss}}$ Scale

Figure 4.9: The parallel and perpendicular $E_{\mathrm{T}}^{\mathrm{miss}}$ distributions as a function of the Z p_{T}. Figure (a) shows the resolution of the $E_{\mathrm{T}}^{\mathrm{miss}}$, and figure (b) shows the scale of the parallel $E_{\mathrm{T}}^{\mathrm{miss}}$. Figure (c) shows the perpendicular $E_{\mathrm{T}}^{\mathrm{miss}}$ distribution. The ATLAS `MET_RefFinal` $E_{\mathrm{T}}^{\mathrm{miss}}$ distribution is shown in red and the PFlow `RefFinal` in black. The blue line shows the distribution from the PFlow `Hybrid CellOut` algorithm. The maroon and purple lines show the distributions of PFlow `Hybrid` algorithm $E_{\mathrm{T}}^{\mathrm{miss}}$ with a jet p_{T} cut for the `RefJet` term of 15 GeV for all η. The purple line also has a JVF cut applied to jets entering the `RefJet` term. The green and cyan lines show the distributions for PFlow `Hybrid` $E_{\mathrm{T}}^{\mathrm{miss}}$ with a forward calorimeter region ($|\eta| > 2.5$) jet p_{T} cut of 20 GeV and a jet cut of 15 GeV for $|\eta| \leq 2.5$. The cyan line also has a JVF cut applied to jets entering the `RefJet` term.

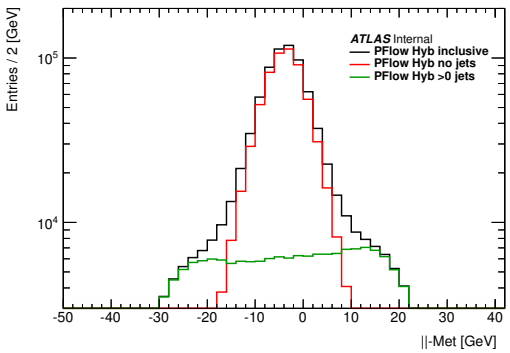

(a) `Hybrid` Parallel-$E_{\mathrm{T}}^{\mathrm{miss}}$ Zp_{T} 0-10 GeV

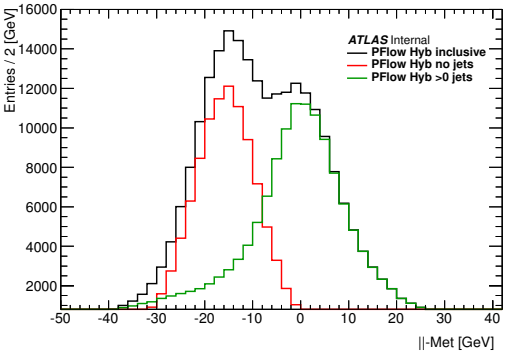

(b) `Hybrid` Parallel-$E_{\mathrm{T}}^{\mathrm{miss}}$ Zp_{T} 20-30 GeV

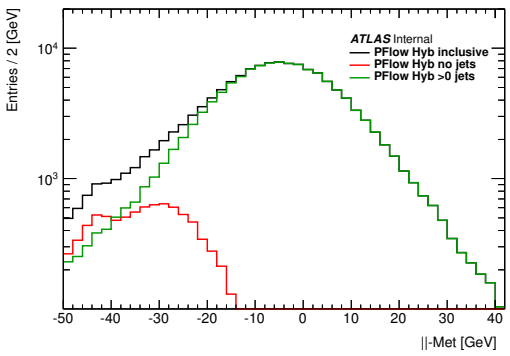

(c) `Hybrid` Parallel-$E_{\mathrm{T}}^{\mathrm{miss}}$ Zp_{T} 40-60 GeV

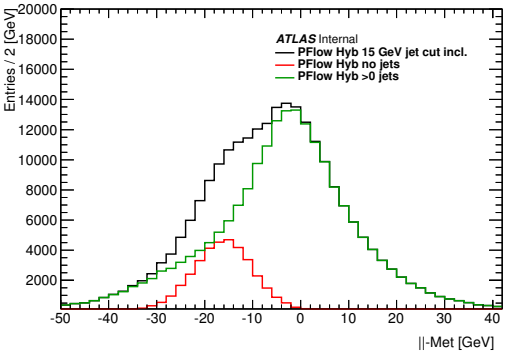

(d) `Hybrid` Parallel-$E_{\mathrm{T}}^{\mathrm{miss}}$ Zp_{T} 20-30 GeV with 15 GeV jet cut

Figure 4.10: The `Hybrid` Parallel $E_{\mathrm{T}}^{\mathrm{miss}}$ distributions in bins of Z p_{T}: 0-10 GeV (a), 20-30 GeV (b) and (d), and 40-60 GeV (c). The inclusive $E_{\mathrm{T}}^{\mathrm{miss}}$ distribution for all Z+jet events is shown in black. The $E_{\mathrm{T}}^{\mathrm{miss}}$ distribution for Z boson events without accompanying jets is shown in red, and for events with accompanying jets is shown in green; (d) shows the distribution for PFlow `Hybrid` $E_{\mathrm{T}}^{\mathrm{miss}}$ with a 15 GeV jet p_{T} cut on the `RefJet` term of the $E_{\mathrm{T}}^{\mathrm{miss}}$ algorithm.

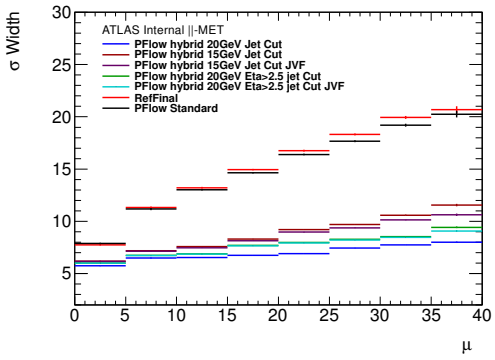

(a) Parallel-$E_{\mathrm{T}}^{\mathrm{miss}}$ Resolution

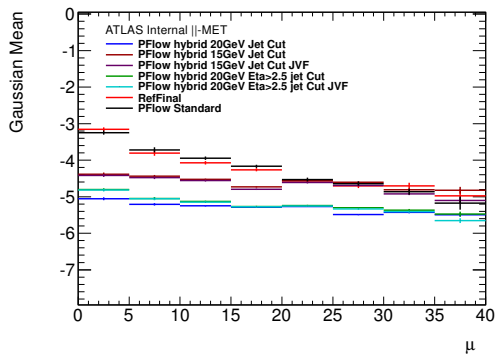

(b) Parallel-$E_{\mathrm{T}}^{\mathrm{miss}}$ Scale

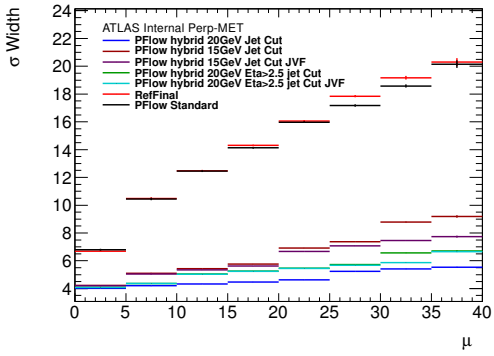

(c) Perp-$E_{\mathrm{T}}^{\mathrm{miss}}$ Resolution

Figure 4.11: The parallel and perpendicular $E_{\mathrm{T}}^{\mathrm{miss}}$ distributions as a function of $\langle\mu\rangle$. Figure (a) shows the resolution of the $E_{\mathrm{T}}^{\mathrm{miss}}$, and figure (b) shows the scale of the parallel $E_{\mathrm{T}}^{\mathrm{miss}}$. Figure (c) shows the perpendicular $E_{\mathrm{T}}^{\mathrm{miss}}$ distribution. The ATLAS `MET_RefFinal` $E_{\mathrm{T}}^{\mathrm{miss}}$ distribution is shown in red and the PFlow `RefFinal` in black. The blue line shows the distribution from the PFlow `Hybrid CellOut` algorithm. The maroon and purple lines show the distributions of PFlow `Hybrid` algorithm $E_{\mathrm{T}}^{\mathrm{miss}}$ with a jet p_{T} cut for the `RefJet` term of 15 GeV for all η. The purple line also has a JVF cut applied to jets entering the `RefJet` term. The green and cyan lines show the distributions for PFlow `Hybrid` $E_{\mathrm{T}}^{\mathrm{miss}}$ with a forward calorimeter region ($|\eta| > 2.5$) jet p_{T} cut of 20 GeV and a jet cut of 15 GeV for $|\eta| \leq 2.5$. The cyan line also has a JVF cut applied to jets entering the `RefJet` term.

Figure 4.11 shows the parallel, (a) and (b), and the perpendicular, (c), $E_{\mathrm{T}}^{\mathrm{miss}}$ distributions as a function of $\langle\mu\rangle$. The key characteristic of the distributions in this figure is the gradient. The $E_{\mathrm{T}}^{\mathrm{miss}}$ algorithm is more pile-up independent if the points remain unchanged as $\langle\mu\rangle$ increases; this means the $E_{\mathrm{T}}^{\mathrm{miss}}$ algorithms are more robust to pile-up effects. In Figure 4.11, the PFlow `RefFinal` algorithm (black) performs slightly better than `MET_RefFinal` (red) over all $\langle\mu\rangle$; however, the most pile-up independent $E_{\mathrm{T}}^{\mathrm{miss}}$ algorithm was the particle flow `Hybrid` algorithm with a jet cut at 20 GeV (blue). The scale of the parallel $E_{\mathrm{T}}^{\mathrm{miss}}$ is shown in Figure 4.11(b). Here, the best performing algorithms were the PFlow `RefFinal` and ATLAS standard `RefFinal` $E_{\mathrm{T}}^{\mathrm{miss}}$ algorithms. Also, it should be noted that the effectiveness of applying a JVF cut rejecting pile-up jets in the `RefJet` term reduces

as the jet p_{T} cut on the `RefJet` term increases; therefore, a JVF cut was not required when the jet p_{T} cut for the `RefJet` term was 20 GeV (for all η).

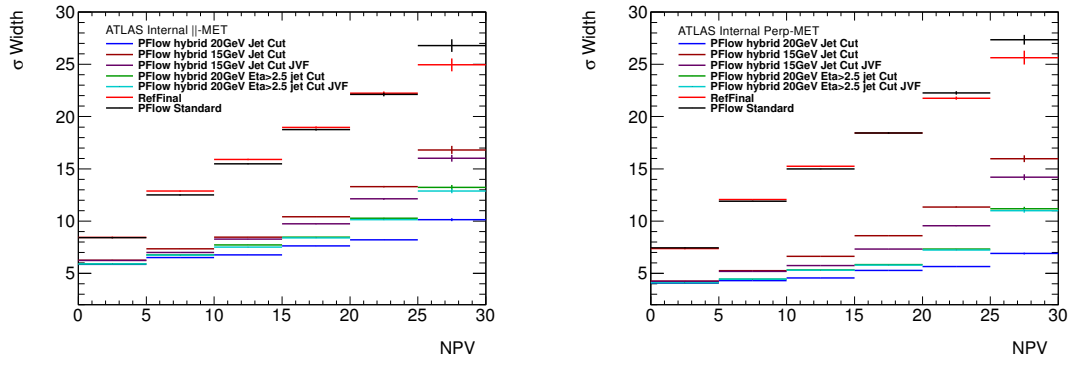

(a) Parallel-$E_{\mathrm{T}}^{\mathrm{miss}}$ Resolution

(b) Perp-$E_{\mathrm{T}}^{\mathrm{miss}}$ Resolution

Figure 4.12: The parallel and perpendicular $E_{\mathrm{T}}^{\mathrm{miss}}$ resolution distributions as a function of NPV. (a) shows the resolution of the parallel $E_{\mathrm{T}}^{\mathrm{miss}}$ and (b) shows the resolution of the perpendicular $E_{\mathrm{T}}^{\mathrm{miss}}$. The ATLAS `MET_RefFinal` $E_{\mathrm{T}}^{\mathrm{miss}}$ distribution is shown in red and the PFlow `RefFinal` in black. The blue line shows the distribution from the PFlow `Hybrid CellOut` algorithm. The maroon and purple lines show the distributions of PFlow `Hybrid` algorithm $E_{\mathrm{T}}^{\mathrm{miss}}$ with a jet p_{T} cut for the `RefJet` term of 15 GeV for all η. The purple line also has a JVF cut applied to jets entering the `RefJet` term. The green and cyan lines show the distributions for PFlow `Hybrid` $E_{\mathrm{T}}^{\mathrm{miss}}$ with a forward calorimeter region ($|\eta| > 2.5$) jet p_{T} cut of 20 GeV and a jet cut of 15 GeV for $|\eta| \leq 2.5$. The cyan line also has a JVF cut applied to jets entering the `RefJet` term.

Figure 4.12 shows the resolution of the parallel and perpendicular $E_{\mathrm{T}}^{\mathrm{miss}}$ distributions as a function of the number of primary vertices (NPV). These distributions are very similar to the $\langle\mu\rangle$ distributions shown in Figure 4.11 and similar conclusions can be drawn from them.

4.4.4 $Z \rightarrow \mu\mu$ Data to MC Comparison Results

It is noteworthy that the $E_{\mathrm{T}}^{\mathrm{miss}}$ algorithms performed in data as well as they did in $Z \rightarrow \mu\mu$ MC. To test the $E_{\mathrm{T}}^{\mathrm{miss}}$ performance in data, three different $E_{\mathrm{T}}^{\mathrm{miss}}$ algorithms were compared in data and MC. The ATLAS standard `MET_RefFinal` algorithm was used as the control sample: it confirmed that the event selection was working correctly in data and also provided a working point against which the particle flow $E_{\mathrm{T}}^{\mathrm{miss}}$ algorithms could be compared. The particle flow `RefFinal` algorithm was used as a direct comparison to `MET_RefFinal`: it directly showed how the particle flow algorithm changed the $E_{\mathrm{T}}^{\mathrm{miss}}$ performance. Finally, the particle flow `Hybrid` algorithm was tested since it showed greater pile-up independence than the `RefFinal CellOut` term $E_{\mathrm{T}}^{\mathrm{miss}}$ algorithms in MC.

Changes with respect to the $Z \rightarrow \mu\mu$ MC results

- A new particle flow jet calibration (JES) (see section 3.6.1) became available for the data and MC comparison study. Particle flow jets were also changed to the EM+JES calibration scheme (see section 3.6.1). Therefore, it should be noted that figures 4.9 and 4.13 are not directly comparable.

- The Z boson p_{T} cut (5(b) in Table 4.1) was applied to MC samples to provide a fair comparison with data events.

- The magnitude of the $E_{\mathrm{T}}^{\mathrm{miss}}$ was also studied (see section 4.4.5).

The parallel $E_{\mathrm{T}}^{\mathrm{miss}}$ distributions for the `MET_RefFinal` and particle flow $E_{\mathrm{T}}^{\mathrm{miss}}$ algorithms as a function of Z boson p_{T} are shown in Figure 4.13. All the $E_{\mathrm{T}}^{\mathrm{miss}}$ algorithms showed good agreement between their performance in data and MC. It can be seen in Figure 4.13(a) that the resolution of the particle flow `RefFinal` $E_{\mathrm{T}}^{\mathrm{miss}}$ distributions improved by $\approx 20\%$ with the new jet calibration, but the scale at high Z p_{T} remained unchanged.

Figure 4.14 shows the parallel $E_{\mathrm{T}}^{\mathrm{miss}}$ distributions for the `MET_RefFinal` and particle flow $E_{\mathrm{T}}^{\mathrm{miss}}$ algorithms as a function of NPV. There was good agreement between data and MC for all of the $E_{\mathrm{T}}^{\mathrm{miss}}$ algorithms except for the last histogram bin (NPV 25-30), where the statistics in data caused issues with the fitting to the distributions. Figure 4.14(c) shows that the particle flow `Hybrid` $E_{\mathrm{T}}^{\mathrm{miss}}$ algorithm was the most pile-up independent in data and MC. It can be seen in Figure 4.14(a) that the resolution of the particle flow `RefFinal` algorithm improved against NPV with the improvements to the particle flow algorithm, and was also more pile-up independent than previously (see Figure 4.12).

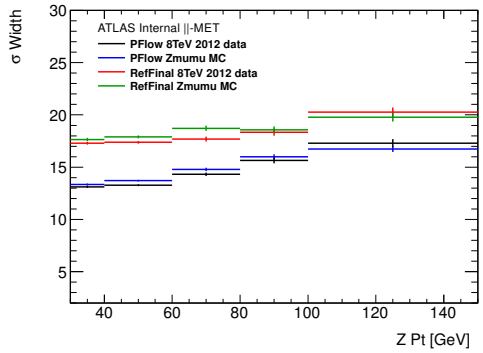

(a) `RefFinal` Parallel-$E_{\mathrm{T}}^{\mathrm{miss}}$ Z p_{T} Resolution

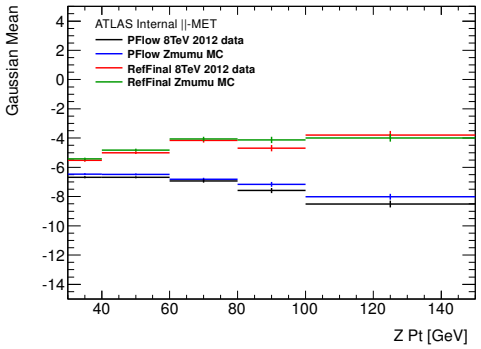

(b) `RefFinal` Parallel-$E_{\mathrm{T}}^{\mathrm{miss}}$ Z p_{T} Scale

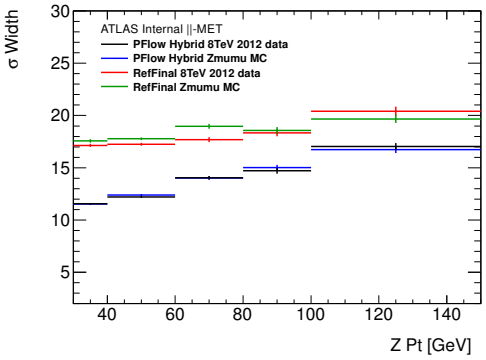

(c) `Hybrid` Parallel-$E_{\mathrm{T}}^{\mathrm{miss}}$ Z p_{T} Resolution

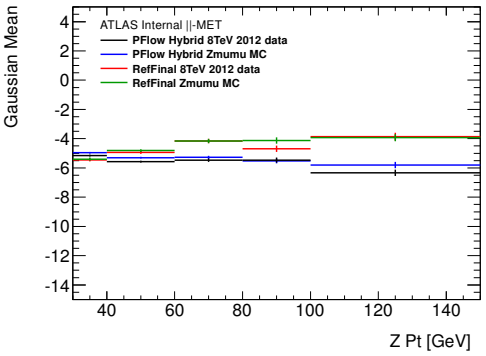

(d) `Hybrid` Parallel-$E_{\mathrm{T}}^{\mathrm{miss}}$ Z p_{T} Scale

Figure 4.13: The `MET_RefFinal` and particle flow parallel $E_{\mathrm{T}}^{\mathrm{miss}}$ distributions in data and MC as a function of Z p_{T}. The black lines show the distribution for particle flow (`RefFinal` and `Hybrid`) in data, whereas the blue lines show the particle flow distribution in MC. The red lines show the `MET_RefFinal` distribution in data, whereas the green lines show the `MET_RefFinal` distribution in MC. Figures (a) and (b) show the resolution (a) and scale (b) using the Particle flow `RefFinal` algorithm compared to the standard ATLAS `MET_RefFinal` algorithm. Figures (c) and (d) show the resolution (c) and scale (d) using the Particle flow `Hybrid` algorithm compared to the standard ATLAS `MET_RefFinal` algorithm. It should be noted that due to the updated jet calibration these figures are not directly comparable with those in figure 4.9.

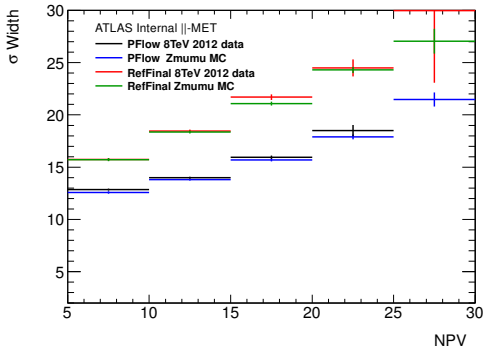

(a) `RefFinal` Parallel-$E_{\mathrm{T}}^{\mathrm{miss}}$ NPV Resolution

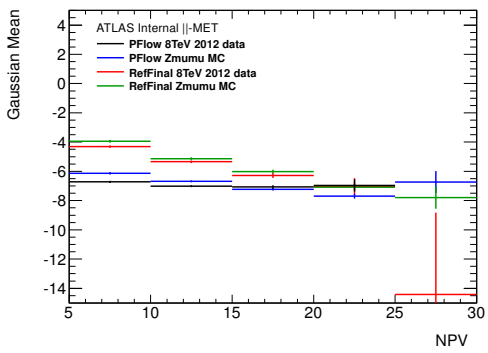

(b) `RefFinal` Parallel-$E_{\mathrm{T}}^{\mathrm{miss}}$ NPV Scale

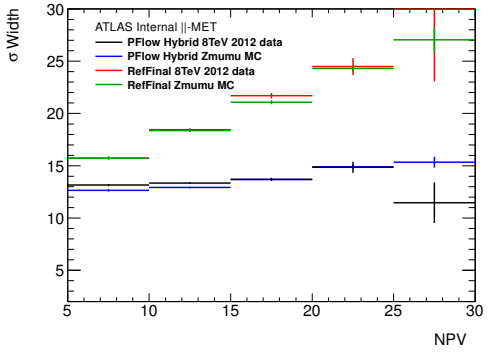

(c) `Hybrid` Parallel-$E_{\mathrm{T}}^{\mathrm{miss}}$ NPV Resolution

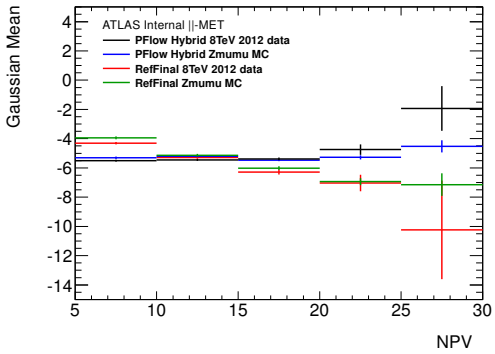

(d) `Hybrid` Parallel-$E_{\mathrm{T}}^{\mathrm{miss}}$ NPV Scale

Figure 4.14: The `MET_RefFinal` and particle flow parallel $E_{\mathrm{T}}^{\mathrm{miss}}$ distributions in data and MC as a function of NPV. The black lines show the distribution for particle flow (`RefFinal` and `Hybrid`) in data, whereas the blue lines show the particle flow distribution in MC. The red lines show the `MET_RefFinal` distribution in data, whereas the green lines show the `MET_RefFinal` distribution in MC. Figures (a) and (b) show the resolution (a) and scale (b) using the Particle flow `RefFinal` algorithm compared to the standard ATLAS `MET_RefFinal` algorithm. Figures (c) and (d) show the resolution (c) and scale (d) using the Particle flow `Hybrid` algorithm compared to the standard ATLAS `MET_RefFinal` algorithm. It should be noted that due to the updated jet calibration these figures are not directly comparable with those in figure 4.12.

4.4.5 Magnitude of the $E_{\mathrm{T}}^{\mathrm{miss}}$ and Muon Event Cleaning

Originally, no event cleaning cuts were applied to the muons used to reconstruct the Z boson. Without these cleaning cuts, high p_{T} 'fake' forward muons were able to pass the selection cuts; this resulted in large tails in the $E_{\mathrm{T}}^{\mathrm{miss}}$ distributions (see Figure 4.15). The majority of these events in data were from $t\bar{t}$, as shown by the $t\bar{t}$ MC distribution in Figure 4.15. However, some of these events in data were from $Z \to \mu\mu$. With further investigation, these events were found to have a forward 'muon' which was most likely a boosted energetic jet which was 'punching-through' into the muon chambers faking the muon signature. To remove events containing fake muons, a muon isolation cut was applied (see section 3.6.5). This reduced the tails of the $E_{\mathrm{T}}^{\mathrm{miss}}$ distribution as a jet would have a large amount of energy within the isolation cone around the reconstructed muon track; hence, the event would be rejected.

A further event cleaning cut required no hard muons (p_{T} >20 GeV) outside the triggering range of the muon chambers ($|\eta| < 2.4$). This was to reject data events which had a muon candidate that was not involved in the triggering process of the event, as a muon of this type cannot be one of the muons from the reconstructed Z boson candidate that the `Draw_Zmumu` stream was searching for. This also provided extra protection against reconstructing the Z boson with an incorrect muon pair (in $Z \to \mu\mu$ data events).

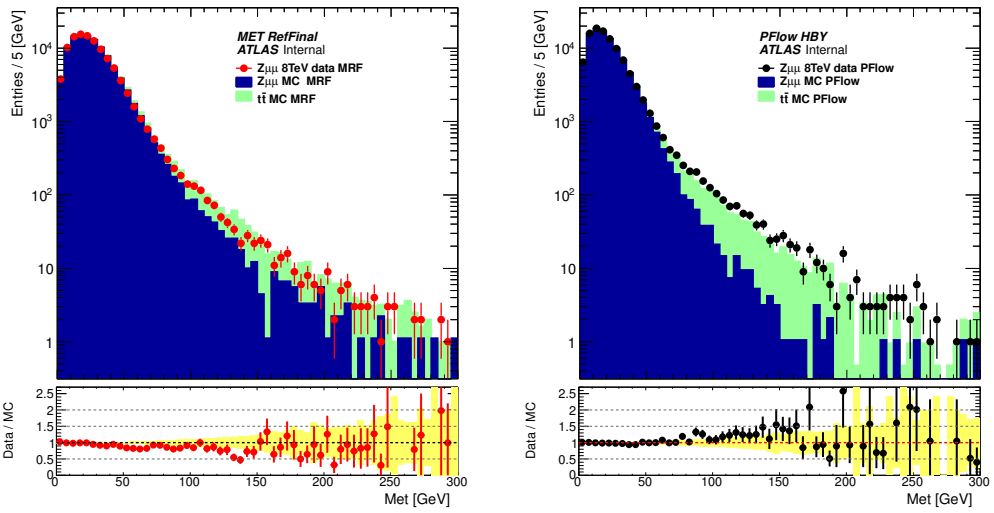

(a) `MET_RefFinal` Total $E_{\mathrm{T}}^{\mathrm{miss}}$ (b) Particle Flow `Hybrid` Total $E_{\mathrm{T}}^{\mathrm{miss}}$

Figure 4.15: The magnitude of the $E_{\mathrm{T}}^{\mathrm{miss}}$ distributions for `MET_RefFinal` and particle flow `Hybrid` $E_{\mathrm{T}}^{\mathrm{miss}}$ in $Z \to \mu\mu$ events without any muon event cleaning cuts. Figure (a) shows the `MET_RefFinal` $E_{\mathrm{T}}^{\mathrm{miss}}$ distribution. The `MET_RefFinal` distribution for the 2012 $\sqrt{s} = 8$ TeV data set is shown in red, and the $Z \to \mu\mu$ and $t\bar{t}$ MC are shown in blue and green respectively. Figure (b) shows the particle flow `Hybrid` $E_{\mathrm{T}}^{\mathrm{miss}}$ distribution. The particle flow `Hybrid` distribution for 2012 $\sqrt{s} = 8$ TeV data set is shown in black, and the $Z \to \mu\mu$ and $t\bar{t}$ MC are also shown in blue and green respectively.

After applying the muon cleaning cuts, it can be seen in Figure 4.16 that the tail in the magnitude of the $E_{\mathrm{T}}^{\mathrm{miss}}$ distribution was reduced significantly in the $Z \to \mu\mu$ MC distribution, particularly for `MET_RefFinal` (figure (a)).

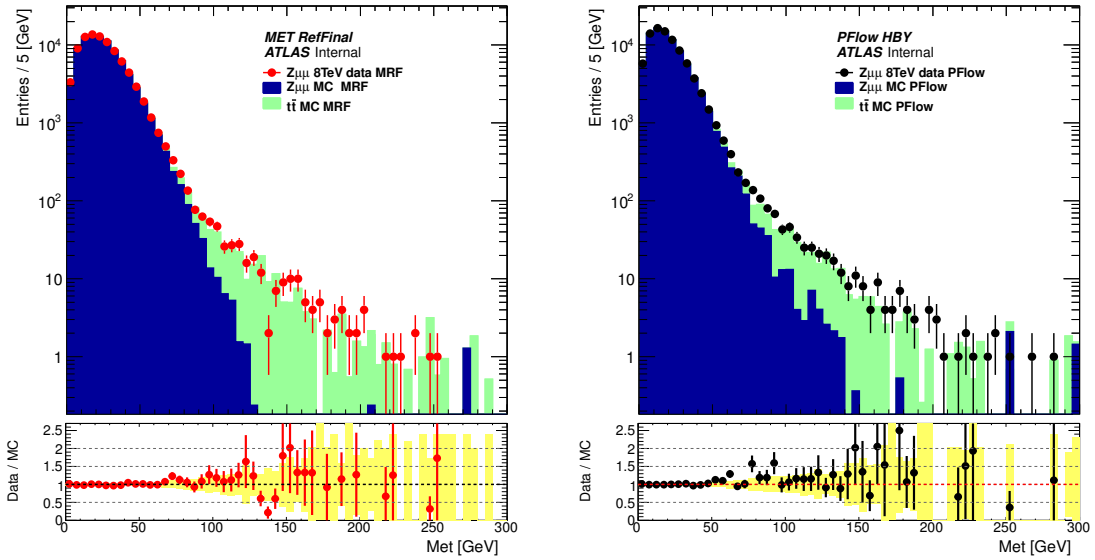

(a) `MET_RefFinal` Total $E_{\mathrm{T}}^{\mathrm{miss}}$

(b) Particle Flow `Hybrid` Total $E_{\mathrm{T}}^{\mathrm{miss}}$

Figure 4.16: The magnitude of the $E_{\mathrm{T}}^{\mathrm{miss}}$ distributions for `MET_RefFinal` and particle flow `Hybrid` $E_{\mathrm{T}}^{\mathrm{miss}}$ in $Z \to \mu\mu$ events after applying the muon event cleaning cuts. Figure (a) shows the `MET_RefFinal` $E_{\mathrm{T}}^{\mathrm{miss}}$ distribution. The `MET_RefFinal` distribution for the 2012 $\sqrt{s} = 8\,\mathrm{TeV}$ data set is shown in red, and the $Z \to \mu\mu$ and $t\bar{t}$ MC is shown in blue and green respectively. Figure (b) shows the particle flow `Hybrid` $E_{\mathrm{T}}^{\mathrm{miss}}$ distribution. The particle flow `Hybrid` distribution for the 2012 $\sqrt{s} = 8\,\mathrm{TeV}$ data set is shown in black, and the $Z \to \mu\mu$ and $t\bar{t}$ MC are also shown in blue and green respectively.

Since the statistics in data were reduced significantly within the tail region ($E_{\mathrm{T}}^{\mathrm{miss}} > 90\,\mathrm{GeV}$), $E_{\mathrm{T}}^{\mathrm{miss}}$ distributions were re-binned to bins of 10 GeV to compare the tail region of the different distributions in more detail (see Figure 4.17). Figure 4.17 shows that the particle flow $Z \to \mu\mu$ MC distributions (4.17(b) and (c)) were more truncated. The data distributions were fitted with a Gaussian function (see Figure A.1(a) for an example) in the Gaussian region of the $E_{\mathrm{T}}^{\mathrm{miss}}$distribution. The results from these fits are shown in the table in Figure 4.17(d). The table shows that the width of particle flow `RefFinal` algorithm was 6% narrower than `Met_RefFinal` and the mean was also 17% closer to zero. The particle flow `Hybrid` algorithm had a width only 1% narrower than `Met_RefFinal`, but the mean was 23% closer to zero. This indicates that the particle flow reconstruction algorithms had a better $E_{\mathrm{T}}^{\mathrm{miss}}$ performance in the $Z \to \mu\mu$ events than the ATLAS standard event reconstruction. Figure 4.17 also shows that the $t\bar{t}$ MC tail is more pronounced (with the reduction of $Z \to \mu\mu$ events) in the particle flow algorithms, hinting that particle flow could be more sensitive to $t\bar{t}$ data events in this region.

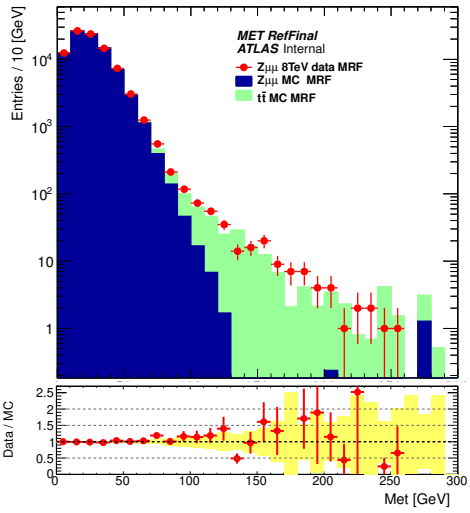

(a) `MET_RefFinal` Total $E_{\mathrm{T}}^{\mathrm{miss}}$

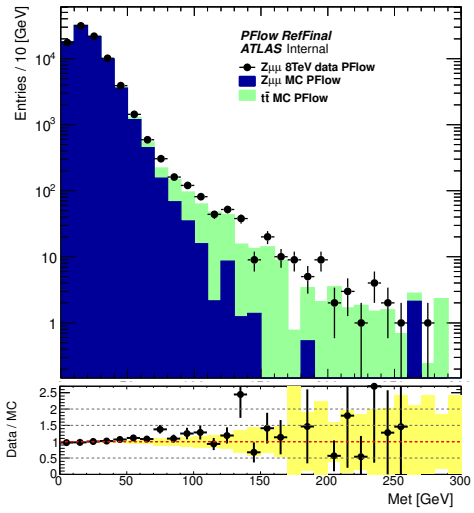

(b) Particle Flow `RefFinal` Total $E_{\mathrm{T}}^{\mathrm{miss}}$

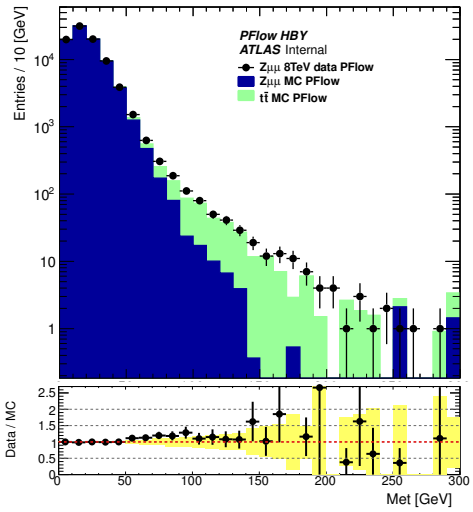

(c) Particle Flow `Hybrid` Total $E_{\mathrm{T}}^{\mathrm{miss}}$

$E_{\mathrm{T}}^{\mathrm{miss}}$ Algorithm	σ [GeV]	Mean [GeV]	σ/Mean
`Met_RefFinal`	12.34	20.41	0.605
PFlow RefFinal	11.59	16.88	0.687
PFlow Hybrid	12.18	15.17	0.782

(d) Gaussian Fitting Results

Figure 4.17: The $\left|E_{\mathrm{T}}^{\mathrm{miss}}\right|$ distributions for `MET_RefFinal` and particle flow in $Z \to \mu\mu$ events after applying the muon event cleaning cuts. Figure (a) shows the `MET_RefFinal` $E_{\mathrm{T}}^{\mathrm{miss}}$ distribution for the 2012 $\sqrt{s} = 8$ TeV data set in red. Figure (b) shows the particle flow `RefFinal` $E_{\mathrm{T}}^{\mathrm{miss}}$ distribution for 2012 $\sqrt{s} = 8$ TeV data set in black. Finally, figure (c) shows the particle flow `Hybrid` $E_{\mathrm{T}}^{\mathrm{miss}}$ distribution for the 2012 $\sqrt{s} = 8$ TeV data set in black. In these figures, the $Z \to \mu\mu$ and $t\bar{t}$ MC are shown in blue and green respectively. Figure (d) shows the results table for the Gaussian fits to the data distributions of the different $E_{\mathrm{T}}^{\mathrm{miss}}$ algorithms.

To test if the particle flow reconstruction algorithm was more sensitive to $t\bar{t}$ events, the tail region of the $E_{\mathrm{T}}^{\mathrm{miss}}$ distribution was analysed more closely. Starting at $E_{\mathrm{T}}^{\mathrm{miss}}$ >50 GeV and ending at $E_{\mathrm{T}}^{\mathrm{miss}}$ >120 GeV (where there were not enough statistics), the total numbers of events in $Z \rightarrow \mu\mu$ data, $Z \rightarrow \mu\mu$ MC and $t\bar{t}$ MC were examined, and the ratio of the number of events in $t\bar{t}$ MC to $Z \rightarrow \mu\mu$ MC was calculated. Tables 4.2, 4.3 and 4.4 show the results of this study.

$E_{\mathrm{T}}^{\mathrm{miss}}$ bin range	Events in $Z \rightarrow \mu\mu$ Data	Events in $Z \rightarrow \mu\mu$ MC	Events in $t\bar{t}$ MC	Ratio $t\bar{t}/Z \rightarrow \mu\mu$
> 50 GeV	12775	13334	684	0.051 ± 0.002
> 60 GeV	5436	5707	591	0.104 ± 0.004
> 70 GeV	2382	2300	478	0.208 ± 0.010
> 80 GeV	1135	856	391	0.468 ± 0.029
> 90 GeV	**582**	**319**	**320**	1.00 ± 0.08
> 100 GeV	370	121	250	2.07 ± 0.23
> 110 GeV	253	43	194	4.51 ± 0.76
> 120 GeV	180	18	144	8.0 ± 2.0

Table 4.2: The number of events in the tail region of the `MET_RefFinal` $E_{\mathrm{T}}^{\mathrm{miss}}$ distribution.

$E_{\mathrm{T}}^{\mathrm{miss}}$ bin range	Events in $Z \rightarrow \mu\mu$ Data	Events in $Z \rightarrow \mu\mu$ MC	Events in $t\bar{t}$ MC	Ratio $t\bar{t}/Z \rightarrow \mu\mu$
> 50 GeV	6811	6384	686	0.107 ± 0.004
> 60 GeV	2901	2332	593	0.254 ± 0.012
> 70 GeV	1470	894	495	0.554 ± 0.031
> 80 GeV	880	334	407	1.22 ± 0.09
> 90 GeV	**574**	**161**	**321**	1.99 ± 0.19
> 100 GeV	413	73	246	3.37 ± 0.45
> 110 GeV	293	36	180	5.0 ± 0.9
> 120 GeV	212	22	129	5.9 ± 1.4

Table 4.3: The number of events in the tail region Particle Flow `RefFinal` of the $E_{\mathrm{T}}^{\mathrm{miss}}$ distribution.

In Tables 4.2, 4.3 and 4.4, it can be seen that the number of $t\bar{t}$ events in each range did not vary between the `MET_RefFinal` and the particle flow $E_{\mathrm{T}}^{\mathrm{miss}}$ algorithms. However, in the particle flow $E_{\mathrm{T}}^{\mathrm{miss}}$ algorithms there was a significant reduction in the predicted number of $Z \rightarrow \mu\mu$ MC events; this increased the ratio of $t\bar{t}/Z \rightarrow \mu\mu$ events up to an $E_{\mathrm{T}}^{\mathrm{miss}}$ cut of 90 GeV. This can be observed more clearly by comparing the $E_{\mathrm{T}}^{\mathrm{miss}} > 90$ GeV bin regions (shown in bold) in the results tables. Figure 4.18 shows the double ratio of $t\bar{t}/Z \rightarrow \mu\mu$ events of the particle flow algorithms compared

$E_{\mathrm{T}}^{\mathrm{miss}}$ bin range	Events in $Z \to \mu\mu$ Data	Events in $Z \to \mu\mu$ MC	Events in $t\bar{t}$ MC	Ratio $t\bar{t}/Z \to \mu\mu$
> 50 GeV	6928	6237	684	0.110 ± 0.004
> 60 GeV	3038	2259	591	0.262 ± 0.012
> 70 GeV	1516	852	493	0.579 ± 0.032
> 80 GeV	887	353	406	1.15 ± 0.08
> 90 GeV	**580**	**159**	**320**	2.00 ± 0.20
> 100 GeV	393	74	245	3.31 ± 0.44
> 110 GeV	282	45	180	4.00 ± 0.67
> 120 GeV	202	28	128	4.57 ± 0.95

Table 4.4: The number of events in the tail region of the Particle Flow `Hybrid` $E_{\mathrm{T}}^{\mathrm{miss}}$ distribution.

to `MET_RefFinal`. It can be seen in this figure that the largest gains in $t\bar{t}$ sensitivity are when the minimum $E_{\mathrm{T}}^{\mathrm{miss}}$ cut is between 60 and 90 GeV.

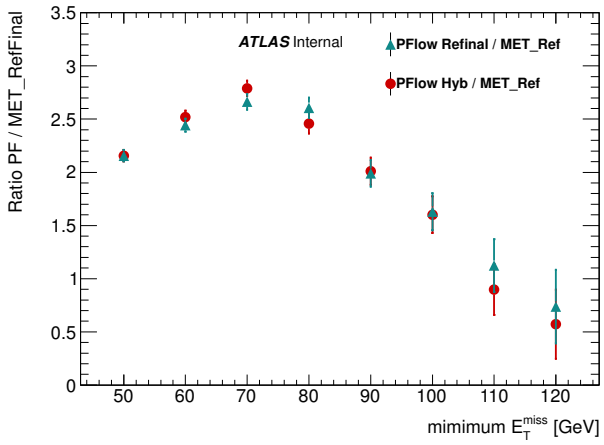

Figure 4.18: The double ratio of $t\bar{t}/Z \to \mu\mu$ for the particle flow algorithms divided by `MET_RefFinal`. Particle flow `RefFinal` is shown in cyan and particle flow `Hybrid` is shown in red. It should be noted that the error bars are highly correlated, because each point includes all points to its right since it is minimum $E_{\mathrm{T}}^{\mathrm{miss}}$.

4.5 $E_{\mathrm{T}}^{\mathrm{miss}}$ Performance in $t\bar{t}$ and Wt Events

The particle flow reconstruction algorithm performed significantly better than the ATLAS standard event reconstruction in $Z \to \mu\mu$ events, with evidence that it may have increased performance in $t\bar{t}$ reconstruction; therefore, further studies into $t\bar{t}$ and Wt event reconstruction were performed.

Both $t\bar{t}$ and Wt events are more difficult to reconstruct than $Z \to \mu\mu$ events, as the events contain

more final state objects than $Z \to \mu\mu$ events and may include $E_{\mathrm{T}}^{\mathrm{miss}}$ from final state neutrinos. In order to reduce the large Z+jets background, the single muon decay channel was chosen. Figure 4.19 shows examples of single muon decays of $t\bar{t}$ (a) and Wt (b) events. The final state objects that were of interest to reconstructing the top quark(s) and W bosons are shown in red[2].

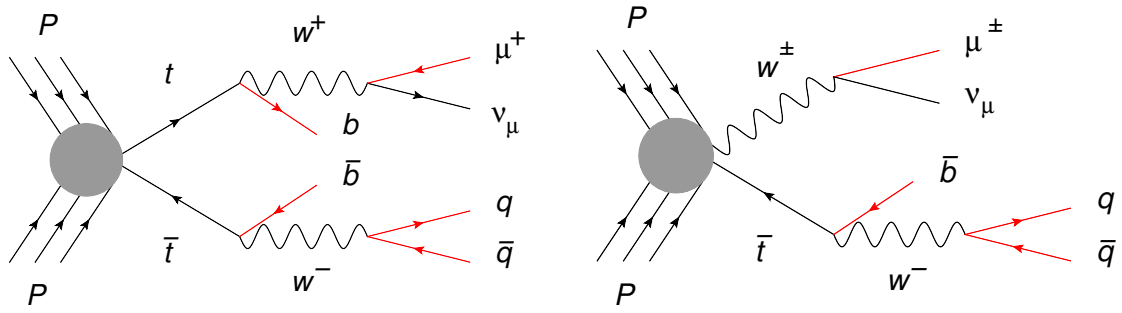

Figure 4.19: Example single muon decays in $t\bar{t}$ and Wt events. The final state objects for reconstructing the top quark(s) and W boson(s) are shown in red.

4.5.1 $E_{\mathrm{T}}^{\mathrm{miss}}$ Algorithms

In the $t\bar{t}$ and Wt $E_{\mathrm{T}}^{\mathrm{miss}}$ performance studies, only the `MET_RefFinal` and PFlow `RefFinal` $E_{\mathrm{T}}^{\mathrm{miss}}$ algorithms were tested. Keeping the $E_{\mathrm{T}}^{\mathrm{miss}}$ algorithms as close as possible provides a direct comparison between the standard ATLAS event reconstruction and the PFlow event reconstruction. The ATLAS standard jet p_{T} cut was used for the `RefJet` term ($p_{\mathrm{T}} > 20\,\mathrm{GeV}$), and no JVF cut was applied to the jets in the `RefJet` term.

4.5.2 Event Selection

The event selection for $t\bar{t}$ and Wt events is shown in Table 4.5. Data events were selected with the EF_mu24i_tight and EF_mu40_medium triggers from the 2012 $\sqrt{s} = 8\,\mathrm{TeV}$ muons stream. The EF_mu24i_tight trigger searches for tight quality muons with $p_{\mathrm{T}} > 24\,\mathrm{GeV}$ and imposes an isolation cut on the muon candidate at L2 of the trigger chain; this is denoted by the **i** in the trigger name. The EF_mu40_medium searches for medium quality muons with $p_{\mathrm{T}} > 40\,\mathrm{GeV}$ but does not apply any muon isolation cut. The $t\bar{t}$ MC was generated with `MC@NLO` [98, 99] interfaced with `Jimmy` [85] using the `CT10` PDF set [103], while the Wt MC sample was generated with `PowHeg` + `PYTHIA` [82, 105] with the `CT10` PDF set [103] using the `Perugia2011C` `PYTHIA` 6 tune.

[2] the neutrino's presence is inferred from looking at the $E_{\mathrm{T}}^{\mathrm{miss}}$ of the event; however, since it is not directly detected, it is not shown in red

Cut	Description	Value
1	Data Quality (Data)	run and luminosity block appears in GRL
2	Trigger (Data)	2012 $\sqrt{s} = 8$ TeV muon stream: Single lepton triggers: EF_mu24i_tight or EF_mu40_medium
3(a)	Event Cleaning (Data)	No bad quality jets: `bad_Loose--`
3(b)	Event Cleaning (MC)	Reconstructed PV near Truth PV: $\lvert PV\ z_{\text{reco}} - PV\ \text{\_truth}\rvert$ <5 mm
4(a)	Number of Muons	Only **one** reconstructed muon
4(b)	Muon type cut	Is a `Combined STACO` muon
4(c)	Muon η cut	Is Non-Forward: $\lvert\eta\rvert < 2.4$
4(d)	Muon isolation cut	Is Isolated: p_{T}cone20 < 1800 MeV
4(e)	Muon p_{T} cut	muon p_{T}> 25 GeV
5(a)	Number of b-jets	At least **two** b-jets
5(b)	b-jet (1,2) p_{T} cut	b-jet p_{T} >35 GeV
6	Number of jets	At least **four** jets with p_{T} >20 GeV

Table 4.5: The $t\bar{t}$ and Wt pre-event selection cuts table. The isolation cleaning cut, 4(d), is still applied to reconstructed muons, as the EF_mu40_medium trigger does not apply a muon isolation cut. Cut 6 is **inclusive** of the two b-jets already in the event.

The two highest p_{T} b-jets[3] and the b-jet p_{T} selection cuts reduced the W+jet background. The minimum number of jets in the event worked in conjunction with the muon isolation cuts to suppress the multijet background, where the event contained a fake muon. Furthermore, a minimum of four jets was required to reconstruct the hadronically decaying W, since the two b-jets are neglected when constructing this variable (see section 4.5.3).

4.5.3 W Boson Reconstruction

After the pre-selection cuts, an attempt was made to reconstruct the W bosons in the event. It can be seen in Figure 4.19 that one of the W bosons in the event decayed leptonically and the other hadronically; this meant that the transverse mass, M_T, (Eq.(4.7)) and the dijet invariant mass, M_{jj},

[3] b-jets were tagged using topo-cluster jets and matched to particle flow jets, since no b-tagging information for particle flow jets was available.

(Eq.(4.8)) variables could be used to reconstruct the W bosons in the event.

The transverse mass (M_T) is constructed from the highest p_{T} lepton (the muon) and the $E_{\mathrm{T}}^{\mathrm{miss}}$:

$$M_T = \sqrt{2p_{\mathrm{T}}^{\mathrm{lep}} E_{\mathrm{T}}^{\mathrm{miss}} - 2\vec{p}_{\mathrm{T}}^{\mathrm{lep}} \cdot \vec{E}_{\mathrm{T}}^{\mathrm{miss}}} \tag{4.7}$$

Transverse mass was used to reconstruct the leptonically decaying W boson. The hadronically decaying W boson was reconstructed using the dijet invariant mass of the two highest p_{T} jets that were **not** b-tagged, as the two leading p_{T} b-jets were associated with the top quark decays.

The dijet invariant mass (M_{jj}) is defined as

$$M_{jj} = \sqrt{(E_{j_1} + E_{j_2})^2 - \left|\vec{p}_{j_1} + \vec{p}_{j_2}\right|^2}, \tag{4.8}$$

where j_1 is the leading jet that was not b-tagged and j_2 is the second leading jet that was not b-tagged.

4.5.4 Results

Figure 4.20 shows the M_T distributions of the leptonically decaying W boson using the ATLAS standard event reconstruction and the particle flow event reconstruction. There was a large number of data events at low M_T ($M_T < 40$ GeV), particularly in Figure 4.20a; these events were from W+jet events and events containing fake muons. Unfortunately, W+jet MC samples were not available in these performance studies. The W boson peak at ≈80 GeV was clearly visible in $t\bar{t}$ and Wt MC in both of the event reconstruction algorithms. However, the W boson peak in data was only observed for the particle flow algorithm (Figure 4.20b); this showed that the $E_{\mathrm{T}}^{\mathrm{miss}}$ resolution at low energies was better in particle flow, as the muon energy resolution remained unchanged by the particle flow algorithm.

Figure 4.21 shows the M_{jj} distribution of the hadronically decaying W boson in the ATLAS standard event reconstruction and the particle flow event reconstruction. The underestimation of the MC again originated from W+jet events and events containing fake muons (multijet sources). The W boson peak at ≈80 GeV was visible in data and MC for both of the event reconstruction algorithms. The M_{jj} distributions in this figure show that, for a significant fraction of the selected events, the selected jets were not from the hadronically decaying W boson, i.e., M_{jj} was outside the W boson invariant mass window (60 GeV $< M_{jj} <$ 100 GeV).

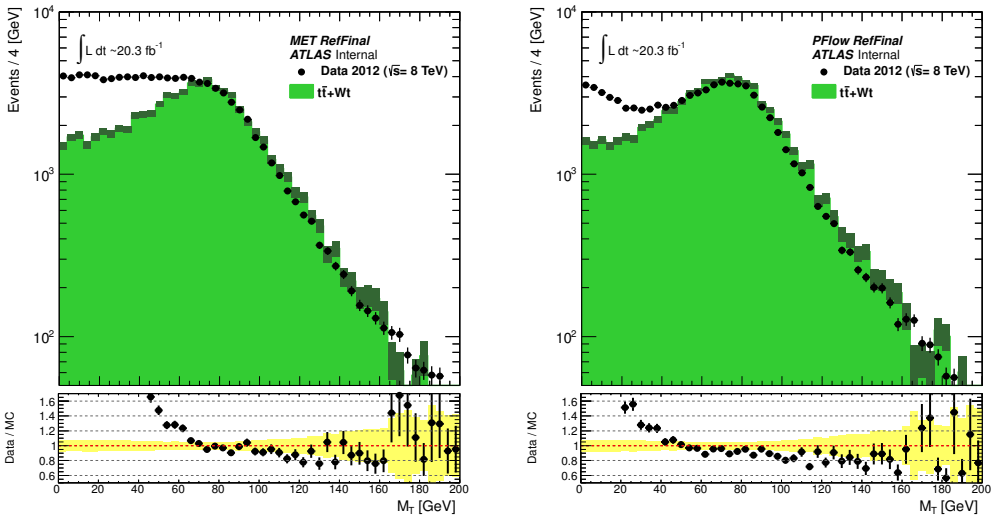

(a) `MET_RefFinal` (b) PFlow `RefFinal`

Figure 4.20: The M_T distribution for the ATLAS 2012 data set in $t\bar{t}$ and Wt events after the pre-event selection. Figure (a) shows the M_T distribution for the ATLAS standard event reconstruction using the `MET_RefFinal` $E_{\mathrm{T}}^{\mathrm{miss}}$ algorithm. Figure (b) shows the M_T distribution for the PFlow event reconstruction using the PFlow `RefFinal` $E_{\mathrm{T}}^{\mathrm{miss}}$ algorithm. Data from the 2012 $\sqrt{s} = 8\,\mathrm{TeV}$ data set is shown in black. Simulated $t\bar{t}$ and Wt events are shown in green, with the dark green band showing the statistical uncertainty on the MC samples.

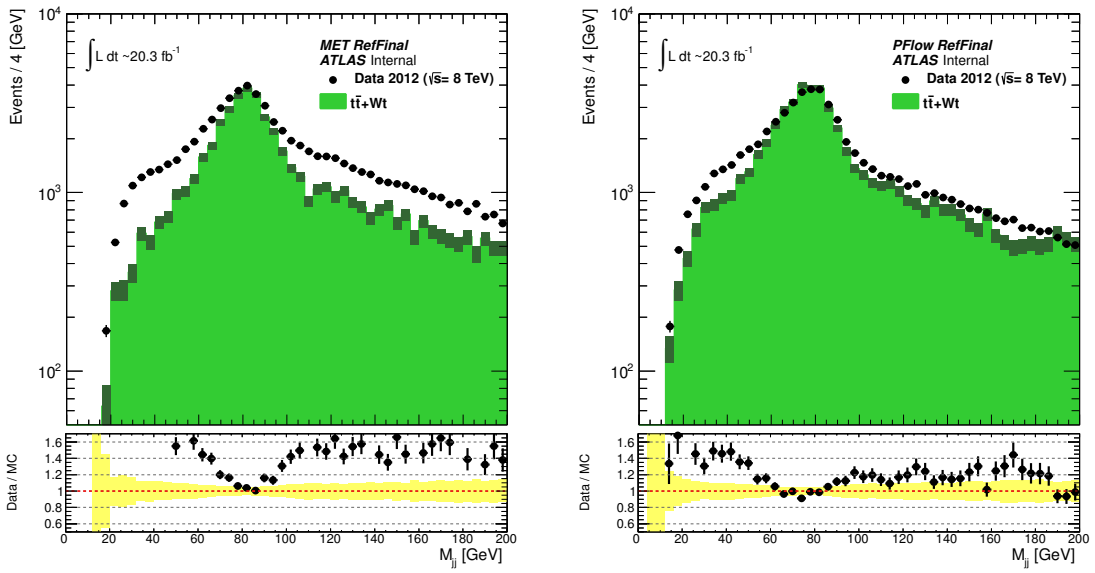

(a) `MET_RefFinal` (b) PFlow `RefFinal`

Figure 4.21: The M_{jj} distribution for the ATLAS 2012 data set in $t\bar{t}$ and Wt events after the pre-event selection. Figure (a) shows the M_{jj} distribution for the ATLAS standard event reconstruction using the `MET_RefFinal` $E_{\mathrm{T}}^{\mathrm{miss}}$ algorithm. Figure (b) shows the M_{jj} distribution for the PFlow event reconstruction using the PFlow `RefFinal` $E_{\mathrm{T}}^{\mathrm{miss}}$ algorithm. Data from the 2012 $\sqrt{s} = 8$ TeV data set is shown in black. Simulated $t\bar{t}$ and Wt events are shown in green, with the dark green band showing the statistical uncertainty on the MC samples.

Since the events contained two W bosons that were independently studied, the event selection for the M_T and M_{jj} distributions could be improved by requiring that the other reconstructed W in the event was within the W boson mass window. For the M_T distribution, this required that the dijet invariant mass of the two leading p_{T} jet was between 60 GeV and 100 GeV (60 GeV $< M_{jj} <$ 100 GeV). The M_{jj} distribution required that the M_T of the event was between 40 GeV and 120 GeV. The larger W boson mass window for M_T in the M_{jj} distribution accounted for M_T using the $E_{\mathrm{T}}^{\mathrm{miss}}$ of the event, which does not contain any information along the z-direction; therefore, the W peak was expected to be broader then the dijet invariant mass peak (compare Figures 4.20 and 4.21).

Figure 4.22 shows the M_T distribution of the leptonically decaying W boson, and Figure 4.23 shows the M_{jj} distribution of the hadronically decaying W. Both distributions are shown for the ATLAS standard event reconstruction and the particle flow event reconstruction. The M_T distribution is shown after the application of the M_{jj} invariant mass cut, and the M_{jj} distribution is shown after the application of the M_T. It can be seen in both figures that the number of background events was reduced significantly with respect to Figures 4.20 and 4.21 and the W boson peaks were more pronounced.

Gaussian fits[4] to Figure 4.22 showed that the mean of the fit to the W boson peak in the particle flow data distribution (Figure 4.22b) was 9 GeV closer to the W boson mass (80.3 GeV) than the `MET_RefFinal` data distribution (Figure 4.22a). The width of the Gaussian fit to the W boson peak in the particle flow data distribution was also 30% narrower than the `MET_RefFinal` data distribution.

The Gaussian fits to Figure 4.23 showed that the mean of the fit to the W boson peak in the particle flow `RefFinal` M_{jj} data distribution (Figure 4.23(b)) was 3 GeV further away from the W boson mass (80.3 GeV) than the `MET_RefFinal` data distribution (Figure 4.23(a)). This is believed to be due to the event pre-selection; since b-tagging information was not available for particle flow jets, particle flow b-jets were flavour tagged by the jet being matched to a LCW topo-cluster b-jet (used by the ATLAS standard event reconstruction and `MET_RefFinal`). Therefore, the jets which made up M_{jj} would be different between `MET_RefFinal` and particle flow `RefFinal`. The width of the Gaussian fit to the W boson peak in the particle flow `RefFinal` M_{jj} data distribution was 14% narrower than the `MET_RefFinal` data distribution. This indicated that the particle flow event reconstruction had a better jet energy resolution; however, this cannot be accurately determined from these distributions, as the M_T distribution was described better by particle flow event reconstruction, so this could have caused the width improvement in M_{jj} after applying the M_T mass cut.

[4] It should be noted that a M_T distribution is actually a Jacobian peak convolved with a Breit-Wigner distribution [134]. The use of a Gaussian function was justified by the proof of principle nature of this study and the complexities involved in fitting the true functional form.

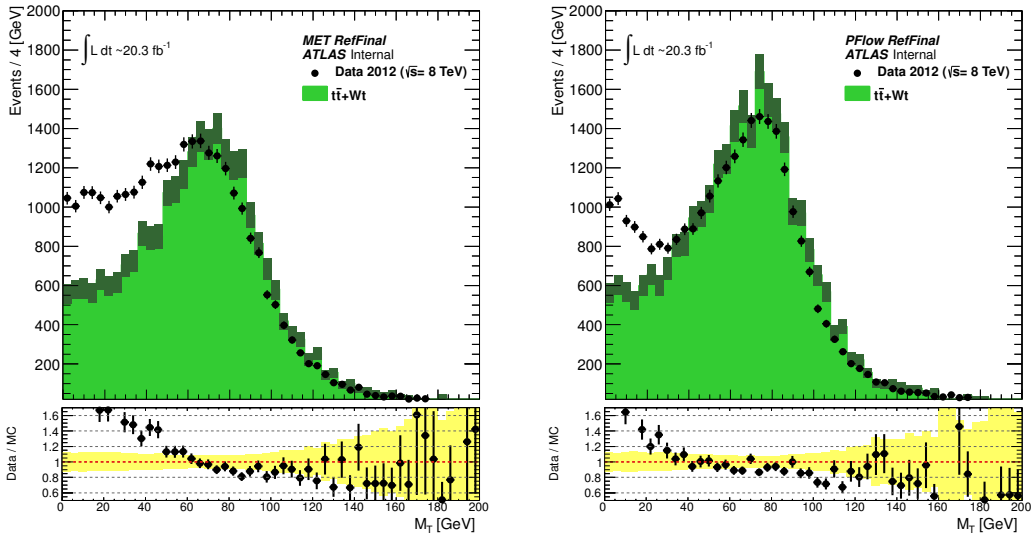

(a) `MET_RefFinal` (b) PFlow `RefFinal`

$E_{\mathrm{T}}^{\mathrm{miss}}$ Algorithm	σ [GeV]	Mean [GeV]	σ/Mean
`Met_RefFinal`	26.82	64.31	0.417
PFlow RefFinal	18.69	73.41	0.255

(c) Gaussian Fitting Results

Figure 4.22: The M_T distribution for the ATLAS 2012 data set in $t\bar{t}$ and Wt events after the pre-event selection with the M_{jj} invariant mass cut applied. Figure (a) shows the M_T distribution for the ATLAS standard reconstruction using the `MET_RefFinal` $E_{\mathrm{T}}^{\mathrm{miss}}$ algorithm. Figure (b) shows the M_T distribution for the PFlow reconstruction using the PFlow `RefFinal` $E_{\mathrm{T}}^{\mathrm{miss}}$ algorithm. Data from the 2012 $\sqrt{s} = 8\,\mathrm{TeV}$ data set is shown in black. Simulated $t\bar{t}$ and Wt events are shown in green, with the dark green band showing the statistical uncertainty on the MC samples. Figure (c) shows the results table for the Gaussian fits to the data distributions of the different $E_{\mathrm{T}}^{\mathrm{miss}}$ algorithms.

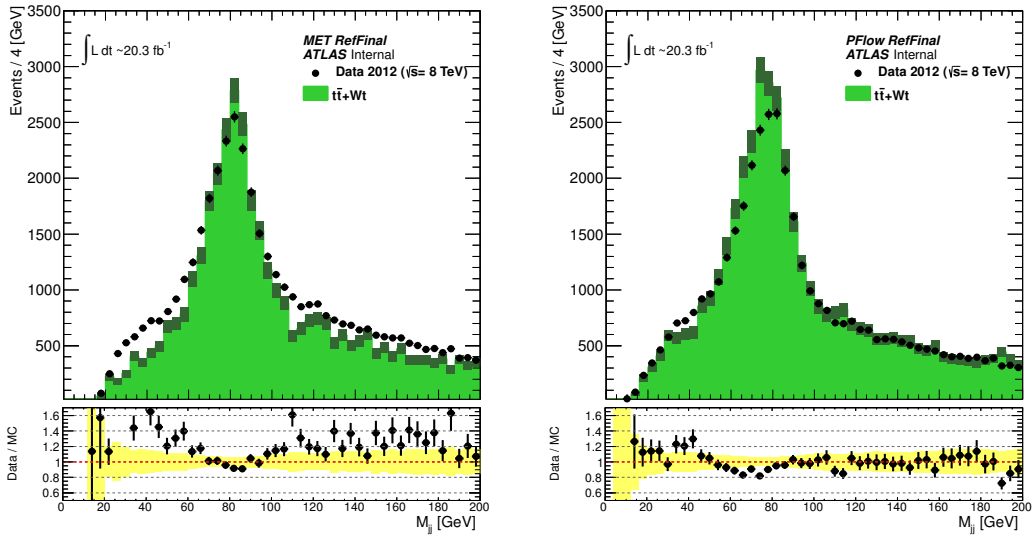

(a) `MET_RefFinal` (b) PFlow `RefFinal`

$E_{\mathrm{T}}^{\mathrm{miss}}$ Algorithm	σ [GeV]	Mean [GeV]	σ/Mean
`Met_RefFinal`	14.26	80.33	0.178
PFlow RefFinal	12.29	77.38	0.159

(c) Gaussian Fitting Results

Figure 4.23: The M_{jj} distribution for the ATLAS 2012 data set in $t\bar{t}$ and Wt events after the pre-event selection with the M_T invariant mass cut applied. Figure (a) shows the M_{jj} distribution for the ATLAS standard reconstruction using the `MET_RefFinal` $E_{\mathrm{T}}^{\mathrm{miss}}$ algorithm. Figure (b) shows the M_{jj} distribution for the PFlow reconstruction using the PFlow `RefFinal` $E_{\mathrm{T}}^{\mathrm{miss}}$ algorithm. Data from the 2012 $\sqrt{s} = 8$ TeV data set is shown in black. Simulated $t\bar{t}$ and Wt events are shown in green, with the dark green band showing the statistical uncertainty on the MC samples. Figure (c) shows the results table for the Gaussian fits to the data distributions of the different $E_{\mathrm{T}}^{\mathrm{miss}}$ algorithms.

4.6 Summary

This chapter documented the ATLAS particle flow reconstruction algorithm and the $E_{\mathrm{T}}^{\mathrm{miss}}$ performance studies performed with the ATLAS 2012 8 TeV data set. The $E_{\mathrm{T}}^{\mathrm{miss}}$ performance studies compared the ATLAS standard $E_{\mathrm{T}}^{\mathrm{miss}}$ definition (`MET_RefFinal`) against two different particle flow reconstruction $E_{\mathrm{T}}^{\mathrm{miss}}$ definitions (`RefFinal` and `Hybrid`). the $E_{\mathrm{T}}^{\mathrm{miss}}$ performance study was performed in $Z \to \mu\mu$, $t\bar{t}$ and Wt events using both ATLAS data and MC simulated samples.

Sections 4.2 and 4.3 presented a brief introduction to particle flow event reconstruction and described the ATLAS particle flow event reconstruction algorithm. More details about the ATLAS particle flow algorithm can be found in references [130] and [135].

Section 4.4 detailed the $E_{\mathrm{T}}^{\mathrm{miss}}$ performance studies in $Z \to \mu\mu$ events using MC simulated samples (section 4.4.3) and the 2012 $\sqrt{s} = 8$ TeV data set (section 4.4.4). It was found in these studies that the particle flow $E_{\mathrm{T}}^{\mathrm{miss}}$ algorithms out-performed `MET_RefFinal` in most aspects, including resolution, scale and pile-up independence. Furthermore, the $E_{\mathrm{T}}^{\mathrm{miss}}$ distribution in $Z \to \mu\mu$ MC events for particle flow $E_{\mathrm{T}}^{\mathrm{miss}}$ algorithms were more truncated than the `MET_RefFinal` algorithm, with a mean 17-23% closer to zero; this showed that the particle flow $E_{\mathrm{T}}^{\mathrm{miss}}$ algorithms had a significantly better $E_{\mathrm{T}}^{\mathrm{miss}}$ performance in $Z \to \mu\mu$ events than the ATLAS standard $E_{\mathrm{T}}^{\mathrm{miss}}$ algorithm. The tail region of the $Z \to \mu\mu$ $E_{\mathrm{T}}^{\mathrm{miss}}$ distribution also showed that particle flow $E_{\mathrm{T}}^{\mathrm{miss}}$ algorithm was more sensitive to $t\bar{t}$ events (see Tables 4.2, 4.3 and 4.4).

Section 4.5 detailed the $E_{\mathrm{T}}^{\mathrm{miss}}$ performance and W boson reconstruction studies of the particle flow event reconstruction algorithm in $t\bar{t}$ and Wt events. The study found that the particle flow algorithm described the expected M_T distribution of $t\bar{t}$ and Wt events better than `MET_RefFinal`, with the mean of the W boson peak in the data M_T distribution 9 GeV closer to the W boson mass and the width 30% narrower. This is evidence for particle flow event reconstruction having a better $E_{\mathrm{T}}^{\mathrm{miss}}$ performance in $t\bar{t}$ and Wt events. The M_{jj} distribution showed that the particle flow algorithm may have a better jet energy resolution, with a width of the W boson peak 14% narrower than the ATLAS standard event reconstruction. Although the improvement in the jet energy resolution cannot be demonstrated directly in this analysis, it has been confirmed by previous studies of the algorithm [74].

Chapter 5

Introduction to the Jet Smearing Method

5.1 Introduction

The jet smearing method is a data-driven method designed to estimate the multijet background in kinematic regions where MC suffers from low statistics. The method involves two main aspects: selecting well-measured events from data and measuring the ATLAS jet response. This chapter focuses on the methods used for selecting well-measured events from data and also provides an introduction to the jet smearing method. The introduction details the motivations and assumptions behind the method, and gives a basic overview of how the method was performed.

It should be noted that the jet smearing method has been documented many times in the past (see references [135, 136, 137]), but this thesis will only document how the jet smearing analysis was performed on the full ATLAS 2011 7 TeV data set [2] and the full ATLAS 2012 8 TeV data set [1]. Both of these analyses were performed by the author.

Section 5.2 introduces the reconstructed jet p_{T} response, which was measured as part of the jet smearing method. Section 5.3 provides an overview of the jet smearing method, and the key motivations and assumptions behind the method. Finally, section 5.4 documents the '*seed*' event selection process, which selects low-$E_{\mathrm{T}}^{\mathrm{miss}}$ seed events to be used in the '*smearing*' process.

5.2 Jet Response

Since no particle detector is capable of reconstructing a physics object perfectly, every quantity of a reconstructed object has some form of resolution or response distribution. The jet p_{T} response (R) is of particular interest. The jet p_{T} response is defined by

$$R = \frac{p_{\mathrm{T}}^{\mathrm{reco}}}{p_{\mathrm{T}}^{\mathrm{truth}}}. \tag{5.1}$$

Here, $p_{\mathrm{T}}^{\mathrm{reco}}$ is the reconstructed p_{T} of the jet and $p_{\mathrm{T}}^{\mathrm{truth}}$ is the truth p_{T} of the jet, using the truth information about the jet contained within the MC simulation.

The jet p_{T} response can be very broad due to the numerous sources of jet p_{T} fluctuation, such as:

- An imperfect calorimeter – the calorimeters of a particle detector are never perfect at measuring the energy deposited by particles, and have a broad energy resolution. A jet can consist of many particles; therefore, it is possible for energy fluctuations to compound producing a large p_{T} fluctuation in the reconstructed jet.

- Dead material – there may be significant amounts of dead material before the calorimeters; this can include the service systems and support structure of the detector, or even damaged regions of the detector. If particles travel through the dead material, they may interact with it causing an energy loss that is not recorded by the calorimeters.

- Non-fully contained jets – jets may not be fully contained within the calorimeters of the detector, particularly if they are very energetic. If a jet punches-through into the muon systems, then a fraction of the jet energy will not be recorded by the calorimeters.

- Out-of-cone effects – a jet can have a very broad lateral shower profile; consequently, some constituent particles of the jet may lie outside the jet reconstruction cone. Therefore, the energy of these particles would not be included in the jet.

- Heavy flavour decays – heavy flavour jets (b-quark jets) can contain neutrinos, which will escape detection. The neutrinos will carry a fraction of the jet energy with them. This is particularly important when measuring the b-jet p_{T} response.

The jet p_{T} response is very complex and dependent on the kinematics of the jet. Clearly, the amount of 'punch-through' into the muon systems depends on the energy of the jet, but also the $|\eta|$ location of the jet. As Chapter 3 details, the ATLAS detector has different technologies in different $|\eta|$ regions of the detector; therefore, the jet p_{T} response for a jet in the central region (low $|\eta|$) may not be the same as the forward region (high $|\eta|$), as these detector regions have different calorimeter systems.

5.3 Overview

The '*jet smearing method*' is a data-driven method for estimating backgrounds in event topologies where the $E_{\mathrm{T}}^{\mathrm{miss}}$ mainly originates from jet mismeasurement. The jet smearing method is primarily

used to estimate multijet backgrounds in SUSY searches, but has also been applied to Z+jet background [7, 138]. Only the multijet background version of this technique will be documented in this thesis.

The original development of the method using Monte Carlo (MC) data is described in [74], and was applied to high $E_{\mathrm{T}}^{\mathrm{miss}}$ topologies. Since then, the method has been documented many times as it is continuously evolving (see references [135, 136, 137] for detailed descriptions of previous versions of the method). This thesis will only document the jet smearing method performed on the ATLAS 2011 7 TeV full data set, which was used in [2, 139], and the ATLAS 2012 8 TeV full data set, which was used in [1, 125].

5.3.1 Motivation

There were two main reasons why a data-driven approach was preferred to Monte Carlo simulation. Firstly, due to the low acceptance of multijet events in SUSY Signal Regions (SRs), it was impossible to generate MC samples that provided sufficient statistics in the SUSY SRs. This led to large statistical uncertainties on the multijet background estimation. Secondly, Monte Carlo simulated events were not expected to fully reproduce the non-Gaussian detector effects of measuring jets in data. Therefore, the systematics involved in modelling the calorimeter could be large.

The first problem is a consequence of the large production cross-section of multijet events at the LHC, which requires strong production SUSY analyses to actively reject multijet events with specialised selection cuts (see section 7.2): this reduces the small fraction of multijet events that pass the Signal Region $E_{\mathrm{T}}^{\mathrm{miss}}$ requirement even further.

The second problem is the imperfections in the full detector simulation of the ATLAS calorimeters. The calorimeter shower simulations are one of the most time consuming parts of simulating MC events; however, the simulation is still not perfect. It is difficult to accurately generate high jet multiplicity multijet events. The non-Gaussian detector effects are often mis-modelled by the detector simulation, causing simulated events to model multijet data events poorly.

The jet smearing method solves these problems by creating a very large sample of '*pseudo-data*' from well-measured '*seed*' events (see section 5.4) and correcting the MC jet response to data in two specialised analyses (see sections 6.3 and 6.5).

5.3.2 Jet Smearing

A '*smeared*' event was generated by multiplying each of the jet four-vectors in a 'seed' event by a random number drawn from a jet response function of the appropriate truth jet p_{T}. The reconstructed p_{T} of jets within the seed events can be used as, by construction, the jets within the seed events are well-measured, and their measured p_{T} is therefore approximately equal to their truth p_{T}. The seed events that were used in the jet smearing analysis were taken from data.

The $\vec{E}_{\mathrm{T}}^{\mathrm{miss}}$ of a smeared event ($\vec{\not{E}}_{\mathrm{T}}{}'$) is given by

$$\vec{\not{E}}_{\mathrm{T}}{}' = \vec{\not{E}}_{\mathrm{T}}^{\mathrm{seed}} - \sum_i \vec{p}_{\mathrm{T}}{}'(j_i) + \sum_i \vec{p}_{\mathrm{T}}(j_i). \tag{5.2}$$

Here, primes are used to distinguish between the smeared and unsmeared quantities.

The jet smearing method was performed in the following steps:

(1) As a starting point for defining the jet response functions, the jet response functions were measured in MC simulated data by comparing the generator truth level jet p_{T} to the reconstructed jet p_{T} (see section 6.2).

(2) Low-$E_{\mathrm{T}}^{\mathrm{miss}}$ seed events were selected from data; these were then used in steps (3) and (4) (see section 5.4).

(3) The initial MC jet response functions from (1) were then modified, until smearing of seed events generated pseudo-data that agreed with data in special control regions sensitive to the jet response (see sections 6.3 and 6.5).

(4) Seed events were smeared using the data-constrained jet response functions from (3) to obtain the multijet distributions of key variables in the Control and Signal Regions in SUSY analyses (see Chapter 7).

Figure 5.1 shows a cartoon schematic of the jet smearing method. The figure shows an example seed event being smeared twice to produce two different pseudo-data events, though in practice seed events are smeared several thousands of times to generate the pseudo-data sample.

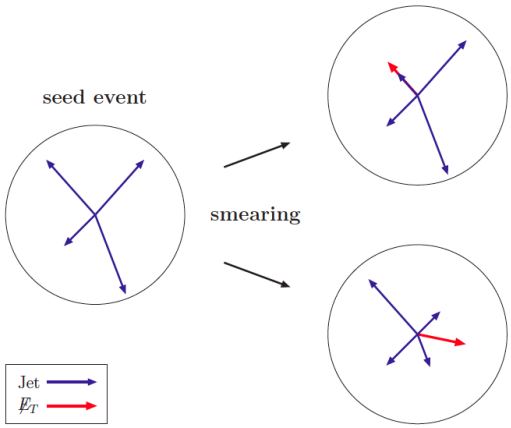

Figure 5.1: A schematic showing the jet smearing process. The schematic shows how one low-$E_{\mathrm{T}}^{\mathrm{miss}}$ seed event is '*smeared*' many times to produce a large number of pseudo-data smeared events with higher amounts of $E_{\mathrm{T}}^{\mathrm{miss}}$. This figure was taken from [135].

5.3.3 Key Assumptions of the Method

The jet smearing technique relies on the following basic assumptions:

(1) The jet responses measured from fluctuating jets in the special control regions can justifiably be applied to jets within the seed events in the main analysis.

(2) Any dependence of jet response on event-wide properties, such as jet multiplicity or the fluctuations of other jets in the event, can be neglected. In other words, jet smearing can justifiably be applied on a jet-by-jet basis.

The main justification for the assumptions above is that the technique has been shown to successfully reproduce the distributions of data in special control regions (see sections 6.3 and 6.5) and the Control and Validation Region distributions of ATLAS SUSY analyses [1, 2, 125, 139] (see sections 7.3.4 and 7.4.4). Futhermore, many validation studies have been performed to validate different aspects of the method (see section 6.7).

5.4 Seed Selection

When selecting prospective seed events, it is essential that the jets in the event are 'well-measured', i.e., their reconstructed jet p_{T} is as close as possible to their truth jet p_{T}. This was achieved by minimising the amount of $E_{\mathrm{T}}^{\mathrm{miss}}$ in the event, which in turn ensures that any double counting of $E_{\mathrm{T}}^{\mathrm{miss}}$ caused by jet p_{T} fluctuations in the seed event is minimal.

A direct cut on $E_{\mathrm{T}}^{\mathrm{miss}}$ could be used to ensure that the jets in the event are well-measured; however, since the $E_{\mathrm{T}}^{\mathrm{miss}}$ resolution varies with the scalar sum of the event energy (ΣE_{T}), this biases the average leading jet p_{T} of the seed events to lower p_{T} [74, 136, 135] (see Figures 5.3(a) and 5.4(a)). The bias happens because events with very high p_{T} jets (high ΣE_{T}) are more likely to contain higher amounts of $E_{\mathrm{T}}^{\mathrm{miss}}$. Therefore, high ΣE_{T} events are less likely to pass the $E_{\mathrm{T}}^{\mathrm{miss}}$ seed selection cut, creating the bias to lower average jet p_{T} in the leading jet p_{T} distributions.

To avoid this problem, a $E_{\mathrm{T}}^{\mathrm{miss}}$-significance ($S$) seed selection cut (Eq.(5.3)) was used [2], since this quantity is found to have litle ΣE_{T} dependence. Figure 5.2 shows the $E_{\mathrm{T}}^{\mathrm{miss}}$-significance distributions for the full 2011 7 TeV (a) and 2012 8 TeV (b) data sets.

$$S = \frac{E_{\mathrm{T}}^{\mathrm{miss}}}{\sqrt{\sum E_{\mathrm{T}}}} \tag{5.3}$$

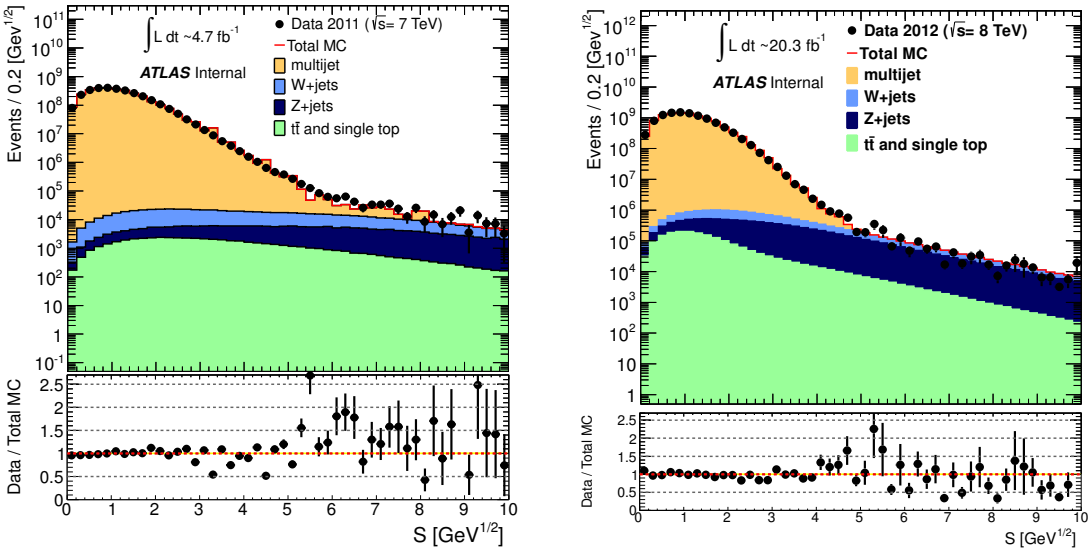

(a) 2011 $\sqrt{s} = 7$ TeV data set

(b) 2012 $\sqrt{s} = 8$ TeV data set

Figure 5.2: The $E_{\mathrm{T}}^{\mathrm{miss}}$-significance (S) distributions for the full 2011 $\sqrt{s} = 7$ TeV and 2012 $\sqrt{s} = 8$ TeV data sets.

The seed selection process was slightly different for the 2011 and 2012 data set analyses; therefore, it will be described independently in the following sections.

5.4.1 Seed Selection in the 2011 Analysis

In the 2011 analysis, seed events had to first pass one of the 2011 single-jet trigger chains (see Table 5.1). The single-jet trigger chains covered a p_{T} range of 70 – 7000 GeV and were all prescaled, except for the EF_j240_a4tc_EFFS trigger and the EF_j180_a4_EFFS trigger (see section 3.3.8 for jet triggers). The prescales were calculated per data period, as the LHC run conditions changed between data taking periods. After Period B of the 2011 data period, the single-jet trigger chains changed to the anti-k_{T} topo-cluster (a4tc) algorithm.

Jet p_{T} Range [GeV]	L1 Seed Trigger	L2 Trigger	Data Period	HL Trigger
50 – 100	L1_J10	L2_j35	B	EF_j30_a4_EFFS
			D – M	EF_j30_a4tc_EFFS
100 – 130	L1_J30	L2_j45	B	EF_j55_a4_EFFS
			D – M	EF_j55_a4tc_EFFS
130 – 160	L1_J55	L2_j70	B	EF_j75_a4_EFFS
			D – M	EF_j75_a4tc_EFFS
160 – 200	L1_J75	L2_j95	B	EF_j100_a4_EFFS
			D – M	EF_j100_a4tc_EFFS
200 – 260	L1_J75	L2_j95	B	EF_j135_a4_EFFS
			D – M	EF_j135_a4tc_EFFS
260 – 7000	L1_J75	L2_j95	B	EF_j180_a4_EFFS
260 – 335			D – M	EF_j180_a4tc_EFFS
N/A	L1_J75	L2_j95	B	N/A
335 – 7000			D – M	EF_j240_a4tc_EFFS

Table 5.1: The 2011 single-jet trigger chains used to collect multijet seed events [140]. The abbreviation 'a4' in the trigger name denotes that the anti-k$_t$ jet reconstruction algorithm was used, 'tc' corresponds to topo-cluster and 'EFFS' denotes that the event filter performed a full scan for jets in the event.

If events passed one of the single-jet trigger chains, they then had to pass the $E_{\mathrm{T}}^{\mathrm{miss}}$-significance seed selection cut ($S < 0.6\ \sqrt{\mathrm{GeV}}$). If events passed the seed selection cut, then they were then used as seed events to generate pseudo-data in the jet smearing method.

The leading jet p_{T} distributions after the seed selection cuts are shown in Figure 5.3. The bias in the leading jet p_{T} of the pseudo-data distributions (discussed in section 5.4) is clearly visible in Figure 5.3(a). There was still a small bias in the leading jet p_{T} when using the $E_{\mathrm{T}}^{\mathrm{miss}}$-significance seed selection cut (Figure 5.3(b)); however, this bias was covered by the mean-shift systematic in the 2011 analysis (see section 6.6.3).

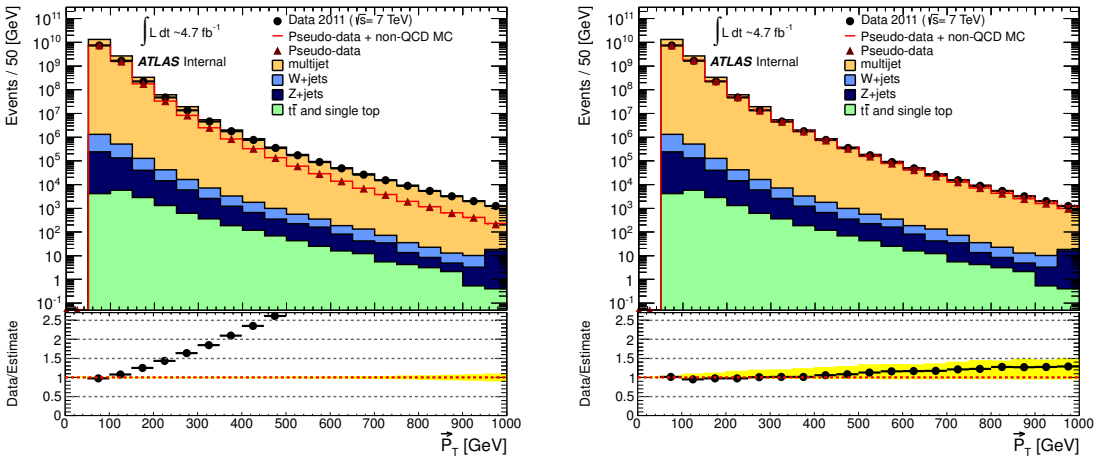

(a) Seed Selection using $E_{\mathrm{T}}^{\mathrm{miss}} < 20\,\mathrm{GeV}$

(b) Seed Selection using $S < 0.6\ \sqrt{\mathrm{GeV}}$

Figure 5.3: The leading jet p_{T} distributions after the seed selection cuts for $E_{\mathrm{T}}^{\mathrm{miss}} < 20\,\mathrm{GeV}$ (a), and $E_{\mathrm{T}}^{\mathrm{miss}}$-significance $S < 0.6\ \sqrt{\mathrm{GeV}}$ (b). The 2011 data set is shown in black, whereas the sum of the pseudo-data and non-multijet MC is shown in red. The yellow uncertainty band in figure (b) includes the mean-shift uncertainty (see section 6.6.3).

5.4.2 Seed Selection in the 2012 Analysis

In the 2012 analysis, seed events had to pass one of the 2012 single-jet trigger chains (see Table 5.2). The single-jet trigger chains in the 2012 analysis covered a p_{T} range of 90 – 8000 GeV and were all prescaled, except for the EF_j460_a4tchad trigger. The prescales were calculated per data period, as in the 2011 analysis, to reflect the change in run conditions from one data taking period to the next.

Jet p_{T} Range [GeV]	L1 Seed Trigger	L2 Trigger	HL Trigger
90 – 130	L1_J15	L2_j50	EF_j55_a4tchad
130 – 160	L1_J30	L2_j65	EF_j80_a4tchad
160 – 230	L1_J50	L2_j105	EF_j110_a4tchad
230 – 270	L1_J75	L2_j165	EF_j180_a4tchad
270 – 330	L1_J75	L2_j165	EF_j220_a4tchad
330 – 410	L1_J75	L2_j165	EF_j280_a4tchad
410 – 510	L1_J75	L2_j165	EF_j360_a4tchad
510 – 8000	L1_J75	L2_j165	EF_j460_a4tchad

Table 5.2: The 2012 single-jet trigger chains used to select multijet seed events [140]. The abbreviation of 'a4' in the trigger name denotes that the anti-k$_t$ was used to reconstruct the jet object, 'tc' corresponds to topo-cluster and 'had' denotes that the jet energy was at the hadronic (LC) calibration scale (not EM).

If events passed one of the 2012 single-jet trigger chains, they then had to pass the $E_{\mathrm{T}}^{\mathrm{miss}}$-significance

seed selection cut. However, since b-jets and light jets were differentiated from each other in the 2012 analysis (b-tag/b-veto), it was important to keep the fraction of b-jets before and after the seed selection cut constant. To ensure that the $E_{\mathrm{T}}^{\mathrm{miss}}$-significance cut was unbiased to prospective seed events irrespective of the number of b-jets in the event[1], an additional 0.02 $\sqrt{\mathrm{GeV}}$ was added to the base value of the $E_{\mathrm{T}}^{\mathrm{miss}}$-significance cut per tagged b-jet [125]. The value, added to the seed selection cut per b-jet, was determined by measuring the shift of the average $E_{\mathrm{T}}^{\mathrm{miss}}$-significance distribution in data events for events containing *one* tagged b-jet with respect to data events containing *no* tagged b-jets [125]. The seed selection cut used in the 2012 analysis is shown in Eq.(5.4).

$$S < 0.70 + 0.02 \times N_{b\text{-jet}} \sqrt{\mathrm{GeV}}. \tag{5.4}$$

$N_{b\text{-jet}}$ is the number of tagged b-jets in the event. The base value of the seed selection cut (0.70) was increased from the value in the 2011 analysis (0.6) to acquire more seed events.

The leading jet p_{T} distributions after the seed selection cuts are shown in Figure 5.4. The leading jet p_{T} distribution of the pseudo-data after the $E_{\mathrm{T}}^{\mathrm{miss}}$-significance cut agrees with data better than in the 2011 analysis. This may be due to the modified seed selection cut or the improved $E_{\mathrm{T}}^{\mathrm{miss}}$ algorithm (`MET_RefFinal`) used in the 2012 analysis.

5.5 Summary

This chapter provided an introduction to the jet smearing method. It detailed the motivations and assumptions behind the method, and gave a basic overview of how the method was implemented in the 2011 $\sqrt{s} = 7\,\mathrm{TeV}$ and 2012 $\sqrt{s} = 8\,\mathrm{TeV}$ data set analyses.

Section 5.2 introduced the jet p_{T} response. Section 5.3 gave a general overview of the jet smearing method. Section 5.4 documented the '*seed*' event selection process in the 2011 and 2012 data set analyses. It showed that the leading jet p_{T} distributions of seed events was biased if a direct cut on $E_{\mathrm{T}}^{\mathrm{miss}}$ was used. Therefore, a cut on $E_{\mathrm{T}}^{\mathrm{miss}}$-significance ($S$) was used instead to select well-measured seed events. In the 2012 analysis, it was also important to maintain the fraction of b-jets before and after the seed selection cut, and consequently the seed selection cut was modified to account for the number of b-jets in the event.

[1] b-jets are expected to contain on average more $E_{\mathrm{T}}^{\mathrm{miss}}$ than light jets due to the emissions of neutrinos and other leptons (BR $10.99 \pm 0.28\%$ [15]) during the decay of B-mesons within the jet.

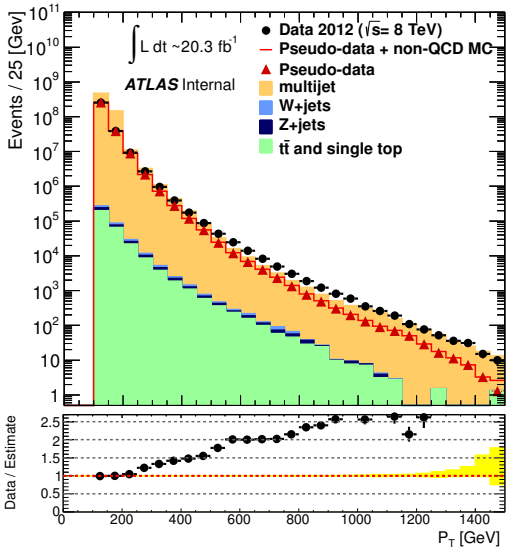

(a) Leading jet p_{T} of seed events using the seed selection cut $E_{\mathrm{T}}^{\mathrm{miss}} < 20$ GeV

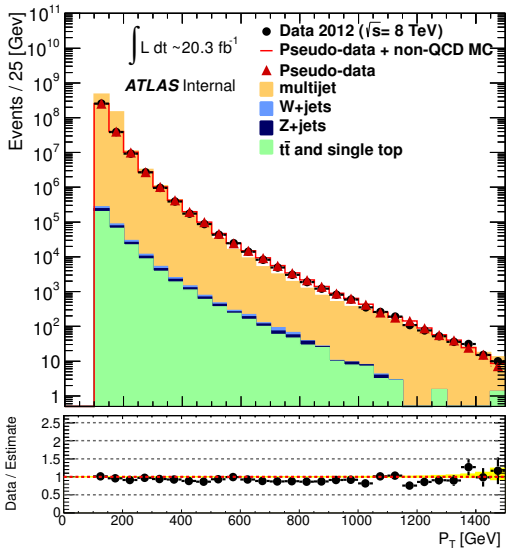

(b) Leading jet p_{T} of seed events using the seed selection cut $\mathrm{S} < 0.70 + 0.02 \times N_{b\text{-jet}} \sqrt{\mathrm{GeV}}$

Figure 5.4: The leading jet p_{T} distributions after the seed selection cuts for $E_{\mathrm{T}}^{\mathrm{miss}} < 20$ GeV (a), and $E_{\mathrm{T}}^{\mathrm{miss}}$-significance $S < 0.7 + 0.02 \times N_{b\text{-jet}} \sqrt{\mathrm{GeV}}$ (b). The data is shown in black, whereas the sum of the pseudo-data and non-multijet MC is shown in red.

Chapter 6

Measuring the Jet Response

6.1 Introduction

This chapter documents how the ATLAS jet response was measured in the 2011 $\sqrt{s} = 7\,\text{TeV}$ and 2012 $\sqrt{s} = 8\,\text{TeV}$ dat set analyses. Measuring the ATLAS jet response is one of the quintessential components of the jet smearing method, and it is used during the smearing of jets in seed events. The jet response is measured using multijet MC samples as a starting point, and then constrained to data in three dedicated analyses.

Section 6.2 describes how the initial MC jet response was measured. Since pseudo-data generated with the MC jet response did not sufficiently reproduce the recorded data, three analyses were used to constrain the jet response to data. The dijet p_{T} balance analysis was used to constrain the Gaussian core of the jet response, and is documented in section 6.3. The Mercedes analysis was used to constrain the non-Gaussian tail of the jet response, and is documented in section 6.5. The dijet $\Delta\phi$ analysis was used to find ϕ angular corrections to smeared jets, and is documented in section 6.4.

The uncertainties of the jet smearing method are documented in section 6.6; this includes the statistical uncertainties on smeared quantities and the systematic uncertainties on constraining the shape of the jet response function to data.

Finally, various investigative studies were used to validate the jet smearing method, which are documented in section 6.7.

6.2 MC Jet Response

A '*jet response map*' refers to the collection of jet response functions (defined in Eq.(5.1)) that are used in the jet four-vector smearing process. Since the jet response function is expected to change

over truth jet p_{T}, the jet response was binned in truth jet p_{T}. Each jet response function covered a different range of truth jet p_{T} and was only applied to reconstructed 'seed' jets of that p_{T} range. The jet response maps were binned in histogram bins of $p_{\mathrm{T}}^{\mathrm{truth}} = 20\,\mathrm{GeV}$. If the jet response functions are normalised, then in basic terms, they are probability density functions. They model the probability distribution of the ATLAS detector reconstructing a jet with a reconstructed jet p_{T}, x, given an initial truth jet p_{T}, y.

Since it is known that the multijet Monte Carlo effectively models the reconstruction of jets in data (at LO) [104], it was used as a starting point for measuring the jet response functions. `PYTHIA` multijet MC samples were used to generate the initial MC jet response functions (see sections 3.4.3 and 3.4.4).

In the 2011 analysis, only an inclusive light and heavy flavour jet response was measured. However, it is expected that the jet response for light jets will be significantly different from that of heavy flavour jets (b-jets); therefore, in the 2012 analysis two separate jet responses were measured, one for light jets (b-veto) and another for b-jets (b-tag) (section 3.6.2 discusses b-flavour tagging of jets). The b-tag jet response described the jet p_{T} response of b-jets much more accurately than the inclusive response, and was one of the main innovations of the 2012 analysis.

6.2.1 Generation of the MC Jet Response

The following method was used to measure the initial MC jet response functions in the 2011 $\sqrt{s} = 7\,\mathrm{TeV}$ and 2012 $\sqrt{s} = 8\,\mathrm{TeV}$ analyses [136, 139, 125]:

(1) Events were taken from the `PYTHIA` multijet MC samples.

(2) The standard SUSY group Release 17 (R17) object definitions (see section 3.6) and overlap removal process (see section 3.6.7) were applied to the selected events.

(3) MC event and jet cleaning cuts were then applied to the selected events.

(4) The jet response function (R) was measured for any reconstructed (reco) jet with the criteria that the jet was isolated from all other reconstructed jets, $\Delta R > 0.1$, and was matched to *only* one truth jet within $\Delta R < 0.1$.

(5) If there were any final state truth neutrinos, muons or electrons within the ΔR jet cone of the truth jet, their four-momenta were added to the four-momentum of the truth jet. This ensured

that the jet response function accounted for genuine sources of $E_{\mathrm{T}}^{\mathrm{miss}}$ produced from heavy flavour decays (important for b-jets).

(6) If there were any *baseline* (see section 3.6) reconstructed muons or electrons within the ΔR cone of the reconstructed jet (before overlap removal), their four-momenta were added to that of the reconstructed jet[1]; this ensured the reconstructed jet p_{T} was as close as possible to the truth level.

(7) The jet response was finally measured for each pair of matched reconstructed and truth jets, and then added to the appropriate jet response function in the jet response map.

6.2.2 2011 MC Response Maps

The initial MC inclusive jet response map used in the 2011 analysis is shown in Figure 6.1. Two truth jet p_{T} projections from this jet response map are shown in Figure 6.2. It can be seen that the 100 GeV truth jet projection (a) has a jet response wider than the 400 GeV projection (b). This is expected, as the jet energy resolution improves with jet energy; therefore, higher p_{T} jets are expected to have a narrower jet response.

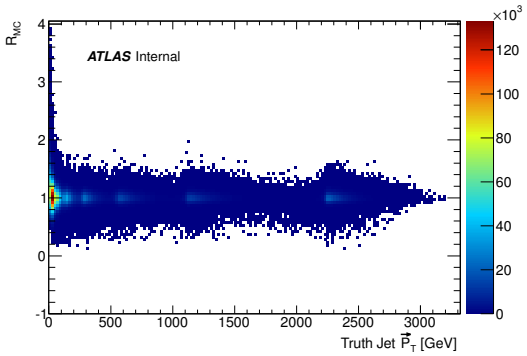

Figure 6.1: The initial Monte Carlo inclusive jet response map used in the 2011 $\sqrt{s} = 7$ TeV data set analysis made from the procedure described in section 6.2. The bumps at 200, 500, 1000 and 2000 GeV are caused by transistions between the multijet MC samples since each sample only generates events for a certain p_{T} range.

6.2.3 2012 MC Response Maps

As mentioned in section 6.2, the 2012 analysis replaced the inclusive jet response map with the b-veto and b-tag jet response maps. Figure 6.3 shows the initial MC b-tag and b-veto jet response

[1] In future, the four-momenta of reconstructed electrons will not be added to the reconstructed jet. This is because the calorimeter deposits from these electrons may already be accounted for in the four-momentum of the reconstructed jet.

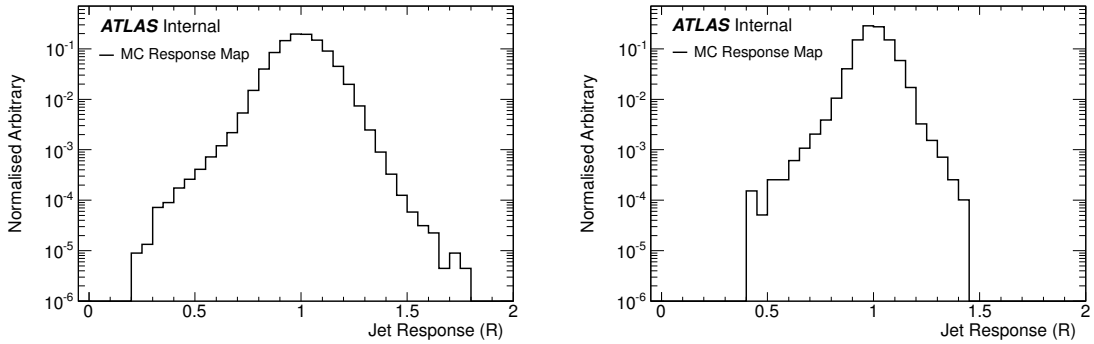

(a) Truth jet p_{T} range of 100 – 120 GeV

(b) Truth jet p_{T} range of 400 – 420 GeV

Figure 6.2: Truth jet p_{T} projections of the 2011 MC jet response map. Figure (a) shows the jet response function for jets in the 100-120 GeV truth jet p_{T} region, figure (b) the jet response function for jets in the 400-420 GeV truth jet p_{T} region.

maps used in the 2012 analysis. The 200-220 GeV truth jet p_{T} projection from the MC b-tag and b-veto jet response maps is shown in Figure 6.4. Figure 6.4 shows that the low-side tail ($0 < R < 0.8$) of the b-tag projection (b) is much larger than the b-veto projection (a). This is expected, as b-jets will contain genuine sources of $E_{\mathrm{T}}^{\mathrm{miss}}$ from neutrinos, which will not be reconstructed in the b-jet. Therefore, the proportion of jets which have a reconstructed jet p_{T} lower than the truth jet p_{T} is expected to be significantly higher for b-jets than light jets (b-veto).

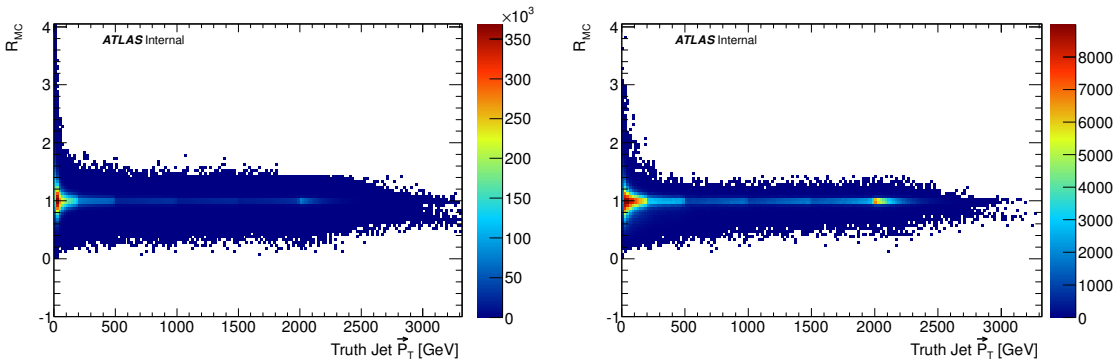

(a) b-veto MC jet response map

(b) b-tag MC jet response map

Figure 6.3: The initial b-tag and b-veto Monte Carlo jet response maps used in the 2012 $\sqrt{s} = 8$ TeV data set analysis made from the procedure described in section 6.2. Figure (a) shows the jet response map for b-veto jets, and figure (b) shows the jet response map for b-tagged jets.

6.2.4 Modifying the MC Jet Response

If the agreement between the pseudo-data and data in multijet distributions was not good, the initial MC jet response was modified in the following ways:

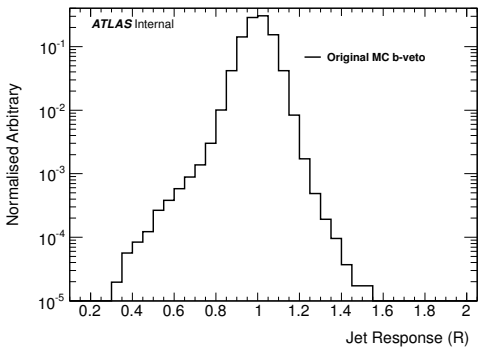

(a) b-veto MC jet response for truth jet p_{T} range of 200-220 GeV

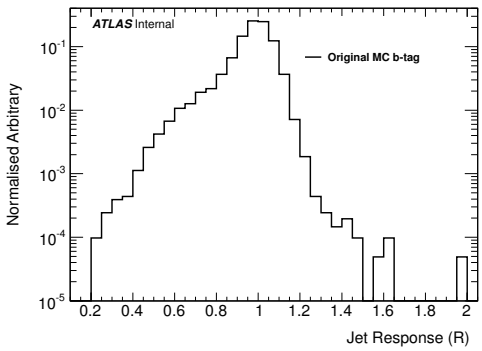

(b) b-tag MC jet response for truth jet p_{T} range of 200-220 GeV

Figure 6.4: Truth jet p_{T} projections of the 2012 MC jet response maps. Figure (a) shows the jet response function for b-veto jets in the 200-220 GeV truth jet p_{T} region, figure (b) shows the jet response function for b-veto jets in the same truth jet p_{T} region.

(1) Additional Gaussian smearing was used to widen the Gaussian core ($0.8 < R < 1.2$) of the jet response. The Gaussian core of the MC jet response can often be too narrow, since it does not account for the full detector effects and pile-up present in the data [136, 139, 125]. Therefore, an additional p_{T}-dependent Gaussian smearing was introduced into the four-vector jet smearing process. This was achieved by multiplying the random four-vector smearing value (drawn from the jet response function) by another random number drawn from a Gaussian distribution, with a mean of one and width of $\sigma_{cor}(p_{\mathrm{T}})$ (found from the dijet p_{T} balance analysis). The full details of the additional Gaussian smearing are documented in section 6.3.

(2) Low-side tail modification. The low-side tail of the jet response models the non-Gaussian fluctuations of jets. The non-Gaussian part of the jet response reproduces the large p_{T} fluctuations of jets in data. This is important for the multijet Control Regions of SUSY analyses (see Chapter 7), since they require significant amount of $E_{\mathrm{T}}^{\mathrm{miss}}$. Consequently, at least one jet must have undergone a sizable p_{T} fluctuation to pass the $E_{\mathrm{T}}^{\mathrm{miss}}$ selection requirement. The '*Mercedes*' analysis describes how the low-side tail of the jet response was modified if the pseudo-data did not agree with data, and is documented in section 6.5.

(3) In the 2012 analysis, additional Gaussian ϕ angular smearing. This was applied to smeared jets to widen the ϕ angular distribution if the ϕ angular distributions were too narrow (for example, see Figure 7.5), and additional ϕ angular smearing was required for the pseudo-data to reproduce the ϕ angular distributions in data (see Figure 7.9). Hence, p_{T}-dependent ϕ angular smearing was applied to smeared jets by drawing a random number from a Gaussian distribution, with a mean of zero and width of $\sigma_{\phi}(p_{\mathrm{T}})$ (found in the dijet $\Delta\phi$ analysis). This number was then added to the ϕ angle of the smeared jet. Full details of the additional ϕ-

smearing can be found in section 6.4.

6.3 Dijet p_{T} Balance Analysis

The dijet p_{T} balance analysis was used to constrain the 'Gaussian core' of the jet response. The analysis compares the p_{T} asymmetry of dijet events in data to pseudo-data generated with the initial MC jet response.

The p_{T} asymmetry of dijet events is given by

$$A(p_{\mathrm{T}j_1}, p_{\mathrm{T}j_2}) = \frac{p_{\mathrm{T}j_1} - p_{\mathrm{T}j_2}}{p_{\mathrm{T}j_1} + p_{\mathrm{T}j_2}}. \tag{6.1}$$

The indices correspond to the p_{T} ordering of the jets, with 1 being the leading jet.

The p_{T} asymmetry was measured against average dijet p_{T} ($\langle p_{\mathrm{T}j_1}, p_{\mathrm{T}j_2} \rangle$) (see Figures 6.5 and 6.7). The analysis used average dijet p_{T} bins of 50 GeV, and a Gaussian function was fitted to each asymmetry distribution. The Gaussian function was fitted to the Gaussian region of the asymmetry distribution typically between $0 < A(p_{\mathrm{T}j_1}, p_{\mathrm{T}j_2}) < 0.15$; the mean of the Gaussian fit was also fixed at 0 to improve the fitting results (see Figures 6.6(a) and 6.8(a) for examples of Gaussian fits to the p_{T} asymmetry distributions).

The width of the fitted Gaussian is given by [120]:

$$\sigma_A = \frac{\sqrt{(\sigma(p_{\mathrm{T}j_1}))^2 + (\sigma(p_{\mathrm{T}j_2}))^2}}{\langle p_{\mathrm{T}j1} + p_{\mathrm{T}j_2} \rangle}. \tag{6.2}$$

If the two jets have approximately the same rapidity, then $\sigma(p_{\mathrm{T}j_1}) = \sigma(p_{\mathrm{T}j_2}) = \sigma(p_{\mathrm{T}})$ and $\langle p_{\mathrm{T}j_1} + p_{\mathrm{T}j_2} \rangle = 2\langle p_{\mathrm{T,average}} \rangle$, giving [120]:

$$\sigma_A \simeq \frac{\sigma(p_{\mathrm{T}})}{\sqrt{2} p_{\mathrm{T}}}. \tag{6.3}$$

The σ_A distributions (for example, Figure 6.6(b)) were fitted using a function with a similar form to the jet energy resolution:

$$\sigma_A = \frac{a}{p_{\mathrm{T}}} + \frac{b}{\sqrt{p_{\mathrm{T}}}} + c. \tag{6.4}$$

If the σ_A distribution for the pseudo-data generated with the MC jet response ($\sigma_{A,\mathrm{MC}}$) was narrower than the width observed in data ($\sigma_{A,\mathrm{data}}$), then a correction ($\sigma_{A,\mathrm{correction}}$) was required for $\sigma_{A,\mathrm{MC}}$ to match the width observed in data. The correction was made from the convolution of two Gaussians:

$$\left(\frac{\sigma_{\mathrm{total}}(p_{\mathrm{T}})}{p_{\mathrm{T}}}\right)^2 = \left(\frac{\sigma_{\mathrm{MC}}(p_{\mathrm{T}})}{p_{\mathrm{T}}}\right)^2 + \sigma_{\mathrm{correction}}(p_{\mathrm{T}})^2, \tag{6.5}$$

where, $\sigma_{\mathrm{total}}(p_{\mathrm{T}})$ is the width of the ***corrected*** pseudo-data, and $\sigma_{\mathrm{correction}}$ is the width of the Gaussian convolved with $\sigma_{A,\mathrm{MC}}$.

If the *total* width matches the width observed in data, i.e., $\sigma_{\mathrm{total}}(p_{\mathrm{T}}) = \sigma_{\mathrm{data}}(p_{\mathrm{T}})$, then using the approximations in Eq.(6.3)

$$(\sqrt{2}\times\sigma_{A,\mathrm{data}}(p_{\mathrm{T}}))^2 = (\sqrt{2}\times\sigma_{A,\mathrm{MC}}(p_{\mathrm{T}}))^2 + \sigma_{\mathrm{correction}}(p_{\mathrm{T}})^2, \tag{6.6}$$

and hence,

$$\sigma_{\mathrm{correction}}(p_{\mathrm{T}}) = \sqrt{2}\times\sqrt{\sigma_{A,\mathrm{data}}(p_{\mathrm{T}})^2 - \sigma_{A,\mathrm{MC}}(p_{\mathrm{T}})^2}. \tag{6.7}$$

Finally, by using Eq.(6.7) and the fits to $\sigma_{A,\mathrm{data}}$ and $\sigma_{A,\mathrm{MC}}$, $\sigma_{\mathrm{correction}}$ can be fully described by the six fit parameters ($a_{\mathrm{data}}, a_{\mathrm{MC}}, b_{\mathrm{data}}, b_{\mathrm{MC}}, c_{\mathrm{data}} and c_{\mathrm{MC}}$).

6.3.1 Event Selection

Events in this analysis first had to pass one of the single-jet trigger chains (see Tables 5.1 and 5.2). The standard ATLAS event cleaning cuts were then applied to remove events which were not fit for physics analysis. The pseudo-data sample was generated using seed events smeared with the MC jet response (see section 6.2). Overall, the seed events were smeared 3000 times to provide a sufficiently large sample of pseudo-data.

The final dijet balance analysis selection cuts for the 2011 and 2012 analyses are shown in Table 6.1.

6.3.2 The 2011 $\sqrt{s} = 7\,\mathrm{TeV}$ Data Set Analysis

The 2011 dijet balance analysis was performed on inclusive dijet distributions. The p_{T} asymmetry distributions for data (a) and pseudo-data (b) as a function of average dijet p_{T} are shown in

Cut	Description	2011 Analysis Value	2012 Analysis Value
1	Events must contain *only* two signal jets		
2	Leading jet (j_1) p_{T} >	70 GeV	100 GeV
3	Sub-leading jet (j_2) p_{T} >	50 GeV	
4	$\left\lvert \pi - \Delta\phi\left(j_1, j_2\right)\right\rvert$ <	0.3	0.25
5	$E_{\mathrm{T}}^{\mathrm{miss}}/\langle p_{\mathrm{T}\,j_1}, p_{\mathrm{T}\,j_2}\rangle$ <	–	0.1

Table 6.1: The dijet p_{T} balance pre-event selection cuts for the 2011 and 2012 analyses. Cut (5) was introduced during the 2012 analysis.

Figure 6.5. This figure shows that large p_{T} asymmetries are observed at low average dijet p_{T}.

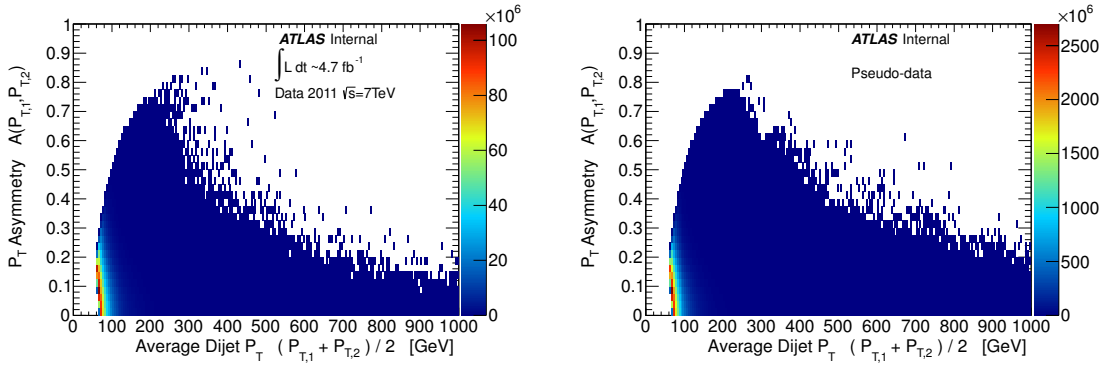

(a) 2011 $\sqrt{s} = 7$ TeV data

(b) 2011 $\sqrt{s} = 7$ TeV pseudo-data

Figure 6.5: The p_{T} asymmetry distributions with respect to average dijet p_{T} in the full 2011 $\sqrt{s} = 7$ TeV data set analysis. The p_{T} asymmetry distribution for data is shown in (a). The p_{T} asymmetry distribution for the pseudo-data generated with the MC response is shown in (b).

Figure 6.6 shows a summary of the results from the 2011 dijet p_{T} balance analysis. An example Gaussian fit to the dijet p_{T} asymmetry distributions is shown in Figure 6.6(a). It can be seen in this figure that the width of the smeared pseudo-data was narrower than the 2011 $\sqrt{s} = 7$ TeV data (by ≈7% see Figure 6.6(b)). Figure 6.6(b) shows the σ_A distributions for data and the pseudo-data without any additional Gaussian smearing. The figure shows that the width of the pseudo-data (shown in red) was narrower than the width in data (shown in black) over the full average dijet p_{T} range; therefore, additional Gaussian smearing was required for pseudo-data generated with the Monte Carlo jet response. Figure 6.6(c) shows the correction ($\sigma_{\mathrm{correction}}(p_{\mathrm{T}})$) as a function of jet p_{T}. It can be seen in this figure that the largest correction was required at low jet p_{T}.

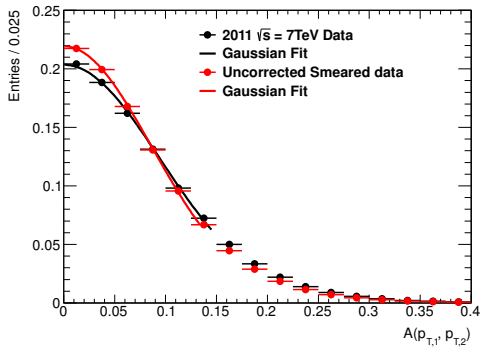

(a) p_{T} asymmetry in the 200 GeV average jet p_{T} bin

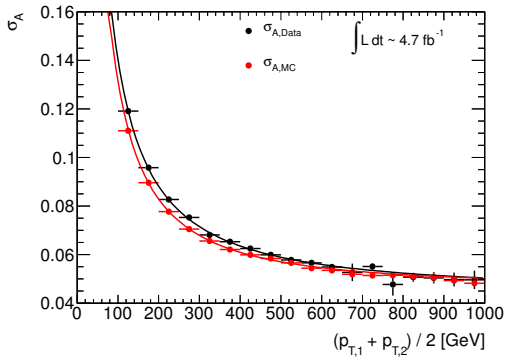

(b) σ_A as a function of average jet p_{T}

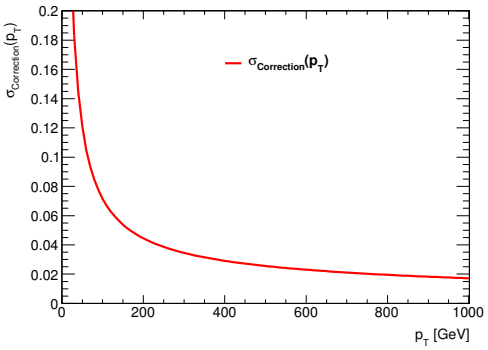

(c) $\sigma_{Correction}(p_{\mathrm{T}})$ as a function of jet p_{T}

Figure 6.6: Summary of the results from the inclusive 2011 dijet p_{T} balance analysis. Figure (a) shows an example Gaussian fit in an average jet p_{T} bin. The p_{T} asymmetry distribution for data is shown by black points, whereas the pseudo-data is shown by the red points. The black line shows the Gaussian fit to the data, and the Gaussian fit to the pseudo-data is shown in red. Figure (b) shows the σ_A distributions for data (black) and the pseudo-data (red) without any additional Gaussian smearing. The solid lines show the fits to data and pseudo-data with a functional form similar to the jet energy resolution. Finally, $\sigma_{correction}$ as a function of jet p_{T} is shown in figure (c).

Table 6.2 shows the σ_A fit parameters from the fits to the p_{T} asymmetry distributions in the 2011 dijet balance analysis.

6.3.3 The 2012 $\sqrt{s} = 8$ TeV Data Set Analysis

The 2012 dijet p_{T} balance analysis was performed only on b-veto dijet events. Unfortunately, there were insufficient statistics to perform a b-tagged dijet p_{T} balance analysis. Therefore, the corrections derived in this analysis were only applied to b-veto jets in the smearing process and b-jets remained unchanged.

σ_A Fit Parameter	Parameter Value
a_{data} [GeV]	11.98
b_{data} [$\sqrt{\text{GeV}}$]	0.26
c_{data}	0.05
a_{MC} [GeV]	11.74
b_{MC} [$\sqrt{\text{GeV}}$]	0.37
c_{MC}	0.05

Table 6.2: σ_A fit parameter values in the 2011 analysis for the data and uncorrected pseudo-data distributions.

A selection cut on $E_{\text{T}}^{\text{miss}}/\langle p_{\text{T}\,j_1}, p_{\text{T}\,j_2}\rangle$ was introduced into the 2012 analysis since a large number of events with a significant amount of $E_{\text{T}}^{\text{miss}}$ passed the event selection cuts. These events were pushing the mean of the asymmetry distribution from 0 (compare Figures 6.6(a) and 6.8(a)). This was an issue, as the dijet balance analysis was aimed at constraining the Gaussian part of the jet response. The $E_{\text{T}}^{\text{miss}}/\langle p_{\text{T}\,j_1}, p_{\text{T}\,j_2}\rangle$ selection cut removes events which contain high $E_{\text{T}}^{\text{miss}}$ compared to the average dijet p_{T}, resulting in a larger fraction of Gaussian dijet p_{T} asymmetry events.

The p_{T} asymmetry distributions for the 2012 data set (a) and pseudo-data (b) as a function of average dijet p_{T} are shown in Figure 6.7. Large dijet asymmetries were observed in the 2012 b-veto dijet balance analysis even with the inclusion of the $E_{\text{T}}^{\text{miss}}/\langle p_{\text{T}\,j_1}, p_{\text{T}\,j_2}\rangle$ selection cut.

Figure 6.8 shows a summary of the results from the 2012 b-veto dijet balance analysis. An example Gaussian fit to a p_{T} asymmetry distribution is shown in Figure 6.8(a). This figure shows that the width of the smeared pseudo-data was also narrower than the data in the 2012 analysis (by ≈9%, see Figure 6.8(b)). Figure 6.8(b) shows the σ_A distributions for data and the pseudo-data without any additional Gaussian smearing. It can be seen in this figure that the width of the pseudo-data (shown in red) was narrower than the width in data (shown in black) over the full average dijet p_{T} range; therefore, additional Gaussian smearing was also required in the 2012 analysis. Figure 6.8(c) shows the correction ($\sigma_{\text{correction}}(p_{\text{T}})$) as a function of jet p_{T} in the 2012 dijet balance analysis. This figure shows that the largest correction to σ_A was again required at low jet p_{T}.

Table 6.3 shows the σ_A fit parameters of the p_{T} asymmetry distributions in the b-veto dijet balance 2012 analysis.

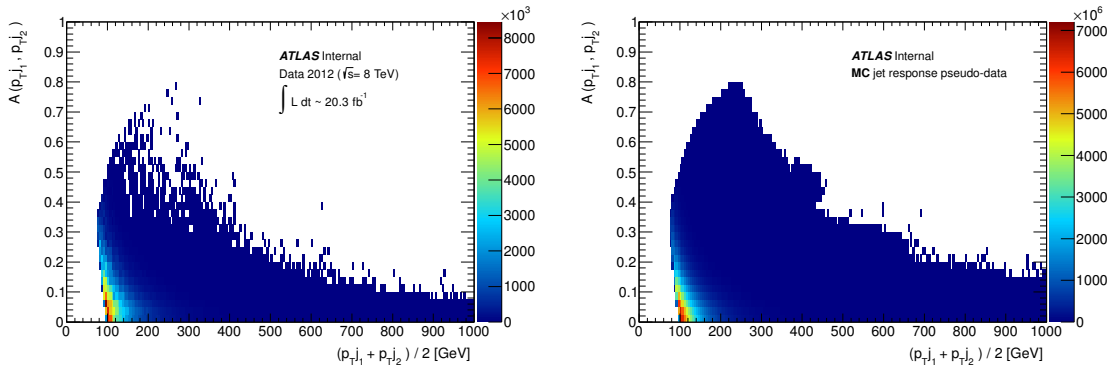

(a) 2012 $\sqrt{s} = 8$ TeV data

(b) 2012 $\sqrt{s} = 8$ TeV pseudo-data

Figure 6.7: The p_{T} asymmetry distributions with respect to average dijet p_{T} in the full 2012 $\sqrt{s} = 8$ TeV data set analysis. The p_{T} asymmetry distribution for data in shown in (a). The p_{T} asymmetry distribution for the pseudo-data generated with the MC response is shown in (b).

σ_A Fit Parameter	Parameter value
a_{data} [GeV]	3.856
b_{data} [$\sqrt{\mathrm{GeV}}$]	0.652
c_{data}	0.003
a_{MC} [GeV]	2.833
b_{MC} [$\sqrt{\mathrm{GeV}}$]	0.616
c_{MC}	0.005

Table 6.3: σ_A fit parameter values in the 2012 b-veto analysis for the data and uncorrected pseudo-data distributions.

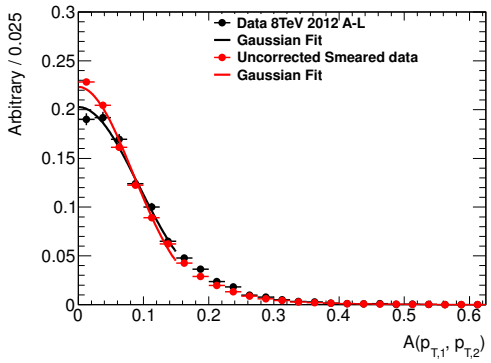

(a) p_{T} asymmetry in the 150 GeV average jet p_{T} bin

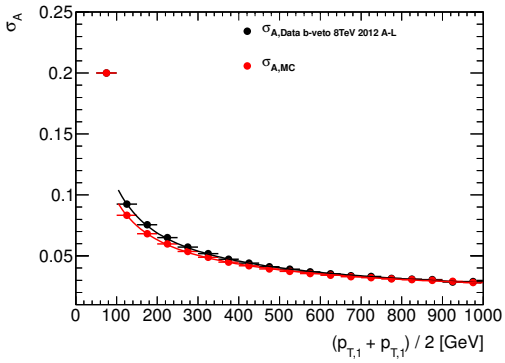

(b) σ_A as a function of average jet p_{T}

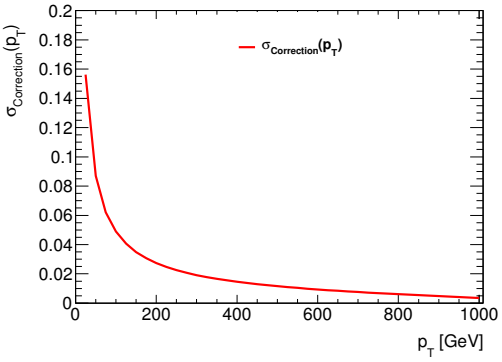

(c) $\sigma_{Correction}(p_{\mathrm{T}})$ as a function of jet p_{T}

Figure 6.8: Summary of the results from the 2012 b-veto dijet p_{T} balance analysis. Figure (a) shows an example Gaussian fit to an average jet p_{T} bin in the 2012 analysis. The p_{T} asymmetry distribution for data is shown by black points, whereas the pseudo-data is shown by the red points. The black line shows the Gaussian fit to the data, and the Gaussian fit to the pseudo-data is shown in red. Figure (b) shows the σ_A distributions for data (black) and the pseudo-data (red) without any additional Gaussian smearing. The solid lines show the fits to data and pseudo-data with a functional form similar to the jet energy resolution. Finally, $\sigma_{\mathrm{correction}}$ as a function of jet p_{T} is shown in figure (c).

6.4 Dijet $\Delta\phi$ Analysis

6.4.1 Introduction and Motivation

The ϕ-smearing of jets was introduced in the 2012 analysis and corresponds to rotating the ϕ angles of smeared jets in the seed event. The rotation was applied by selecting a random number from a Gaussian distribution with a mean of zero and a width found in the $\Delta\phi$ dijet balance analysis, using Eq.(6.7). The random number was then added to the ϕ angle of the seed jet; this process was repeated for each jet in the seed event.

The ϕ rotation accounts for the difference in ϕ resolution after the seed jet has been smeared down in p_{T}. The seed event selection cut may also bias the $\Delta\phi$ angle between the jets in a dijet seed event to a more back-to-back topology, since the jets are well-measured by construction (assuming the jets are of similar $|\eta|$). Since there is no direct intrinsic ϕ-smearing within the default smearing process, the smeared jets produced from one of these seed events would remain back-to-back even if one of the jets has undergone a very large p_{T} fluctuation. This is not what would be expected when looking at dijet events in data, as a jet which had lost a large fraction of its energy (and constitute particles) due to jet mismeasurement would probably have a different jet axis compared to its truth jet axis. Therefore, the $\Delta\phi$-distributions of the pseudo-data in the multijet Control Regions of SUSY analyses could be biased by the seed event selection (see Figure 7.5).

6.4.2 Analysis Method

The 2012 dijet $\Delta\phi$ analysis was performed only on b-veto dijet events, and the ϕ-smearing corrections were found after the Gaussian p_{T} corrections were applied to pseudo-data.

The same selection cuts as the dijet p_{T} balance analysis were used (see section 6.3 and Table 6.1) except for the selection cut on $\Delta\phi$ between the two jets ($|\pi - \Delta\phi_{(j1,j2)}| < 0.25$). Table 6.4 shows a summary of the final event selection cuts used in the 2012 dijet $\Delta\phi$ analysis.

The $\Delta\phi$ ($|\pi - \Delta\phi_{(j_1,j_2)}|$) between the two jets was measured against average dijet p_{T} (see Figure 6.9. The analysis also used average dijet p_{T} bins of 50 GeV, and a Gaussian function was fitted to each $\Delta\phi$ distribution as was the case in the dijet p_{T} balance analysis. The Gaussian function was fitted to the Gaussian region of the $\Delta\phi$ distribution, typically $0 < A(p_{\mathrm{T}j_1}, p_{\mathrm{T}j_2}) < 0.15$; the mean of this Gaussian fit was also fixed to 0 to improve the fitting (see Figure 6.10(a)) for examples of the Gaussian fits). This was the same process that was used in the dijet p_{T} balance analysis except $\Delta\phi_{(j_1,j_2)}$ was used instead of p_{T} asymmetry. Finally, by using Eq.(6.7) and the fits to $\sigma_{\Delta\phi,\mathrm{data}}$ and $\sigma_{\Delta\phi,\mathrm{MC}}$, $\sigma_{\mathrm{correction}}(\Delta\phi)$ was fully described by six fit parameters.

Cut	Description	Analysis Value
1	Events must contain *only* two signal jets	
2	Leading jet (j_1) p_{T} >	100 GeV
3	Sub-leading jet (j_2) p_{T} >	50 GeV
4	$E_{\mathrm{T}}^{\mathrm{miss}}/\langle p_{\mathrm{T}\,j_1}, p_{\mathrm{T}\,j_2}\rangle$ <	0.1

Table 6.4: The dijet $\Delta\phi$ analysis final event selection cuts.

6.4.3 Results

The dijet $|\pi - \Delta\phi_{(j1,j2)}|$ distributions for the 2012 data set (a) and pseudo-data (b) as a function of average dijet p_{T} are shown in Figure 6.9.

Figure 6.10 shows a summary of the results from the 2012 dijet $\Delta\phi$ analysis. An example of the Gaussian fitting to the $\Delta\phi$ distributions is shown in Figure 6.10(a). This figure shows that the smeared pseudo-data width was *slightly* narrower than the width in data in this average dijet p_{T} bin. Figure 6.10(b) shows the $\sigma_{\Delta\phi}$ distributions for data and the pseudo-data with the additional Gaussian p_{T} smearing. It can be seen in this figure that the width of the pseudo-data (shown in red) was narrower than the width in data (shown in black) for average dijet $p_{\mathrm{T}} < 400$ GeV; therefore, an additional Gaussian ϕ-angular smearing was required for smeared jets in the pseudo-data within this p_{T} region. Figure 6.10(c) shows the ϕ correction ($\sigma_{\Delta\phi}$) as a function of jet p_{T} for the 2012 dijet $\Delta\phi$ analysis. This figure shows that the majority of the $\Delta\phi$ correction was required at low jet p_{T} and no correction was required for jets with $p_{\mathrm{T}} > 400$ GeV.

The parameters of the fits to the $\sigma_{\Delta\phi}$ distributions can be found in Table 6.5. The parameters in Table 6.5 were then used to apply corrections to b-veto jets during the smearing process **after** the additional Gaussian smearing was applied; this was to retain the order in which the corrections were derived.

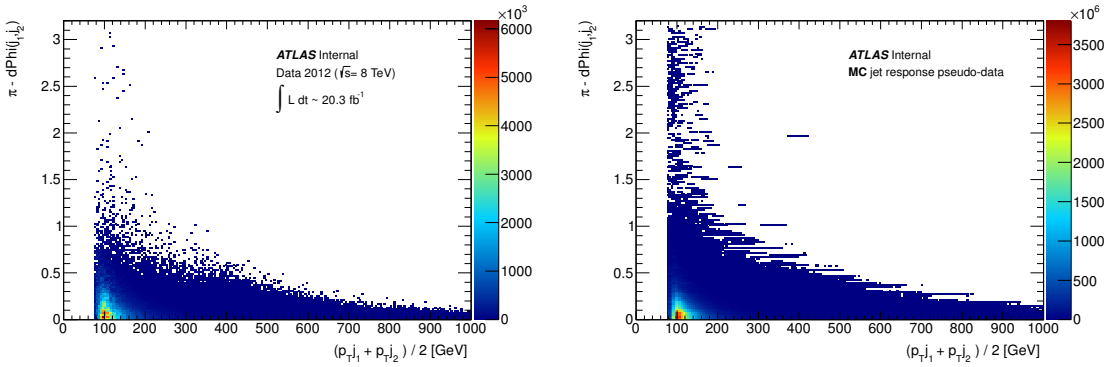

(a) 2012 $\sqrt{s} = 8\,\text{TeV}$ data

(b) 2012 $\sqrt{s} = 8\,\text{TeV}$ pseudo-data

Figure 6.9: The $|\pi - \Delta\phi_{(j_1,j_2)}|$ distributions with respect to average dijet p_{T} in the full 2012 $\sqrt{s} = 8\,\text{TeV}$ data analysis. The $\Delta\phi$ distribution for data in shown in figure (a). The $\Delta\phi$ distribution for the pseudo-data generated with the MC response is shown in figure (b).

$\sigma_{\Delta\phi(j_1,j_2)}$ Fit Parameter	Parameter Value
a_{data} [GeV]	11.284
b_{data} [$\sqrt{\text{GeV}}$]	0.202
c_{data}	0.018
a_{MC} [GeV]	10.564
b_{MC} [$\sqrt{\text{GeV}}$]	0.144
c_{MC}	0.023

Table 6.5: $\sigma_{\Delta\phi(j_1,j_2)}$ fit parameter values for the data and uncorrected pseudo-data in the 2012 b-veto dijet $\Delta\phi$ analysis.

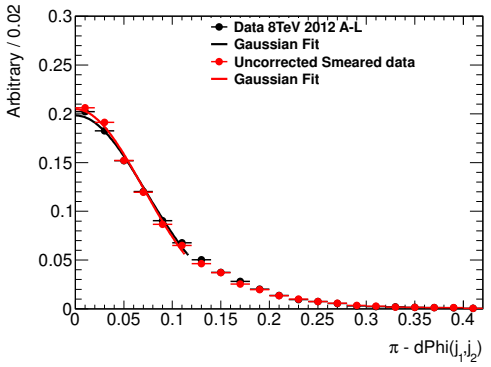

(a) $\Delta\phi_{(j1,j2)}$ in the 250 GeV average jet p_{T} bin

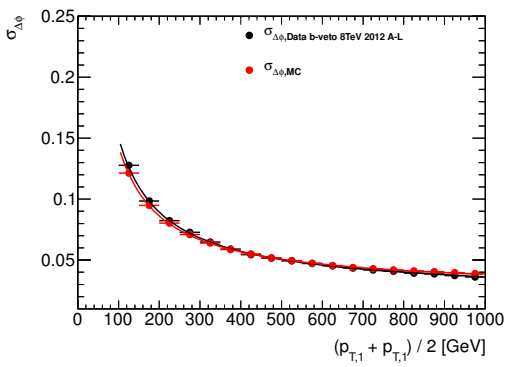

(b) $\sigma_{\Delta\phi}$ as a function of average jet p_{T}

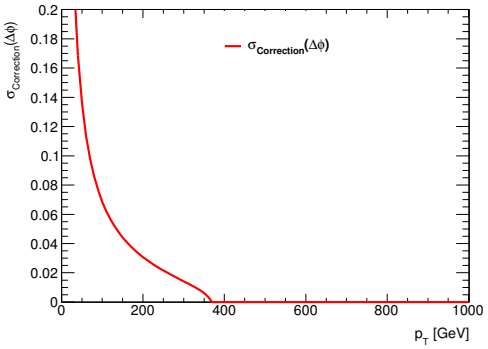

(c) $\sigma_{Correction}(\Delta\phi)$ as a function of jet p_{T}

Figure 6.10: Summary of the results from the 2012 b-veto dijet $\Delta\phi$ analysis. Figure (a) shows an example Gaussian fit to the $\Delta\phi_{(j1,j2)}$ distribution in an average jet p_{T} bin. The $|\pi - \Delta\phi_{(j_1,j_2)}|$ distribution for data is shown by black points, whereas the pseudo-data is shown by the red points. The black line shows the Gaussian fit to the data, and the Gaussian fit to the pseudo-data is shown in red. Figure (b) shows the $\sigma_{\Delta\phi}$ distributions for data (black) and the pseudo-data (red) with additional Gaussian smearing. The solid lines show the fits to data and pseudo-data with a functional form similar to Eq.(6.4). Finally, $\sigma_{\mathrm{correction}}(\Delta\phi)$ as a function of jet p_{T} is shown in figure (c).

6.5 Mercedes Analysis

6.5.1 Introduction

The '*Mercedes*' analysis is designed to probe the non-Gaussian jet response of a single jet. Unlike the dijet balance analysis, the Mercedes analysis can distinguish between high and low p_{T} fluctuations of the candidate jet by looking at the ϕ direction of the $E_{\mathrm{T}}^{\mathrm{miss}}$.

The analysis studied the R_2 (Eq.(6.10)) distribution in multijet events, where the topological selection cuts ensured that one jet was *unambiguously associated*[2] with the $E_{\mathrm{T}}^{\mathrm{miss}}$ (see Figure 6.11). In addition to this, the selection cuts also ensured that any other jets in the event did not also point along the ϕ direction of the $E_{\mathrm{T}}^{\mathrm{miss}}$.

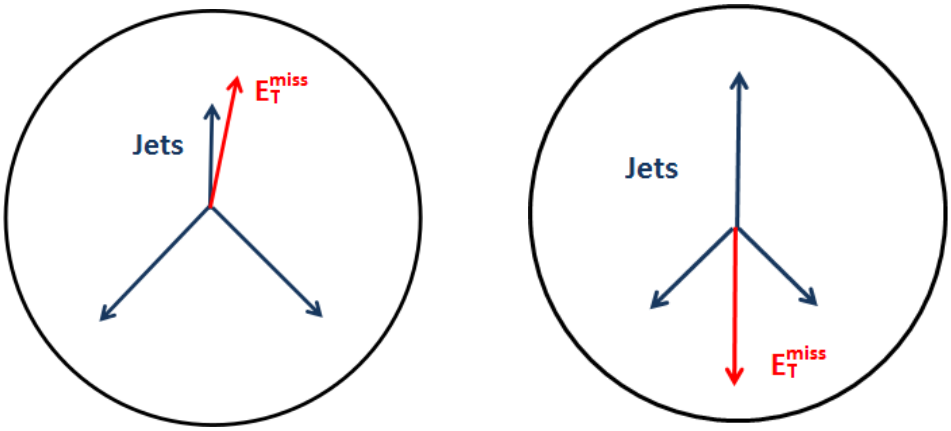

(a) Parallel Selection (b) Antiparallel Selection

Figure 6.11: Examples of the parallel and antiparallel Mercedes event topologies, with the $\vec{E}_{\mathrm{T}}^{\mathrm{miss}}$ unambiguously associated with a jet in the event [137].

The jet p_{T} response (R) of a fluctuating jet can be expressed as

$$R = \frac{\vec{p}_{\mathrm{T}}^{\,\mathrm{J}}\,(\mathrm{reco}) \cdot \vec{p}_{\mathrm{T}}^{\,\mathrm{J}}\,(\mathrm{truth})}{\left|\vec{p}_{\mathrm{T}}^{\,\mathrm{J}}\,(\mathrm{truth})\right|^2}. \tag{6.8}$$

Since the $\vec{E}_{\mathrm{T}}^{\mathrm{miss}}$ is unambiguously associated with the candidate jet, $\vec{p}_{\mathrm{T}}^{\,\mathrm{J}}\,(\mathrm{truth})$ can be approximated to:

$$\vec{p}_{\mathrm{T}}^{\,\mathrm{J}}\,(\mathrm{truth}) \simeq \vec{p}_{\mathrm{T}}^{\,\mathrm{J}}\,(\mathrm{reco}) + \vec{E}_{\mathrm{T}}^{\mathrm{miss}}. \tag{6.9}$$

[2] A jet is said to be unambiguously associated with the $E_{\mathrm{T}}^{\mathrm{miss}}$ if either $\Delta\phi(jet, E_{\mathrm{T}}^{\mathrm{miss}}) < 0.1$ or $\pi - \Delta\phi(jet, E_{\mathrm{T}}^{\mathrm{miss}}) < 0.1$.

Hence, Eq.(6.8) can be approximated to:

$$R_2 \simeq \frac{\vec{p}_{\mathrm{T}}^{\,\mathrm{J}} \cdot (\vec{p}_{\mathrm{T}}^{\,\mathrm{J}} + \vec{E}_{\mathrm{T}}^{\mathrm{miss}})}{\left|\vec{p}_{\mathrm{T}}^{\,\mathrm{J}} + \vec{E}_{\mathrm{T}}^{\mathrm{miss}}\right|^2}. \tag{6.10}$$

Here, $\vec{p}_{\mathrm{T}}^{\,\mathrm{J}}$ is the $\vec{p}_{\mathrm{T}}$ of the reconstructed jet unambiguously associated with the $\vec{E}_{\mathrm{T}}^{\mathrm{miss}}$.

6.5.2 Event Selection

Events in this analysis first had to pass one of the single jet trigger chains (see Tables 5.1 and 5.2). The standard ATLAS event cleaning cuts were then applied to remove events which were not fit for physics analysis. The initial pseudo-data sample was generated using seed events smeared with the MC jet response (see section 6.2) with the additional Gaussian and ϕ angle smearing corrections (see sections 6.3 and 6.4). Overall, the seed events were smeared 3000 times to provide a sufficiently large sample of pseudo-data.

The Mercedes analysis pre-selection cuts for the 2011 and 2012 analysis are shown in Table 6.6.

Cut	Description	2011 Analysis Value	2012 Analysis Value
1	Events must pass one of the single-jet triggers.		
2	Events must contain at least three signal jets.		
3	Leading jet (j_1) p_{T} >	260 GeV	210 GeV
4	Sub-leading jet (j_2) p_{T} >	50 GeV	
5	Third leading jet (j_3) p_{T} >	30 GeV	40 GeV
6	$E_{\mathrm{T}}^{\mathrm{miss}}$ >	30 GeV	

Table 6.6: The Mercedes analysis event pre-selection cuts for the 2011 and 2012 analysis.

The leading jet p_{T} cut removed data events from very high pre-scaled triggers, as a smooth data distribution was required to determine the optimal shape of the low-side tail of the jet response function. In the 2012 analysis, the leading jet p_{T} cut was lowered to 210 GeV to provide more data statistics for the b-tagged Mercedes analysis. The jet p_{T} cuts also reduce the $Z(\rightarrow \nu\nu)$ + jets and other SM backgrounds which contain $E_{\mathrm{T}}^{\mathrm{miss}}$ from final state objects. The $E_{\mathrm{T}}^{\mathrm{miss}}$ selection cut was to enforce that the candidate jet associated with the $E_{\mathrm{T}}^{\mathrm{miss}}$ had undergone a significant p_{T} fluctuation.

After pre-selection cuts, the jets within the events were reordered in $\Delta\phi$ direction from the $\vec{E}_{\mathrm{T}}^{\mathrm{miss}}$, such that j_1 was the jet that was closest to $\vec{E}_{\mathrm{T}}^{\mathrm{miss}}$ in ϕ and j_{N} was the jet that was furthest from

the $\vec{E}_{\mathrm{T}}^{\mathrm{miss}}$ in ϕ, or closest to being back-to-back with the $\vec{E}_{\mathrm{T}}^{\mathrm{miss}}$. If the $E_{\mathrm{T}}^{\mathrm{miss}}$ was dominated by the mis-measurement of a jet in the event, then the $\vec{E}_{\mathrm{T}}^{\mathrm{miss}}$ would align with that jet; however, since the jet mis-measurement can either be an upward or downward fluctuation, both cases must be taken into account. Consequently, there were two different jet configurations requiring two different sets of angular selection cuts.

The parallel selection was targeted at selecting events in which one jet had undergone a large downward p_{T} fluctuation; this caused the $\vec{E}_{\mathrm{T}}^{\mathrm{miss}}$ to become parallel with the candidate jet that had undergone the p_{T} fluctuation. The antiparallel selection was aimed at selecting events in which one of the jets had undergone a significant upward p_{T} fluctuation. In this case, the $\vec{E}_{\mathrm{T}}^{\mathrm{miss}}$ was antiparallel to the candidate jet, since there was an excess of energy in the direction of the candidate jet; therefore, the angular selection cuts were designed to select a candidate jet that was back-to-back (b2b) with the $\vec{E}_{\mathrm{T}}^{\mathrm{miss}}$.

The ϕ-angular selection cuts for the parallel configuration were

$$\left|\Delta\phi\left(j_1, \vec{E}_{\mathrm{T}}^{\mathrm{miss}}\right)\right| < \pi - \left|\Delta\phi\left(j_{\mathrm{N}}, \vec{E}_{\mathrm{T}}^{\mathrm{miss}}\right)\right|, \tag{6.11a}$$

$$\left|\Delta\phi\left(j_1, \vec{E}_{\mathrm{T}}^{\mathrm{miss}}\right)\right| < \Delta\phi^{\mathrm{match}}, \tag{6.11b}$$

$$\left|\Delta\phi\left(j_2, \vec{E}_{\mathrm{T}}^{\mathrm{miss}}\right)\right| > \Delta\phi_1^{\mathrm{iso}}. \tag{6.11c}$$

The ϕ-angular selection cuts for the antiparallel configuration were

$$\pi - \left|\Delta\phi\left(j_{\mathrm{N}}, \vec{E}_{\mathrm{T}}^{\mathrm{miss}}\right)\right| < \left|\Delta\phi\left(j_1, \vec{E}_{\mathrm{T}}^{\mathrm{miss}}\right)\right|, \tag{6.12a}$$

$$\pi - \left|\Delta\phi\left(j_{\mathrm{N}}, \vec{E}_{\mathrm{T}}^{\mathrm{miss}}\right)\right| < \Delta\phi^{\mathrm{match}}, \tag{6.12b}$$

$$\pi - \left|\Delta\phi\left(j_{\mathrm{N}-1}, \vec{E}_{\mathrm{T}}^{\mathrm{miss}}\right)\right| > \Delta\phi_1^{\mathrm{iso}}. \tag{6.12c}$$

Here, $\Delta\phi^{\mathrm{match}}$ is the angular cut which considers the candidate jet matched to the $\vec{E}_{\mathrm{T}}^{\mathrm{miss}}$ and $\Delta\phi_1^{\mathrm{iso}}$ is the first angular isolation cut. The first angular isolation cut ensured that j_2 or $j_{\mathrm{N}-1}$ was not associated with the $\vec{E}_{\mathrm{T}}^{\mathrm{miss}}$ as well. Values for the angular selection cuts in the 2011 and 2012 analyses can be found in Table 6.7.

For better clarity, the candidate jet associated with $\vec{E}_{\mathrm{T}}^{\mathrm{miss}}$ was relabelled to j_{min}, as an ambiguity can arise in Mercedes events. For the parallel selection, j_{min} refers to the jet that was closest to the $\vec{E}_{\mathrm{T}}^{\mathrm{miss}}$ in ϕ (formerly j_1). However, for the antiparallel selection, j_{min} refers to the jet which was furthest away from the $\vec{E}_{\mathrm{T}}^{\mathrm{miss}}$ in ϕ (formerly j_{N}), due to the back-to-back configuration of the jet and the $\vec{E}_{\mathrm{T}}^{\mathrm{miss}}$. The jet which was closest to being back-to-back with the *candidate jet* was referred

to as the '*second candidate jet*' and was relabelled to j_{b2b}; this jet was formerly j_{N} in the parallel configuration and j_1 in the antiparallel configuration. Figure 6.12 shows examples of the relabelled jets in the parallel and antiparallel selections.

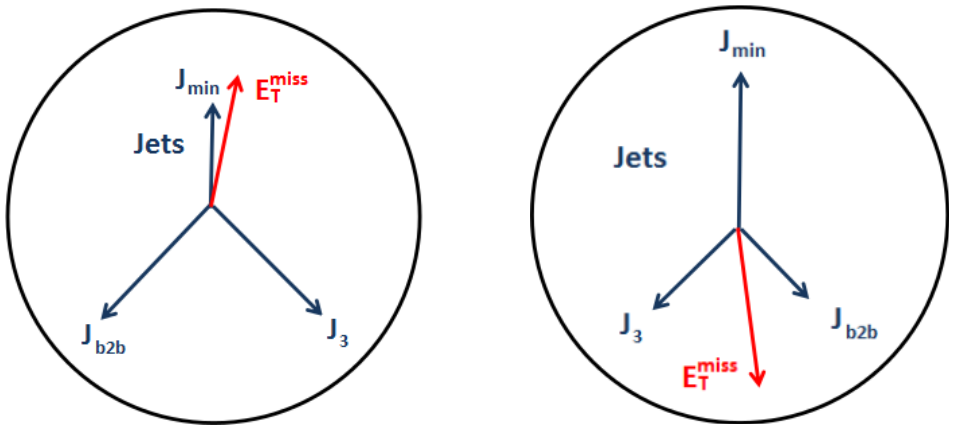

(a) Parallel Selection (b) Antiparallel Selection

Figure 6.12: Examples of the parallel and antiparallel Mercedes event topologies, with the relabeling of jets after the first angular section cuts.

An ambiguity arises in some Mercedes events when the $\vec{E}_{\mathrm{T}}^{\mathrm{miss}}$ could be associated with either j_{min} or j_{b2b}. Since it is impossible to tell, these events are vetoed by requiring a further angular isolation cut on the *second candidate jet*:

$$\pi - \left|\Delta\phi\left(j_{\mathrm{b2b}}, \vec{E}_{\mathrm{T}}^{\mathrm{miss}}\right)\right| > \Delta\phi_2^{\mathrm{iso}} \qquad \text{Parallel selection.} \tag{6.13a}$$

$$\left|\Delta\phi\left(j_{\mathrm{b2b}}, \vec{E}_{\mathrm{T}}^{\mathrm{miss}}\right)\right| > \Delta\phi_2^{\mathrm{iso}} \qquad \text{Antiparallel selection.} \tag{6.13b}$$

Here, $\Delta\phi_2^{\mathrm{iso}}$ is the second angular isolation cut and its value can be found in Table 6.7.

Variable	Value
$\Delta\phi_1^{\mathrm{match}}$	0.10 [rad.]
$\Delta\phi_1^{\mathrm{iso}}$	1.00 [rad.]
$\Delta\phi_2^{\mathrm{iso}}$	0.25 [rad.]

Table 6.7: Summary table of the Mercedes event angular selection cuts.

The $\Delta\phi$ angular distributions for j_{min} and j_{b2b} are shown in Figure 6.13. The multijet distributions in this figure were predicted using multijet MC samples. It can be seen in Figure 6.13(a) that there was a discrepancy in the middle of the $\Delta\phi$ angular distributions between MC and data. However,

the selection of Mercedes events was not affected by the disagreement since events were only selected from the first and last bin of the $\Delta\phi$ angular distribution, where there was good agreement. Figure 6.13 shows that j_{min} and j_{b2b} were back-to-back in a large fraction of events, creating the ambiguity mentioned earlier in this section.

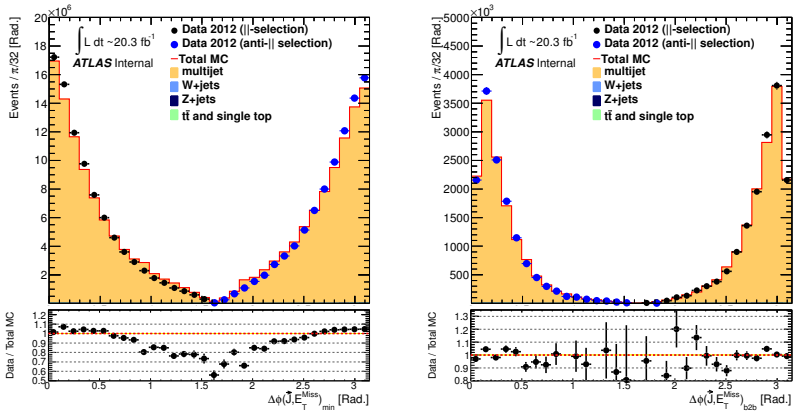

(a) j_{min} (b) j_{b2b}

Figure 6.13: The $\Delta\phi$ distributions for candidate Mercedes events. Multijet MC is shown in orange. Data from the parallel angular selection is shown in black, whereas data from the antiparallel selection is shown in blue. Figure (a) shows the $\Delta\phi$ distribution between j_{min} and the $\vec{E}_{\text{T}}^{\text{miss}}$ for the parallel and antiparallel selections. Figure (b) shows the $\Delta\phi$ distribution between j_{b2b} and $\vec{E}_{\text{T}}^{\text{miss}}$ for parallel and antiparallel selections after the angular selection cuts ($\Delta\phi^{\text{match}}$ and $\Delta\phi_1^{\text{iso}}$) have been applied.

The third jet p_{T} cut was reapplied to the candidate jet, ensuring that the candidate jet had a p_{T} above the minimum jet p_{T} selection cut. The leading and sub-leading jet p_{T} cuts were also reapplied to the other jets in the event in case the candidate jet was the leading or sub-leading jet in the event. The event displays of two candidate Mercedes events from the ATLAS 2011 $\sqrt{s} = 7$ TeV data set are shown in Figure 6.14.

6.5.3 Non-Modified Jet Response R_2 Distributions

It is expected that the low-side tail shape ($0.0 < R_2 < 0.8$) will change with respect to the truth jet p_{T} of the fluctuating jet; therefore, the shape of the low-side tail was independently measured in different truth jet p_{T} regions. However, data statistics within the low-side tail region of the R_2 distributions limited the level of granularity (in truth jet p_{T}) that could be achieved, particularly for the b-tag jet response in the 2012 analysis. The 2011 Mercedes analysis was performed on the inclusive jet response in two different truth jet p_{T} regions: 100-300 GeV and 300-1000 GeV. The 2012 Mercedes analysis was performed separately on the b-tag and b-veto jet responses. The b-tag Mercedes analysis used two different truth jet p_{T} regions: 100-300 GeV and 300-1500 GeV. The

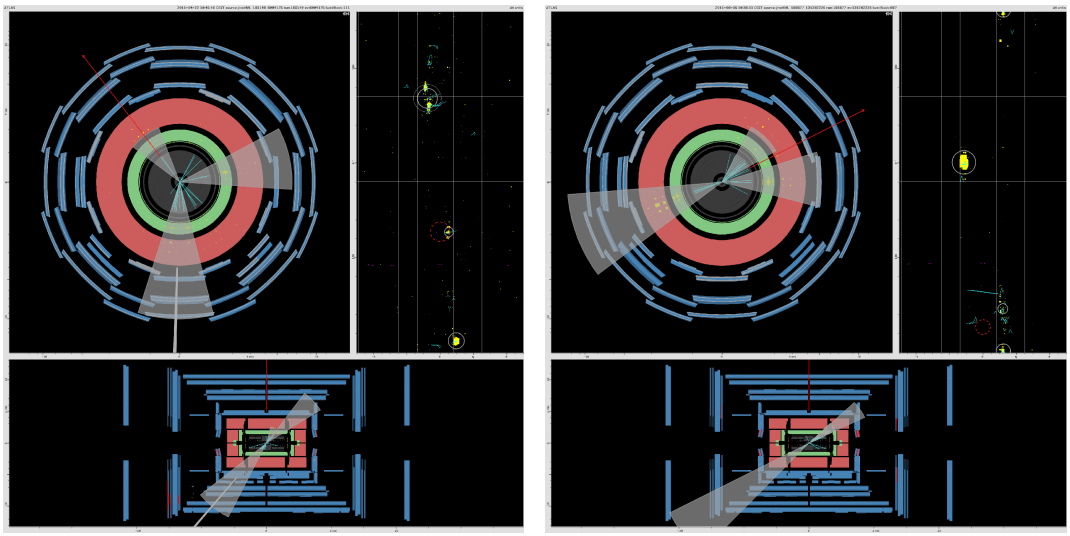

(a) Parallel selection (b) Antiparallel selection

Figure 6.14: Candidate Mercedes events from the ATLAS 2011 $\sqrt{s} = 7$ TeV data set. Figure (a) shows a candidate Mercedes event in the parallel configuration, whereas figure (b) shows a candidate Mercedes event in the antiparallel configuration.

b-veto used three different truth jet p_{T} regions: 100-300 GeV, 300-600 GeV and 600-1500 GeV.

Figure 6.15 shows the R_2 distributions of candidate jets for the inclusive jet response in the 2011 Mercedes analysis. Though it can be seen that the MC jet response effectively described the low-side tail in the 100-300 GeV truth jet p_{T} region, the low-side tail region in the 300-1000 GeV did not agree with the observed data.

Figures 6.16 and 6.17 show the R_2 distributions for b-tagged and b-veto candidate jets. The figures show that the pseudo-data generated from the Monte Carlo jet response did not adequately describe the observed data distribution in the low-side tail region; hence, the low-side tail of the b-veto and b-tag jet responses required modification.

The process that was used to modify the low-side tail of the jet response is described in section 6.5.4. Updated versions of these Figures (6.15, 6.16 and 6.17) after the low-side tail modification process are shown in Figures 6.23, 6.24 and 6.25.

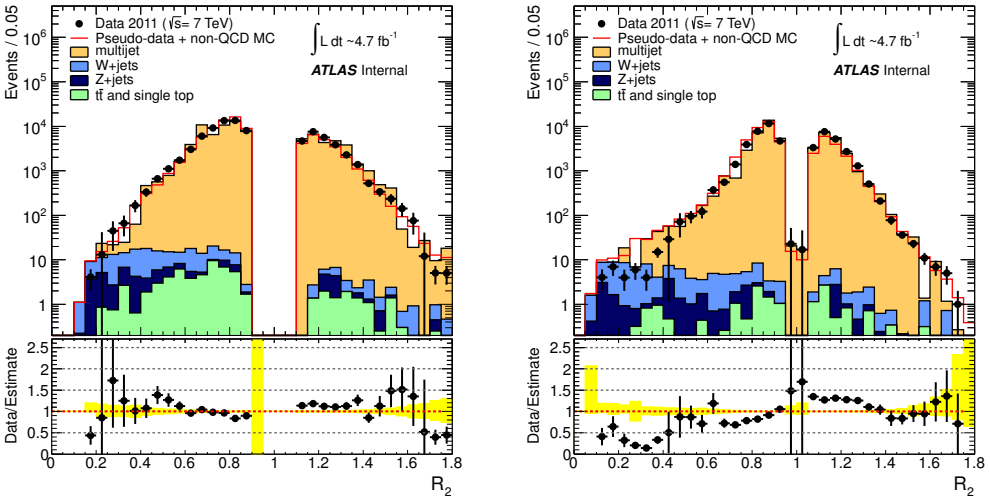

(a) truth jet p_{T} range of 100-300 GeV (b) truth jet p_{T} range of 300-1000 GeV

Figure 6.15: The R_2 distributions for inclusive jets are shown for two bins of truth jet p_{T}: 100 to 300 GeV (a) and 300 to 1500 GeV (b). The 2011 data is shown in black and the sum of pseudo-data and non-QCD Monte Carlo is shown in red. These distributions have no low-side tail modification applied to the jet response. The yellow uncertainty band only includes statistical uncertainties on the Monte Carlo and pseudo-data samples.

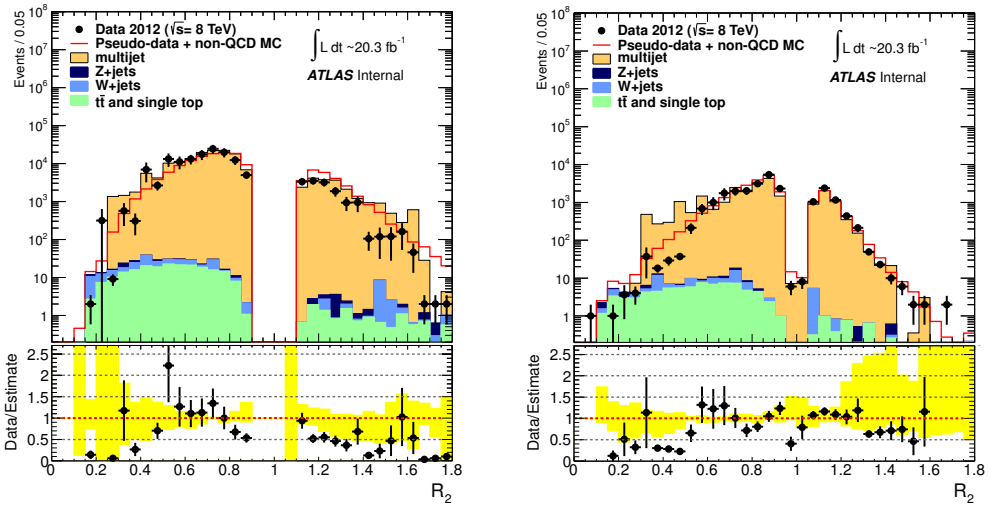

(a) truth jet p_{T} range of 100-300 GeV (b) truth jet p_{T} range of 300-1500 GeV

Figure 6.16: The R_2 distribution for b-tag jets is shown for two bins of truth jet p_{T}: 100 to 300 GeV (a) and 300 to 1500 GeV (b). The 2012 data is shown in black and the sum of pseudo-data and non-QCD Monte Carlo is shown in red. These distributions have no low-side tail modification applied to the jet response. The yellow uncertainty band only includes statistical uncertainties on the Monte Carlo and pseudo-data samples, and the shape of the Gaussian region of the jet response.

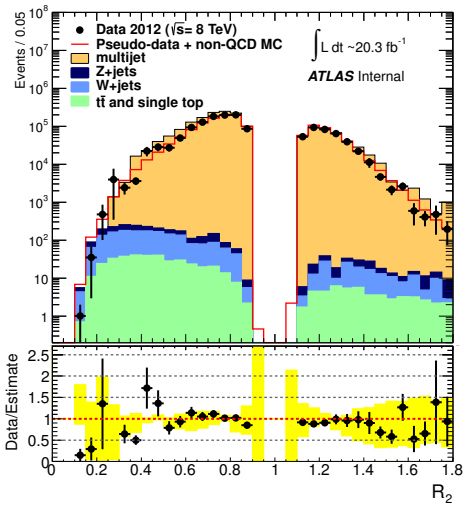

(a) truth jet p_{T} range of 100-300 GeV

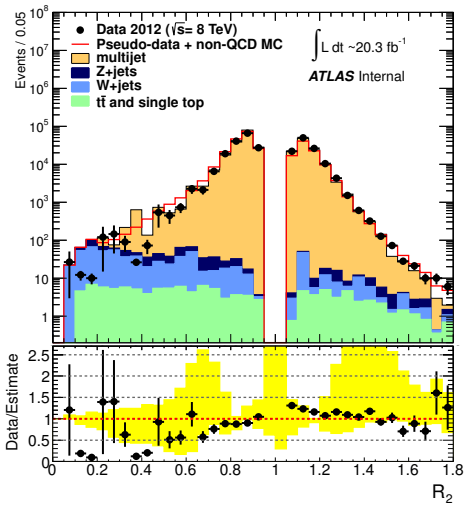

(b) truth jet p_{T} range of 300-600 GeV

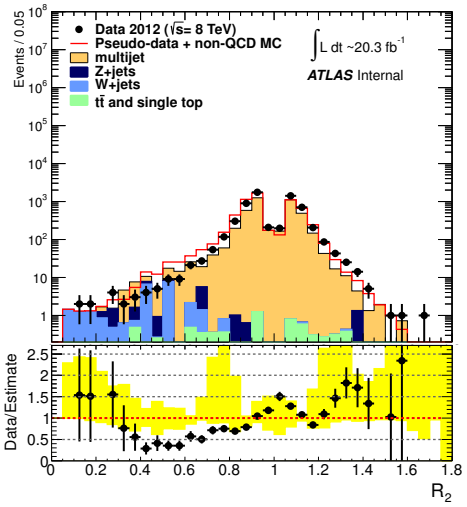

(c) truth jet p_{T} range of 600-1500 GeV

Figure 6.17: The R_2 distributions for b-veto jets is shown for three bins of truth jet p_{T}: 100 to 300 GeV (a), 300 to 600 GeV (b) and 600 to 1500 GeV (c). The 2012 data is shown in black and the sum of pseudo-data and non-QCD Monte Carlo is shown in red. These distributions have no low-side tail modification applied to the jet response. The yellow uncertainty band only includes statistical uncertainties on the Monte Carlo and pseudo-data samples, and the shape of the Gaussian region of the jet response.

6.5.4 Low-Side Tail Modification

The pseudo-data generated with the MC jet response did not accurately reproduce the observed data in the low-side tail region ($0 < R_2 < 0.8$) of the R_2 distributions in the 2011 and 2012 Mercedes analyses (see Figures 6.15-6.17). Therefore, the low-side tail of the 2011 inclusive and 2012 b-tag and b-veto jet responses were modified. The shape of the low-side tail was modified using the *double Gaussian fitting* method [2, 125, 136].

The double Gaussian fitting method consisted of the following steps:

(1) The low-side tail region of the Monte Carlo jet response was defined for each truth jet p_{T} bin using a Crystal Ball function (see Eq.(6.14)) [141].

(2) A Gaussian function was fitted to each low-side tail region in Monte Carlo jet response; a Gaussian function was found to be the best type of fit to the tail distribution [137, 136].

(3) The width of the fitted Gaussian was then multiplied by a value ($\Delta\sigma_{\mathrm{tail}}$) which changed the shape of the tail. The normalisation of the Gaussian function was also changed so that the response value at the start of the low-side tail region remained constant before and after the change in width. The resultant collection of modified jet responses were called the low-side tail jet response maps, and $\Delta\sigma_{\mathrm{tail}}$ values between ≈ 0.4 and 1.4 in steps of 0.05 were used to create them.

(4) Smeared pseudo-data was then produced with each of the low-side tail jet response maps, and the optimal $\Delta\sigma_{\mathrm{tail}}$ ($\Delta\sigma_{\mathrm{tail}}^{\mathrm{optimal}}$) was found for each truth jet p_{T} region of the Mercedes R_2 analysis. The optimal low-side tail shape produced pseudo-data that provided the best agreement with data in the R_2 distributions. The low-side tail jet response maps were also used to find $\Delta\sigma_{\mathrm{tail}}$ values for the low-side tail uncertainties ($\Delta\sigma_{\mathrm{tail}}^{\mathrm{low}}$ and $\Delta\sigma_{\mathrm{tail}}^{\mathrm{high}}$) in each truth jet p_{T} region (see section 6.6.2 for details on how the values were obtained and what uncertainty they cover).

Defining the Low-Side Tail Region

To define the low-side tail region of the jet response function, a Crystal Ball function [141] was used which has a continuous derivative over the full fitting region, $0.0 < R < 1.2$. However, it is important to stress that the Crystal Ball fit was *only* used as a tool to find the low-side tail region, and was only expected to fit properly in the Gaussian dominated region of jet response function

($0.8 < R < 1.2$). The Crystal Ball function has the functional form

$$f(x;\alpha,n,\bar{x},\sigma,N) = N\cdot\begin{cases}\exp\left(-\dfrac{(x-\bar{x})^2}{2\sigma^2}\right) & \text{for } \dfrac{x-\bar{x}}{\sigma} > -\alpha \\ A\cdot\left(B-\dfrac{x-\bar{x}}{\sigma}\right)^{-n} & \text{for } \dfrac{x-\bar{x}}{\sigma} \leq -\alpha,\end{cases} \tag{6.14}$$

where A and B are defined as

$$A = \left(\frac{n}{|\alpha|}\right)^n \cdot \exp\left(-\frac{|\alpha|^2}{2}\right), \tag{6.15a}$$

$$B = \frac{n}{|\alpha|} - |\alpha|\,. \tag{6.15b}$$

A Crystal Ball fit to the 2012 b-veto jet response in the 200-220 GeV truth jet p_{T} region is shown in Figure 6.18. This figure shows that the Crystal Ball function fits well to the Gaussian core of the jet response before turning away from the jet response function at the transition point (turning point). The transition point marks the end of the Gaussian region and the start of the low-side tail region of the jet response fucntion.

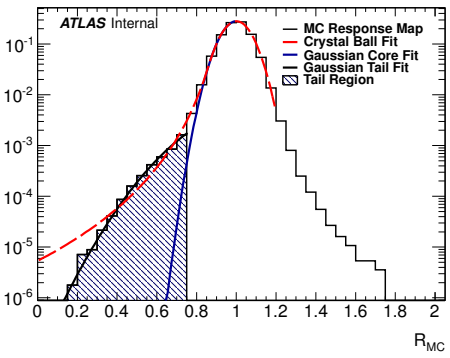

Figure 6.18: The Crystal Ball and Gaussian fits to the b-veto Monte Carlo jet response in the 200-220 GeV truth jet p_{T} region. The red dashed line shows the Crystal Ball fit, which was only used to find the transition point (turning point) in the MC jet response function. The blue dashed area shows the low-side tail region; this part of the jet response function will be modified to gain agreement in the Mercedes R_2 analysis. The black line shows the Gaussian fit to the low-side tail region of the Monte Carlo jet response. The width of the Gaussian fit was multiplied by $\Delta\sigma_{tail}$ to change the width of the tail. The blue line shows the fit to the Gaussian core of the Monte Carlo response; this will remain unchanged and is shown to demonstrate the Gaussian contribution in the low-side tail region.

The transition point (turning point) of the Crystal Ball function is the point where the Crystal Ball function changes from an exponential tail to a Gaussian function; it is defined from Eq.(6.14), as $x = \bar{x} - \alpha\sigma$. The transition point was used to find the region of the jet response function where the non-Gaussian contributions were dominant, and hence, the end of the low-side tail region. However, the end point of the low-side tail region was actually taken as $x = \bar{x} - \alpha\sigma - 0.1$. This was a conservative approach to modifying the low-side tail of the jet response, as this is two response bins lower than the transition point found from the Crystal Ball fitting. The impact of changing transition point on the generated pseudo-data was studied in detail, and the full details of this study can be found in section 6.7.2.

After the low-side tail region of the jet response function was defined by the Crystal Ball function, a Gaussian function was fitted to this region of the jet response. The Gaussian 'tail' fit had a mean fixed at the end of the low-side tail region, and the width was multiplied by $\Delta\sigma_{tail}$ to produce the modified low-side tail shape. The normalisation of the Gaussian tail function was also changed to keep the value of the jet response at the end of the tail region ($x = \bar{x} - \alpha\sigma - 0.1$) constant. This preserved the continuous nature of the jet response function before and after the modification of the low-side tail.

The low-side tail modification process was repeated for each truth jet p_{T} bin of the original Monte Carlo jet response maps to create the low-side tail jet response maps. These jet response maps were then used to find the optimal low-side tail shape in each truth jet p_{T} region. Figure 6.19 shows a few examples of the low-side tail shapes that were produced using the double Gaussian fitting method.

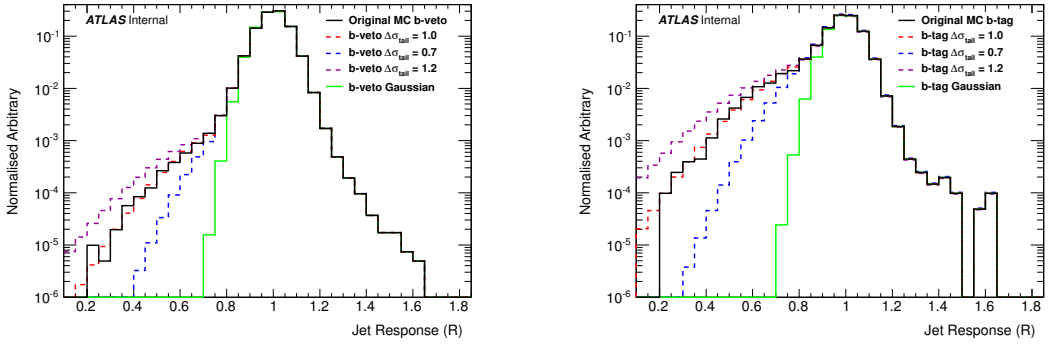

(a) b-veto truth jet p_{T} range 200-220 GeV

(b) b-tagged truth jet p_{T} range 200-220 GeV

Figure 6.19: Examples of different low-side tail shapes produced with the double Gaussian fitting method for a b-veto (a) and b-tagged (b) truth jet p_{T} region. The black histogram shows the original MC jet response. The red, blue and magenta histograms show various different low-side tail shapes produced for determining the optimal low-side tail shape of the jet response. The green histogram shows the Gaussian jet response, which was used in determining the low-side tail region of the R_2 distributions in the Mercedes analysis.

Determining the Optimal Low-Side Tail

The R_2 distributions were used to determine the optimal low-side tail shape of the jet response; however, to provide a fair comparison between the data and pseudo-data generated with the different low-side tail jet response maps, a 'tail' region also needed to be defined in the R_2 distributions. In this region, events should have predominantly originated from non-Gaussian jet fluctuations; this was important as the Mercedes analysis was only designed to probe the non-Gaussian tail of the jet response function.

To find the low-side tail region of the R_2 distributions, pseudo-data was generated with a Gaussian jet response. This jet response was created with the Gaussian **core** fit to the Monte Carlo jet response during the low-side tail modification process (see Figure 6.19). The pseudo-data generated from the Gaussian jet response was then used to obtain the Gaussian contribution to the R_2 distributions (see Figure 6.20). Finally, the end of the low-side tail region in the R_2 distribution was defined as the R_2 bin in which the contribution from the Gaussian pseudo-data estimate was more than 50% of the observed data.

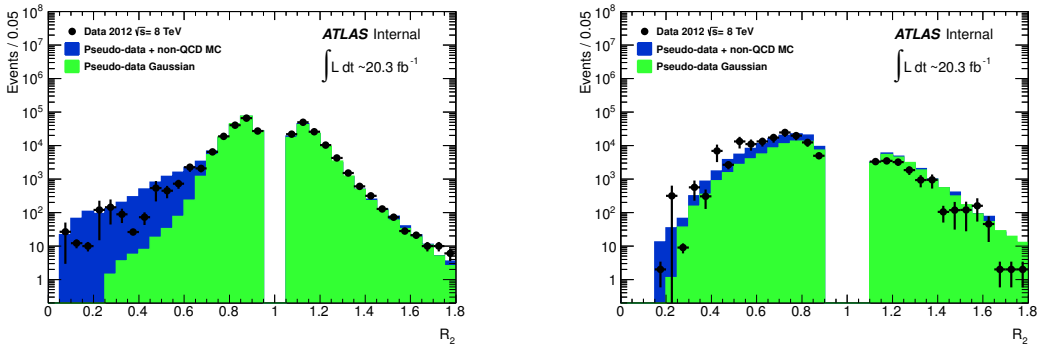

(a) b-veto 300-600 GeV truth jet p_{T} region

(b) b-tagged 100-300 GeV truth jet p_{T} region

Figure 6.20: The R_2 Gaussian pseudo-data distributions for the b-veto 300-600 GeV truth jet p_{T} region and b-tagged 100-300 GeV truth jet p_{T} region. The data is shown by the black points. The pseudo-data estimation from the Gaussian jet response is shown in light green, whereas the estimation from the MC jet response function is shown in blue.

Now that the low-side tail region of the R_2 distributions has been defined, the R_2 distributions produced from each of the low-side tail jet response maps can be compared to the data. However, not all of the data events within this region were from multijet processes. Therefore, to compare 'multijet data' to 'multijet pseudo-data', the contributions from non-multijet Monte Carlo (W+jets, Z+jets and $t\bar{t}$) were removed from the data distribution and the pseudo-data was renormalised to the 'multijet data'. If this resulted in the first bin of the multijet data distribution becoming negative, then that bin was combined with the adjacent bin in the histogram until the multijet data distribution was positive in the combined bin.

A χ^2 test was then performed on the two 'multijet' distributions to determine how well the pseudo-data generated from a particular low-side tail jet response agreed with the 'multijet data'. However, in some of the truth jet p_{T} regions in the 2012 analysis, the 'multijet data' distribution was not smooth (see Figure 6.22). This was a consequence of events from high pre-scaled triggers being included in only some of the R_2 histogram bins[3]. This effect limited the effectiveness of the χ^2 tests in these truth jet p_{T} regions. Therefore, the direct comparisons between the pseudo-data and observed data in the R_2 distributions were also taken into account when determining the optimal low-side tail shape of the jet response.

The optimal $\Delta\sigma_{\mathrm{tail}}$ for each truth jet p_{T} region was found using the normalised multijet tail region (see Figure 6.21 for an example). $\Delta\sigma_{\mathrm{tail}}^{\mathrm{optimal}}$ was the low-side tail shape that generated the pseudo-data which had the best comparison to the multijet data. In other words, it was the low-side tail shape that had one of the best χ^2 probability values and also had good agreement with data in the R_2 distribution. Values for $\Delta\sigma_{\mathrm{tail}}^{\mathrm{high}}$ and $\Delta\sigma_{\mathrm{tail}}^{\mathrm{low}}$ were also found for each truth jet p_{T} region using the normalised multijet tail region (more information can be found in section 6.6.2, which details the systematics of the jet smearing method).

Figure 6.21 shows the normalised tail region R_2 distributions for the 2011 inclusive jet response. It can be seen that the pseudo-data generated with the jet response that had the optimal tail (shown in red) agreed with the data better than the pseudo-data from the MC jet response (shown in grey). The normalised multijet tail region R_2 distributions in the 100-300 GeV truth jet p_{T} region for the 2012 b-veto and b-tag jet responses are shown in Figure 6.22. In Figure 6.22, the non-smooth nature of the observed data distribution in the low-side tail region presented a greater challenge to constrain the optimal shape of the low-side tail.

Tables 6.8-6.10 show the values of $\Delta\sigma_{\mathrm{tail}}^{\mathrm{low}}$, $\Delta\sigma_{\mathrm{tail}}^{\mathrm{optimal}}$ and $\Delta\sigma_{\mathrm{tail}}^{\mathrm{high}}$ for each truth jet p_{T} region of the 2011 inclusive jet response and the 2012 b-veto and b-tagged jet responses.

[3]This happened in the 2012 Mercedes analysis because of the lower leading jet p_{T} cut that was used; also the single-jet trigger prescales were larger during the 2012 data taking period

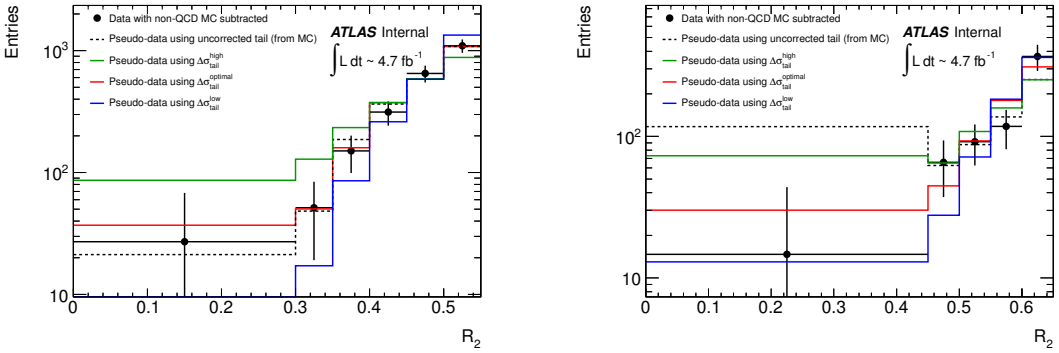

(a) Truth jet p_T range 100-300 GeV

(b) Truth jet p_T range 300-1000 GeV

Figure 6.21: The normalised low-side tail regions within the R_2 distribution for the 2011 inclusive jet response in truth jet p_T regions: 100-300 GeV (a) and 300-1000 GeV (b). The black points show the distribution from 2011 data - non-multijet MC. The red histogram shows the multijet distribution from the optimal jet response with the non-multijet MC subtracted, and the blue and green histograms show the distributions from the low-side tail high and low systematic tail response shapes respectively.

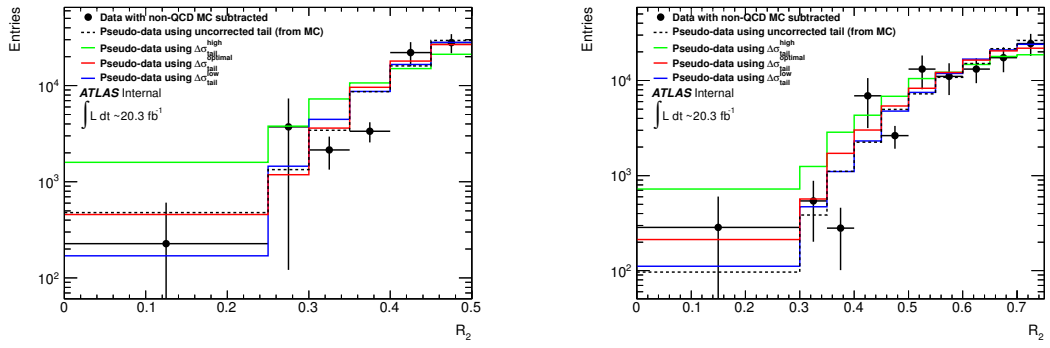

(a) b-veto truth jet p_T range 100-300 GeV

(b) b-tag truth jet p_T range 100-300 GeV

Figure 6.22: The normalised low-side tail regions within the R_2 distributions in the 100-300 GeV truth jet p_T region for the 2012 b-veto (a) and b-tag (b) jet responses. The black points show the distribution from 2012 data - non-multijet MC. The red histogram shows the multijet distribution from the optimal jet response with the non-multijet MC subtracted, and the blue and green histograms show the distributions from the low-side tail high and low systematic tail response shapes respectively.

Truth jet p_{T} range [GeV]	Parameter value		
	$\Delta\sigma_{\mathrm{tail}}^{\mathrm{low}}$	$\Delta\sigma_{\mathrm{tail}}^{\mathrm{optimal}}$	$\Delta\sigma_{\mathrm{tail}}^{\mathrm{high}}$
$100 < p_{\mathrm{T}} < 300$	0.70	0.95	1.15
$p_{\mathrm{T}} > 300$	0.80	0.85	1.00

Table 6.8: Values of $\Delta\sigma_{\mathrm{tail}}$ for the 2011 inclusive jet response.

Truth jet p_{T} range [GeV]	Parameter value		
	$\Delta\sigma_{\mathrm{tail}}^{\mathrm{low}}$	$\Delta\sigma_{\mathrm{tail}}^{\mathrm{optimal}}$	$\Delta\sigma_{\mathrm{tail}}^{\mathrm{high}}$
$100 < p_{\mathrm{T}} < 300$	1.10	1.30	1.45
$300 < p_{\mathrm{T}} < 600$	0.65	0.80	0.95
$p_{\mathrm{T}} > 600$	0.55	0.70	0.85

Table 6.9: Values of $\Delta\sigma_{\mathrm{tail}}$ for the 2012 b-veto jet response.

Truth jet p_{T} range [GeV]	Parameter value		
	$\Delta\sigma_{\mathrm{tail}}^{\mathrm{low}}$	$\Delta\sigma_{\mathrm{tail}}^{\mathrm{optimal}}$	$\Delta\sigma_{\mathrm{tail}}^{\mathrm{high}}$
$100 < p_{\mathrm{T}} < 300$	0.85	1.00	1.20
$p_{\mathrm{T}} > 300$	0.80	0.95	1.10

Table 6.10: Values of $\Delta\sigma_{\mathrm{tail}}$ for the 2012 b-tag jet response.

6.5.5 R_2 Distributions with the Modified Low-Side Tail

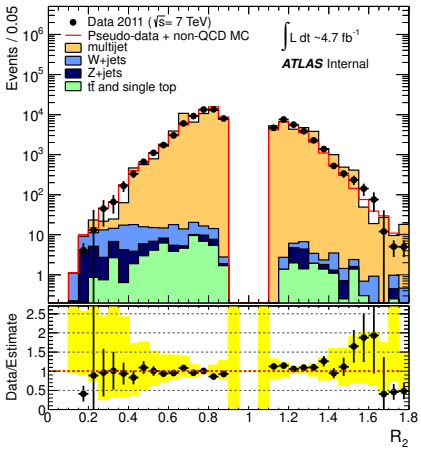

(a) Truth jet p_T range of 100-300 GeV

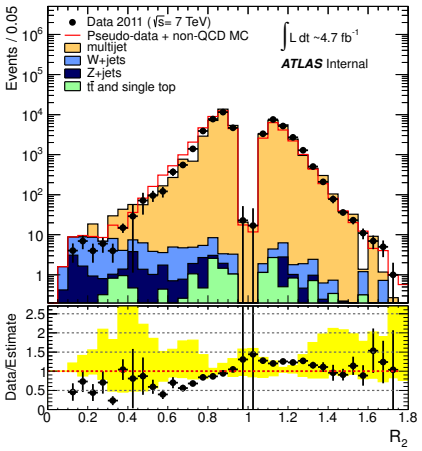

(b) Truth jet p_T range of 300-1000 GeV

Figure 6.23: The R_2 distribution for candidate jets in 2011 data set shown for two bins of truth jet p_T: 100-300 GeV (a) and 300-1000 GeV (b). The 2011 data is shown in black, and the sum of pseudo-data and non-multijet Monte Carlo is shown in red. The yellow uncertainty band includes uncertainties from MC statistics, seed statistics, pseudo-data statistics, mean-shift up, constraining the low-side tail and Gaussian shape of the jet response function.

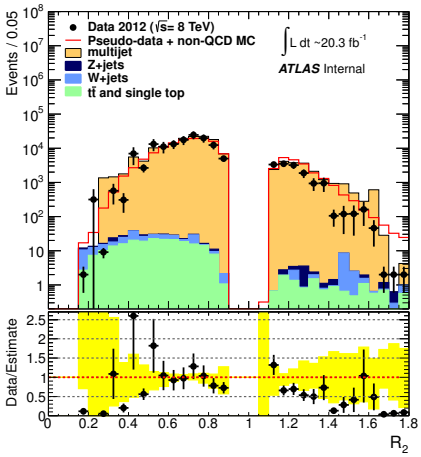

(a) Truth jet p_T range of 100-300 GeV

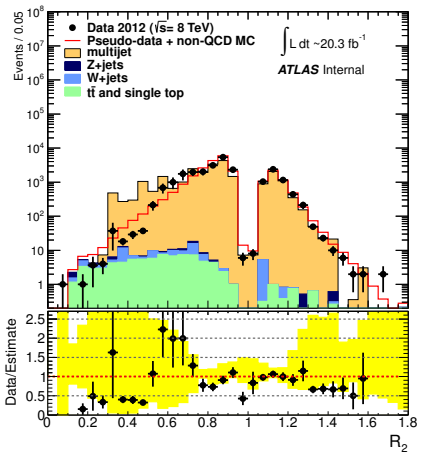

(b) Truth jet p_T range of 300-1500 GeV

Figure 6.24: The R_2 distribution for b-tagged candidate jets in 2012 data set shown for two bins of truth jet p_T: 100-300 GeV (a) and 300-1500 GeV (b). The 2012 data is shown in black, and the sum of pseudo-data and non-multijet Monte Carlo is shown in red. The yellow uncertainty band includes uncertainties from MC statistics, seed statistics, pseudo-data statistics, constraining the low-side tail and Gaussian shape of the jet response function.

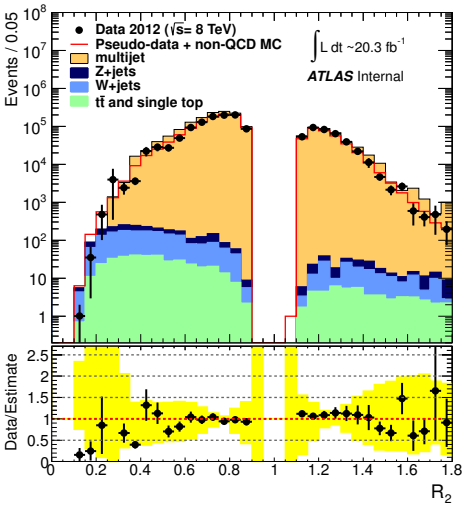

(a) Truth jet p_{T} range of 100-300 GeV

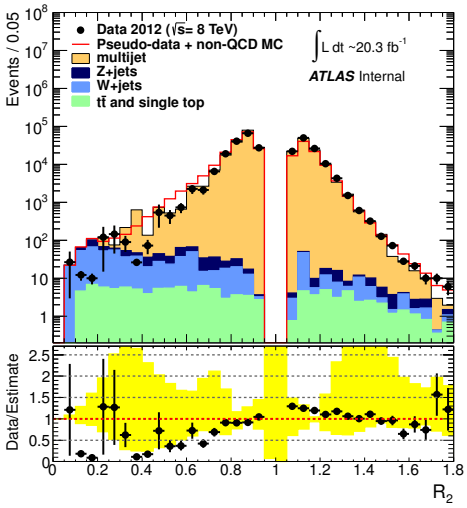

(b) Truth jet p_{T} range of 300-600 GeV

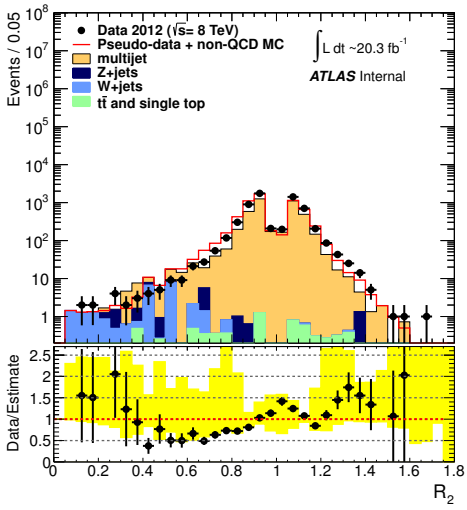

(c) Truth jet p_{T} range of 600-1500 GeV

Figure 6.25: The R_2 distribution for b-veto candidate jets in the 2012 data set shown for three bins of truth jet p_{T}: 100-300 GeV (a), 300-600 GeV (b) and 600-1500 GeV (c). The 2012 data is shown in black and the sum of pseudo-data and non-multijet Monte Carlo is shown in red. The yellow uncertainty band includes uncertainties from MC statistics, seed statistics, pseudo-data statistics, constraining the low-side tail and Gaussian shape of the jet response function.

Figure 6.23 shows the R_2 distribution for candidate jets in the 2011 analysis. The pseudo-data (shown in red) was generated using the jet response map with the optimal low-side tail corrections with the additional Gaussian smearing. It can be seen that the agreement between the pseudo-data and data has improved in both truth jet p_{T} bins.

Figures 6.24 and 6.25 show the R_2 distributions for b-veto and b-tagged jets in 2012 analysis. The pseudo-data was generated with the jet response that had optimal low-side tail and with the additional Gaussian and ϕ smearing corrections applied. The agreement in the low-side tail region of the Mercedes R_2 distributions has improved compared to the 2012 Monte Carlo jet responses.

The jet response functions with the optimal low-side tail shape were then used in the searches for SUSY to estimate multijet background contribution (see Chapter 7).

6.6 Uncertainties of the Jet Smearing Method

The uncertainties of the jet smearing method originate from three different sources: the statistical uncertainty on both the number of seed events and the number of smeared events, the uncertainty on how well the jet response is understood and constrained to data should be considered, and finally any uncertainty or bias in the seed selection process.

6.6.1 Statistical Uncertainties

Seed Statistics

To derive the statistical uncertainty due to a finite number of seed events, a seed sample of n_{seed} events which are each smeared N_{smear} times is considered. The total number of smeared events is $N_{\mathrm{tot}} = n_{\mathrm{seed}} N_{\mathrm{smear}}$, and these smeared events are plotted in a histogram, for example a $E_{\mathrm{T}}^{\mathrm{miss}}$ distribution. The total number of events in bin j of the histogram (N_j) is

$$N_j = N_{\mathrm{smear}} \sum_{i=1}^{n_{\mathrm{seed}}} w_{ij}, \tag{6.16}$$

where the weight w_{ij} is the probability that a smeared (pseudo-data) version of the i^{th} seed event will be registered in the j^{th} histogram bin. The weights are calculated from the jet response function, and in the context of statistical errors may be considered to be known with perfect accuracy. The bins of the histogram are also approximated to be uncorrelated.

It is a standard statistical result that "the variance of the sum is the sum of the variances",

$$\sigma^2\left(\sum_i w_{ij}\right) = \sum_i \sigma^2(w_{ij}). \tag{6.17}$$

if there is no uncertainty on w_{ij}, this is just a constant. Since $\sigma(kx) = k\sigma(x)$,

$$\sigma^2(w_{ij}) = w_{ij}^2\sigma^2(1 \text{ event}) = w_{ij}^2. \tag{6.18}$$

If a further assumption that the seed statistics are Poissonian (and hence the variance is equal to the mean, i.e. 1 in this case), $\sigma(N_j)$ is given by

$$\sigma(N_j) = N_{\text{smear}}\sqrt{\sum_i w_{ij}^2}. \tag{6.19}$$

To normalise the histogram to unit area, N_j and $\sigma(N_j)$ have to be divided by N_{tot}, giving

$$\rho_j = \frac{1}{n_{\text{seed}}}\sum_i w_{ij}; \tag{6.20}$$

$$\sigma_{\text{seed}}(\rho_j) = \frac{1}{n_{\text{seed}}}\sqrt{\sum_i w_{ij}^2} \tag{6.21}$$

Figure 6.26 shows how the weights work in practice. In this Figure, two seeds (i) in different $E_{\text{T}}^{\text{miss}}$ histogram bins (j) are smeared to generate the distributions shown in blue and green. It can be seen that each bin in the $E_{\text{T}}^{\text{miss}}$ histogram receives a certain number of entries from each seed event, and since the pseudo-data distributions are normalised to the total number of smearings, this number can be interpreted as a weight (w_{ij}).

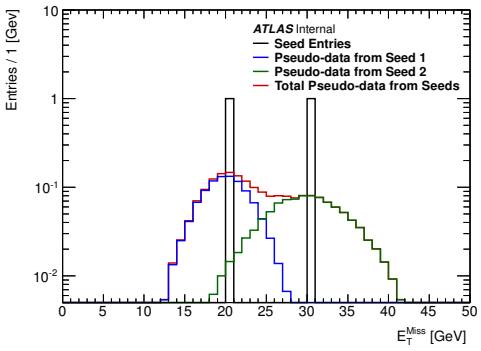

Figure 6.26: An example of smearing two seed events in a $E_{\mathrm{T}}^{\mathrm{miss}}$ histogram. The original entries from the two seed events are shown in black. Example pseudo-data distributions (normalised to the total number of smearings) from each seed are shown in blue and green. The total pseudo-data distribution generated from all of the seeds is shown in red; this distribution would be equivalent to the final pseudo-data $E_{\mathrm{T}}^{\mathrm{miss}}$ histogram (before normalisation) if only these two seed events were smeared.

Smearing Statistics

N_{smear} was always chosen to be sufficiently large (3000-10000); therefore this uncertainty is negligible. Its derivation is only included for completeness. The number of smeared events in the j^{th} bin of the histogram arising from the i^{th} seed event is

$$N_{ij} = N_{\mathrm{smear}}\, w_{ij} \tag{6.22}$$

The Poissonian statistical error on this is simply $\sigma_{ij} = \sqrt{N_{ij}}$. Furthermore, the statistical error σ_j on N_j is just given again by the sum of the variances:

$$\sigma_j^2 = \sum_i \sigma_{ij}^2 = \sum_i N_{ij}. \tag{6.23}$$

Normalising this to unit area gives

$$\sigma_{\mathrm{smr}}(\rho_j) = \frac{1}{N_{\mathrm{tot}}} \sqrt{\sum_i N_{ij}} \tag{6.24}$$

Full statistical uncertainty

The uncertainties due to finite seed and smearing statistics can be combined to obtain the full statistical uncertainty by adding the variances:

$$\sigma^2(\rho_j) = \sigma^2_{\text{seed}} + \sigma^2_{\text{smr}} = \frac{1}{N_{\text{tot}^2}} \left(\sum_i N_{ij}^2 + \sum_i N_{ij} \right), \tag{6.25}$$

using $w_{ij} = {}^{N_{ij}}/_{N_{\text{smear}}}$ from Eq.(6.16). Finally, combining the summations gives

$$\sigma(\rho_j) = \frac{1}{n_{\text{seed}}\, N_{\text{smear}}} \sqrt{\sum_i N_{ij}\,(N_{ij}+1)}. \tag{6.26}$$

6.6.2 Uncertainties on the Shape of the Jet Response Function

The uncertainties on constraining the shape of the jet response function fall into two types:

- The uncertainty on the Gaussian response width. This was introduced through the uncertainty on $\sigma_{correction}(p_{\text{T}})$ (described in section 6.3), where ±0.05 was added to $\sigma_{correction}(p_{\text{T}})$ during the additional Gaussian p_{T} smearing process. The motivation behind this number comes from studies in the high R_2 region of 2011 $\sqrt{s} = 7$ TeV data Mercedes analysis [125, 139]. Events in this region originate from multiple Gaussian jet p_{T} fluctuations causing the $E_{\text{T}}^{\text{miss}}$ in the event. To be conservative, this uncertainty was retained for the 2012 $\sqrt{s} = 8$ TeV data, where ±0.05 spans the difference between the data and pseudo-data in the R_2 distributions and also the p_{T} asymmetry distributions.

- The uncertainty on the optimal shape of the non-Gaussian tail. This was introduced with an uncertainty on the tail value parameter, $\Delta\sigma_{tail}$. This quantifies the amount within which the low-side tail shape can change within the statistical uncertainties of the observed data points in the normalised low-side tail region R_2 distributions (see Figures 6.21 and 6.22). It is a measure of our ability to constrain the low-side tail to data. The values of $\Delta\sigma_{tail}^{high}$ and $\Delta\sigma_{tail}^{low}$ were chosen to encompass the region of statistical uncertainty on the data points, and give a minimum 1σ deviation from the optimal tail value. However, this was not always possible with events from high prescaled triggers in the low-side tail generating large statistical uncertainties. Normally, the values of $\Delta\sigma_{tail}^{high}$ and $\Delta\sigma_{tail}^{low}$ were of the order of ±0.15 away from $\Delta\sigma_{tail}^{optimal}$. Tables 6.8-6.10 show the values of $\Delta\sigma_{tail}^{high}$ and $\Delta\sigma_{tail}^{low}$ for the 2011 and 2012 data set analyses.

6.6.3 Seed Selection Cut

In the 2011 data set analysis, the seed selection cut created a minor bias on the leading jet p_{T} of the seed events (see section 5.4.1 and Figure 5.3(b)). To cover this bias, an uncertainty was introduced called the 'mean-shift up'. This uncertainty shifted the mean of the optimal jet response function up by 10%. It was only applied in the 2011 analysis, since no bias in the leading jet p_{T} of seed events was observed in the 2012 data set analysis (see Figure 5.4(b)).

6.7 Validation Studies

This section details the investigative studies that were used to validate the jet smearing method in the 2011 and 2012 data set analyses.

6.7.1 The $|\eta|$ Dependence of the Jet Response

The jet response could also depend on the $|\eta|$ coordinate of the fluctuating jet since the ATLAS detector has different calorimeter systems in different $|\eta|$ regions of the detector. For example, a jet within the 'crack' region of the calorimeter (approximately $1.4 < |\eta| < 1.6$) may have a broader response than a jet within the 'central region' ($|\eta| < 0.8$) because of the gap between the electromagnetic and hadronic calorimeters. Whilst binning the jet response in $p_{\mathrm{T}}^{\mathrm{truth}}$ partially accounts for the dependency on the $|\eta|$ coordinate, if the low-side tail shape of the jet response was strongly dependent on the $|\eta|$ coordinate of the fluctuating jet, a different tail correction would be required for each $|\eta|$ region. Therefore, the $|\eta|$ dependence of the jet response was investigated. The following $|\eta|$ regions were studied:

- Central region ($|\eta| < 0.8$).
- Extended tile barrel ($0.8 < |\eta| < 1.2$).
- Extended crack region ($1.2 < |\eta| < 2.1$).
- Endcap region ($2.1 < |\eta| < 2.8$).

The Mercedes R_2 distributions for each $|\eta|$ region are shown in Figure 6.27 for the inclusive candidate jets in the 2011 data set analysis, and for b-veto and b-tagged candidate jets in the 2012 analysis in Figures 6.28 and 6.29. The pseudo-data distributions in these figures were made with the optimal smearing configuration, which included the ϕ smearing corrections in the 2012 data set analysis. The full systematics of the jet smearing method (see section 6.6) were applied to the pseudo-data in each analysis.

Since Figures 6.27-6.29 show good agreement between the pseudo-data estimate and data within the systematic uncertainties, the jet response did not require a different low-side tail correction derived for each $|\eta|$ region of the calorimeter. Figures 6.29(c) and (d) also show that the statistics in data were not sufficient to probe the extended crack and endcap regions of the calorimeter in the 2012 b-tag Mercedes analysis; therefore, it would not have been possible to make special low-side tail corrections for these $|\eta|$ regions.

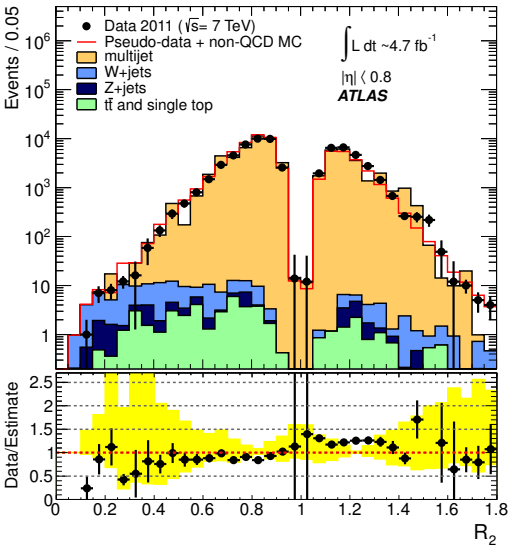

(a) Central Region $|\eta| < 0.8$

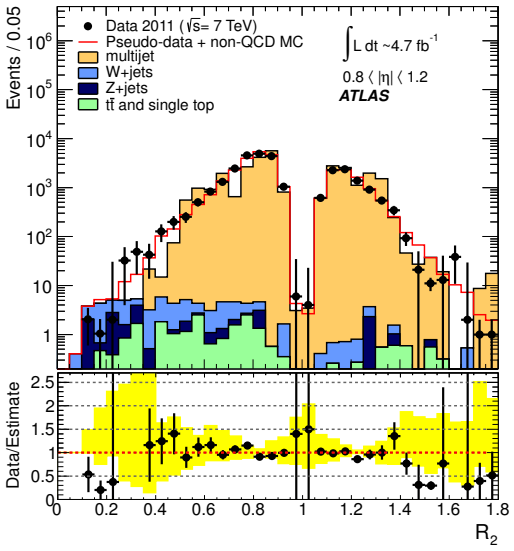

(b) Extended Tile Region $0.8 < |\eta| < 1.2$

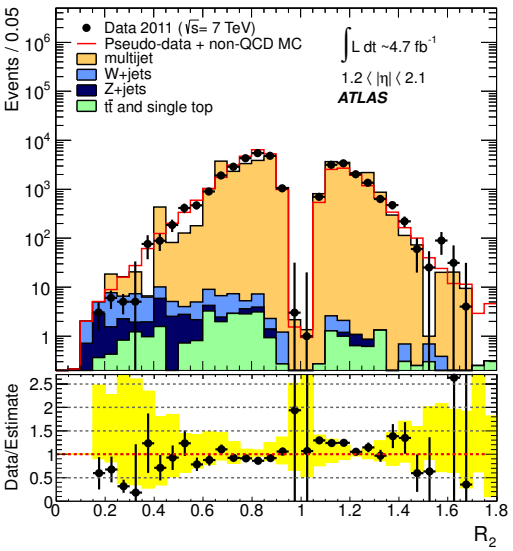

(c) Extended Crack Region $1.2 < |\eta| < 2.1$

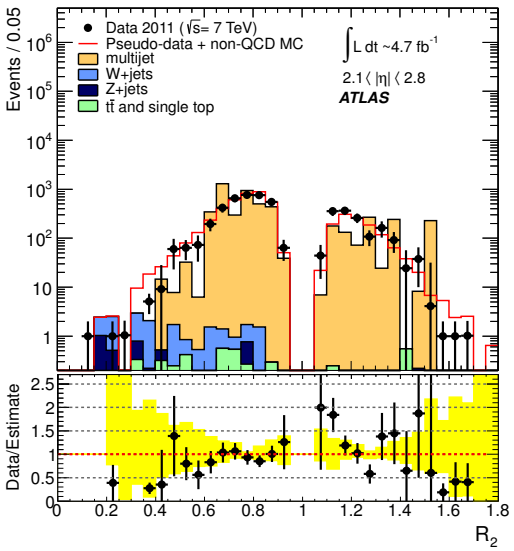

(d) Endcap Region $2.1 < |\eta| < 2.8$

Figure 6.27: The R_2 distribution for candidate jets in the 2011 analysis shown for each of the four different $|\eta|$ regions: central (a), extended tile (b), extended crack (c) and endcap (d). The 2011 data is shown in black and the sum of pseudo-data from the optimal jet response and non-multijet Monte Carlo is shown in red. The yellow uncertainty band includes uncertainties due to MC statistics, seed statistics, pseudo-data statistics, constraining the low-side tail and Gaussian shape of the jet response function.

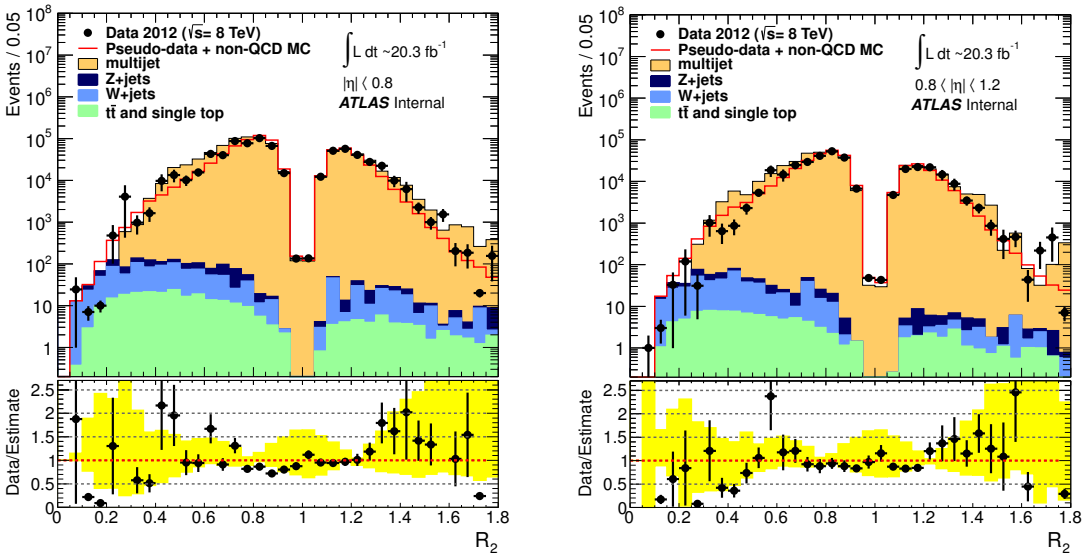

(a) Central Region $|\eta| < 0.8$

(b) Extended Tile Region $0.8 < |\eta| < 1.2$

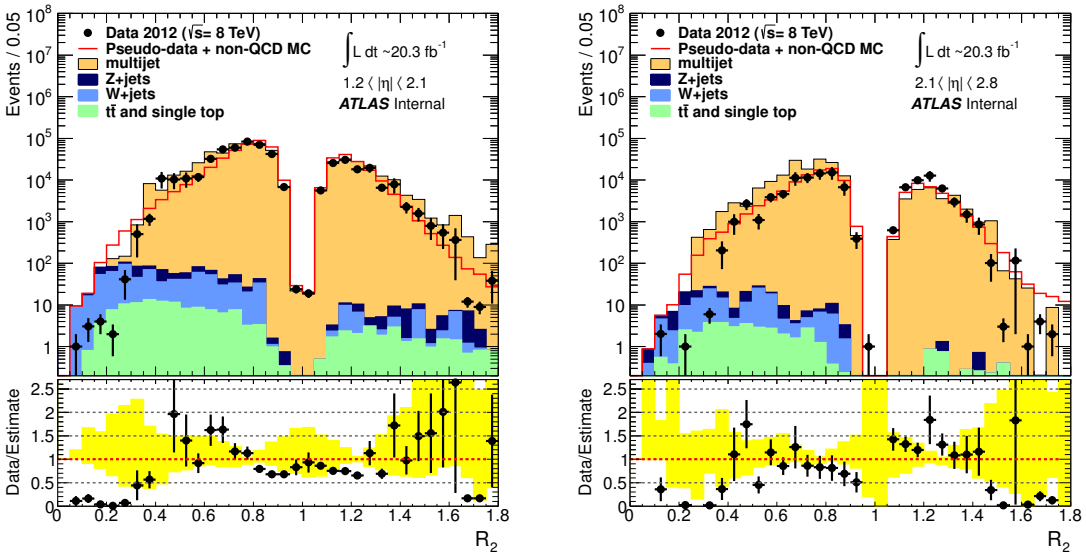

(c) Extended Crack Region $1.2 < |\eta| < 2.1$

(d) Endcap Region $2.1 < |\eta| < 2.8$

Figure 6.28: The R_2 distribution for b-veto candidate jets in the 2012 data set analysis shown for each of the four different $|\eta|$ regions: central (a), extended tile (b), extended crack (c) and endcap (d). The 2012 data is shown in black and the sum of pseudo-data from the optimal jet response and non-multijet Monte Carlo is shown in red. The yellow uncertainty band includes uncertainties due to MC statistics, seed statistics, pseudo-data statistics, constraining the low-side tail and Gaussian shape of the jet response function.

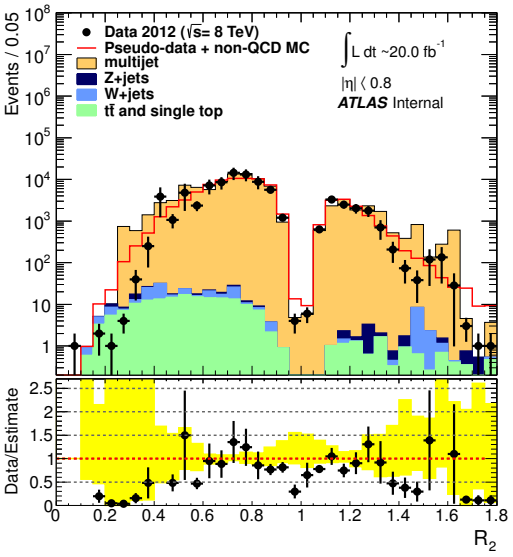

(a) Central Region $|\eta| < 0.8$

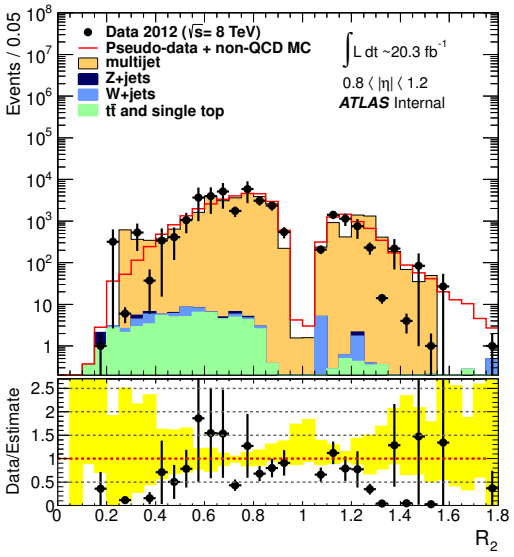

(b) Extended Tile Region $0.8 < |\eta| < 1.2$

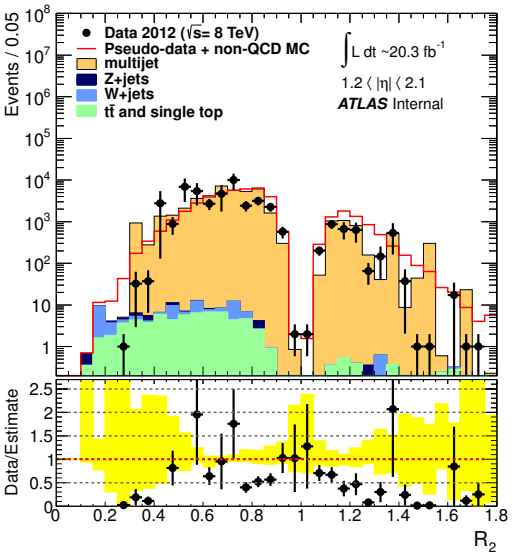

(c) Extended Crack Region $1.2 < |\eta| < 2.1$

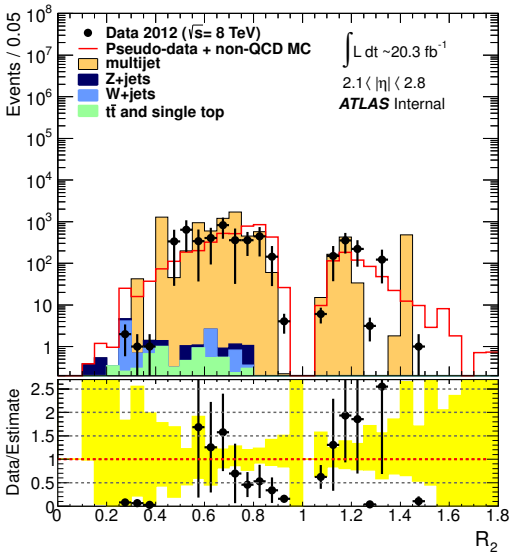

(d) Endcap Region $2.1 < |\eta| < 2.8$

Figure 6.29: The R_2 distribution for b-tagged candidate jets in the 2012 data set analysis shown for each of the the four different $|\eta|$ regions: central (a), extended tile (b), extended crack (c) and endcap (d). The 2012 data is shown in black and the sum of pseudo-data from the optimal jet response and non-multijet Monte Carlo is shown in red. The yellow uncertainty band includes uncertainties due to MC statistics, seed statistics, pseudo-data statistics, constraining the low-side tail and Gaussian shape of the jet response function.

6.7.2 Transition Point Study

The transition point investigative study was used to determine whether changing the transition/turning point of the low-side tail region affected the baseline multijet estimate. The transition point was defined by the Crystal Ball function (Eq.(6.14)), where the exponential tail turns into the Gaussian function, i.e., when $x = \bar{x} - \alpha\sigma$. The dependence of the baseline estimate on the Crystal Ball fit was modelled by artificially moving the transition point two response bins either side (± 0.1) of the transition point obtained from the Crystal Ball fit[4]. The value of ± 0.1 was chosen as this covered a significant region of change in the transition point. Figure 6.18 shows that the Crystal Ball function fits the Gaussian region of the jet response well; therefore, it is unlikely that the transition point would be incorrect by two response histogram bins.

The seed events were smeared 3000 times with the transition point up and down jet response maps to produce the different pseudo-data samples. Example jet response functions from these maps are shown in Figure 6.30. The Mercedes analysis selection cuts were then applied to the transition point pseudo-data samples. The Mercedes analysis was chosen because the R_2 distributions were most sensitive to a change in the shape of the low-side tail of the jet response. This made the Mercedes analysis ideal for testing the different transition points. The b-veto and b-tagged R_2 distributions made from the transition point jet responses maps are shown in Figures 6.31 and 6.32.

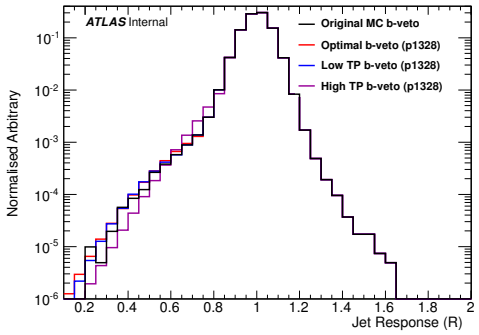

(a) R_2 distribution

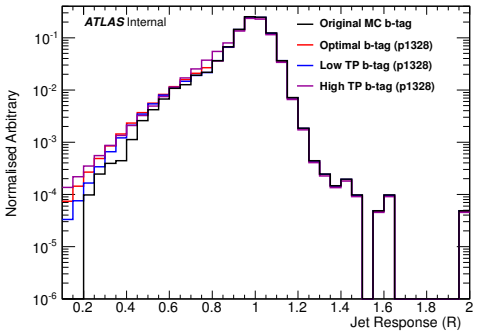

(b) R_2 distribution

Figure 6.30: The b-veto and b-tag transition point jet response functions for the $200 - 220\,\text{GeV}$ truth jet p_T region. The black histogram shows the shape of the MC jet response. The red histogram shows the optimal jet response; this was used to make the baseline estimate. The blue and magenta histograms show the transition point low ($x = \bar{x} - \alpha\sigma - 0.2$) and high ($x = \bar{x} - \alpha\sigma$) jet response shapes respectively. These were used to provide an uncertainty on the baseline estimation associated with the definition of the low-side tail region. It should be noted that the optimal transition point was defined as $x = \bar{x} - \alpha\sigma - 0.1$.

[4]The baseline jet smearing method uses $x = \bar{x} - \alpha\sigma - 0.1$ as the transition point, see section 6.5.4

Figures 6.31 and 6.32 show the Mercedes R_2 distributions for b-veto and b-tagged candidate jets in the 2012 transition point investigative study. The figures show that changing the transition point of the low-side tail in the jet response function only marginally affects the pseudo-data distribution. This can be seen more clearly in the normalised low-side tail region R_2 distributions (Figures 6.31(b) and 6.32(b)), where there was only a minor difference between the different pseudo-data estimates (red, green and blue distributions). Any difference due to the transition point definition was covered by the low-side tail uncertainty. Finally, the results from this study showed that using the Crystal Ball fit to define the low-side tail region of the jet response was a robust method.

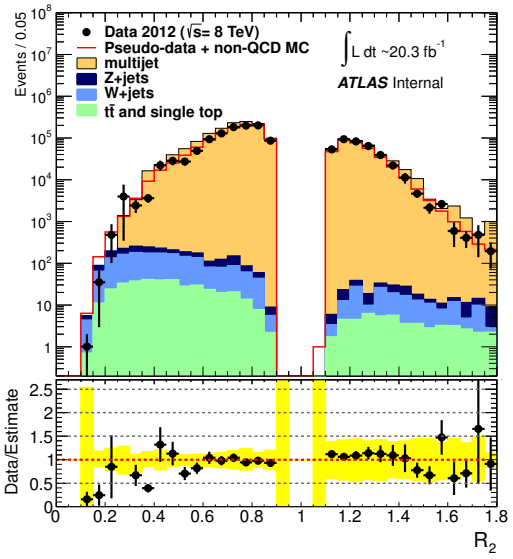

(a) R_2 with the fluctuating jets in the truth jet p_T range of 100-300 GeV

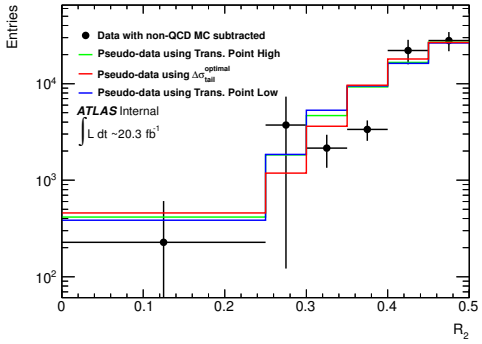

(b) R_2 with the fluctuating jets in the truth jet p_T range of 100-300 GeV in the normalised low-side tail region

Figure 6.31: The R_2 distribution (a) and the normalised multijet low-side tail region R_2 distribution (b) shown for b-veto candidate jets in the 100-300 GeV truth jet p_T region. In figure (a), the 2012 data is shown in black and the sum of pseudo-data generated with the optimal jet response and non-multijet Monte Carlo is shown in red. The yellow uncertainty band shows the uncertainties due to MC statistics and the change in transition point. In figure (b), the black points show the R_2 distribution from 2012 data - the non-multijet MC. The red distribution shows the multijet distribution from the optimal jet response with the non-multijet MC subtracted, and the green and blue distributions show the distributions from the transition point high and low systematic response shapes respectively.

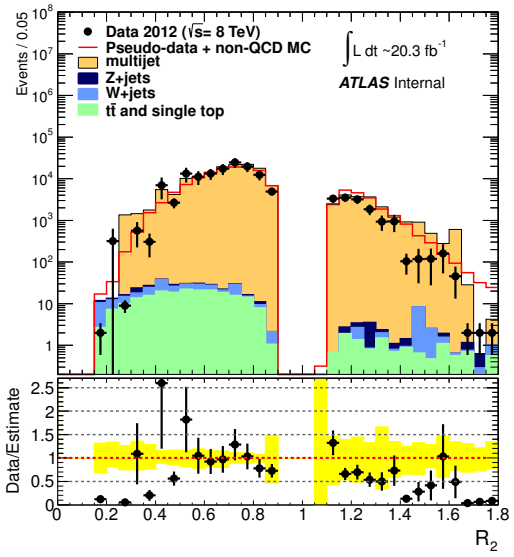

(a) R_2 with the fluctuating jets truth jet p_T range of 100-300 GeV

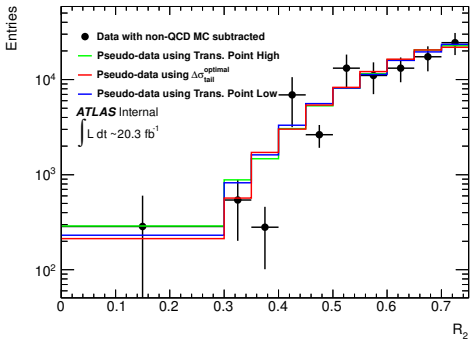

(b) R_2 with the fluctuating jets truth jet p_T range of 100-300 GeV in the normalised low-side tail region

Figure 6.32: The R_2 distribution (a) and the normalised multijet low-side tail region R_2 distribution (b) shown for b-tagged candidate jets in the 100-300 GeV truth jet p_T region. In figure (a), the 2012 data is shown in black and the sum of pseudo-data generated with the optimal jet response and non-multijet Monte Carlo is shown in red. The yellow uncertainty band shows the uncertainties due to MC statistics and the change in transition point. In figure (b), the black points show the R_2 distribution from 2012 data - the non-multijet MC. The red distribution shows the multijet distribution from the optimal jet response with the non-multijet MC subtracted, and the green and blue distributions show the distributions from the transition point high and low systematic response shapes respectively.

6.7.3 Forward Jet Smearing Study

Only signal jets within the seed event are normally smeared during the smearing process. Signal jets are defined in the object definitions in section 3.6.1, with one of their key selection criteria being $|\eta| < 2.8$. However, all of the jets within the event can contribute to the $E_{\mathrm{T}}^{\mathrm{miss}}$. Therefore, to ensure that the $E_{\mathrm{T}}^{\mathrm{miss}}$ of the pseudo-data was not affected by 'forward' jets ($2.8 < |\eta| < 4.5$), the forward jets were also smeared with the optimal jet response. It should be noted that the optimal jet response was derived using only signal jets; however, from the η dependent investigative study it was found that the jet response was not strongly dependent on the $|\eta|$ of the jet (section 6.7.1).

The Mercedes analysis was chosen to investigate the effect of smearing forward jets due to its sensitivity to a change in the shape of the low-side tail of the jet response. Therefore, if the smearing of forward jets was going to significantly change the baseline estimate in the multijet CR of SUSY analyses, then the R_2 distributions with forward jet smearing would be significantly different from the distribution from the optimal tail shape.

Figures 6.33 and 6.34 show the b-veto and b-tag R_2 distribution in the 2012 analysis when forward jets were included in the smearing process. It can be seen that if the pseudo-data distributions have sufficient statistics, then the inclusion of the forward jets into the smearing process only produces a minor effect in the R_2 distribution of the pseudo-data. This can be seen more clearly in the normalised multijet low-side tail region of the R_2 distribution in Figures 6.33(b) and 6.34(b). Clearly, any differences between the distributions as a result of including forward jets into the smearing process were covered by the low-side tail systematics of the jet smearing method (see section 6.6.2).

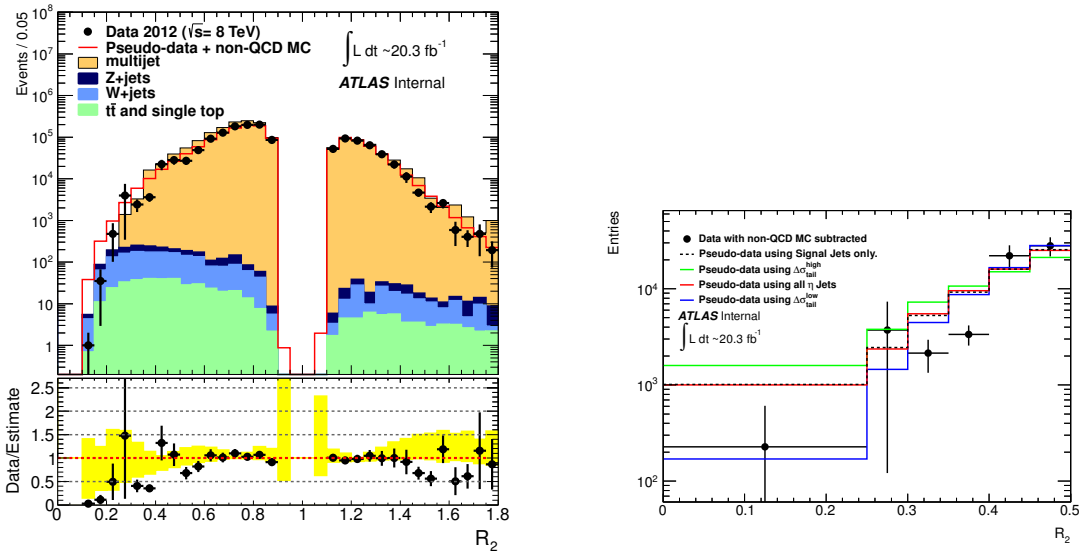

(a) R_2 distribution

(b) Normalised Low-side Tail Region

Figure 6.33: The R_2 distribution (a) and the normalised multijet low-side tail region R_2 distribution (b) for b-veto jets in the 100 to 300 GeV truth jet p_T region. In figure (a) the 2012 data is shown in black. The sum of the pseudo-data generated with the optimal jet response (smearing jets with $|\eta| < 4.5$) and the non-multijet Monte Carlo is shown in red. The yellow uncertainty band shows the uncertainties due to: MC statistics, seed statistics, pseudo-data statistics. In figure (b) the black points show the distribution from 2012 data - non-multijet MC. The black dashed line shows the multijet distribution from the optimal jet response (smearing signal jets only: $|\eta| < 2.8$) with the non-multijet MC subtracted, and the red line shows the distribution from smearing signal jets with $|\eta| <$ 4.5 with the non-multijet MC subtracted. The blue and green histograms show the R_2 distributions from the high and low jet response tail systematics respectively.

6.8 Summary

This chapter described how the jet response functions were measured and constrained to data in the 2011 and 2012 data set analyses. The final data constrained jet responses described in the Chapter were used to estimate the multijet background in the SUSY analyses described in Chapter 7.

Section 6.2 described how the initial MC jet p_{T} response was generated using multijet MC samples. Section 6.3 documented the dijet p_{T} balance analysis which was used to constrain the Gaussian core of the jet response to data. The dijet $\Delta\phi$ analysis was described in Section 6.4, which explained how the ϕ-smearing corrections were found for the 2012 data set analysis and the reasons why ϕ-smearing of jets was introduced into the jet smearing method. Section 6.5 described the Mercedes analysis, which was used to constrain the non-Gaussian tail of the jet response. Section 6.6 documented the statistical and systematic uncertainties considered in the jet smearing method; these included statistical uncertainties on the pseudo-data and systematic uncertainties on the jet response

function. Finally, Section 6.7 documented the validation studies performed in the 2011 and 2012 analyses used to validate the jet smearing method. These validation studies included checking the η dependency of the jet response, studying the inclusion of forward jets in the smearing process, and changing the transition point of the low-side tail in the jet response function.

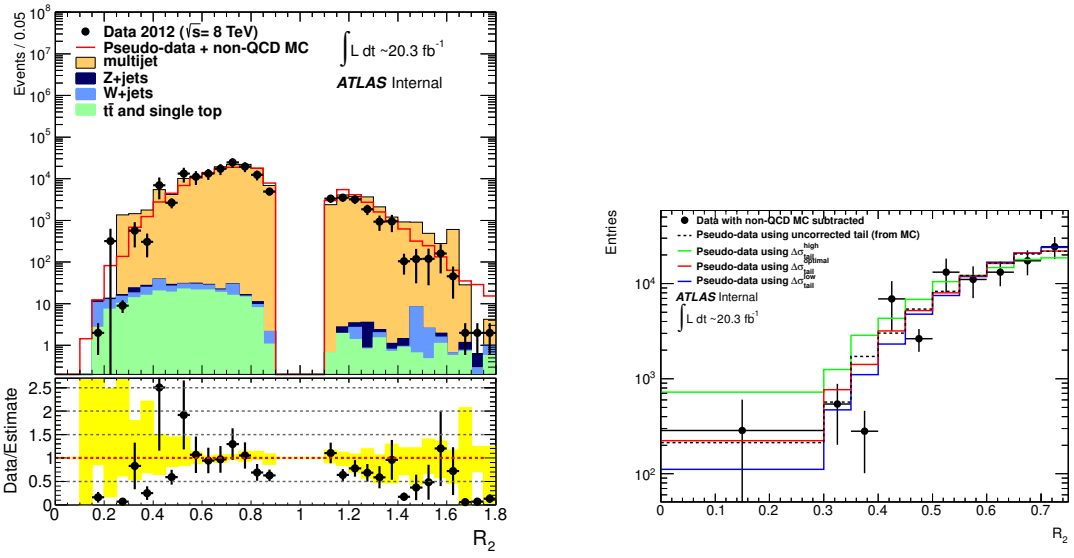

(a) R_2 distribution

(b) Normalised Low-side Tail Region

Figure 6.34: The R_2 distribution (a) and the normalised multijet low-side tail region R_2 distribution (b) for b-tag jets in the 100 to 300 GeV truth jet p_T region. In figure (a) the data is shown in black. The sum of the pseudo-data generated with the optimal jet response (smearing jets with $|\eta| < 4.5$) and the non-multijet Monte Carlo is shown in red. The yellow uncertainty band shows the uncertainties due to MC statistics, seed statistics and pseudo-data statistics. In figure (b) the black points show the distribution from data - non-multijet MC. The black dashed line shows the multijet distribution from the optimal jet response (smearing signal jets with $|\eta| < 2.8$) with the non-multijet MC subtracted, and the red line shows the distribution from smearing signal jets with $|\eta| < 4.5$ with the non-multijet MC subtracted. The blue and green histograms show the R_2 distributions from the high and low jet response tail systematics respectively.

Chapter 7

Jets, Missing Transverse Energy and Zero Leptons Analysis Search for SUSY

7.1 Introduction

All of the work in this thesis was motivated by searches for Supersymmetry. This chapter will detail the "ATLAS jets, missing transverse energy with zero leptons" searches for supersymmetry. There have been multiple publications and conference notes describing this analysis during run I of the LHC. Two publications will be documented in this chapter describing the final 2011 $\sqrt{s} = 7\,\text{TeV}$ [2] and 2012 $\sqrt{s} = 8\,\text{TeV}$ [1] data set analyses. The author provided the QCD multijets background estimation for all of the Signal, Validation and Control Regions in both of these analyses using the jet smearing method (documented in Chapters 5 and 6). The author also documented the jet smearing analysis in the internal documentation for both of these analyses (see references [125] and [139]).

Section 7.2 will outline the analysis strategy for searching for strongly produced squarks and gluinos. Section 7.3 documents the final 2011 $4.7\,\text{fb}^{-1}$ $\sqrt{s} = 7\,\text{TeV}$ analysis published in August 2012 [2]. Section 7.4 will summarise the final 2012 $20.3\,\text{fb}^{-1}$ $\sqrt{s} = 8\,\text{TeV}$ analysis which was published in September 2014 [1]. Finally, Section 7.5 will provide a general conclusion of the results from these searches.

7.2 Analysis Strategy

The "ATLAS jets, $E_{\text{T}}^{\text{miss}}$ and zero leptons" analysis targeted strongly produced squarks and gluinos in zero lepton final states. Both direct decays to the LSP, as shown in Figure 2.10, and one-step decays to the LSP, as shown in Figure 7.1, were considered. In Figure 7.1, only hadronic W boson decays are considered due to the zero lepton final state requirement. Also, specific analysis variables (see

section 7.2.1) were used in conjunction with the final state signatures to optimise the Signal Regions (SRs) of the analysis.

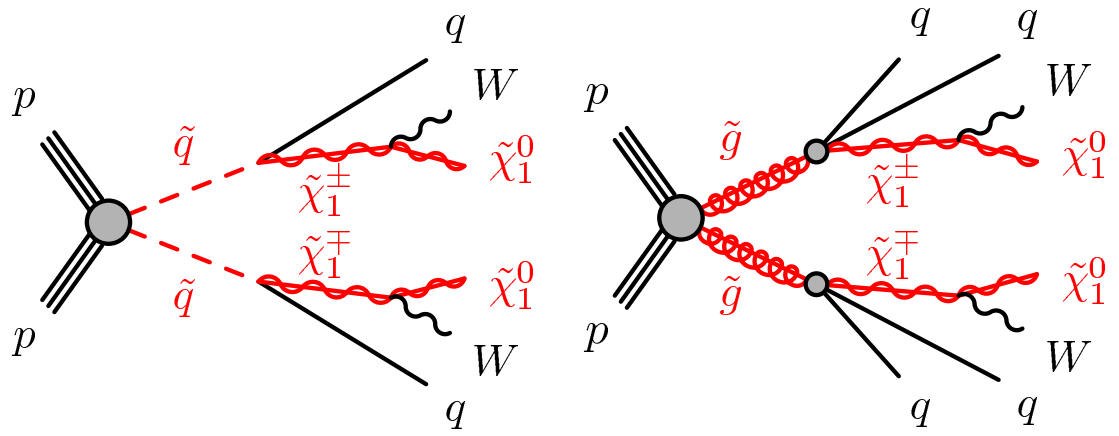

(a) One-step $\tilde{q}$ decay

(b) One-step $\tilde{g}$ decay

Figure 7.1: One-step indirect $\tilde{q}$ (a) and $\tilde{g}$ (b) decays to the LSP ($\tilde{\chi}_1^0$) via an intermediate Chargino $\chi_1^{\pm}$ decaying to a W boson and $\tilde{\chi}_1^0$.

An example event display of a candidate SUSY event with zero leptons is shown in Figure 7.2. This event contained approximately 1 TeV of $E_{\mathrm{T}}^{\mathrm{miss}}$ and approximately 2500 GeV of m_{eff} (see section 7.2.1).

7.2.1 Analysis Variables

This analysis uses specific variables to maximise the amount of signal events in the Signal Regions and reject background events. This section will define the variables used and explain their use.

Effective Mass

Effective mass (m_{eff}) [142] is a measure of the overall activity of the event. Strongly produced Supersymmetric events are expected to be very 'busy', with multiple high p_{T} jets and a significant amount of $E_{\mathrm{T}}^{\mathrm{miss}}$; therefore, Supersymmetric events will on average have a higher m_{eff} than Standard Model events.

The effective mass is defined as the scalar sum of the p_{T} of the n selected jets in the search channel plus the $E_{\mathrm{T}}^{\mathrm{miss}}$:

$$m_{\mathrm{eff}}(n_j) = \sum_{i=1}^{n} \left|\vec{p}_{\mathrm{T}}^{\,(i)}\right| + E_{\mathrm{T}}^{\mathrm{miss}}. \tag{7.1}$$

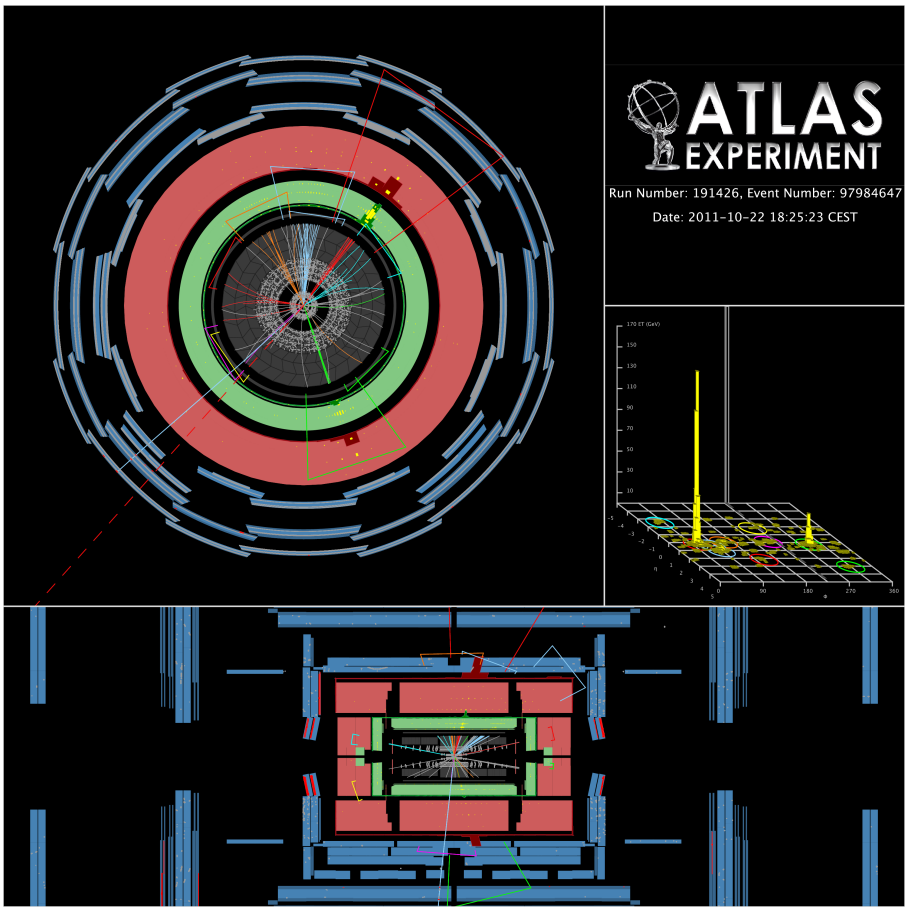

Figure 7.2: An ATLAS candidate for a SUSY event with zero leptons considered in the "zero lepton, jets and $E_{\mathrm{T}}^{\mathrm{miss}}$" analysis. This figure was taken from [2].

The jets are ordered in p_{T} with 1 being the highest p_{T} jet ('leading jet') in the event. The inclusive version of m_{eff} is also used in this analysis, where the scalar sum of the p_{T} of all jets with a $p_{\mathrm{T}} \geq 40\,\mathrm{GeV}$ is used (see Eq.(7.2)); this version of the scalar sum over the jet p_{T} ($\sum_{p_{\mathrm{T}} \geq 40\,\mathrm{GeV}}$) is equivalent to the H_{T} of the event.

$$m_{\mathrm{eff}}(\mathrm{incl.}) = \sum_{p_{\mathrm{T}} \geq 40\,\mathrm{GeV}} \left|\vec{p}_{\mathrm{T}}\right| + E_{\mathrm{T}}^{\mathrm{miss}} = H_{\mathrm{T}} + E_{\mathrm{T}}^{\mathrm{miss}}. \tag{7.2}$$

Minimum $\Delta\phi$ or $\Delta\phi_{\mathrm{min}}$

Minimum $\Delta\phi$ is primarily used to reject events from the multijet background. If one of the jets in the event is mismeasured by the detector, a significant amount of 'fake' $E_{\mathrm{T}}^{\mathrm{miss}}$ will appear in the event. The $E_{\mathrm{T}}^{\mathrm{miss}}$ will align with the jet that was mismeasured, as this tends to be the dominant

contribution; therefore, if a large minimum $\Delta\phi$ between the selected jets and $E_{\mathrm{T}}^{\mathrm{miss}}$ is required, a significant fraction of the multijet background can be eliminated.

Minimum $\Delta\phi$ is defined as the minimum difference in ϕ angle between the $E_{\mathrm{T}}^{\mathrm{miss}}$ and leading n jets; it is defined as

$$\Delta\phi_{\mathrm{min}} = \min\left(\left|\phi_1 - \phi_{E_{\mathrm{T}}^{\mathrm{miss}}}\right| \ , \ \ldots \ , \ \left|\phi_n - \phi_{E_{\mathrm{T}}^{\mathrm{miss}}}\right|\right). \tag{7.3}$$

Ratio of $E_{\mathrm{T}}^{\mathrm{miss}}/m_{\mathrm{eff}}(n_j)$

The ratio of $E_{\mathrm{T}}^{\mathrm{miss}}/m_{\mathrm{eff}}(n_j)$ is also used to reject multijet background events. At low $E_{\mathrm{T}}^{\mathrm{miss}}/m_{\mathrm{eff}}$, the H_{T} part of the $m_{\mathrm{eff}}(n_j)$ variable is dominant; this means that the m_{eff} in the event is mainly associated with the selected jets. This is typical of multijet events, where the $E_{\mathrm{T}}^{\mathrm{miss}}$ is associated with jet mismeasurement, and there is little/no $E_{\mathrm{T}}^{\mathrm{miss}}$ from final state objects. Clearly, events containing a significant amount of $E_{\mathrm{T}}^{\mathrm{miss}}$ from final state objects, such as Supersymmetric events, would have a higher $E_{\mathrm{T}}^{\mathrm{miss}}/m_{\mathrm{eff}}(n_j)$, since the $E_{\mathrm{T}}^{\mathrm{miss}}$ would contribute a larger fraction to the $m_{\mathrm{eff}}(n_j)$. Therefore, a selection cut to remove low $E_{\mathrm{T}}^{\mathrm{miss}}/m_{\mathrm{eff}}(n_j)$ events can further reduce the multijet background.

7.2.2 Event Selection

A general overview of the event selection procedure is provided in this section. First, events had to pass a single jet plus missing transverse energy trigger chain (see 7.3.1 and 7.4.1); this required data events to contain at least one jet and a significant amount of $E_{\mathrm{T}}^{\mathrm{miss}}$. Next, events containing light charged leptons (electrons or muons) were vetoed. After this, the final state number of jets and jet p_{T} cuts were applied. Then, a number of background rejection cuts were applied before the final discriminating variable m_{eff}(incl.) was applied, which defined the analysis Signal Regions.

7.2.3 SM Background Estimation

There are a number of Standard Model backgrounds that can produce the same final state signature as SUSY events. The most significant backgrounds are listed below:

- Multijets – significant amounts of $E_{\mathrm{T}}^{\mathrm{miss}}$ can be produced from jet mismeasurement or heavy flavour quark decays. It is possible for a jet to fluctuate to the point that it is not even reconstructed, therefore providing the event with significant amounts of $E_{\mathrm{T}}^{\mathrm{miss}}$ and a large minimum $\Delta\phi(\mathrm{jet},E_{\mathrm{T}}^{\mathrm{miss}})$, identical to signal events. It is also possible for multiple jets in the event to

fluctuate, and the combined effect can permit multijet events to pass the Signal Region event selection.

- W+jets – leptonic decays of the W boson ($W \to \ell\nu$) produce an unmeasurable neutrino in the event. The charged lepton is not always reconstructed in $W \to \tau\nu$ events if the τ decays hadronically to pions. Furthermore, in light lepton events, it is possible for the lepton to be misidentified or not reconstructed; this will result in the W+jet events having the same final state signature as signal events. Also, since there is significant $E_{\mathrm{T}}^{\mathrm{miss}}$ from the neutrino, these events are not expected to be rejected by the minimum $\Delta\phi$ and $E_{\mathrm{T}}^{\mathrm{miss}}/m_{\mathrm{eff}}$ selection cuts.

- Z+jets – Z boson decays to two neutrinos ($Z \to \nu\nu$) produce two unmeasurable neutrinos in the event; this can produce significant $E_{\mathrm{T}}^{\mathrm{miss}}$ with the same final state as signal events. This background is irreducible, as it is indistinguishable from the signal.

- $t\bar{t}$ and single top – fully hadronic top quark decays can contain $E_{\mathrm{T}}^{\mathrm{miss}}$ from mismeasured jets or the heavy flavour decay of the b-quarks. Events from leptonic decays of W bosons produced in the top quark decay can also pass the selection if the lepton is not reconstructed or is misidentified, identical to the W+jets background.

The Standard Model backgrounds were estimated in *each* SR by calculating a *Transfer Factor* (TF) (see Eq.(7.4)). There is one TF for *every* major background, and a dedicated Control Region (CR) was used to calculate it for each background. The dedicated Control Region of each background has a kinematic selection as close as possible to the Signal Region, but with modified event selection cuts to enrich the Control Region with events from the target background [1, 2]. Figure 7.3 shows a simplistic version of this type of analysis, with the Control Region having reversed $\Delta\phi$ and $E_{\mathrm{T}}^{\mathrm{miss}}/m_{\mathrm{eff}}$ selection cuts compared to the Signal Region. Two Validation Regions (VR1 and VR2) are also shown, where only one of the SR region cuts is reversed. The Validation Regions allow the background prediction to be cross-checked in a region that more closely resembles the Signal Region. This provides feedback on the validity of the background extrapolation from the Control Region to the Signal Region.

The number of predicted events from a particular background (N(SR, est)) in a Signal Region can then be expressed as [1]:

$$N(\mathrm{SR},\mathrm{est}) = N(\mathrm{CR},\mathrm{obs}) \times \left[\frac{N(\mathrm{SR},\mathrm{raw})}{N(\mathrm{CR},\mathrm{raw})}\right], \tag{7.4}$$

where N(CR, obs) is the observed number of data events in the CR of the background process, and N(SR, raw) and N(CR, raw) are the raw unnormalised contributions from the background to the

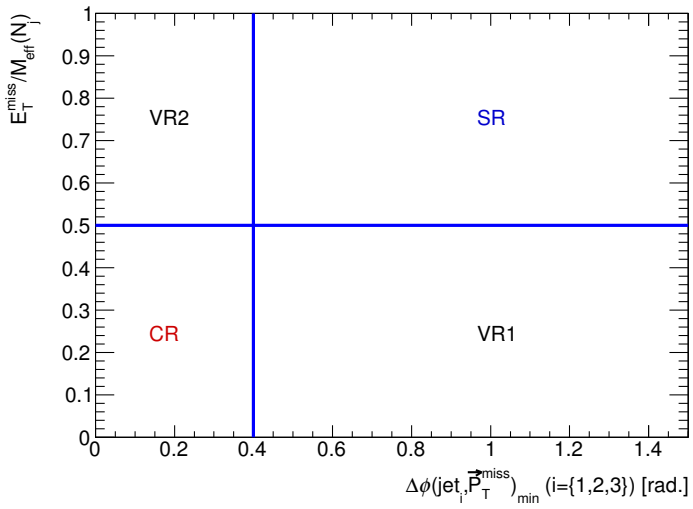

Figure 7.3: A schematic showing an example simplistic analysis region layout that could be used to generate background Transfer Factors.

SR and CR respectively. The ratio appearing in the square brackets in Eq.(7.4) is defined to be the Transfer Factor (TF).

One advantage of using this approach is that some of the systematic uncertainties on the Transfer Factors that were common to both of the Signal and Control Regions will cancel [1]. However, care must be taken to minimise any systematic uncertainties that were brought in by the extrapolation from the Control Region to the Signal Region. All of the Transfer Factors were measured using MC samples except for the multijets background, which used the jet smearing method (see Chapters 5 and 6) to estimate the multijet Transfer Factors.

7.2.4 Statistical Interpretation

The main possible outcomes in searches for new physics beyond the Standard Model are confirmation of new physics, outright exclusion of the proposed theory or restriction of the parameter space of the proposed theory.

A 'cut and count' approach was taken in this analysis. The number of events in a SR (λ_{SR}) interpreted in terms of a proposed BSM model is given by [139, 125]

$$\lambda_{SR} = \mu \times s + b_{SM}, \tag{7.5}$$

where s is the number of signal events, μ is the signal strength of the proposed BSM theory and b_{SM} is the expected number of SM background events in the Signal Region. A value of $\mu = 1$ corresponds to a signal strength fully consistent with that predicted by the proposed BSM theory [139, 125]. If $\mu = 0$, then this is consistent with no signal being present, and the observed number of events in the Signal Region is consistent with the SM [139, 125]. b_{SM} is the combined sum of all the different SM backgrounds (multijet, $t\bar{t}$,...) modulated by the background Transfer Factor extrapolation to the SR [139, 125]:

$$b_{SM} = \sum_{j} \left(\mathrm{TF}_{CR\to SR} \times b_{CR}\right)_j, \tag{7.6}$$

where j runs over all the different background processes.

A likelihood function for each SR n was constructed for the profile likelihood ratio statistical test [143]. The likelihood function for the discovery fit had the functional form [139, 125]

$$L\left(n|\,\mu, b, \theta\right) = P_{SR} \times P_{CR} \times C_{Sys}\left(\theta, \theta^0\right). \tag{7.7}$$

λ_{SR} is encapsulated into the Poisson distribution that described the expected number of events in the signal region (P_{SR}) in the likelihood function. P_{CR} is the product of the Poisson distributions describing the four major backgrounds (multijets, W+jets, Z+jets and top) after the normalisation factors were found from the simultaneous background fit of all the Control Regions [139, 125]. The systematic uncertainties are modelled by nuisance parameters (θ) in C_{Sys}. The nuisance parameters were Gaussian distributions allowed to vary around the nominal value (θ) by a certain amount (θ^0) [139, 125]. The nuisance parameters also appear in the Poisson distributions of the SRs and CRs through the TFs, as the TFs depend on the systematic uncertainties of the analysis.

After the likelihood was maximised, if no observation of SUSY was found, then the likelihood model was used to set 95% Confidence Level (C.L.) exclusion limits on the proposed SUSY models (see [143, 144]).

7.3 SUSY Search using the 2011 Data Set

This section describes the final 2011 analysis using the full ATLAS 2011 $\sqrt{s} = 7$ TeV data set (see section 3.5). The analysis is documented in full detail in references [2] and [139]. Late 2011 SUSY group object definitions were used; more information about the reconstruction of these objects can be found in section 3.6. The analysis set mass exclusion contours in the mSUGRA/CMSSM m_0 –

$m_{1/2}$ mass plane and pMSSM model (see section 7.3.4).

7.3.1 Triggers and Simulated Samples

Data events were collected using three different jet plus $E_{\mathrm{T}}^{\mathrm{miss}}$ trigger chains. This was to cope with the increasing instantaneous luminosity and pile-up over the 2011 data taking period. Table 7.1 shows the trigger chains used in each of the data taking periods. Events were required to contain at least one jet-like object with a $p_{\mathrm{T}} > 75\,\mathrm{GeV}$ and $E_{\mathrm{T}}^{\mathrm{miss}} > 45\,\mathrm{GeV}/55\,\mathrm{GeV}$, both at the EM scale, to pass the EF trigger. However, to ensure that the EF trigger was fully efficient, tighter offline selection cuts were required. A leading jet $p_{\mathrm{T}} > 130\,\mathrm{GeV}$ and `MET_Simplified20` $> 160\,\mathrm{GeV}$ was required; this protected the analysis against any turn-on bias effects of the EF trigger [139].

Period	HL-Trigger	L1 Seed	L2 Seed
A + B	EF_j75_a4_xe45_loose_noMu	L1_J50_XE20	L2_j70_xe20_noMu
D – K	EF_j75_a4tc_xe45_loose_noMu		
L + M	EF_j75_a4tc_xe55_loose_noMu	L1_J50_XE35	L2_j70_xe35_noMu

Table 7.1: Triggers used for collecting data events in the 2011 analysis.

Simulated MC samples were used in this analysis to predict the Standard Model backgrounds. The MC samples that were used in this analysis are shown in Table 7.2. More information about how the samples were produced can be found in section 3.4.3. SUSY signal samples were generated with `HERWIG++` [145] or `MadGraph/PYTHIA` [81, 146, 147] to NLO accuracy [2].

SM process	Generator(s) used (perturbative order)	$\sigma\times$ BR [pb]
Dijet (QCD)	`PYTHIA` (LO)	$10\,470 \times 10^6$
$Z \to \nu\nu$ + jets	`ALPGEN` (NNLO)	5.82×10^3
$Z \to \ell\ell$ + jets	`ALPGEN` (NNLO)	3.20×10^3
$W \to \ell\nu$ + jets	`ALPGEN` (NNLO)	31.4×10^3
$t\bar{t}$	`ALPGEN` (NNLO), `MC@NLO` (NLO+NLL)	50.8, 75.2
Single top	`Acer` (LO)	39.86

Table 7.2: MC simulated samples used in the 2011 analysis.

7.3.2 Event Selection

The general analysis strategy has already been outlined in section 7.2. The Signal Region selection criteria are discussed in more detail in this section. Table 7.3 shows a summary of the Signal Region

selection criteria. After events had passed the trigger and DQ selection, the Standard ATLAS event cleaning cuts were applied; these selection cuts aimed to remove events which contained poorly reconstructed physics objects. They included requirements to have a primary vertex with ≥ 5 tracks, no poorly reconstructed jets and no fake $E_{\mathrm{T}}^{\mathrm{miss}}$ associated with calorimeter noise or cosmic-ray muons.

Cut	Description	Channel (minimum number of jets)					
		A (2j)	A′ (2j)	B (3j)	C (4j)	D (5j)	E (6j)
1	DQ (data)	Run / lumi block appears in SUSY GRL					
2	HL Trigger (data)	EF_j75_a4_EFFS_xe45_loose_noMu (data period B) EF_j75_a4tc_EFFS_xe45_loose_noMu (D ≤ data period ≤ K) EF_j75_a4tc_EFFS_xe55_noMu (data period ≥ L)					
3	Event cleaning	Event Cleaning on data and MC					
4	Lepton veto	No selected e/μ after overlap removal with $p_{\mathrm{T}} > 20/10$ GeV.					
5	$E_{\mathrm{T}}^{\mathrm{miss}}$[GeV] >	160					
6	$p_{\mathrm{T}}(j_1)$ [GeV] >	130					
7	$p_{\mathrm{T}}(j_2)$ [GeV] >	60					
8	$p_{\mathrm{T}}(j_3)$ [GeV] >	–	–	60	60	60	60
9	$p_{\mathrm{T}}(j_4)$ [GeV] >	–	–	–	60	60	60
10	$p_{\mathrm{T}}(j_5)$ [GeV] >	–	–	–	–	40	40
11	$p_{\mathrm{T}}(j_6)$ [GeV] >	–	–	–	–	–	40
12	min $\Delta\phi(\mathrm{jet}^{\mathrm{i}}, \vec{p}_{\mathrm{T}}^{\mathrm{miss}})$ >	0.4 ($i = \{1, 2, (3)\}$)			0.4 ($i = \{1, 2, 3\}$), 0.2 (jets with $p_{\mathrm{T}} > 40$ GeV)		
13	$E_{\mathrm{T}}^{\mathrm{miss}}/m_{\mathrm{eff}}(Nj)$ >	0.3 (2j)	0.4 (2j)	0.25 (3j)	0.25 (4j)	0.2 (5j)	0.15 (6j)
14	m_{eff}(incl.) [GeV] >	1900/1400/–	–/1200/–	1900/–/–	1500/1200/900	1500/–/–	1400/1200/900

Table 7.3: Summary of the 2011 analysis Signal Region selection criteria.

The Signal Regions in each channel (corresponding to the minimum number of jets required) were defined by the m_{eff}(incl.) cut (cut number 14 in Table 7.3). Some search channels had up to three different Signal Regions each with a different m_{eff}(incl.) criteria. The Signal Region with the loosest m_{eff}(incl.) cut is referred to as *Loose*; the Signal Region with the medium m_{eff}(incl.) cut is called *Medium*, and the Signal Region with the tightest m_{eff}(incl.) cut is called *Tight*.

During Period E of the 2011 data taking period, a 'hole' appeared in the coverage of the LAr calorimeter. This was due to a failure in part of the readout system [139]. The LAr 'hole' was located at $0 < \eta < 1.4$ and $-0.8 < \phi < -0.6$ for the second and third layer of the LAr calorimeter, which corresponded to 0.4% of the calorimeter [139]. Since no energy could be readout in this section of the calorimeter, jets in this region of the detector were poorly reconstructed; this could lead to large amounts of 'fake' $E_{\mathrm{T}}^{\mathrm{miss}}$ if the event contained jet(s) in this region of the detector. These events could contaminate the Signal Regions of the analysis; therefore, a '*SMART LAr hole*' veto was applied to data events in Period E. The LAr hole veto removed events which had a jet pointing

into the LAr hole that had made a significant contribution to the $E_{\mathrm{T}}^{\mathrm{miss}}$ of the event [139]. More information about the impact of the LAr hole can be found in references [139] and [148].

7.3.3 Background Estimation

The SM backgrounds to this SUSY search were outlined in section 7.2. The SM backgrounds were estimated by calculating TFs using dedicated Control Regions. Table 7.4 shows the Control Regions used for each SR of the analysis. The CR selection column in Table 7.4 displays the modified/additional cut(s) used to construct the background Control Region. The calculation of the background Transfer Factors used MC samples (see Table 7.2) except for the multijet background, which used a data-driven method called the jet smearing method.

CR name	SR background	CR process	CR selection
CR1a	Z + jets	γ + jets	Isolated photon
CR1b	Z + jets	$Z \rightarrow \ell\ell$ + jets	$66 > M_Z < 116$ [GeV]
CR2	Multijets	Multijets	min $\Delta\phi(\text{jet}, \vec{p}_{\mathrm{T}}^{\,\mathrm{miss}}) < 0.2$
CR3	$W \rightarrow \ell\nu$ + jets	$W \rightarrow \ell\nu$ + jets	$30 > M_T < 100$ [GeV], b-jet veto
CR4	$t\bar{t}$ and single top	$t\bar{t} \rightarrow b\bar{b}qq\ell\nu$	$30 > M_T < 100$ [GeV], b-tag

Table 7.4: Summary of the SM background CRs used in the 2011 analysis, created using information from [2] and [139].

Multijet Background Estimation

The multijet background was estimated using the jet smearing method (described in Chapters 5 and 6) due to the low acceptance of multijet events into the Signal Region; this resulted in very few multijet MC events passing the SR criteria, which led to large statistical uncertainties on the multijet TFs [139]. The jet smearing method used a large sample of pseudo-data that was generated with the 2011 inclusive jet response map (see Chapter 6), and then normalised in the multijet Control Region (CR2). This allowed the jet smearing method to calculate the multijet TFs with greater accuracy than using multijet MC. The multijet TFs for each SR are shown in Table 7.5 with their associated uncertainties (see section 6.6).

Figure 7.4 shows the CR2 m_{eff}(incl.) distributions for search channels A (a), C (b) and D (c). The multijet distributions (shown in orange) were produced with the jet smearing method. The yellow

uncertainty band in the ratio plot includes the jet smearing systematics discussed in section 6.6. It can be seen in Figure 7.4 that the data agreed with the SM prediction; this provided confidence that the jet smearing method was accurately modelling the multijet background.

Figure 7.5 shows the minimum $\Delta\phi(\text{jet},E_{\text{T}}^{\text{miss}})$ distributions for search channels A (a), C (b) and D (c). The multijet distribution produced with the jet smearing method is shown by the maroon data points, whereas the multijet MC distribution is shown in orange. It should be noted that there was no ϕ-smearing of jets in the pseudo-data (see section 6.4) in the 2011 analysis. This was the cause of the disagreement between the data and total estimate in the low minimum $\Delta\phi$ region. The disagreement at low minimum $\Delta\phi$ was one of the key motivations for performing the ϕ-smearing in the jet smearing method. It was very important that the shape of the minimum $\Delta\phi\left(E_{\text{T}}^{\text{miss}},\text{j}_{1\to3}\right)$ distribution in the pseudo-data agreed with the data, as minimum $\Delta\phi$ was used to define the multijet CR regions and also to remove multijet events from the SRs. If the minimum $\Delta\phi$ was mis-modelled, then this may have led to the multijet TFs being miscalculated. However, it can be seen in Figure 7.5 that there was still reasonable agreement (taking into account the uncertainties) between the observed data and total SM background estimation.

Signal Region	$N_{\text{SR}}/N_{\text{CR2}}$ (TF) [$\times10^{-3}$]
A Medium	$32.0\pm5.7(\text{stat.})\pm6.6(R_{mean-shift})\,^{+0.0}_{-2.5}(\sigma_{cor}^{Gaus})\,^{+12.0}_{-11.9}(\Delta\sigma_{tail})$
A Tight	$9.0\pm3.3(\text{stat.})\pm0.3(R_{mean-shift})\,^{+4.4}_{-3.0}(\sigma_{cor}^{Gaus})\,^{+6.4}_{-1.6}(\Delta\sigma_{tail})$
A$'$ Medium	$104.9\pm13.5(\text{stat.})\pm29.0(R_{mean-shift})\,^{+0.0}_{-30.7}(\sigma_{cor}^{Gaus})\,^{+29.5}_{-17.1}(\Delta\sigma_{tail})$
B Tight	$11.4\pm2.7(\text{stat.})\pm1.5(R_{mean-shift})\,^{+5.4}_{-0.2}(\sigma_{cor}^{Gaus})\,^{+4.7}_{-0.0}(\Delta\sigma_{tail})$
C Loose	$16.0\pm4.6(\text{stat.})\pm1.5(R_{mean-shift})\,^{+5.1}_{-9.7}(\sigma_{cor}^{Gaus})\,^{+1.5}_{-0.0}(\Delta\sigma_{tail})$
C Medium	$3.0\pm0.6(\text{stat.})\pm0.8(R_{mean-shift})\,^{+4.1}_{-0.9}(\sigma_{cor}^{Gaus})\,^{+1.4}_{-1.1}(\Delta\sigma_{tail})$
C Tight	$3.4\pm1.5(\text{stat.})\pm0.1(R_{mean-shift})\,^{+3.6}_{-0.4}(\sigma_{cor}^{Gaus})\,^{+1.8}_{-0.0}(\Delta\sigma_{tail})$
D Tight	$19.5\pm3.1(\text{stat.})\pm4.5(R_{mean-shift})\,^{+6.1}_{-6.2}(\sigma_{cor}^{Gaus})\,^{+0.0}_{-6.8}(\Delta\sigma_{tail})$
E Loose	$48.3\pm2.5(\text{stat.})\pm0.8(R_{mean-shift})\,^{+37.4}_{-14.6}(\sigma_{cor}^{Gaus})\,^{+2.2}_{-1.3}(\Delta\sigma_{tail})$
E Medium	$38.4\pm1.8(\text{stat.})\pm3.7(R_{mean-shift})\,^{+29.6}_{-6.4}(\sigma_{cor}^{Gaus})\,^{+0.4}_{-2.5}(\Delta\sigma_{tail})$
E Tight	$40.3\pm2.3(\text{stat.})\pm6.3(R_{mean-shift})\,^{+20.1}_{-4.0}(\sigma_{cor}^{Gaus})\,^{+0.0}_{-3.6}(\Delta\sigma_{tail})$

Table 7.5: The multijet background Transfer Factors calculated in the 2011 analysis, taken from [139].

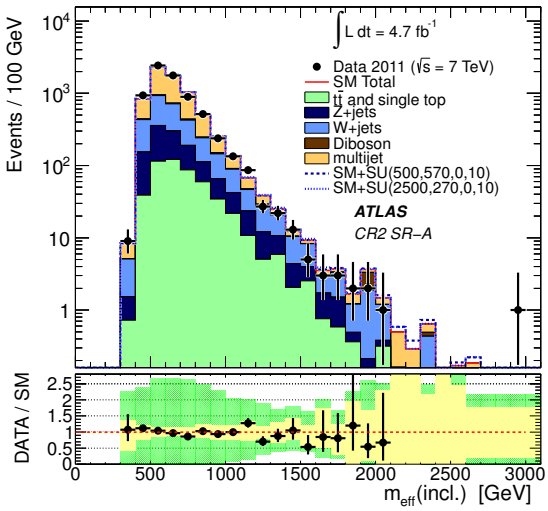

(a) **CR2 – A**

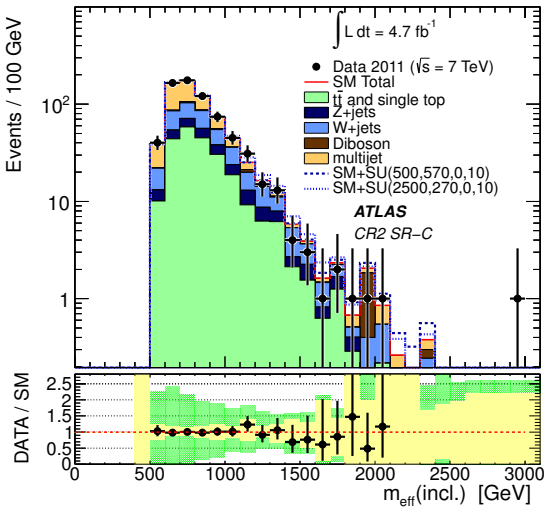

(b) **CR2 – C**

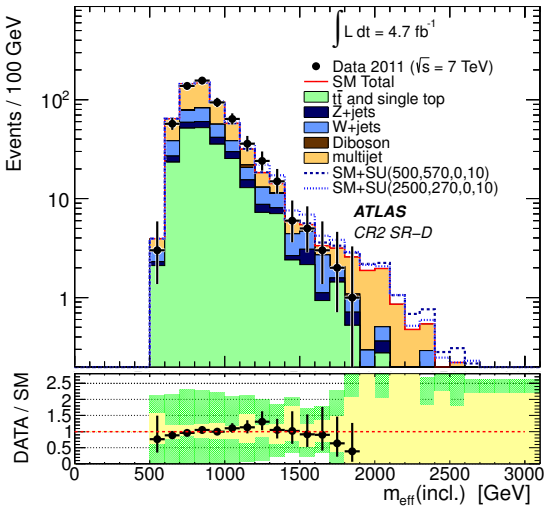

(c) **CR2 – D**

Figure 7.4: The CR2 m_{eff} (incl.) distributions for SRs A (a), C (b) and D (c). The distribution from the 2011 $\sqrt{s} = 7\,\text{TeV}$ data is shown by the black points. The multijet distribution produced using the jet smearing method is shown in orange. The total SM background estimation is shown by the red line. The SM $t\bar{t}$ and single top, W + jets, Z + jets and diboson backgrounds are shown in green, light blue, dark blue and brown respectively. Two benchmark points from a simplified SUSY model are shown by the blue dashed lines. The yellow uncertainty band on the ratio plot shows the total uncertainty on the jet smearing method, and the green uncertainty shows the total theoretical uncertainty. These figures were taken from [2, 139].

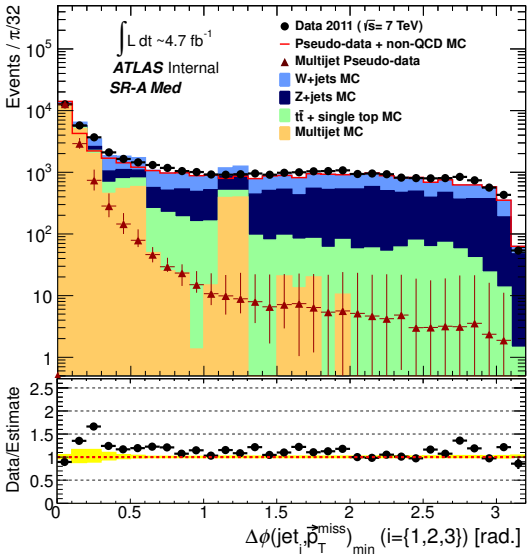

(a) **SR – A**

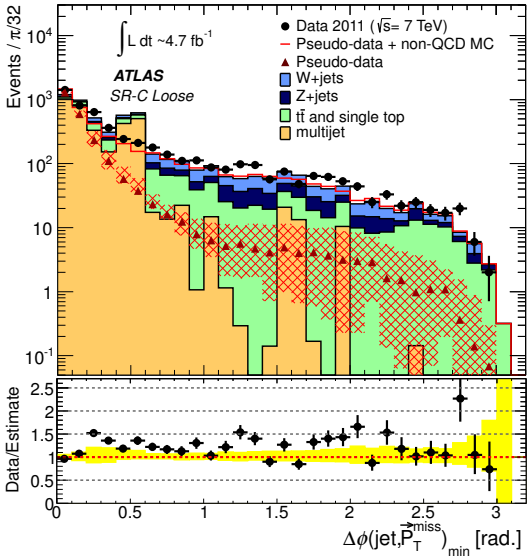

(b) **SR – C**

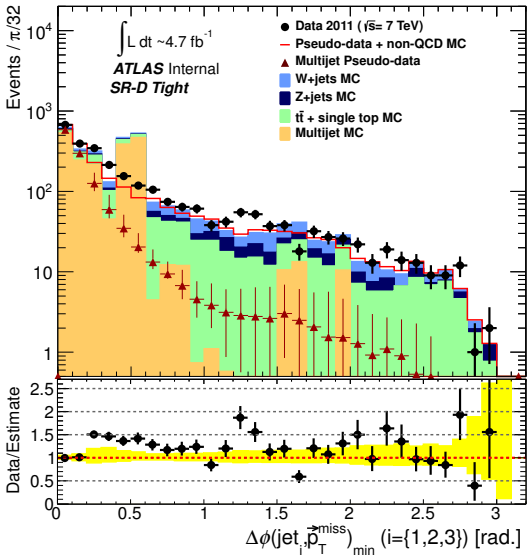

(c) **SR – D**

Figure 7.5: The minimum $\Delta\phi(\text{jet},E_{\text{T}}^{\text{miss}})$ distributions for SRs A (a), C (b) and D (c) after the jet and $E_{\text{T}}^{\text{miss}}$ selection cuts. The distribution from the 2011 $\sqrt{s} =$ 7 TeV data is shown by the black points. The multijet distribution produced using the jet smearing method is shown by the maroon points. The total SM background estimation is shown by the red line. The SM $t\bar{t}$ and single top, W + jets, Z + jets and multijet backgrounds are shown in green, light blue, dark blue and orange respectively. The yellow uncertainty band on the ratio plot shows the total uncertainty on the jet smearing method and the total statistical uncertainty on the MC samples (except multijets). Figure (b) is the ATLAS approved version, taken from [2].

7.3.4 Results

The full set of analysis results and interpretations can be found in references [2, 139]; this section will summarise the main results of the analysis and show some of the interpretations in the SUSY models that were targeted.

Table 7.6 shows the observed number of data events in each of the analysis Signal Regions. The expected contributions from background processes listed after the simultaneous background fit are also shown in this table. The table shows that no statistically significant excess was found and that the data agreed with the predictions from the SM.

Since no statistically significant excess was found, exclusion limits were set on a simplified pMSSM sq-gl-neutralino model (7.6(a)) and the $m_0 - m_{1/2}$ mSUGRA/CMSSM mass plane (7.6(b)). In the simplified pMSSM sq-gl-neutralino model, only strong production of first and second generation squarks occurs and everything decays directly to the LSP ($\tilde{\chi}_1^0$), i.e., $\tilde{q} \rightarrow q\tilde{\chi}_1^0$ and $\tilde{g} \rightarrow qq\tilde{\chi}_1^0$. The exclusion limits were obtained from the combination of all of the SRs, choosing the SR that had the best sensitivity at each point of the respective model [139].

Figure 7.6(a) shows the 95% exclusion limit for a simplified pMSSM squark-gluino-neutralino scenario with only strong production of the first and second generation of squarks and decays directly to the LSP. The figure shows that in the case of a massless $\tilde{\chi}_1^0$, masses of squarks and gluons up to $m_{sq} = m_{gl} \approx 1500\,\text{GeV}$ were excluded to a 95% confidence level. The figure also shows that the observed limit performs better than the expected limit; this may have been caused by the under fluctuation of data events in the *Tight* Signal Regions (see Table 7.6), which were most sensitive to high mass squarks and gluinos.

The 95% exclusion limit in the $m_0 - m_{1/2}$ mass plane for the mSUGRA/CMSSM model with $\tan\beta = 10$, $A_0 = 0$ and $\mu > 0$ is shown in Figure 7.6(b). It can be seen in this figure that masses $m_{1/2} < 650\,\text{GeV}$ for $m_0 = 0\,\text{GeV}$ and $m_0 < 3500\,\text{GeV}$ for $m_{1/2} = 0\,\text{GeV}$ were excluded to a 95% confidence level.

Process	Signal Region					
	SRA Medium	SRA Tight	SRA' Medium	SRB Tight	SRC Loose	SRC Medium
$t\bar{t}$+ Single Top	$6.8 \pm 4.4(sys) \pm 1.8(stat)$	$0.17 \pm 0.21(sys) \pm 0.06(stat)$	$11 \pm 3.3(sys) \pm 1.9(stat)$	$0.25 \pm 0.24(sys) \pm 0.10(stat)$	$74 \pm 12(sys) \pm 7(stat)$	$13 \pm 4.3(sys) \pm 2.2(stat)$
Z/γ+jets	$32.0 \pm 8.6(sys) \pm 3.1(stat)$	$3.30 \pm 1.00(sys) \pm 1.10(stat)$	$66 \pm 17.0(sys) \pm 4.6(stat)$	$2 \pm 0.74(sys) \pm 0.84(stat)$	$71 \pm 19.0(sys) \pm 4.6(stat)$	$16 \pm 4.6(sys) \pm 2.3(stat)$
W+jets	$19.0 \pm 3.6(sys) \pm 2.9(stat)$	$2.20 \pm 0.70(sys) \pm 0.72(stat)$	$25 \pm 4.1(sys) \pm 2.6(stat)$	$0.98 \pm 0.46(sys) \pm 0.37(stat)$	$61 \pm 9.9(sys) \pm 5.9(stat)$	$7.7 \pm 2.5(sys) \pm 1.7(stat)$
QCD jets	$0.14 \pm 0.20(sys) \pm 0.15(stat)$	$0.00 \pm 0.01(sys) \pm 0.01(stat)$	$0 \pm 0.06(sys) \pm 0.10(stat)$	$0 \pm 0.06(sys) \pm 0.03(stat)$	$0.92 \pm 1.10(sys) \pm 0.18(stat)$	$0.03 \pm 0.04(sys) \pm 0.02(stat)$
Di-Bosons	7 ± 4	1.8 ± 0.9	14 ± 7	1.8 ± 0.9	8 ± 4	1.7 ± 0.9
Total SM	$65.4 \pm 10.9(sys) \pm 4.13(stat)$	$7.38 \pm 1.86(sys) \pm 1.26(stat)$	$116 \pm 18.8(sys) \pm 5.2(stat)$	$5 \pm 1.67(sys) \pm 0.91(stat)$	$214 \pm 22.1(sys) \pm 8.4(stat)$	$39.3 \pm 6.76(sys) \pm 3.08(stat)$
Data	59	1	85	1	210	36

Process	Signal Region				
	SRC Tight	SRD Tight	SRE Loose	SRE Medium	SRE Tight
$t\bar{t}$+ Single Top	$2 \pm 1.40(sys) \pm 0.59(stat)$	$2.4 \pm 1.6(sys) \pm 0.7(stat)$	$73 \pm 23(sys) \pm 9(stat)$	$19 \pm 4.2(sys) \pm 3.9(stat)$	$4.2 \pm 4.5(sys) \pm 1.3(stat)$
Z/γ+jets	$2 \pm 0.67(sys) \pm 0.68(stat)$	$0.93 \pm 0.34(sys) \pm 0.44(stat)$	$21 \pm 6.3(sys) \pm 2.4(stat)$	$8.4 \pm 2.7(sys) \pm 1.7(stat)$	$3.4 \pm 1.2(sys) \pm 1.0(stat)$
W+jets	$1.5 \pm 1.10(sys) \pm 0.71(stat)$	$2.4 \pm 0.95(sys) \pm 1.00(stat)$	$23 \pm 11(sys) \pm 6(stat)$	$6.2 \pm 1.6(sys) \pm 2.1(stat)$	$2.8 \pm 1.6(sys) \pm 1.0(stat)$
QCD jets	$0 \pm 0.02(sys) \pm 0.02(stat)$	$0 \pm 0.22(sys) \pm 0.18(stat)$	$8.4 \pm 7.2(sys) \pm 1.0(stat)$	$1.4 \pm 1.1(sys) \pm 0.4(stat)$	$0.46 \pm 0.37(sys) \pm 0.23(stat)$
Di-Bosons	0.50 ± 0.25	2 ± 1	4 ± 2	3.0 ± 1.5	3.0 ± 1.5
Total SM	$5.98 \pm 2.02(sys) \pm 0.98(stat)$	$7.82 \pm 2.42(sys) \pm 0.97(stat)$	$129 \pm 30.2(sys) \pm 8.3(stat)$	$37.8 \pm 5.4(sys) \pm 3.7(stat)$	$13.3 \pm 6.26(sys) \pm 1.59(stat)$
Data	14	9	148	25	13

Table 7.6: The observed number of events in data compared to the fitted expected number of events from SM background processes in each SR. The expected background numbers are quoted with their systematic and statistical uncertainty. This table was made with information from reference [2].

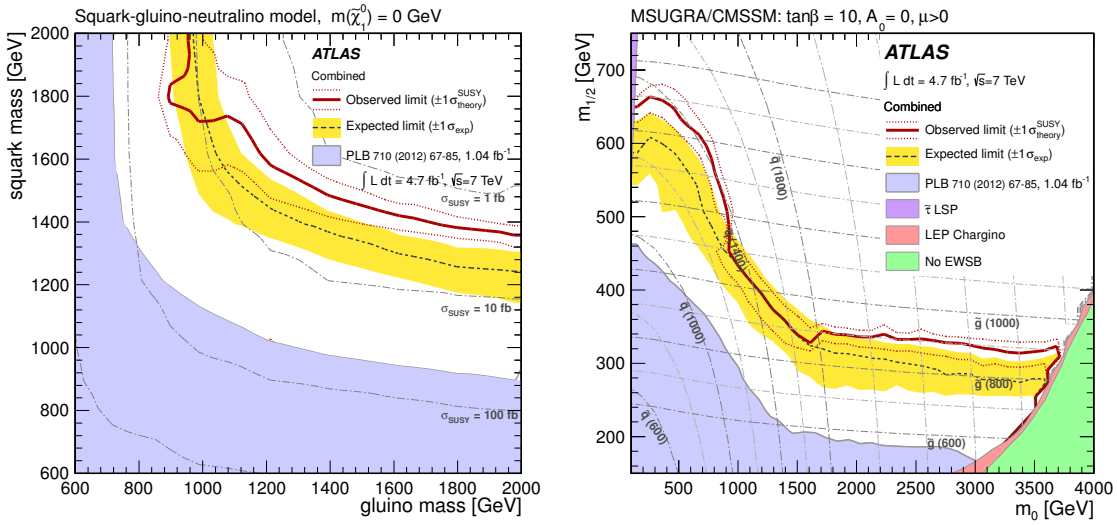

(a) Simplified $\tilde{q}$-$\tilde{g}$-$\tilde{\chi}_1^0$ pMSSM model

(b) mSUGRA/CMSSM simplified model

Figure 7.6: The 95% C.L. exclusion limits for the sq-gl-neutralino simplified pMSSM model (a) and the $m_0 - m_{1/2}$ mSUGRA/CMSSM mass plane (b). The black dotted lines show the expected exclusion limit, with the yellow band showing the one σ uncertainty on the expected limit. The observed limit is shown by the red line, with the red dotted line showing the one σ uncertainty bands. Previous experimental results and regions ruled out by theoretical limits are shown by the coloured shaded regions. These figures were taken from [2].

7.4 SUSY Search using the 2012 Data Set

This section summarises the final 2012 analysis using the full ATLAS 2012 $\sqrt{s} = 8\,\text{TeV}$ data set (see section 3.5). This analysis is documented in full detail in references [1] and [125]. The final SUSY group 2012 object definitions were used; more information about the reconstruction of these objects in 2012 data can also be found in section 3.6. Since no excess was observed, mass exclusion contours were set in the mSUGRA/CMSSM $m_0 - m_{1/2}$ model and the squark-gluino-neutralino simplified pMSSM model (see section 7.4.4).

7.4.1 Triggers and Simulated Samples

Data events were also collected with a jet plus $E_{\text{T}}^{\text{miss}}$ trigger in the 2012 analysis. However, only one trigger chain was used to select signal events over the 2012 data taking period. Table 7.7 shows the trigger chain that was used to collect data events over the 2012 data taking period. When compared to 2011, the $E_{\text{T}}^{\text{miss}}$ and jet p_{T} requirements to pass the 2012 EF trigger were higher; this was due to the higher instantaneous luminosity and pile-up run conditions during the 2012 data taking period, which required higher trigger thresholds to reduce the triggering rate of the jet plus $E_{\text{T}}^{\text{miss}}$ trigger. Offline selection cuts on the leading jet p_{T} and $E_{\text{T}}^{\text{miss}}$ were still required in the 2012 analysis to ensure the trigger was operating at full efficiency. Events required a leading jet $p_{\text{T}} > 130\,\text{GeV}$ and `MET_RefFinal` $> 160\,\text{GeV}$ at the LCW scale.

Period	HL-Trigger	L1 Seed	L2 Seed
A – L	EF_j80_a4tchad_xe100_tclcw_veryloose	L1_J50_XE40	L2_j75_c4cchad_xe55

Table 7.7: The trigger chain used for collecting data events in the 2012 analysis.

MC simulated samples were also used in the 2012 analysis to predict the Standard Model background processes. The MC samples used in the 2012 analysis are shown in Table 7.8. More information about these samples can be found in section 3.4.4. SUSY signal samples were generated with `HERWIG++` [145] for the mSUGRA/CMSSM models and `MadGraph/PYTHIA` [81, 146, 147] for the sq-gl-neutrino simplified pMSSM model; both had cross-sections computed to NLO accuracy [1, 125].

7.4.2 Event Selection

The Signal Region selection criteria for the 2012 analysis are discussed in more detail in this section. Table 7.9 shows a summary of the Signal Region selection criteria for the 2012 analysis. After data events had passed the trigger and DQ selection, the standard 2012 ATLAS event cleaning cuts were

SM process	Generator(s) used (perturbative order)	$\sigma \times$ BR [pb]
Dijet (QCD)	PYTHIA (LO)	$72\,850 \times 10^6$
$Z \to \nu\nu$ + jets	SHERPA (NNLO)	6.70×10^3
$Z \to \ell\ell$ + jets	SHERPA (NNLO)	3.43×10^3
$W \to \ell\nu$ + jets	SHERPA (NNLO)	33.7×10^3
$t\bar{t}$	PowHeg + PYTHIA (NNLO)	137
Single top	MC@NLO (NLO+NLL)	22.4
Diboson	SHERPA (NNLO)	25.3

Table 7.8: The simulated MC samples used in the 2012 analysis.

applied; these cuts were similar to the 2011 analysis cleaning cuts with the same aim of removing data events which contained poorly reconstructed physics objects. They included requirements to have a primary vertex with ≥ 4 tracks, no poorly reconstructed jets, and no 'fake' $E_{\mathrm{T}}^{\mathrm{miss}}$ associated with calorimeter noise, hot calorimeter tiles or cosmic-ray muons. Full details of the data event cleaning cuts are provided in reference [125].

The Signal Regions for each channel (corresponding to the minimum number of required jets in the event) were defined by the m_{eff}(incl.) cut (cut 10 in Table 7.9). Some of the search channels contained up to four different Signal Regions, each corresponding to a different event selection criterion.

Changes with Respect to the 2011 Data Set Analysis

The main change with respect to the 2011 analysis was the increased number of Signal Regions, which made it possible for Signal Regions to be tuned to a particular SUSY process; the targeted process of each Signal Region is shown in Table 7.9. Two new W boson Signal Regions (2jW and 4jW) were introduced: these were specialised for one-step decay searches, where the definition of the Signal Region included an attempt to reconstruct the intermediate W boson. The W boson Signal Regions improved the sensitivity of the analysis to one-step decay scenarios [1, 125]. During the SR optimisation process, it was found that a $E_{\mathrm{T}}^{\mathrm{miss}}/\sqrt{H_{\mathrm{T}}}$ cut provided better sensitivity in the direct squark channels than the standard $E_{\mathrm{T}}^{\mathrm{miss}}/m_{\mathrm{eff}}$ ratio cut; therefore, a $E_{\mathrm{T}}^{\mathrm{miss}}/\sqrt{H_{\mathrm{T}}}$ ratio cut was used instead of the $E_{\mathrm{T}}^{\mathrm{miss}}/m_{\mathrm{eff}}$ ratio cut in signal channels searching for direct squark production (2jl, 2jm, 2jt, 4jl- and 4jl) [1, 125].

Cut Number	Requirement	Channel																
		2j			2j(W)	3j	4j(W)	4j				5j	6j					
		2jl	2jm	2jt				4jl-	4jl	4jm	4jt		6jl	6jm	6jt	6jt+		
Targetted signal		$\tilde{q}\tilde{q}$ direct			$\tilde{g}\tilde{g}$ one-step	$\tilde{q}\tilde{g}$ direct	$\tilde{q}\tilde{q}$ one-step	$\tilde{q}\tilde{q}$		$\tilde{q}\tilde{g}$ & $\tilde{g}\tilde{g}$ direct		$\tilde{q}\tilde{q}$ one-step		$\tilde{g}\tilde{g}$ one-step			NUHM	
1	DQ (data)	Run / lumi block appears in SUSY GRL																
2	HL Trigger (data)	Pass EF_j80_a4tchad_xe100_tclcw_veryloose																
3	Event cleaning	Event Cleaning on data and MC																
4	Lepton veto	No selected e/μ after overlap removal with $p_{\mathrm{T}} > 10$ GeV																
5	$E_{\mathrm{T}}^{\mathrm{miss}}$[GeV] >	160			160	160	160	160				160	160					
6(a)	$p_{\mathrm{T}}(j_1)$ [GeV] >	130			130	130	130	130				130	130					
6(b)	$p_{\mathrm{T}}(j_2)$ [GeV] >	60			60	60	60	60				60	60					
6(c)	$p_{\mathrm{T}}(j_3)$ [GeV] >	–			–	60	40	60				60	60					
6(d)	$p_{\mathrm{T}}(j_4)$ [GeV] >	–			–	–	40	60				60	60					
6(e)	$p_{\mathrm{T}}(j_5)$ [GeV] >	–			–	–	–	–				60	60					
6(f)	$p_{\mathrm{T}}(j_6)$ [GeV] >	–			–	–	–	–				–	60					
7(a)	$\Delta\phi(j_{1,2,(3)}, E_{\mathrm{T}}^{\mathrm{miss}})$ >	0.4			0.4	0.4	0.4	0.4				0.4	0.4					
7(b)	$\Delta\phi(j_{i>3}, E_{\mathrm{T}}^{\mathrm{miss}})$ >	–			–	–	0.2	0.2				0.2	0.2					
8	W candidates	–			$2\,W \to j$ 60<m(W)<100GeV	–	$W \to j +$ $W \to jj$ 60<m(W)<100GeV	–				–	–					
9(a)	$E_{\mathrm{T}}^{\mathrm{miss}} / \sqrt{H_T}$ >	8	15	15	–	–	–	10	10	–	–	–	–	–	–	–		
9(b)	$E_{\mathrm{T}}^{\mathrm{miss}} / m_{\mathrm{eff}}(Nj)$ >	–	–	–	0.25	0.3	0.35	–	–	0.4	0.25	0.2	0.2	0.2	0.25	0.15		
10	m_{eff}(incl.) [GeV] >	800	1200	1600	1800	2200	1100	700	1000	1300	2200	1200	900	1200	1500	1700		

Table 7.9: The 2012 analysis Signal Region selection criteria summary table.

7.4.3 Background Estimation

Similarly to the 2011 analysis, the main SM backgrounds were estimated by calculating TFs using dedicated Control Regions. Table 7.10 shows the different Control Regions used for each SR in the 2012 analysis to calculate the background TFs. The CR selection column in Table 7.10 displays the modified/additional cuts used to define the Control Region. The calculations of the background Transfer Factors all used MC samples (listed in Table 7.8) except for the multijet background, which again used the jet smearing method.

CR name	SR background	CR process	CR selection
CRγ	Z + jets	γ + jets	Isolated photon
CRQ	Multijets	Multijets	min $\Delta\phi$(jet,$\vec{p}_{\mathrm{T}}^{\,\mathrm{miss}}$) < 0.2 and reversed $E_{\mathrm{T}}^{\mathrm{miss}}/m_{\mathrm{eff}}$ or $E_{\mathrm{T}}^{\mathrm{miss}}/\sqrt{H_{\mathrm{T}}}$ cut
CRW	$W \to \ell\nu$ + jets	$W \to \ell\nu$ + jets	30 > M_T < 100 [GeV], b-jet veto
CRT	$t\bar{t}$ and single top	$t\bar{t} \to b\bar{b}qq\ell\nu$	30 > M_T < 100 [GeV], b-tag

Table 7.10: Summary of the SM background CRs used in the 2012 analysis, created using information from [1, 125].

Multijet Background Estimation

The multijet background was once again estimated using the jet smearing method in the 2012 analysis. The jet smearing method used a large sample of pseudo-data that was generated with the 2012 b-veto/b-tag jet response maps (see Chapter 6) with the additional ϕ-smearing corrections applied to smeared jets (see section 6.4). The pseudo-data generated using the jet smearing method was normalised in the multijet Control Region (CRQ).

The multijet background Transfer Factors for each Signal Region are shown in Figure 7.7. It can be seen that most of the Transfer Factors were of the order of 10^{-3}.

Figure 7.8 shows the CRQ m_{eff}(incl.) distributions for search channels 2j (a), 3j (b) and 5j (c). The multijet distributions produced using the jet smearing method are shown in orange. The yellow uncertainty band in the ratio plot includes the jet smearing systematics discussed in section 6.6. It can be seen in Figure 7.8 that the data agreed with the total SM prediction. This once more provided confidence that the jet smearing method was accurately modelling the multijet background.

Figure 7.9 shows the minimum $\Delta\phi$(jet,$E_{\mathrm{T}}^{\mathrm{miss}}$) distributions for search channels 2j (a), 3j (b) and 5j (c). The multijet distributions produced with the jet smearing method are shown by the orange histograms. It should be noted that ϕ-smearing of smeared jets was introduced in the 2012 analysis:

this is the origin of the improvement between the observed data and total estimate in the low $\Delta\phi$ region compared to the 2011 analysis. Figure 7.9 shows that the pseudo-data agreed well with the total expected SM background estimate in all of the Signal Regions.

Figure 7.10 shows the $E_{\mathrm{T}}^{\mathrm{miss}}/m_{\mathrm{eff}}$ ratio distributions in the low minimum $\Delta\phi$ region (min $\Delta\phi < 0.2$) for search channels 2j (a), 3j (b) and 5j (c). Since the $E_{\mathrm{T}}^{\mathrm{miss}}/m_{\mathrm{eff}}$ ratio cut was also used to reject multijet events from the Signal Regions and define the multijet Control Regions, it was also important that the predicted distribution matches the observed distribution in the data. Figure 7.10 shows that there was a disagreement between total background and the observed data in the high $E_{\mathrm{T}}^{\mathrm{miss}}/m_{\mathrm{eff}}$ region of channel 2j (Figure 7.10(a)). However, this region was dominanted by non-multijet events; therefore, the disagreement was believed to be due to overestimation of the other SM backgrounds rather than the multijet prediction from the jet smearing method.

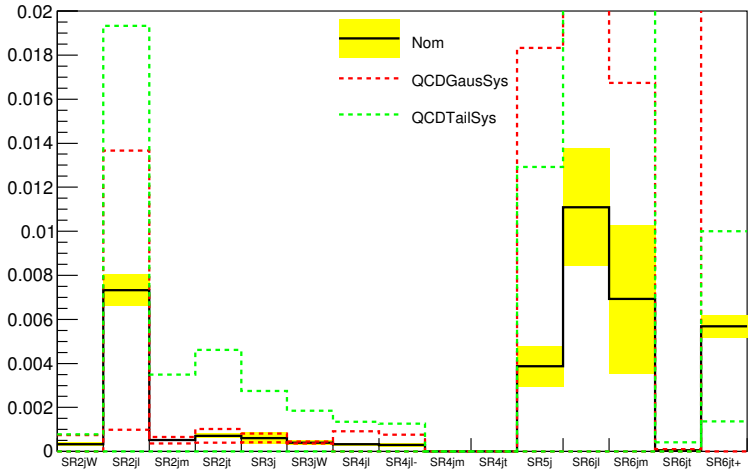

Figure 7.7: The multijet background Transfer Factors for each of the different Signal Regions in the 2012 data set analysis. The systematic uncertainties of the jet smearing method are shown by the dashed green and red lines. The yellow uncertainty bands show the statistical uncertainty on the TFs. This figure was taken from [125].

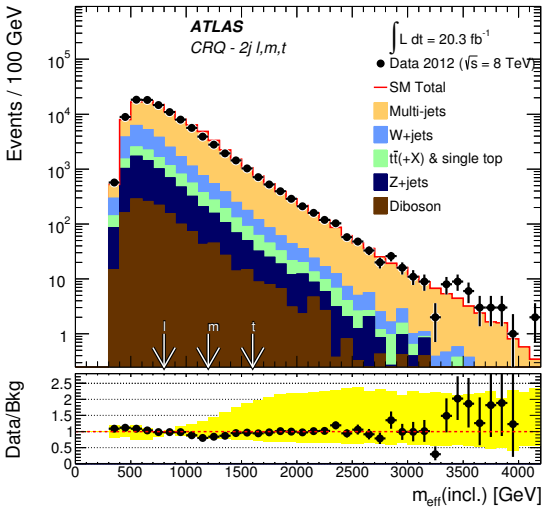

(a) **CRQ – 2j**

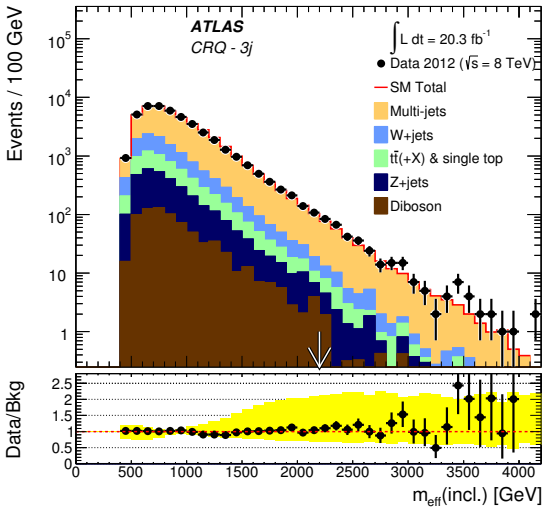

(b) **CRQ – 3j**

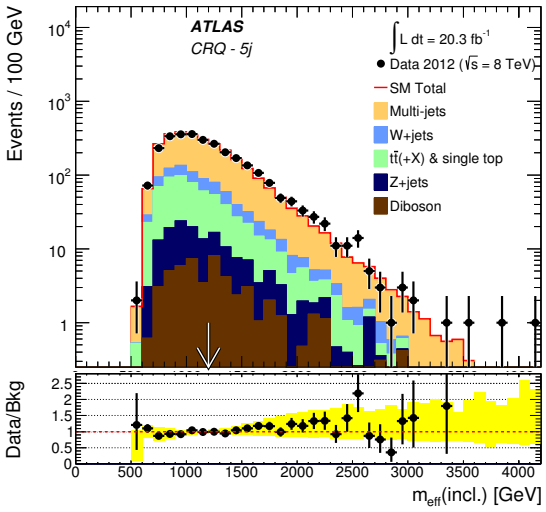

(c) **CRQ – 5j**

Figure 7.8: The CRQ m_{eff} (incl.) distributions for CRQs 2j (a), 3j (b) and 5j (c). The distribution from the 2012 $\sqrt{s} =$ 8 TeV data is shown by the black points. The multijet distribution produced using the jet smearing method is shown in orange. The total SM background estimation is shown by the red line. The SM $t\bar{t}$ and single top, W + jets, Z + jets and diboson backgrounds are shown in green, light blue, dark blue and brown respectively. The yellow uncertainty band on the ratio plot shows the total uncertainty on the jet smearing method and the statistical uncertainty on the MC samples (except multijets). These figures were taken from [1, 125].

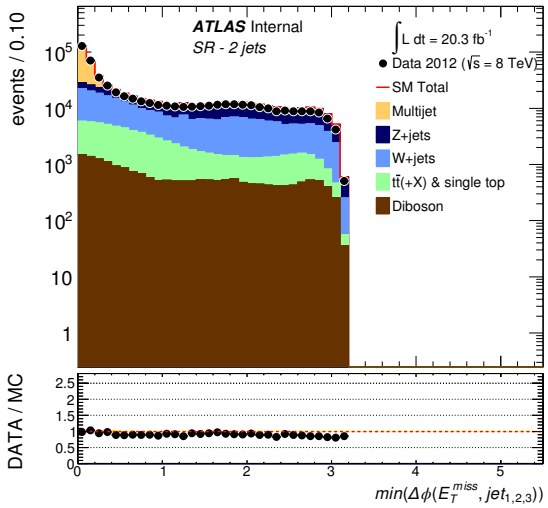

(a) **SR – 2j**

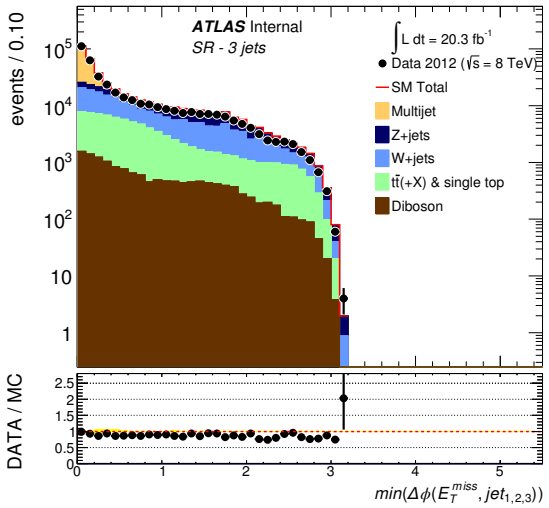

(b) **SR – 3j**

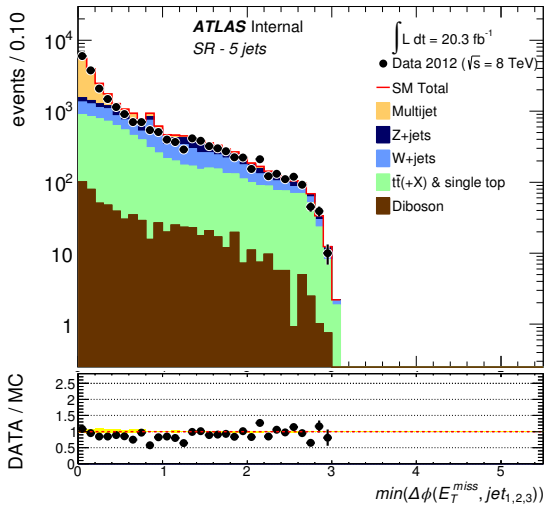

(c) **SR – 5j**

Figure 7.9: The minimum $\Delta\phi$(jet,$E_{\mathrm{T}}^{\mathrm{miss}}$) distributions for SRs 2j (a), 3j (b) and 5j (c) after the jet and $E_{\mathrm{T}}^{\mathrm{miss}}$ selection cuts. The distribution from the 2012 $\sqrt{s} =$ 8 TeV data is shown by the black points. The multijet distribution produced using the jet smearing method is shown by the orange histogram. The total SM background estimation is shown by the red line. The SM $t\bar{t}$ and single top, W + jets, Z + jets and multijet backgrounds are shown in green, light blue, dark blue and orange respectively. The yellow uncertainty band on the ratio plot shows the total uncertainty on the jet smearing method, and the total statistical uncertainty on the MC samples (except multijets). These figures were taken from [125].

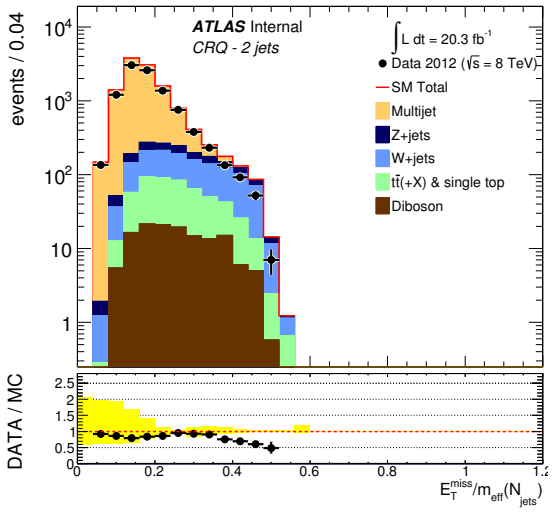

(a) **CRQ – 2j**

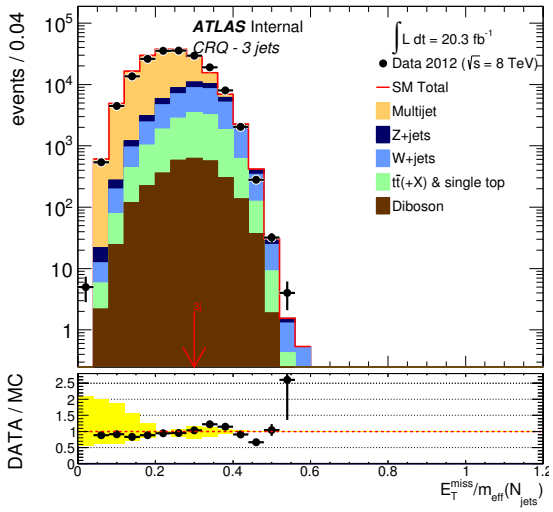

(b) **CRQ – 3j**

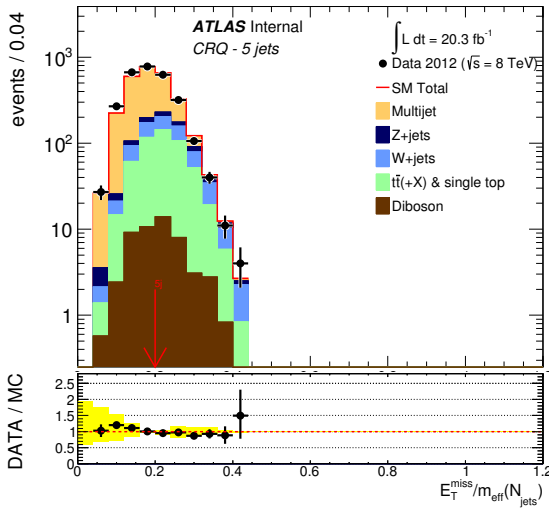

(c) **CRQ – 5j**

Figure 7.10: The $E_{\mathrm{T}}^{\mathrm{miss}}/m_{\mathrm{eff}}$ distributions in the low minimum $\Delta\phi(\mathrm{jet},E_{\mathrm{T}}^{\mathrm{miss}})$ (< 0.2) region for CRQs 2j (a), 3j (b) and 5j (c) before the final m_{eff} selection cut. The distribution from the 2012 $\sqrt{s} =$ 8 TeV data is shown by the black points. The multijet distribution produced using the jet smearing method is shown in orange. The total SM background estimation is shown by the red line. The SM $t\bar{t}$ and single top, W + jets, Z + jets and diboson backgrounds are shown in green, light blue, dark blue and brown respectively. The yellow uncertainty band on the ratio plot shows the total uncertainty on the jet smearing method and the MC statistical uncertainties. These figures were taken from [125]

7.4.4 Results

The full set of analysis results and interpretations for the 2012 data set analysis can be found in references [1, 125]; this section will summarise the main results from the 2012 analysis and show some of the interpretations in SUSY models that were targeted by the 2012 analysis. The mass exclusion limits were obtained from the combination of all of the SRs, and using the SR which had the best sensitivity at each point in the theoretical model.

Figure 7.11 shows the observed number of data events for each Signal Region of the 2012 analysis. The expected contribution from each background process after the simultaneous background fit is also shown in this figure. No data events were observed in Signal Regions 2jW and 4jt. The figure shows that no statistically significant excess was observed in data, which agreed well with predictions from the SM.

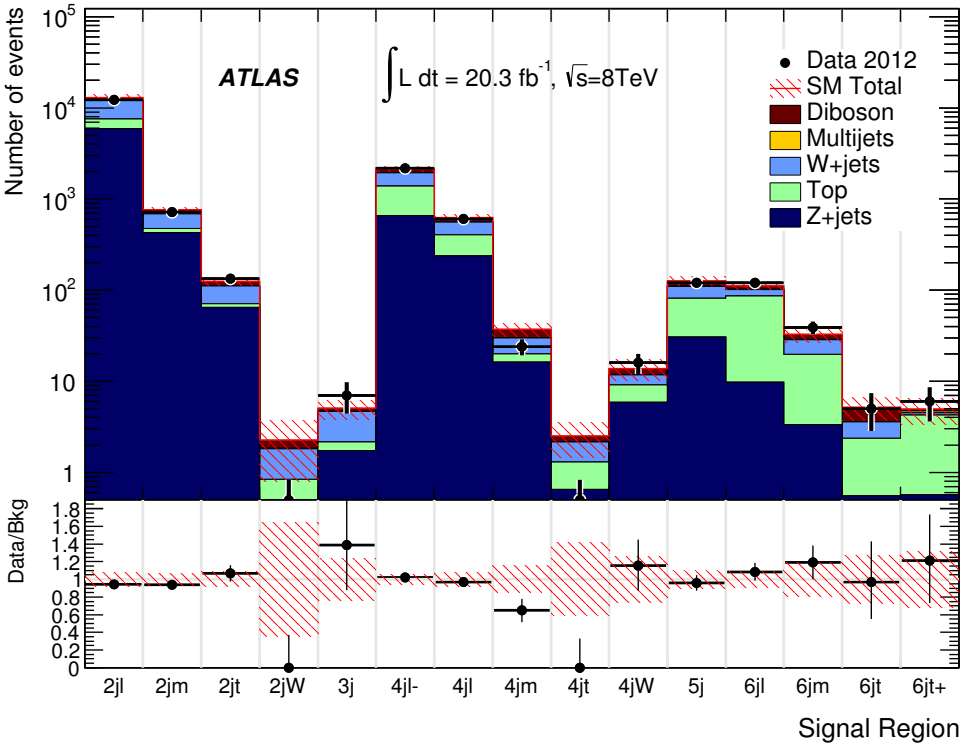

Figure 7.11: The summary of the analysis Signal Region results. The systematic and statistical uncertainties are shown by the red band. No data events were observed in Signal Regions 2jW and 4jt. This figure was taken from [1].

The 95% C.L. exclusion limits for the $m_0 - m_{1/2}$ (a) and $m_{\tilde{q}} - m_{\tilde{g}}$ (b) mass planes in the mSUGRA/CMSSM SUSY model with $\tan\beta = 30$, $A_0 = -2m_0$ and $\mu > 0$ are shown in Figure 7.12. It can be seen that mass values of m_0 up to 6 TeV for $m_{1/2} < 500$ GeV were excluded at a 95% con-

fidence level (see Figure 7.12(a)), and masses of $m_{1/2} < 800\,\text{GeV}$ were excluded at low m_0. This translates to a $m_{\tilde{q}} = m_{\tilde{g}} = 1400\,\text{GeV}$ being excluded at a 95% confidence level in this model (see Figure 7.12(b).

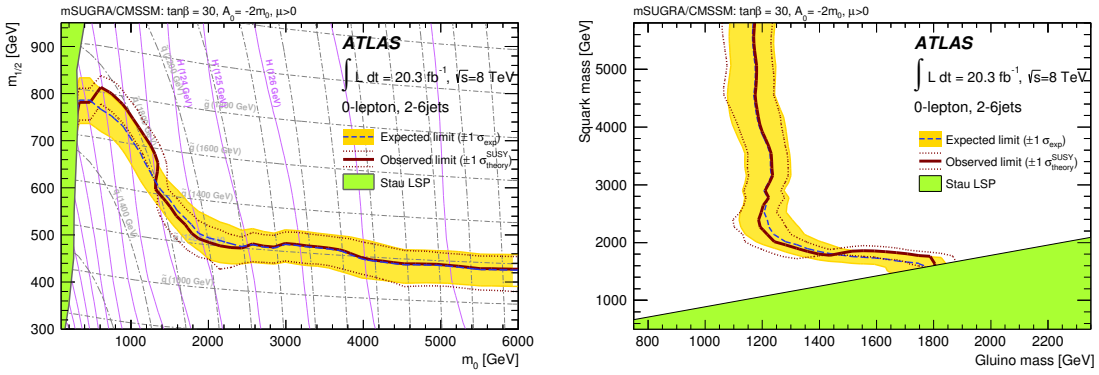

(a) $m_0 - m_{1/2}$ plane

(b) $m_{\tilde{q}} - m_{\tilde{g}}$ plane

Figure 7.12: The 95% C.L. mass exclusion limits on the mSUGRA/CMSSM model in the $m_0 - m_{1/2}$ (a) and $m_{\tilde{q}} - m_{\tilde{g}}$ (b) mass planes. The blue dashed lines show the expected exclusion limit, with the yellow band showing the 1σ uncertainty bounds on the expected limit. The observed limit is shown by the red line, with the red dashed line showing the 1σ uncertainty bands. The green shaded region shows the exclusion regions from theory. These figures were taken from [1].

Figure 7.13 shows the 95% C.L. mass exclusion limit for a simplified pMSSM sq-gl-neutralino model. The Figure shows that $m_{\tilde{q}} = m_{\tilde{g}} \approx 1800\,\text{GeV}$ were excluded at a 95% confidence level with a massless neutralino. Two other exclusion limits are also shown with different $\tilde{\chi}_1^0$ masses (395 GeV and 695 GeV). It can be seen that the mass exclusion limit decreased when a non-massless $\tilde{\chi}_1^0$ was used, leading to the case where a $\tilde{\chi}_1^0$ mass = 695 GeV had a similar mass exclusion limit to the 2011 data set analysis (see section 7.3.4 and Figure 7.6(a)).

The 95% C.L. mass exclusion limit for strong production of squarks and gluinos in direct decays to jets and neutralinos in the simplified pMSSM model is shown in Figure 7.14. The strong production of $\tilde{q}\tilde{q}$ pairs (a) was excluded for masses $m_{\tilde{q}} < 900\,\text{GeV}$ with a massless $\tilde{\chi}_1^0$, and strong production of $\tilde{g}\tilde{g}$ pairs (b) was excluded for masses $m_{\tilde{g}} < 1400\,\text{GeV}$ with a massless $\tilde{\chi}_1^0$. The 2012 analysis also set a new exclusion mass limit on the strong production of $\tilde{q}\tilde{g}$ pairs (c), with masses $m_{\tilde{g}} < 1600\,\text{GeV}$ excluded to a 95% C.L. with a massless $\tilde{\chi}_1^0$. Exclusion limits for the 2011 data set analysis are also shown for the $\tilde{q}\tilde{q}$ and $\tilde{g}\tilde{g}$ processes in these figures. It can be seen that the 2012 data set analysis excludes more phase space than the 2011 data set analysis, which was expected with the increased CoM energy and integrated luminosity of the 2012 data set.

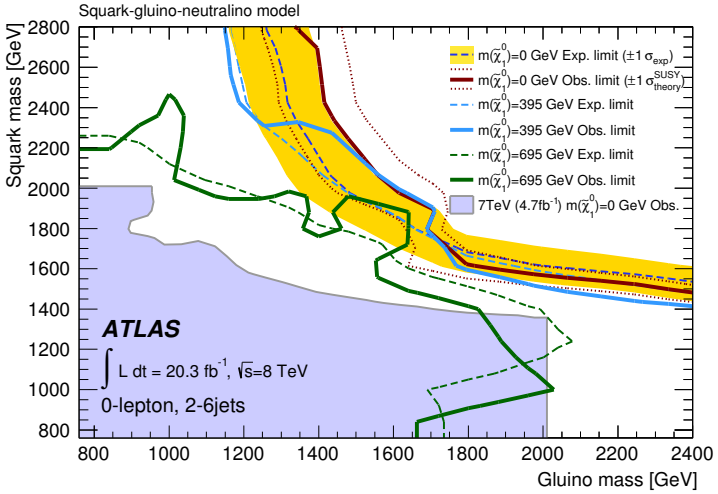

Figure 7.13: The 95% C.L. exclusion limits on the sq-gl-neutrino simplified pMSSM model in the $m_{\tilde{q}} - m_{\tilde{g}}$ mass plane. Three different exclusion limits are shown for different values of the mass of the $\tilde{\chi}_1^0$ (0 GeV, 395 GeV and 695 GeV). For the case of a massless neutralino, the dark blue dashed line shows the expected 95% C.L. exclusion limit with the yellow band showing the 1σ uncertainty bounds on the expected limit. The observed limit is shown by the red line, with the red dashed lines showing the 1σ uncertainty band. The exclusion limit from the previous 2011 ATLAS analysis [2] is shown by the light blue shaded region. Cases in which the neutralino was massive are shown by the green ($\tilde{\chi}_1^0 =$ 395 GeV) and blue ($\tilde{\chi}_i^0 =$ 695 GeV) lines with the solid lines showing the observed exclusion limit and the dashed lines showing the expected exclusion limit. This figure was taken from [1].

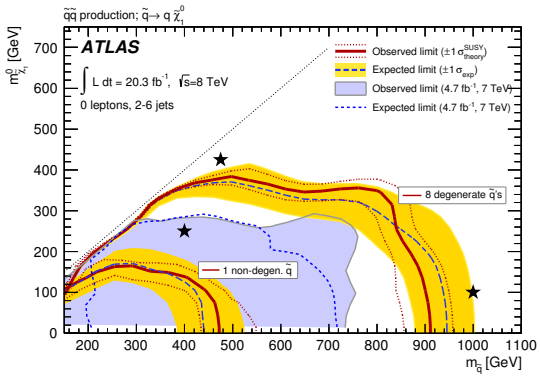

(a) Direct $\tilde{q}\tilde{q}$ decay

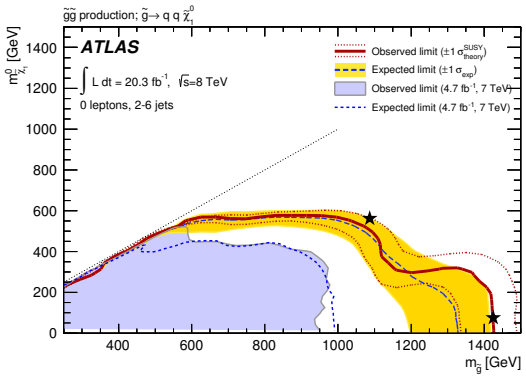

(b) Direct $\tilde{g}\tilde{g}$ decay

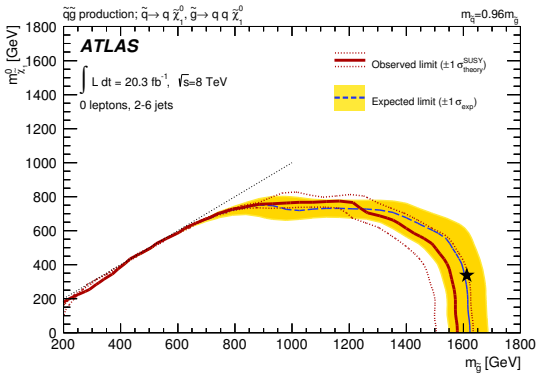

(c) Direct $\tilde{q}\tilde{g}$ decay

Figure 7.14: The 95% C.L. mass exclusion limits for strong production of squarks and gluinos decaying direct to jets and neutralinos in the simplified sq-gl-neutralino pMSSM model. The $\tilde{q}\tilde{q}$ process is shown in (a) for 8 degenerate $\tilde{q}$s and 1 non-degenerate $\tilde{q}$. The $\tilde{g}\tilde{g}$ process is shown in (b), and the $\tilde{q}\tilde{g}$ process is shown in (c). The dark blue dashed lines show the expected 95% mass exclusion limits, with the yellow bands showing the 1σ uncertainty on the expected limits. The observed limits are shown by the red lines, with the red dashed lines showing the 1σ uncertainty bands. The black stars show the reference points where the analysis was optimised. The mass exclusion limits from the ATLAS 2011 analysis [2] (for $\tilde{q}\tilde{q}$ and $\tilde{g}\tilde{g}$ processes) are shown by the light blue shaded regions. These figures were taken from [1].

7.5 Summary

This chapter presented two analyses searching for strongly produced squarks and gluinos in zero lepton final states. The searches used the ATLAS 2011 4.7 fb^{-1} $\sqrt{s} = 7$ TeV and 2012 20.3 fb^{-1} $\sqrt{s} = 8$ TeV data sets. Unfortunately, no statistically significant excess was found in either of the analyses; therefore, 95% C.L. mass exclusion limits were set on the mSUGRA/CMSSM $m_0 - m_{1/2}$ and $m_{\tilde{q}} - m_{\tilde{g}}$ mass planes, and the simplified squark-gluino-neutralino pMSSM model. Figure 7.15 shows a summary of all of the ATLAS searches for supersymmetry in the mSUGRA/CMSSM $m_0 - m_{1/2}$ mass plane using the full 2012 $\sqrt{s} = 8$ TeV data set. It can be seen that the zero lepton, 2-6 jets + $E_{\mathrm{T}}^{\mathrm{miss}}$ analysis (documented in this chapter) provided a significant contribution to the exclusion of the phase space in this supersymmetric model for $m_0 < 1300$ GeV.

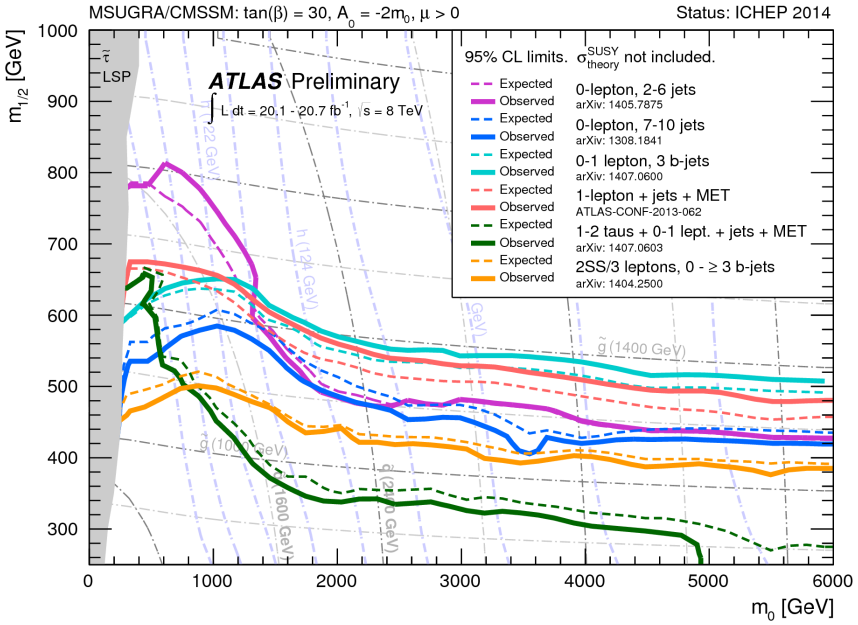

Figure 7.15: The summary of ATLAS searches for SUSY with the 2012 $\sqrt{s} = 8$ TeV data set. Exclusion contours are shown for the mSUGRA/CMSSM $m_0 - m_{1/2}$ mass plane. This figure was taken from [63].

Chapter 8

Summary

The Standard Model has been one of the cornerstones of particle physics. With the recent discovery of the Higgs boson at the LHC in 2012 further validating the theory, the pressing issues of the hierarchy problem and nature of dark matter have become increasingly important. SUSY still remains one of the favoured extensions to the SM, although probably in a more complex form than first thought. This is due to the natural solutions it provides to the problems with the Standard Model. SUSY is expected to produce new particles beyond the SM at the LHC, which should be detectable by the ATLAS detector. Over two years of data analysis has already taken place over run I of the LHC, with no tangible results for the discovery of any of the new particles SUSY proposes. However, world leading exclusion limits on many simplified models have been set, such as the results in Chapter 7.

This thesis has focused on the searches for SUSY with the ATLAS detector over run-I of the LHC. A data-driven technique for estimating the multijet background in SUSY searches was described in Chapters 5 and 6. A potential improvement to the ATLAS event reconstruction algorithm using particle flow was described in Chapter 4. The improved event reconstruction has the potential to significantly improve the jet energy and $E_{\mathrm{T}}^{\mathrm{miss}}$ resolutions, and consequently, the sensitivity of R-parity conserving SUSY analyses. Two direct searches for SUSY in the zero lepton, jets and $E_{\mathrm{T}}^{\mathrm{miss}}$ final state were described in Chapter 7. These searches used the full 2011 $\sqrt{s} = 7\,\mathrm{TeV}$ and 2012 $\sqrt{s} = 8\,\mathrm{TeV}$ data sets. Although no observation of SUSY was found, the analyses set 95% C.L. exclusion limits in the mass planes of the mSUGRA/CMSSM and pMSSM simplified models. $m_{\tilde{q}} = m_{\tilde{g}} = 1400\,\mathrm{GeV}$ were excluded at a 95% confidence level in the mSUGRA/CMSSM simplified model, and $m_{\tilde{q}} = m_{\tilde{g}} \approx 1800\,\mathrm{GeV}$ were excluded at a 95% confidence level with a massless neutralino in the simplified pMSSM model.

The LHC is due to restart recording data in 2015 at the much higher centre-of-mass energy of 13 TeV. The increased centre-of-mass energy will increase the theoretical cross-section for the production of SUSY particles, particularly above 1 TeV. Therefore, the gain in mass reach of SUSY analyses makes this a very exciting time. Even if SUSY is not observed at this higher centre-of-mass energy, that itself would be a very exciting result. The possible implications for naturalness in theoretical SUSY models and the SM would be ground breaking.

Appendix A

Particle Flow Auxiliary Information

A.1 Gaussian Fitting to $E_{\mathrm{T}}^{\mathrm{miss}}$ Distributions

In Chapter 4, various distributions were fitted with a Gaussian function to obtain quantitative results to compare the different $E_{\mathrm{T}}^{\mathrm{miss}}$ algorithms. The σ and mean of the Gaussian were obtained from the fits for these comparisons (see Figures 4.17(d) , 4.22(c) and 4.23(c)). It should be noted that a M_T distribution is actually a Jacobian peak convolved with a Breit-Wigner distribution [134]. The use of a Gaussian function in Figure 4.22 was justified by the proof of principle nature of the study and the complexities involved in fitting the true functional form.

The data distributions of the magnitude of the $E_{\mathrm{T}}^{\mathrm{miss}}$ in $Z \to \mu\mu$ events and the M_T and M_{jj} distributions in $t\bar{t}$ and Wt events were all fitted with a Gaussian function in a region of interest. For the magnitude of the $E_{\mathrm{T}}^{\mathrm{miss}}$ distribution, this region was the Gaussian dominated region of the $E_{\mathrm{T}}^{\mathrm{miss}}$ distribution (approximately $|E_{\mathrm{T}}^{\mathrm{miss}}| < 50$ GeV). In the M_T and M_{jj} distributions, the region of interest was the W boson mass peak (approximately $60 - 100$ GeV). Examples of the Gaussian fits are shown in Figure A.1, which shows the Gaussian fits to the data distributions of the particle flow `RefFinal` $E_{\mathrm{T}}^{\mathrm{miss}}$ algorithm.

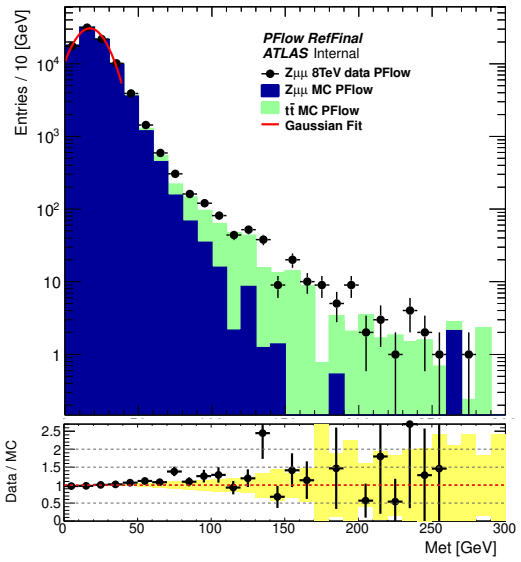

(a) $E_{\mathrm{T}}^{\mathrm{miss}}$ Magnitude

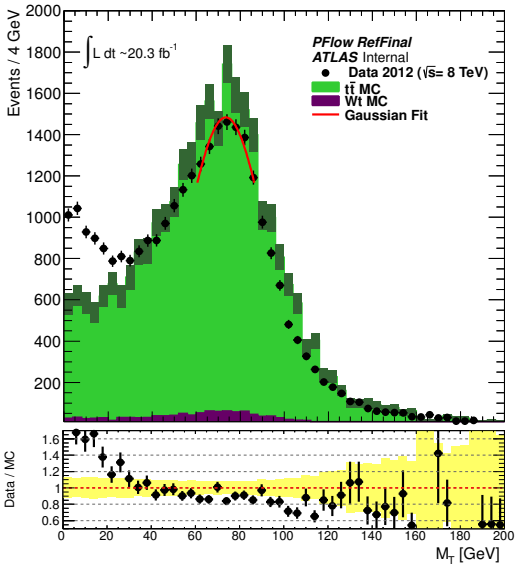

(b) M_T

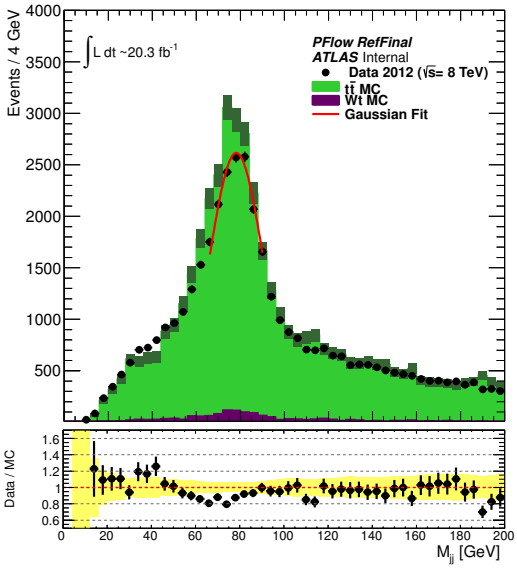

(c) M_{jj}

Figure A.1: Gaussian fits (red lines) to the data $E_{\mathrm{T}}^{\mathrm{miss}}$ distributions for the particle flow `RefFinal` $E_{\mathrm{T}}^{\mathrm{miss}}$ algorithm. Figure (a) shows the magnitude $E_{\mathrm{T}}^{\mathrm{miss}}$ distribution, where the particle flow `RefFinal` distribution for the 2012 $\sqrt{s} = 8\,\mathrm{TeV}$ data set is shown in black and the $Z \to \mu\mu$ and $t\bar{t}$ MC are shown in blue and light green respectively. Figure (b) shows the M_T distribution in $t\bar{t}$ and Wt events, whereas figure (c) shows the M_{jj} distribution in $t\bar{t}$ and Wt events. In figures (b) and (c) the particle flow `RefFinal` distribution for 2012 $\sqrt{s} = 8\,\mathrm{TeV}$ data set is shown in black and the $t\bar{t}$ and Wt MC are shown in green and purple respectively.

Bibliography

[1] ATLAS Collaboration, *Search for squarks and gluinos with the ATLAS detector in final states with jets and missing transverse momentum using* $\sqrt{s}$= *8* TeV *proton-proton collision data*, CERN-PH-EP-2014-093, 2014. JHEP **09** (2014) 176.

[2] ATLAS Collaboration, *Search for squarks and gluinos with the ATLAS detector in final states with jets and missing transverse momentum using 4.7* fb^{-1} *of* $\sqrt{s}$= *7* TeV *proton-proton collision data*, ATL-COM-PHYS-2012-023, 2012. Phys. Rev. **D 87** (2012) 012008.

[3] ATLAS Collaboration, *Search for squarks and gluinos with the ATLAS detector in final states with jets and missing transverse momentum and 20.3* fb^{-1} *of* $\sqrt{s} = 8$ TeV *proton-proton collision data*, ATLAS-COM-CONF-2013-049, Apr, 2013. https://cds.cern.ch/record/1540249.

[4] ATLAS Collaboration, *Search for squarks and gluinos with the ATLAS detector using final states with jets and missing transverse momentum and 5.8* fb^{-1} *of* $\sqrt{s}$=*8* TeV *proton-proton collision data*, ATLAS-CONF-2012-109, Aug, 2012. https://cds.cern.ch/record/1472710.

[5] ATLAS Collaboration, *Search for squarks and gluinos using final states with jets and missing transverse momentum with the ATLAS detector in* $\sqrt{s}$= *7* TeV *proton-proton collisions*, ATLAS-CONF-2012-033, Mar, 2012. https://cds.cern.ch/record/1648042.

[6] ATLAS Collaboration, *Search for direct pair production of the top squark in all-hadronic final states in proton-proton collisions at* $\sqrt{s} = 8$ TeV *with the ATLAS detector*, CERN-PH-EP-2014-112, 2014. JHEP **09** (2014) 015, arXiv:1406.1122 [hep-ex].

[7] ATLAS Collaboration, *Search for direct top squark pair production in events with a Z boson, b-jets and missing transverse momentum in* $\sqrt{s} = 8$ *TeV pp collisions with the ATLAS detector*, Eur. Phys. J. **C 74** (2014) 2883.

[8] G. T. Fletcher, M. Hodgkinson, and M. Schreyer, *A data-driven method for measuring the mismeasured jet background for missing transverse energy searches in multijet, Z+jet and* γ*+jet events*, ATL-COM-PHYS-2014-1243 [ATLAS INTERNAL NOTE], Sept, 2014.

[9] T. Aoyama et al., *Tenth-order QED lepton anomalous magnetic moment: Eighth-order vertices containing a second-order vacuum polarization*, 2012. Phys. Rev. **D 85** (2012) .

[10] W. N. Cottingham and D. A. Greenwood, *An Introduction To The Standard Model of Particle Physics*. Cambridge University Press, 2007.

[11] R. Mann, *An Introduction To Particle Physics and The Standard Model*. Taylor and Francis Group, 2011.

[12] D. Griffiths, *Introduction to Elementary Particles*. Wiley, 2008.

[13] F. Halzen and A. D. Martin, *Quarks & Leptons: An Introductory course in Modern Particle Physics* . John Wiley & Sons, 1984.

[14] *Figure was made by AAAS*, http://www.aaas.org/.

[15] Beringer , J. and others, *The Review of Particle Physics*, Phys. Rev. **D 86** (2012) . http://link.aps.org/doi/10.1103/PhysRevD.86.010001.

[16] M. Srednicki, *Quantum Field Theory*. Cambridge, 2010.

[17] P. W. Higgs, *Broken symmetries and the masses of gauge bosons*, Phys. Rev. Lett. **13** (1964) .

[18] P. W. Higgs, *Broken symmetries, massless particles and gauge fields*, Phys. Lett. **12** (1964) .

[19] R. Brout and F. Englert, *Broken symmetries and the mass of vector mesons*, Phys. Rev. Lett. **13** (1964) .

[20] ATLAS Collaboration, *Observation of a new particle in the search for the Standard Model Higgs boson with the ATLAS detector at the LHC*, Phys. Lett. **B 716** (2012) , arXiv:1207.7214 [hep-ex]. http://arxiv.org/abs/1207.7214.

[21] CMS Collaboration, *Observation of a new particle in the search for the Standard Model Higgs boson with the ATLAS detector at the LHC*, Phys. Lett. **B 716** (2012) , arXiv:1207.7235 [hep-ex]. http://arxiv.org/abs/1207.7235.

[22] ATLAS Collaboration, *Evidence for the spin-0 nature of the Higgs boson using ATLAS data*, Phys. Lett. **B 726** (2013) no. 13, 120 – 144.

[23] Super-Kamiokande Collaboration, *Evidence for oscillation of atmospheric neutrinos*, Phys. Rev. Lett. **81** (1998) 1562.

[24] SNO Collaboration, *Direct Evidence for Neutrino Flavor Transformation from Neutral Current Interactions in the Sudbury Neutrino Observatory*, Phys. Rev. Lett. **89** (2002) 011301.

[25] K. Garrett and G. Duda, *Dark matter: a primer*, Adv. Astron. **2011** (2011) , arXiv:1006.2483 [hep-ph].

[26] J. L. Feng, *Dark Matter Candidates from Particle Physics and Methods of Detection*, Annu. Rev. Astron. Astrophys. **48** (2010) 495.

[27] Planck Collaboration, *Planck 2015 results. I. Overview of products and scientific results*, Feb, 2015. arXiv:1502.01582 [astro-ph.CO].

[28] ATLAS Collaboration, *Measurement of the Higgs boson mass from the $H \to \gamma\gamma$ and $H \to ZZ^* \to 4\ell$ channels in pp collisions at center-of-mass energies of 7 and 8* TeV *with the ATLAS detector*, 2014. Phys. Rev. **D 90** (2014) 052004, http://link.aps.org/doi/10.1103/PhysRevD.90.052004.

[29] A. Nima, D. Savas, and D. Gia, *The Hierarchy Problem and New Dimensions at a Millimeter*, Phys. Lett. **B 429** (1998) .

[30] H. Miyazawa, *Baryon Number Changing Currents*, *Prog. Theor. Phys.* **36 (6)** (1966) 1266–1276.

[31] P. Ramond, *Dual Theory for Free Fermions*, *Phys. Rev.* **D 3** (1971) 2415–2418.

[32] Y. A. Golfand and E. P. Likhtman, *Extension of the Algebra of Poincare Group Generators and Violation of p Invariance*, JETP Lett. **13** (1971) 323–326.

[33] A. Neveu and J. H. Schwarz, *Factorizable dual model of pions*, *Nucl. Phys.* **B 31** (1971) 86–112.

[34] A. Neveu and J. H. Schwarz, *Quark Model of Dual Pions*, *Phys. Rev.* **D 4** (1971) 1109–1111.

[35] J. Gervais and B. Sakita, *Field theory interpretation of supergauges in dual models*, *Nucl. Phys.* **B 34** (1971) 632–639.

[36] D. V. Volkov and V. P. Akulov, *Is the Neutrino a Goldstone Particle?*, *Phys. Lett.* **B 46** (1973) 109–110.

[37] J. Wess and B. Zumino, *A Lagrangian Model Invariant Under Supergauge Transformations*, *Phys. Lett.* **B 49** (1974) 52.

[38] J. Wess and B. Zumino, *Supergauge Transformations in Four-Dimensions*, *Nucl. Phys.* **B 70** (1974) 39–50.

[39] P. M. Stephen, *A Supersymmetry Primer*, Sep, 2011. arXiv:9709356v6 [hep-ph].

[40] I. J. R. Aitchison, *Supersymmetry and the MSSM: An Elementary Introduction*, May, 2005. arXiv:0505105 [hep-ph], http://arxiv.org/abs/hep-ph/0505105.

[41] P. Fayet, *Supersymmetry and Weak, Electrousing LHC Run 1 data using LHC Run 1 data using LHC Run 1 data magnetic and Strong Interactions*, *Phys. Lett.* **B 64** (1976) 159.

[42] G. R. Farrar and P. Fayet, *Phenomenology of the Production, Decay, and Detection of New Hadronic States Associated with Supersymmetry*, *Phys. Lett.* **B 76** (1978) 575–579.

[43] P. Fayet, *Relations Between the Masses of the Superpartners of Leptons and Quarks, the Goldstino Couplings and the Neutral Currents*, *Phys. Lett.* **B 84** (1979) 416.

[44] S. Dimopoulos and H. Georgi, *Softly Broken Supersymmetry and SU(5)*, *Nucl. Phys.* **B 193** (1981) 150.

[45] R. Kaul and P. Majumdar, *Cancellation of Quadratically Divergent Mass Corrections in Globally Supersymmetric Spontaneously Broken Gauge Theories*, *Nucl. Phys.* **B 199** (1982) 36.

[46] A. H. Chamseddine, R. L. Arnowitt, and P. Nath, *Locally Supersymmetric Grand Unification*, *Phys. Rev. Lett.* **49** (1982) 970.

[47] R. Barbieri, S. Ferrara, and C. A. Savoy, *Gauge Models with Spontaneously Broken Local Supersymmetry*, *Phys. Lett.* **B 119** (1982) 343.

[48] L. E. Ibanez, *Locally Supersymmetric SU(5) Grand Unification*, *Phys. Lett.* **B 118** (1982) 73.

[49] L. J. Hall, J. D. Lykken, and S. Weinberg, *Supergravity as the Messenger of Supersymmetry Breaking*, *Phys. Rev.* **D 27** (1983) 2359–2378.

[50] N. Ohta, *Grand unified theories based on local supersymmetry*, *Prog. Theor. Phys.* **70** (1983) 542.

[51] G. L. Kane, C. F. Kolda, L. Roszkowski, and J. D. Wells, *Study of constrained minimal supersymmetry*, *Phys. Rev.* **D 49** (1994) 6173–6210, arXiv:hep-ph/9312272 [hep-ph].

[52] L. J. Hall, D. Pinner, and J. T. Ruderman, *A Natural SUSY Higgs Near* 125 GeV, Feb, 2012. arXiv:1112.2703 [hep-ph], http://arxiv.org/abs/1112.2703.

[53] E. Bagnaschi, G. F. Giudice, P. Slavich, and A. Strumia, *Higgs Mass and Unnatural Supersymmetry*, 2014. JHEP **1409** (2014) 092, arXiv:1407.4081 [hep-ph], http://arxiv.org/abs/1407.4081.

[54] K. J. Bae, H. Baer, V. Barger, D. Mickelson, and M. Savoy, *Implications of naturalness for the heavy Higgs bosons of supersymmetry*, Phys. Rev. **D 90** (2014) , arXiv:1407.3853 [hep-ph].

[55] Cahill-Rowley, M. and Hewett, J.L. and Ismail, A. and Rizzo, T.G., *pMSSM Studies at the 7, 8 and 14 TeV LHC*, July, 2013. arXiv:1307.8444 [hep-ph].

[56] S. Borowka, T. Hahn, S. Heinemeyer, G. Heinrich, and W. Hollik, *Momentum-dependent two-loop QCD corrections to the neutral Higgs-boson masses in the MSSM*, 2014. Eur. Phys. J. **C 74** (2014) no. 8, 2994.

[57] Djouadia, A. and Kneura, J.-L. and Moultaka, G., *SuSpect: A Fortran code for the Supersymmetric and Higgs particle spectrum in the MSSM*, 2007. Comput. Phys. Commun. **176** (2007) .

[58] M. Krmer, A. Kulesza, R. van der Leeuw, M. Mangano, S. Padhi, T. Plehn, and X. Portell, *Supersymmetry production cross sections in pp collisions at* $\sqrt{s} = 7$ TeV, CERN-PH-TH-2012-163, Jun, 2012. arXiv:1206.2892 [hep-ph].

[59] Buttar, C. and others , *Standard Model Handles and Candles Working Group: Tools and Jets Summary Report*, March, 2008. arXiv:0803.0678 [hep-ph].

[60] T. Gleisberg, S. Hoeche, F. Krauss, M. Schonherr, S. Schumann, et al., *Event generation with SHERPA 1.1*, 2009. JHEP **0902** (2009) 007, arXiv:0811.4622 [hep-ph].

[61] ATLAS Collaboration, G. Aad et al., *Jet energy measurement with the ATLAS detector in proton-proton collisions at* $\sqrt{s} = 7$ TeV, CERN-PH-EP-2011-191, 2011. Eur. Phys. J. **C 73** (2011) 2304.

[62] ATLAS and CMS Collaboration, *Supersymmetry searches at the LHC*, ATL-PHYS-PROC-2012-244, Nov, 2012. arXiv:1211.3887 [hep-ex].

[63] *Figure from CERN webpage:*, https://twiki.cern.ch/twiki/bin/view/AtlasPublic/SupersymmetryPublicResults.

[64] *Figure from CERN webpage:*, https://twiki.cern.ch/twiki/bin/view/CMSPublic/PhysicsResultsSUS.

[65] CMS Collaboration, *Search for Supersymmetry at the LHC in Events with Jets and Missing Transverse Energy*, 2011. Phys. Rev. Lett. **107** (2011) 221804, http://link.aps.org/doi/10.1103/PhysRevLett.107.221804.

[66] ATLAS Collaboration, *Multi-channel search for squarks and gluinos in* $\sqrt{s} = 7$ TeV *pp collisions with the ATLAS detector at the LHC*, 2013. Eur. Phys. J. **C 73** (2013) no. 3, 2362, http://dx.doi.org/10.1140/epjc/s10052-013-2362-5.

[67] L. Evans and P. Bryant, *LHC Machine*, 2008. JINST **3** (2008) S08001.

[68] ATLAS Collaboration, *ATLAS Fact Sheet*, 2011. http://www.atlas.ch/fact-sheets-view.html.

[69] ATLAS Collaboration, *The ATLAS Experiment at the CERN Large Hadron Collider*, JINST **3** (2008) S08003.

[70] CMS Collaboration, *The CMS experiment at the CERN LHC*, 2008. JINST **3** (2008) S08004.

[71] LHCb Collaboration, *The LHCb Detector at the LHC*, 2008. JINST **3** (2008) S08005.

[72] ALICE Collaboration, *The ATLAS Experiment at the CERN Large Hadron Collider*, JINST **3** (2008) S08002.

[73] *Figure from CERN webpage:*, http://te-epc-lpc.web.cern.ch/te-epc-lpc/machines/lhc/general.stm.

[74] ATLAS Collaboration, *Expected Performance of the ATLAS Experiment Detector,Trigger and Physics*, CERN-OPEN-2008-020, Aug, 2009. arXiv:0901.0512v4 [hep-ex], https://cds.cern.ch/record/1125884.

[75] M. Schott and M. Dunford, *Review of single vector boson production in pp collisions at* $\sqrt{s}$ *= 7* TeV, Eur. Phys. J. **C 74** (2014) 2916.

[76] A. Andronic and J. Wessels, *Transition Radiation Detectors*, November, 2011. arXiv:1111.4188 [physics.ins-det].

[77] C. W. Fabjan and F. Gianotti, *Calorimetry for particle physics*, Rev. Mod. Phys. **75** (2003) 1243–1286. http://link.aps.org/doi/10.1103/RevModPhys.75.1243.

[78] W. R. Leo, *Techniques for Nuclear and Particle Physics Experiments*. Springer, 1994.

[79] *Figure from CERN webpage:*, https://cds.cern.ch/record/910381.

[80] ATLAS Collaboration, *The ATLAS Simulation Infrastructure*, CERN-PH-EP-2010-044, 2010. Eur. Phys. J. **C 70** (2010) 823.

[81] Sjstrand, T. and Mrenna, S. and Skands, P., *PYTHIA 6.4 physics and manual*, 2006. JHEP **05** (2006) 026.

[82] Sjstrand, T. and Mrenna, S. and Skands, P., *A Brief Introduction to PYTHIA 8.1*, CERN-LCGAPP-2007-04, 2008. Comput. Phys. Commun. **178** (2008) , arXiv:0710.3820 [hep-ph].

[83] M. L. Mangano, M. Moretti, F. Piccinini, R. Pittau, and A. D. Polosa, *ALPGEN, a generator for hard multiparton processes in hadronic collisions*, 2003. JHEP **07** (2003) 001, arXiv:hep-ph/0206293.

[84] A. Martin, W. Stirling, R. Thorne, and G. Watt, *Parton distributions for the LHC*, 2009. Eur. Phys. J. **C 63** (2009) 189–285, arXiv:0901.0002 [hep-ph].

[85] J. M. Butterworth, J. R. Forshaw, and M. H. Seymour, *Multiparton interactions in photoproduction at HERA*, Z. Phys. **C 72** (1996) 637–646, arXiv:hep-ph/9601371.

[86] GEANT4 Collaboration, S. Agostinelli, J. Allison, K. Amako, J. Apostolakis, and H. Araujo, *Geant4a simulation toolkit*, 2003. Nucl. Inst. and Meth. **A 506** (2003) no. 3, 250 – 303, http://www.sciencedirect.com/science/article/pii/S0168900203013688.

[87] ATLAS Collaboration, W. Lukas, *Fast Simulation for ATLAS: Atlfast-II and ISF*, ATL-COM-SOFT-2012-137, June, 2012.

[88] https://twiki.cern.ch/twiki/bin/view/AtlasProtected/AtlasProductionGroupMC12a.

[89] https://twiki.cern.ch/twiki/bin/view/AtlasProtected/PileupReweighting.

[90] ATLAS Collaboration, *Electron and photon energy calibration with the ATLAS detector using LHC Run 1 data*, Eur. Phys J. **C 74** (2014) 3071, arXiv:1407.5063 [hep-ex].

[91] ATLAS Collaboration, *Measurement of the muon reconstruction performance of the ATLAS detector using 2011 and 2012 LHC proton-proton collision data*, Eur. Phys J. **C 74** (2014) 3130, arXiv:1407.3935 [hep-ex].

[92] https://twiki.cern.ch/twiki/bin/view/AtlasProtected/AtlasProductionGroupMC11b.

[93] https://twiki.cern.ch/twiki/bin/view/AtlasProtected/AtlasProductionGroupMC11c.

[94] G. Corcella et al., *HERWIG 6.5: an event generator for Hadron Emission Reactions With Interfering Gluons (including supersymmetric processes)*, 2001. JHEP **01** (2001) 010, arXiv:hep-ph/0011363.

[95] G. Corcella et al., *HERWIG 6.5 release note*, 2002. arXiv:hep-ph/0210213.

[96] A. Sherstnev and R. S. Thorne, *Parton Distributions for LO Generators*, Eur. Phys. J. **C 55** (2008) 553–575, arXiv:0711.2473 [hep-ph].

[97] H.-J. Lai, J. Huston, S. Mrenna, P. Nadolsky, D. Stump, et al., *Parton Distributions for Event Generators*, 2010. JHEP **1004** (2010) 035, arXiv:0910.4183 [hep-ph].

[98] S. Frixione and B. R. Webber, *Matching NLO QCD computations and parton shower simulations*, 2002. JHEP **06** (2002) 029, arXiv:hep-ph/0204244.

[99] S. Frixione, P. Nason, and B. R. Webber, *Matching NLO QCD and parton showers in heavy flavour production*, 2003. JHEP **08** (2003) 007, arXiv:hep-ph/0305252.

[100] P. M. Nadolsky et al., *Implications of CTEQ global analysis for collider observables*, Phys. Rev. **D 78** (2008) 013004.

[101] B. P. Kersevan and E. Richter-Was, *The Monte Carlo event generator AcerMC version 2.0 with interfaces to PYTHIA 6.2 and HERWIG 6.5*, arXiv:hep-ph/0405247 [hep-ph].

[102] https://twiki.cern.ch/twiki/bin/view/AtlasProtected/AtlasProductionGroupMC12b.

[103] H.-L. Lai, M. Guzzi, J. Huston, Z. Li, P. M. Nadolsky, J. Pumplin, and C.-P. Yuan, *New parton distributions for collider physics*, Phys. Rev. **D 82** (2010) 074024. http://link.aps.org/doi/10.1103/PhysRevD.82.074024.

[104] ATLAS Collaboration, *ATLAS Run 1 Pythia8 tunes*, ATL-PHYS-PUB-2014-021, Nov, 2014.

[105] P. Nason, *A New method for combining NLO QCD with shower Monte Carlo algorithms*, 2004. JHEP **0411** (2004) 040, arXiv:hep-ph/0409146 [hep-ph].

[106] http://atlasdqm.web.cern.ch/atlasdqm/grlgen/Susy/Susy_v01/.

[107] https://twiki.cern.ch/twiki/bin/viewauth/AtlasProtected/GoodRunListsForAnalysis.

[108] https://twiki.cern.ch/twiki/bin/view/AtlasPublic/LuminosityPublicResults.

[109] ATLAS Collaboration, W. Lampl, S. Laplace, D. Lelas, P. Loch, H. Ma, S. Menke, S. Rajagopalan, D. Rousseau, S. Snyder, and G. Unal, *Calorimeter Clustering Algorithms: Description and Performance*, ATL-LARG-PUB-2008-002, Apr, 2008.

[110] M. Cacciari, G. P. Salam, and G. Soyez, *The anti-k_t jet clustering algorithm*, 2008. JHEP **0804** (2008) 063, arXiv:0802.1189 [hep-ph].

[111] ATLAS Collaboration, *Commissioning of high performance b-tagging algorithms with the ATLAS detector*, ATLAS-CONF-2011-102, Jul, 2011.

[112] ATLAS Collaboration, *Performance of the ATLAS Secondary Vertex b-tagging Algorithm in 7* TeV *Collision Data*, ATLAS-CONF-2010-042, Jul, 2010.

[113] ATLAS Collaboration, *Calibration of the performance of b-tagging for c and light-flavour jets in the 2012 ATLAS data*, ATLAS-CONF-2014-046, Jul, 2014.

[114] ATLAS Collaboration, *Electron reconstruction and identification efficiency measurements with the ATLAS detector using the 2011 LHC protonproton collision data*, CERN-PH-EP-2014-040, 2014. Eur. Phys. J. **C 74** (2014) 2941.

[115] ATLAS Collaboration, *Electron efficiency measurements with the ATLAS detector using the 2012 LHC proton-proton collision data*, ATLAS-CONF-2014-032, Jun, 2014.

[116] ATLAS Collaboration, *Measurements of the photon identification efficiency with the ATLAS detector using 4.9 fb^1 of pp collision data collected in 2011*, ATLAS-CONF-2012-123, Aug, 2012.

[117] https://twiki.cern.ch/twiki/bin/viewauth/AtlasProtected/MCPAnalysisGuidelinesData2012.

[118] ATLAS Collaboration, *Performance of Missing Transverse Momentum Reconstruction in Proton-Proton Collisions at 7* TeV *with ATLAS*, Eur. Phys. J. **C 72** (2012) 1844, arXiv:1108.5602 [hep-ex].

[119] ATLAS Collaboration, *Data-driven determination of the energy scale and resolution of jets reconstructed in the ATLAS calorimeters using dijet and multijet events at* $\sqrt{s} = 8\ TeV$, ATLAS-CONF-2015-017, Apr, 2015.

[120] ATLAS Collaboration, *Jet energy resolution in proton-proton collisions at* $\sqrt{s} = 7$ TeV *recorded in 2010 with the ATLAS detector*, Eur. Phys. J. **C 73** (2013) 2306.

[121] ATLAS Collaboration, *Measurement of the b-tag Efficiency in a Sample of Jets Containing Muons with 5* fb^1 *of Data from the ATLAS Detector*, ATLAS-CONF-2012-043, Mar, 2012.

[122] ATLAS Collaboration, *Electron performance measurements with the ATLAS detector using the 2010 LHC protonproton collision data*, Eur. Phys. J. **C 72** (2012) 1909.

[123] ATLAS Collaboration, *Improved luminosity determination in pp collisions at* $\sqrt{s} = 7$ TeV *using the ATLAS detector at the LHC*, Eur. Phys. J **C 73** (2013) 2518, arXiv:1302.4393 [hep-ex].

[124] S. van der Meer, *Calibration of the effective beam height in the ISR*, CERN-ISR-PO-68-31, 1968.

[125] ATLAS Collaboration, *Search for squarks and gluinos with the ATLAS detector in final states with jets and missing transverse momentum and* $20.3 fb^1$ *of* $\sqrt{s} = 8$ TeV *proton-proton collision data: supporting documentation*, ATL-COM-PHYS-2013-1224 [ATLAS INTERNAL NOTE], March, 2014. https://cds.cern.ch/record/1595965.

[126] ALEPH Collaboration, *Performance of the ALEPH detector at LEP*, Nucl. Inst. and Meth. **A 360** (1995) 481.

[127] DELPHI Collaboration, *Performance of the DELPHI detector*, Nucl. Inst. and Meth. **A 378** (1996) 57.

[128] A. Elagin, P. Murat, A. Pranko, and A. Safonov, *Probabilistic particle flow algorithm for high occupancy environment*, Nucl. Inst. and Meth. **A 705** (2012) 93.

[129] CMS Collaboration, *Commissioning of the Particle-flow Event Reconstruction with the first LHC collisions recorded in the CMS detector*, CMS-PAS-PFT-10-001, 2010.

[130] M. Hodgkinson, D. Tovey, and R. Duxfield, *Energy Flow Reconstruction with the eflowRec Combined Reconstruction Software in Athena 15.6.9.8*, ATL-PHYS-INT-2011-031 [ATLAS INTERNAL NOTE], 2011.

[131] ATLAS Collaboration, *Search for Single Production of Vector-like Quarks Coupling to Light Generations in 4.64 fb^{-1} of ATLAS Data at $\sqrt{s} = 7$ TeV*, ATLAS-CONF-2012-137, Sep, 2012.

[132] D. W. Miller, A. Schwartzman, and D. Su, *Jet-Vertex Association Algorithm*, ATL-COM-PHYS-2008-008 [ATLAS INTERNAL NOTE], Jan, 2008.

[133] D. W. Miller, A. Schwartzman, and D. Su, *Pile-up jet energy scale corrections using the jet-vertex fraction method*, ATL-PHYS-INT-2009-090 [ATLAS INTERNAL NOTE], Sep, 2009.

[134] A. S. Gordon, *Measurement of the W Boson Mass With the Collider Detector at Fermilab*, http://lppc.physics.harvard.edu/theses/agordon.pdf, 1998.

[135] R. Duxfield, *Background control in inclusive supersymmetry searches and offline reconstruction at ATLAS*, EThOS:uk.bl.ethos.537964, 2008.

[136] S. Owen, *Multijet Background Estimation for Supersymmetry Searches Using the ATLAS Detector at the Large Hadron Collider*, eTheses:2854, 2012.

[137] S. Owen, *Data-driven estimation of the multijet background 1 to SUSY searches with jets and missing transverse momentum at ATLAS using jet smearing*, ATL-PHYS-INT-2012-008 [ATLAS INTERNAL NOTE], Feb, 2012. https://cds.cern.ch/record/1423310.

[138] ATLAS Collaboration, *Search for direct production of charginos, neutralinos and sleptons in final states with two leptons and missing transverse momentum in pp collisions at $\sqrt{s} =$ 8* TeV *with the ATLAS detector*, 2014. JHEP **05** (2014) 071.

[139] S. Asai et al., *Search for squarks and gluinos using final states with jets and missing transverse momentum with the ATLAS experiment in $\sqrt{s} = 7$ TeV proton-proton collisions: supporting documentation*, ATL-PHYS-INT-2012-061 [ATLAS INTERNAL NOTE], Sep, 2012.

[140] https://twiki.cern.ch/twiki/bin/view/Atlas/TrigJetMenu.

[141] T. Skwarnicki, *A study of the radiative CASCADE transitions between the Upsilon-Prime and Upsilon resonances*, DESY-F31-86-02.

[142] I. Hinchliffe, F. E. Paige, M. D. Shapiro, J. Söderqvist, and W. Yao, *Precision SUSY measurements at CERN LHC*, 1997. Phys. Rev. **D 55** (1997) 5520.

[143] G. Cowan, K. Cranmer, E. Gross, and O. Vitells, *Asymptotic formulae for likelihood-based tests of new physics*, Eur. Phys. J. **C 71** (2011) 1554.

[144] R. Bruneliere, M. Baak, J. Lundberg, M. C. Rammensee, and T. J. Khoo, *Setting exclusion limits in ATLAS supersymmetry searches with a likelihood ratio based method*, ATL-PHYS-INT-2011-032 [ATLAS INTERNAL NOTE], Apr, 2011.

[145] Bahr, M. and others, *Herwig++ Physics and Manual*, Eur. Phys. J. **C 58** (2008) 639, arXiv:0803.0883 [hep-ph].

[146] Alwall, J. and others , *MadGraph/MadEvent v4: The New Web Generation*, 2007. JHEP **09** (2007) 028, arXiv:0706.2334 [hep-ph].

[147] Maltoni, F. and Stelzer, T. , *MadEvent: Automatic event generation with MadGraph*, 2003. JHEP **0302** (2003) 027, arXiv:hep-ph/0208156 [hep-ph].

[148] S. Asai et al., *Further search for squarks and gluinos using final states with jets and missing transverse momentum with the ATLAS detector in* $\sqrt{s} = 7$ TeV *proton-proton collisions: supporting documentation*, ATL-PHYS-INT-2011-085 [ATLAS INTERNAL NOTE], 2011.